Development of Advanced Diagnostics for High Energy Density Plasmas

Hannah Poole

Lady Margaret Hall

University of Oxford

Work submitted for the degree of

Doctor of Philosophy in Atomic and Laser Physics

Hilary, 2024

For C.M.

~

"Even if the last move did not succeed,

the inner command says move again."

- Seamus Heaney

Abstract

The field of high-energy density physics explores the properties of matter at extreme conditions, crucial for both astrophysical insights and in the pursuit of fusion energy. However, the complexity of competing forces influencing material behaviour within this regime necessitates experimental validation of theoretical models. One powerful experimental technique capable of probing the equation of state is Thomson scattering.

This thesis investigates the use of Thomson scattering across diverse experimental setups in the high-energy density regime. Bayesian inference techniques are employed for inferring thermodynamic conditions from experimental observations. Firstly, the feasibility of using Thomson scattering to discern in-flight conditions within inertial confinement fusion implosions is presented. Spatially-integrated synthetic scattering spectra are generated to infer information about the inhomogeneous compressed shell under various adiabat capsule conditions. Secondly, a multi-messenger platform using velocimetry and *in situ* angularly and spectrally resolved X-ray scattering is fielded to measure the thermodynamic conditions and ion structure factor of warm dense matter silicon. The observed liquid scattering is used to infer the pressure, density and temperature state without relying on equation of state models. In addition, the measurements are sufficient to distinguish between and rule out some ion screening models. Finally, temporally-resolved optical Thomson scattering is utilised to characterise turbulent plasmas generated at two high-power laser facilities. These platforms aim to understand magnetic-field generation and amplification to reconcile observations in the universe. Perturbative heating effects induced by the Thomson probe are observed on one platform, affecting the inferred conditions and influencing the mechanisms driving magnetic field amplification. The results from these experiments demonstrate the power of Thomson scattering to benchmark theoretical modelling, in particular when used in conjunction with alternate *in situ* diagnostics.

Acknowledgements

To thank all those who have contributed and supported me in the completion of this work, would, I fear, be to write a thesis in and of itself. However, I will attempt to cover all I can. First and foremost, I extend my gratitude to my supervisors, Gianluca Gregori and Sean Regan. Your guidance provided me with the opportunity to work on diverse projects, broaden my horizons, and engage in a wide range of collaborations. I never anticipated that my academic journey would culminate in a DPhil, and I am profoundly grateful that you took a chance on me. I would also like to thank my one and forever post-doc, Charlotte Palmer. Without your patience and support, I doubt I would have ever navigated the OMEGA shot request form, and I have learned so much about being a PI from you. To Archie Bott and Petros Tzeferacos, I am grateful for your tireless support and enthusiasm, and for always taking the time to explain the theoretical beast that is the TDYNO campaign.

It would, however, be remiss of me to only acknowledge the academic support received through this thesis. My journey in Physics would not have been possible without the exceptional teaching and encouragement from my teacher, Mr Jacobs. I will never forget how he nurtured my curiosity, culminating in his remark, "Well, to learn this, you will have to study Physics at University". His words were a catalyst that set me on this path. A special mention also to my maths teachers, Mr Williamson and Mr Riggs-Long, who managed to make maths fun; the pleasure of their classes was all mine.

This journey most certainly wouldn't have been possible without the support and humour of my friends and colleagues. Charlie and Tom, my partners in crime, I feel incredibly fortunate to have had such amazing friends by my side. You were there to laugh and support me through all the good and bad times. I can only hope that I have reciprocated in kind. Oliver, my colleague, your German reasoning was often the grounding I needed. Though, alas, I never did take up rowing! Pontus, your famous quote, "It's not what you want, it's what you have", has stayed with me not only in my

academic work but also in my personal life. You can take comfort in knowing that I will no longer be a distraction in the Simon room! Robin, and of course Ella, thank you for the many meals provided and for often dragging me out of the DPhil rabbit holes. Alessandro, my not-in-air-quotes friend, I will never hear the word 'beautiful' again without your wondrous accent coming to mind. To Oscar, you are far from forgotten, and words cannot express how much I wish you were finishing this journey with me.

To my former colleagues, Pete, Dave, Guy, John and Tim. You brought humour back to the study of Physics and taught me so much about being an experimental physicist. I certainly would not be the researcher I am today without your support and friendship.

Those who deserve the greatest thanks are my long-suffering family. Mum and Dad, my lifelong support system, thank you for enduring the never-ending highs and lows of my academic journey. Knowing that you are always just a phone call away is a blessing for which I will be forever grateful. My brother Matthew, I am sure you will be glad to never hear about the DPhil again, and I thank you for always being my gaming partner! To my aunts, Mary-Frances, Theresa, and Kathleen, thank you for always being there to house me or feed me. I appreciate all your love and support immensely.

Finally, this acknowledgement would be far from complete without mentioning Adrien. When we first met, I swore I would never embark on a DPhil, and yet, not two hours later, Gianluca approached me with the opportunity to undertake this work. There is a part of me that can't help but feel that moment was one of fate. You have provided support both academically and through all the moments where I doubted myself. Wherever our journeys take us, I will be forever grateful that you were there for this part of mine.

Funding Acknowledgements

This material is based upon work supported by the Department of Energy [National Nuclear Security Administration] University of Rochester "National Inertial Confinement Fusion Program" under Award Number DE-NA0004144.

Table of Contents

List of Figures

List of Tables

Chapter 1

Diagnosing High Energy Density Matter

In times defined by the urgent need to address the escalating threat of global warming, with the planet inching closer to the critical threshold of 1.5°C, scientists face the challenge of devising sustainable, carbon-neutral methods for energy production. In pursuit of this, attention has turned to harnessing natural processes such as fission and fusion. However, despite decades of dedicated research, the realisation of fusion energy remains elusive, primarily due to the formidable obstacles inherent in generating and sustaining the extreme conditions requisite for fusion reactions. This challenge has sparked the expansion and training of a new generation of scientists in a multidisciplinary field known as high-energy density physics (HEDP).

1.1 High Energy Density Physics

High-energy density physics represents a captivating field, encompassing plasma physics, condensed matter physics and material science. At its core, this field focuses on understanding material behaviour under extreme conditions, typically surpassing 100 GPa - equivalent to 10^6 times the Earth's atmospheric pressure. Within this domain, temperatures range from $10^3 - 10^8$ K ($0.1 - 10^4$ eV), and densities spanning $1 - 100\,\mathrm{g/cm^3}$. These conditions push beyond the boundaries of the conventional frameworks of classical plasma physics or condensed matter physics. Instead, they give rise to a unique amalgamation of traits, where materials exhibit characteristics of both condensed matter and plasma physics. This fusion of characteristics makes modelling HED matter incredibly challenging, necessitating a deeper understanding through experimental validation and the development of innovative diagnostic techniques tailored to high-energy density matter.

With the advent of high-power lasers, a laboratory-based exploration into extreme

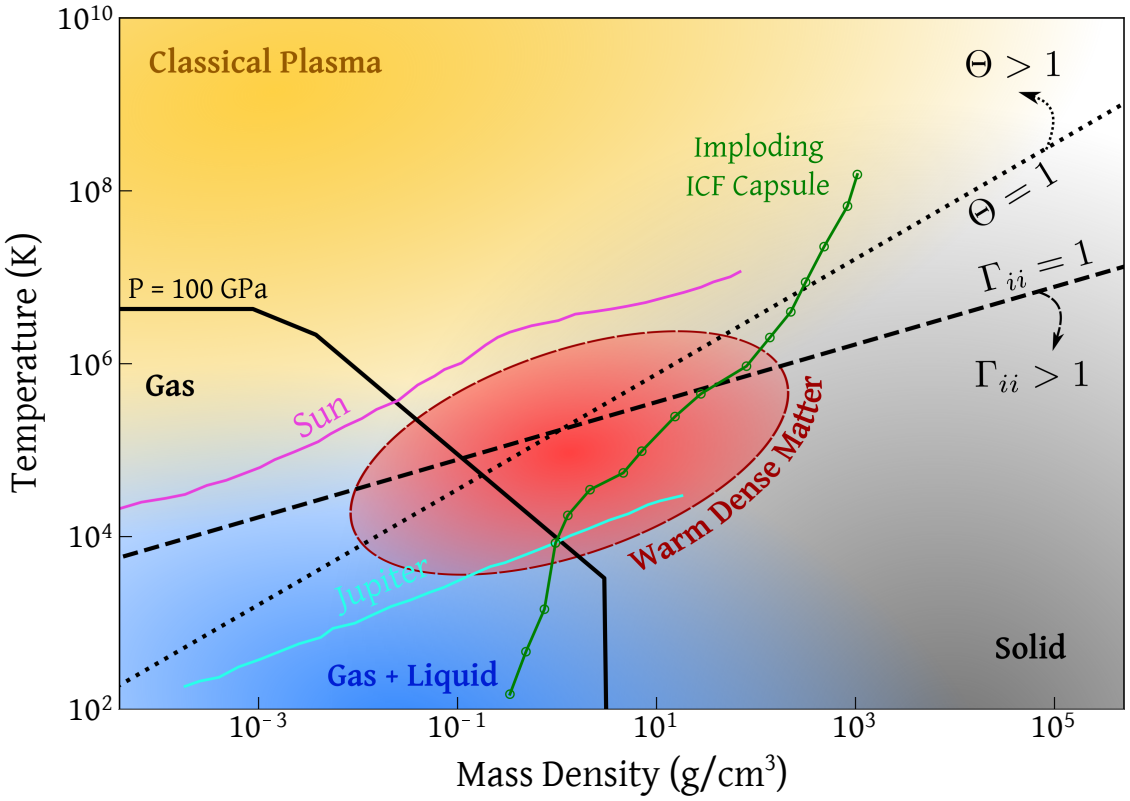

Figure 1.1: Phase diagram of matter in density-temperature space. The region defined as warm dense matter is highlighted in red in the centre. As shown, this regime can be found at the centre of giant gas planets such a Jupiter (light blue line), and during the implosion of an ICF capsule (green line). The phase-space trajectories of the Sun and Jupiter trace the conditions from the outer to inner radii of the objects from left to right. WDM is often characterised as $\Gamma \sim 1$ and $\Theta \sim 1$. This means that common approximations used in condensed matter (bottom right) or classical plasma physics (top left) are not valid.

states of matter, such as those found in planetary interiors [1] or during asteroid impacts [2], has been realised. The phase diagram shown in Figure 1.1 illustrates the variety of conditions encapsulated within HEDP, and its applicability to many astrophysical objects. This vast phase-space means that many competing physical forces must be considered in understanding and predicting material behaviour under these extreme conditions. Such complexity underscores the critical need for experimental validation to complement theoretical models used in the pursuit of fusion energy [3, 4] and for modelling planetary phenomena [5–8], where dynamic geophysics processes are dominated by changes in solid- and liquid-state structure.

However, achieving the extreme conditions characteristic of HEDP has demanded not only monumental research efforts but also the development of specialised instruments capable of diagnosing these exotic states. Many conventional diagnostics are unable to probe matter that is either too hot or too dense. For instance, consider a thermometer made of liquid mercury, which has a boiling point of 630 K. Within the moderate temperatures ranges we are accustomed to on Earth (~ 300 K), the relationship between temperature and mercury's thermal expansion allows for a near-direct temperature measurement. However, the 'coldest' temperature encountered within the realm of HEDP often exceeds ~ 1000 K, rendering such a conventional temperature measurement ineffective.

Furthermore, an additional diagnostic challenge lies in the pursuit of accuracy. Direct measurement of conditions is not always feasible, and instead, metrics with appropriate dependencies must be utilised. The application of models to diagnostic measurements, therefore, becomes indispensable for inferring conditions. However, the implementation of these models introduces uncertainties, which are compounded by the complexity of material behaviour in these extreme environments. Statistical methodologies must therefore be applied to these inferred conditions, with optimal approaches often involving the integration of multiple *in situ* diagnostics.

1.1.1 Warm Dense Matter

The term warm dense matter (WDM) encapsulates the subset of high-energy density material with near solid densities and temperatures between 1 and 10's of eV. Within this regime, multiple forces compete to influence the material's behaviour, rendering standard simplifications inadequate. Neither the ideal gas model, typically applicable to classical plasmas at low densities, nor condensed matter theory, designed for understanding crystalline solids, can fully characterise WDM behaviour. The phase space of WDM, highlighted in red in Figure 1.1, bears relevance to diverse phenomena, including

planetary interiors [1, 9] and inertial confinement fusion [3, 10].

The warm dense matter regime is often characterised with several dimensionless parameters, each playing a crucial role in shaping the experimentally observable properties. These parameters encompass the dominance of quantum effects, the impact of inter-particle coupling, and the interplay between collective and non-collective behaviours. To quantify the influence of quantum effects, the ratio of the electron's thermal energy, $k_B T_e$, to its Fermi energy, E_F, is determined via the electron degeneracy parameter,

$$\Theta = \frac{k_B T_e}{E_F} \,. \tag{1.1.1}$$

Here, k_B is the Boltzmann constant and the Fermi energy is expressed as,

$$E_F = \frac{\hbar^2 k_F^2}{2m_e} = \frac{\hbar^2}{2m_e} \left(3\pi^2 n_e\right)^{2/3} \,, \tag{1.1.2}$$

where k_F is the Fermi wavevector and n_e is the electron number density. In the regime where $\Theta \gg 1$, implying non-degenerate conditions, classical plasma physics can be aptly applied, with electrons described by the Maxwell-Boltzmann distribution. Conversely, when $\Theta \ll 1$, the electrons become fully degenerate, and their energy levels are described by the Fermi-Dirac distribution.

The effect of inter-particle correlations is estimated by a generalised coupling parameter,

$$\Gamma_{aa} = \frac{\langle V_{aa} \rangle}{\langle K_a \rangle} \tag{1.1.3}$$

which compares the mean kinetic energy of free (non-interacting) particles, $\langle K_a \rangle$, with the mean energy due to interactions, $\langle V_{aa} \rangle$. For a charged-particle system in equilibrium

these are given by,

$$\langle V_{aa} \rangle = \frac{Q_a^2}{4\pi\epsilon_0 R_{aa}}\,, \tag{1.1.4}$$

$$\langle K_a \rangle = \frac{3}{2} k_B T_a \frac{\mathcal{F}_{3/2}(\eta_a)}{\mathcal{F}_{1/2}(\eta_a)}\,, \tag{1.1.5}$$

where Q_a is the particle charge, $R_{aa} = (3/4\pi n_a)^{1/3}$ is the mean inter-particle separation and $\mathcal{F}_j(\eta_a)$ is the j^{th} order Fermi-Dirac integral of the dimensionless chemical potential, $\eta_a = \mu_a / k_B T_a$. The electron-ion coupling parameter is defined as [11],

$$\Gamma_{ei} = \frac{\Gamma_{ii}}{Z} \frac{\mathcal{F}_{1/2}(\eta_e)}{\mathcal{F}_{3/2}(\eta_e)}\,. \tag{1.1.6}$$

The characteristic radius of the degenerate bulk of electrons near the ion is set by the chemical potential. This can be related to the comparison of the mean number density to the volume associated with the mean spatial extent of the wavefunction of an individual particle,

$$\mathcal{F}_{1/2}(\eta_a) \equiv \frac{n_a \Lambda_a^3}{2s_a + 1}\,, \tag{1.1.7}$$

where the factor $2s_a + 1$ accounts for spin statistics. The wavefunction of an individual particle is given by the thermal de Broglie wavelength, Λ_a, taken at a mean thermal speed $v_{th} = \sqrt{k_B T_a / m_a}$,

$$\Lambda_a = \sqrt{\frac{2\pi\hbar^2}{m_a k_B T_a}}\,. \tag{1.1.8}$$

In a degenerate plasma $\eta_a \to -\infty$ and $\langle K_a \rangle \to 3E_{Fa}/5$, whilst in a non-degenerate plasma $\eta_a \to +\infty$ and $\langle K_a \rangle \to 3k_B T_a/2$.

In warm dense matter $\Gamma_{ii} \sim 1$ and $\Theta \sim 1$. This signifies a state where the plasma is moderately coupled, exhibiting both long- and short-range order attributed to ion correlations, similar to the behaviour of liquids. This contrasts with the behaviour of ideal plasmas, where $\Gamma_{ii} \ll 1$, allowing atoms to be described solely by their isolated

motions. In addition, the WDM plasma is moderately degenerate, necessitating the simultaneous consideration of quantum and thermal effects. Given these complexities, it is paramount within the HEDP community to generate well characterised WDM states in the laboratory. These experimental endeavours serve not only to validate theoretical models but also to improve the understanding of material behaviour within this exotic regime.

1.1.2 Inertial Confinement Fusion

One of the most captivating applications of high-energy density research is in the pursuit of producing 'clean', or carbon-neutral, energy. This research aims to replicate the fusion processes that fuel the Sun. While fusion is a naturally occurring process in the highly pressurised core of the Sun, emulating these conditions on Earth within a laboratory has proven to be a formidable challenge. This is in part due to both the immense energy requirements and the complexity of material behaviour at such extreme conditions.

For a fusion reaction to occur, as depicted in Figure 1.2, the two colliding atoms must have sufficient energy to overcome their Coulomb barrier. While the temperatures within stellar cores often fall below the required energy, they are still sufficiently hot for atoms to quantum tunnel through the remaining energy barrier. However, this means that the fusion efficiency, even within the core of the Sun, is relatively poor. The Sun's core only generates $\sim 300\,\mathrm{W/m^3}$, which amounts to approximately a quarter of the heat produced by a resting adult human [12]. While the sheer size of the Sun compensates for its inefficiency, replicating these fusion processes on Earth necessitates substantially higher efficiencies if it is to be used as a practical energy source. As illustrated in Figure 1.1, this means that laboratory-based fusion experiments generate conditions that are hotter and denser than those within the Sun.

One method employed for producing this energy is known as inertial confinement

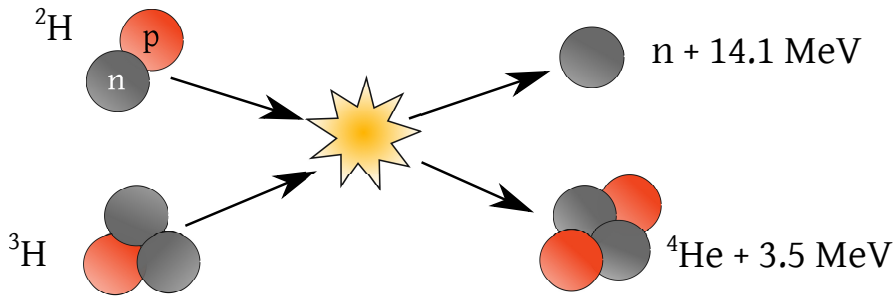

Figure 1.2: Schematic of a fusion reaction between a deuterium, ^{2}H, and tritium, ^{3}H atom. Once the Coulomb barrier has been overcome, the fusion reaction generates 17.6 MeV of energy, 80% of which is parted in the neutron (shown as a grey circle).

fusion (ICF). In this process, laser energy is focused onto very small spherical targets (with diameters < 1 mm), compressing them to ~ 0.1 times their original size. As illustrated in Figure 1.3, direct-drive ICF focuses laser beams uniformly onto the outer surface of the target, inducing heating and ablation of the shell. To optimise this process, the drive laser pulse is shaped to enhance the efficiency and symmetry of the target compression. This is achieved using a 'picket pulse' design, which consists of a series of short laser pulses delivered before the main laser compression pulse [13]. To achieve ignition, the drive pressure must reach $\sim 10^4$ GPa. However, a steep rise at the beginning of the drive pulse would create a very strong shock, preheating the fuel, increasing the shell entropy, and reducing the shell density, which would result in a low final pressure. Utilising initial picket pulses allows for a gradual increase in pressure, preventing a large initial increase in entropy. The entropy increase across a strong shock is proportional to $\Delta P/\rho^{5/3}$, where ΔP is the pressure jump and ρ is the pre-shock density. As the density increases due to multiple shock compressions, the entropy increase diminishes, and the compression approaches an adiabatic compression. Optimal shell compression is achieved when all shocks break out of the shell nearly simultaneously, minimising decompression resulting from rarefaction waves launched at each shock breakout. The use of multiple shocks has the additional benefit of reducing the shell nonuniformity growth factor associated with Rayleigh-Taylor instabilities.

Due to momentum conservation, as the outer shell ablates, its inner surface begins

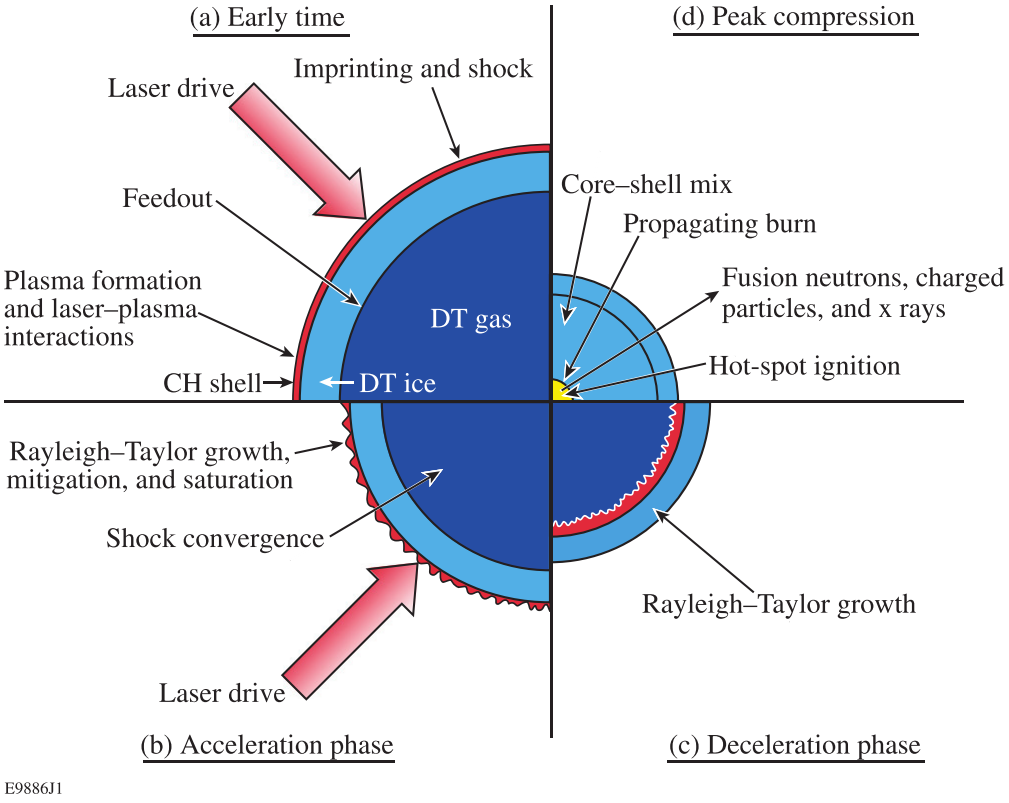

Figure 1.3: Reproduced from Ref. [3]: Schematic of the four main stages of a direct-drive inertial confinement fusion target implosion. **(a)** At early times the drive lasers heat the outer surface (ablator) of the fusion target. **(b)** The plasma begins to ablate which, due to momentum conservation, causes the inner surface of the target shell to accelerate inwards. **(c)** Once the main shock wave reflects from the target centre the shell compression begins to decelerate. The shell's kinetic energy is converted into thermal energy and the fusion fuel is compressed and heated. **(d)** At peak compression, a thermonuclear burn wave propagates outwards through the fuel from the formed hot-spot until the target completely dis-assembles.

to accelerate inward, compressing the fusion fuel, typically deuterium and tritium (DT), at the centre of the capsule. The greatest concern at this stage is the integrity of the shell and the growth of instabilities. These effects are, in part, dependent on the shell adiabat, α_f, defined as the ratio of the shell pressure, P_{Shell}, to the Fermi-degenerate pressure [14, 15]. For DT fuel, the adiabat is given by [3],

$$\alpha_f \simeq \frac{P_{\text{Shell}}[\text{Mbar}]}{2.2\left(\rho\left[\text{g/cm}^3\right]\right)^{5/3}}\,. \tag{1.1.9}$$

The target compression continues and a 'hot spot' is generated within the centre of the capsule. The central hot spot is sustained by the capsule's own inertia for a duration sufficient to initiate fusion reactions. Energetic particles generated in these reactions can spread into the outer layers of the target, triggering additional fusion reactions, creating a self-sustaining thermonuclear burn. If this fuel burn yields more energy than the laser energy used to compress the capsule, target ignition has been achieved.

Confinement properties of an ICF capsule depend on the areal density, ρR (where R is the capsule radius), of the compressed shell and hot-spot. The areal density is controlled by varying the entropy of the fuel, which is determined by the fuel adiabat. For ignition to occur, a large enough areal density (low adiabat), $> 0.2-0.5\,\mathrm{g/cm^2}$, and hot enough core, $\sim 5-12\,\mathrm{keV}$, are required [16, 17]. However, targets imploded on a low adiabat are susceptible to hydrodynamic instabilities [18] that drive the rapid growth of non-uniformities. Therefore, an important part of ICF research involves optimisation of the target adiabat [19–21].

Experimental demonstration of ignition has only been realised in recent years [22], though with direct-drive designs yet to witness this milestone [23]. This accomplishment was the result of a series of mitigation strategies, complemented by diagnostic techniques, including neutron and X-ray emission [24], and target development. The design of inertial confinement fusion ignition targets requires radiation-hydrodynamics simulations with accurate models accounting for fundamental material properties, such as the equation of state, opacity, and conductivity. Validation of these models is required through experimentation. However, direct diagnosis of the physical properties of dense plasmas produced in ICF implosions is limited due to the difficulty in achieving the required accuracy and spatial resolutions [10, 25, 26], essential for testing various model predictions.

1.1.3 Laboratory Astrophysics

A growing application of high-energy density and warm dense matter physics lies within the field of laboratory astrophysics. Telescopic observations of astrophysical objects encounter many limitations [27, 28]. Consequently, the capability to replicate comparable conditions within a controlled laboratory setting provides a wealth of additional insights into plasma behaviour via the use of diagnostic probes. These insights can subsequently be compared with numerical simulations, enhancing the understanding of the underlying phenomena. Despite the vast size of the astrophysical objects, ranging from hundreds of kilometres to many parsecs ($\sim 3 \times 10^{13}\,\mathrm{km}$), and their evolutionary timelines extending over billions of years, the intricacies of these phenomena can still be effectively replicated in a laboratory plasma, operating on length scales ranging from a few microns to millimetres. This replicability is facilitated by the establishment of scaling relationships that connect laboratory processes with their astrophysical counterparts.

This scaling capability lies in the well-established principle that, in the absence of dissipation, two systems with differing length and time scales can be modelled by the same governing equations [29]. Therefore, when the relevant dimensionless numbers quantifying dissipation in the laboratory plasma, such as the Reynolds and Péclet numbers, adhere to the same asymptotic hierarchy as the astrophysical plasma of interest, the experimental results become pertinent to their cosmic analogues [30].

As depicted in Figure 1.1, the conditions within planetary interiors, ranging from the size of Jupiter and beyond, can be replicated in laboratory settings. This emulation is realised through various means, including high-power laser facilities, z-pinches, or the use of diamond anvil cells [31]. A significant focus of research revolves around understanding the atomic composition and structure of planetary cores, which informs planetary formation theories [9, 32, 33]. For example, one theory posits that at the immense pressures within Jupiter's core, hydrogen undergoes a transition to a metallic

state [34]. The experimental demonstration of this phenomena has captured considerable scientific interest, yet, to date, a reliable confirmation remains elusive [35–38].

Laboratory research on WDM therefore presents a myriad of applications for improving our understanding of astrophysical bodies by exploring the behaviour of matter under the extreme conditions that naturally occur throughout the universe.

1.2 Thesis Structure and Author Contributions

The research presented in this thesis is built upon the foundations laid by numerous predecessors, reflecting the collaborative nature inherent in modern experimental science. This section serves to outline the content of subsequent chapters while delineating the specific contributions of the author. All contributions and references to the work of others are explicitly acknowledged both within this section and throughout the thesis.

Chapter 2 provides an overview of the relevant theoretical concepts employed throughout the thesis, drawing from well-established material covered in various textbooks. The primary diagnostic utilised throughout this research is Thomson scattering. Therefore, this chapter aims to offer an understanding of the dependencies and challenges associated with the use of such a diagnostic. The demonstrative scattering spectra presented in this chapter were generated by the author using the X-ray scattering (XRS) and Optical Thomson Scattering (OTS) code developed by Professor Gianluca Gregori at the University of Oxford.

The data analysis presented in the subsequent chapters are all the work of the author. In many instances, the analysis makes use of the Markov Chain Monte Carlo modelled developed by Dr. Muhammad Kasim and Dr. Sam Vinko at the University of Oxford (detailed in Appendix B), alongside the aforementioned scattering models.

Chapter 3 presents research into the feasibility and effectiveness of utilising an X-ray scattering diagnostic on a direct-drive cryogenic fusion implosion. This work incorporates 1-D LILAC and 2-D DRACO cryogenic simulations provided by Dr. Duc Cao at

the Laboratory for Laser Energetics (LLE). These simulations are integrated into the SPECT3D code developed by Dr. Igor Golovkin and Dr. Tim Walton at Prism Computational Sciences (detailed further in Appendix A). A novel methodology to isolate scattering from specified regions is detailed, and was implemented into SPECT3D by Dr. Walton. The SPECT3D simulations and subsequent analysis are the work of the author.

Chapter 4 is the culmination of an extensive experimental campaign spanning several years, conducted at the OMEGA-EP facility at LLE. The campaign was proposed and overseen by Dr. Ryan Rygg and Dr. Sean Regan at LLE, with significant contributions from a large group of scientists and technicians within the facility. The experimental results presented in this chapter derive from two separate shot days. The first was conducted by Rahul Saha and Dr. Rygg, while the second was conducted remotely by the author, with Mary Kate Ginnane working on-site to construct the PXRDIP targets. The data analysis performed by the author employs the AnalyzePXRDIP code developed by Dr. Marius Millot at the Lawrence Livermore National Laboratory (LLNL), and the Multi-Component Scattering Spectra (MCSS) published by Dr. David Chapman at the Atomic Weapons Establishment. The determination of pressure from the MCSS structure, as detailed in Appendix C, builds on the work of Dr. Jan Vorberger and Dr. Tobias Dornheim at Helmholtz-Zentrum Dresden-Rossendorf. The data analysis was complemented by 1-D HELIOS simulations which were carried out by the author using the Prism Computational Sciences software.

Chapter 5 provides a detailed exploration of a subset of the extensive collaboration studying the turbulent dynamo (TDYNO) effect. This collaboration is spearheaded by Professor Petros Tzeferacos at the FLASH centre at the University of Rochester, Professor Don Lamb at the University of Chicago, and Dr. Archie Bott and Professor Gianluca Gregori at the University of Oxford. This chapter encompasses two experimental shot days, one conducted by the author at the OMEGA laser facility at LLE,

and the other at the National Ignition Facility (NIF), where the author acted as a trainee responsible individual under the guidance of Dr. Steven Ross at LLNL. Analysis on the proton radiography to infer magnetic field information was performed by Dr. Bott and Dr. Richard Petrasso's research group at the Massachusetts Institute of Technology. The optical Thomson scattering diagnostics were overseen by Dr. Joseph Katz at OMEGA and Dr. George Swadling at the NIF. Furthermore, the implementation of instrument broadening in the OTS system is performed by the author using an adaptation of the Thomson scattering analysis code developed by Dr. Colin Bruulsema at LLNL. The X-ray emission analysis performed by the author builds on the work by Dr. Jena Meinecke at Gettysburg College.

The thesis is concluded in Chapter 6 which provides a summary of the key findings, implications and contributions to the field. A brief outline is provided with suggestions for future research directions, identifying potential areas of inquiry that stem from the findings of this thesis. These suggestions proffer opportunities for further exploration and expansion of the research domain.

1.3 Author Publications

5. **H. Poole** *et al.*, Multimessenger measurements of the static structure of shock-compressed liquid silicon at 100 GPa, *Physical Review Research* **6**, 023144 (2024)

4. T. G. White, **H. Poole** *et al.*, Speed of sound in methane under conditions of planetary interiors, *Physical Review Research* **6**, L022029 (2024)

3. H. G. Rinderknecht, [...], **H. Poole** *et al.*, Electron-beam-based Compton scattering x-ray source for probing high-energy-density physics, *Physical Review Accelerators and Beams* **27**, 034701 (2024)

2. **H. Poole** *et al.*, A case study of using X-ray Thomson Scattering to diagnose the in-flight plasma conditions of DT cryogenic implosions, *Physics of Plasmas* **29**, 072703

(2022)

1. J. Meinecke, [...], **H. Poole** *et al.*, Strong suppression of heat conduction in a laboratory replica of galaxy-cluster turbulent plasmas, *Science Advances* **8**, eabj6799 (2022)

Chapter 2

Thomson Scattering as a Probe for HED Matter

Understanding and predicting the behaviour of high-energy density matter, as outlined in Chapter 1, is crucial across diverse fields, ranging from fusion research to astrophysics. However, the development of accurate equation of state (EOS) models for these complex conditions necessitates knowledge of fundamental system parameters, including electron density, temperature and ionisation. One powerful tool for investigated HED matter is scattering techniques, employing either particles or light. Light scattering experiments illuminate the compressed matter with a narrow energy band of photons. Subsequently, the scattered photons are captured either across k-space in a diffraction experiment or via a Bragg crystal, enabling the resolution of the frequency (ω-space) power spectrum at a finite scattering angle. The resulting spectrum yields valuable insights into the atomic and electronic structure of the matter under scrutiny.

2.1 Scattering Power

Thomson scattering is the process by which an incident photon applies an electric field to an electron, causing it to oscillate and consequently emit radiation. This process is frequently termed as elastic scattering, as the emitted photon matches the frequency of the incident photon. While the designation 'Thomson scattering' is commonly employed within the HED field to encompass all aspects of scattering experiments, it is essential to note that it is not the exclusive contributor to a power spectrum.

In any scattering experiment, a fundamental consideration involves ensuring that the probing electromagnetic radiation can effectively propagate through the HED matter. The ability of an incident photon to penetrate a plasma is dependent on whether its

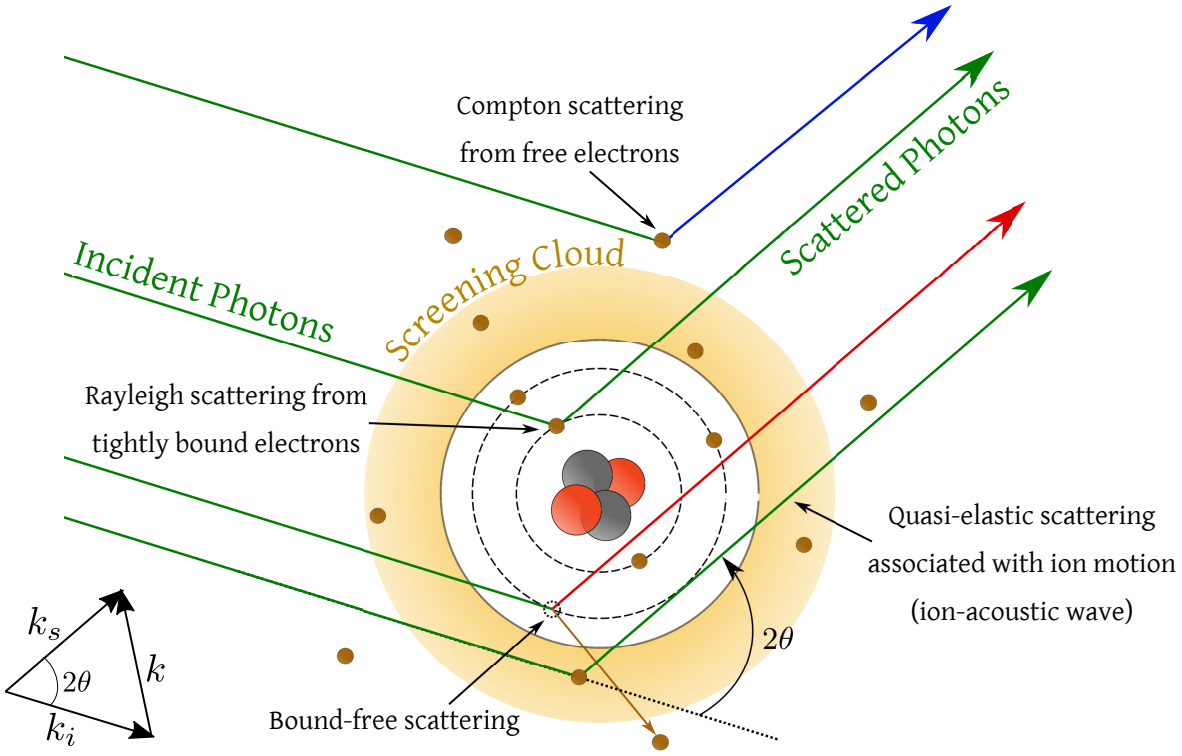

Figure 2.1: Schematic of the sources of scattering from a partially ionised plasma. The incident photons can scatter elastically from electrons that are tightly bound to the ionic core, known as Rayleigh scattering. They can inelastically Compton scatter from free electrons resulting in red- and blue-shifted photons. A weakly bound electron can be photoionised by a incident photon resulting in a red-shifted scattered photon.

frequency, ω_i, surpasses the plasma frequency,

$$\omega_{pa}^2 = \frac{e^2 n_a}{\epsilon_0 m_a} \,. \tag{2.1.1}$$

Due to its dependence on m_a, the plasma frequency for electrons significantly exceeds that for ions, $\omega_{pe} \gg \omega_{pi}$. Consequently, when $\omega_i < \omega_{pe}$, the incident wave experiences strong damping and reflection. It is worth noting that the range of electron densities that optical Thomson scattering (OTS) can effectively probe is therefore limited in comparison to X-ray Thomson scattering (XRTS).

For incident photons with an energy $\hbar\omega_i \lesssim 10\,\mathrm{keV}$, the probability of the radiation

scattering in any direction is given by the Thomson cross section,

$$\sigma_{\mathrm{Th}} = \frac{8\pi}{3} r_0^2 = 6.65 \times 10^{-29}\,\mathrm{m}^2\,, \tag{2.1.2}$$

where $r_0 \equiv e^2/m_e c^2$ is the classical electron radius. For energies beyond 10 keV, higher order corrections given by the low-energy limit of the Klein-Nishina cross section must be accounted for [39],

$$\sigma_{\mathrm{KN}} = \sigma_{\mathrm{Th}} \left[1 - 2\frac{\hbar\omega_i}{m_e c^2} + \dots \right]. \tag{2.1.3}$$

This very small scattering cross section highlights the necessity for the incident radiation to possess a sufficiently large number of photons to yield an observable scattering signal. In numerous scattering experiments carried out at facilities such as XFELs, the number of scattered photons per experiment can be around the order of unity. In such instances, it becomes imperative to conduct the experiment at a high repetition rate to accumulate a sufficiently robust signal at observable levels.

An illustration of the geometry in a scattering experiment is shown in Figure 2.1. The incident radiation has a wave vector $\mathbf{k_i}$ and frequency ω_i It is scattered through an angle 2θ towards a distant detector with a wave vector $\mathbf{k_s}$ and frequency ω_s. This produces an observed shift in the wave vector and frequency given by,

$$\mathbf{k} = \mathbf{k_i} - \mathbf{k_s}\,, \tag{2.1.4}$$

$$\omega = \omega_i - \omega_s\,. \tag{2.1.5}$$

The scale length accessed by the probe is given by the wave number shift $k = |\mathbf{k}|$,

$$k = \frac{4\pi}{\lambda_i} \sin\theta \sqrt{1 - \frac{\omega_{pe}^2}{\omega_i^2}}\,, \tag{2.1.6}$$

where $\lambda_i = 2\pi c/\omega_i$ is the incident wavelength. The factor $(1 - \omega_{pe}^2/\omega_i^2)^{1/2} = \epsilon_{\mathrm{D}}$, is

known as the dielectric permittivity. When $\omega_i \gg \omega_{pe}$, $\epsilon_{\mathrm{D}} \approx 1$ and is often disregarded in equation 2.1.6.

The power spectrum for an incident beam of intensity $I_i = c\epsilon_0 E_i^2/2$, where E_i is the energy of the beam, scattering from a homogeneous volume of plasma $\mathcal{V}$ containing a number of electrons $N_e = \mathcal{V}n_e$ is characterised per solid angle per unit frequency as [40],

$$\frac{\partial^2 P_s}{\partial\Omega\partial\omega_s} = \frac{3\sigma_{\mathrm{Th}}}{2\pi} I_i \mathcal{P}\left(2\theta, \phi\right) \left(\frac{\omega_s}{\omega_i}\right)^2 N_e S\left(\mathbf{k}, \omega\right) . \tag{2.1.7}$$

This power spectrum is dependent on the polarisation of the incident beam, defined as,

$$\mathcal{P}\left(2\theta, \phi\right) = \begin{cases} \frac{1}{2}\left(1 + \cos^2 2\theta\right) & \text{Unpolarised} \\ 1 - \sin^2 2\theta \cos^2 \phi & \text{Linearly polarised} \end{cases} . \tag{2.1.8}$$

It is important to note that the form of scattered power in equation 2.1.7 assumes the incident radiation is monochromatic. In reality, all sources of electromagnetic radiation have a finite bandwidth. Additionally, detectors used to measure the spectrally resolved power spectrum have a finite frequency resolution, leading to further broadening of the scattering spectrum. The coupling of these two factor is referred to as the source function, $\Sigma(\omega)$, which is convolved with the scattered radiation to give the observed power spectrum,

$$\frac{\partial^2 P_s^{\mathrm{obs}}(\omega_s)}{\partial\Omega\partial\omega_s} \equiv \Sigma(\omega) * \frac{\partial^2 P_s(\omega_s)}{\partial\Omega\partial\omega_s} = \int_{-\infty}^{\infty} \mathrm{d}\omega' \Sigma(\omega - \omega') \frac{\partial^2 P_s(\omega')}{\partial\Omega\partial\omega'} . \tag{2.1.9}$$

2.2 Structure Factor

The factor $S(\mathbf{k}, \omega)$ in equation 2.1.7 is known as the total electron dynamic structure. It captures the fact that the scattered power is dependent on the ensemble average of the spectral electron density. If the electrons within the system were completely uniformly distributed there would be no net scattering of the beam, as each scattered

field component in one direction would always have an equal but opposite component to cancel it. Whilst it is assumed the average electron density is uniform within the scattering volume, on a finite sale the electrons are in fact fluctuating. The scattering components from these fluctuations can combine constructively, giving rise to spectral features. An approximation of the dynamic structure factor was derived by Chihara [41] which breaks it down into three main scattering components,

$$S(\mathbf{k},\omega) = S_{bb}(\mathbf{k},\omega) + S_{ff}(\mathbf{k},\omega) + S_{bf}(\mathbf{k},\omega)\,. \tag{2.2.1}$$

The first term accounts for the density correlations of electrons that are either bound or dynamically follow the ions' motion,

$$S_{bb}(\mathbf{k},\omega) = |f_i(\mathbf{k}) + q(\mathbf{k})|^2 S_{ii}(\mathbf{k},\omega)\,. \tag{2.2.2}$$

The bound electrons are represented by the ionic form factor of the core, $f_i(\mathbf{k})$. The Fourier transform of the electron screening cloud is given by $q(\mathbf{k})$, which here, represents the response of the free electrons to the low-frequency fluctuations of the ions. In many X-ray scattering experiments the dynamic response of the ions cannot be resolved. In such instances the ions can be approximated as static and the scattering on the time scales of the ions is therefore assumed to be elastic,

$$S_{bb}(\mathbf{k},\omega) \approx |f_i(\mathbf{k}) + q(\mathbf{k})|^2 S_{ii}(\mathbf{k})\delta(\omega) = W_R(\mathbf{k})\delta(\omega)\,. \tag{2.2.3}$$

The factor $W_R(\mathbf{k})$ is known as the Rayleigh weight and is the dominate term of interest in X-ray diffraction experiments with weakly-ionised warm dense matter conditions. The static structure factor can be evaluated by the Fourier transform of the pair dis-

tribution function, $g_{ii}(\mathbf{r})$,

$$S_{ii}(\mathbf{k}) = 1 + n_i \int \mathrm{d}\mathbf{r}\, e^{-i\mathbf{k}\cdot\mathbf{r}} \left[g_{ii}(\mathbf{r}) - 1\right] . \tag{2.2.4}$$

The pair distribution function represents the radially averaged distribution of inter-atomic distances. The form of the ion-ion structure factor is therefore dependent on the ionic interactions and conditions.

The second term in equation 2.2.1 gives the contribution to the scattering from the high-frequency motion of the free electrons, which the ions are unable to respond to,

$$S_{ff}(\mathbf{k}, \omega) = Z_f S_{ee}(\mathbf{k}, \omega) . \tag{2.2.5}$$

This free-free component, which scales with the ionisation Z_f, can be considered as the structure of an interacting electron gas, $S_{ee}(\mathbf{k}, \omega)$, in which the ions are considered as a static neutralising background. It gives rise to inelastic scattering features associated with the collective and non-collective motion of the electrons.

The final term in equation 2.2.1 corresponds to inelastic scattering due to Raman-like transitions. This phenomenon arises when the incident photons excite tightly bound electrons to the continuum, a process also referred to as 'bound-free' transitions. It is of particular interest in studies involving partially ionised systems [42]. However, it is not considered in detail within the scope of this thesis.

To characterise the inelastic scattering features observed on a power spectrum it is beneficial to compare the scale length interrogated by the incident beam, $k = 2\pi/\lambda$, to the characteristic scale length for correlations between electrons. This comparison is defined as the scattering parameter [43],

$$\alpha = \frac{1}{k\lambda_s} , \tag{2.2.6}$$

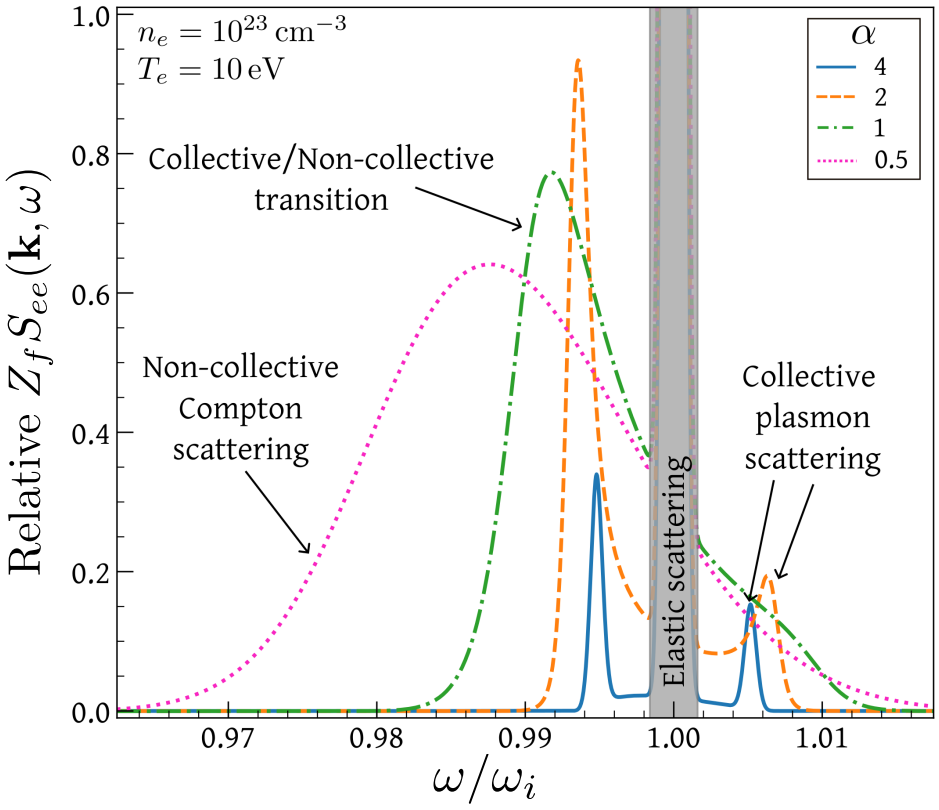

Figure 2.2: Evolution of the free-free inelastic scattering feature from the collective to non-collective regime. In the $\alpha > 1$ regime, weakly damped plasmon scattering features are observed. As the transition point $\alpha = 1$ is reached, both strongly damped plasmon features and broadening attributed to non-collective scattering is observed. In the $\alpha < 1$ regime, a broad Compton scattering feature is observed. These examples were generated using a carbon sample with an ionisation $Z_f = 4$ and an incident probe of $E_{ph} = 2.5\,\mathrm{keV}$.

where the electron screening length, λ_s, is determined as,

$$\kappa_e = \frac{1}{\lambda_s} = \sqrt{\frac{n_e e^2}{k_B T_e \epsilon_0} \frac{\mathcal{F}_{-1/2}(\eta_e)}{\mathcal{F}_{1/2}(\eta_e)}}\,. \tag{2.2.7}$$

For non-degenerate and degenerate systems, this form returns the commonly known Debye [44] and Thomas-Fermi [45, 46] screening lengths, respectively,

$$\lambda_s = \begin{cases} \lambda_{De} = \sqrt{\frac{\epsilon_0 k_B T_e}{n_e e^2}} & \text{Non-degenerate } (\eta_e \to -\infty) \\ \lambda_{TF} = \sqrt{\frac{2\epsilon_0 E_F}{3 n_e e^2}} & \text{Degenerate } (\eta_e \to +\infty) \end{cases}. \tag{2.2.8}$$

The effect on the observed inelastic scattering features by changing α is illustrated in Figure 2.2.

Whilst the screening length can be determined analytically via equation 2.2.7, for conditions such as those found in WDM plasmas an effective temperature, T_{eff}, which interpolates between the classical and degenerate regimes is often employed [47]. The scattering parameter is therefore given by,

$$\alpha = \frac{\lambda_i}{4\pi \sin\theta}\sqrt{\frac{e^2 n_e}{\epsilon_0 k_B T_{\text{eff}}}}, \tag{2.2.9}$$

$$T_{\text{eff}} = \sqrt{T_e^2 + \left(\frac{T_F}{1.3251 - 0.1779\sqrt{r_s}}\right)^2}, \tag{2.2.10}$$

where $T_F = E_F/k_B$ is the Fermi temperature and $r_s = R_{ee}/a_B$ is the ratio of average inter-particle spacing to the Bohr radius, $a_B = 4\pi\epsilon_0\hbar^2/e^2 m_e$.

2.3 Collective Scattering

When the scattering parameter $\alpha > 1$, the power spectrum reflects the coherent scattering from the plasma, arising from the collective motion of the electrons. This collective scattering can be categorised into two regimes, which are distinguished by the ions' capability to respond to the electron motion.

2.3.1 Electron Plasma Wave

At high frequencies, where $\omega \gtrsim \omega_{pe}$, the ions are unable to respond to the rapid electron motion. The observed scattering features are therefore dominated by the collective response of the free electrons. The spectrum exhibits resonances at the characteristic frequency of the wave-like fluctuations in the electron density, commonly referred to as electron plasma waves (EPW), plasmons or Langmuir waves [48]. The position of this resonance is governed by the plasmon dispersion relation, which, in the classical limit

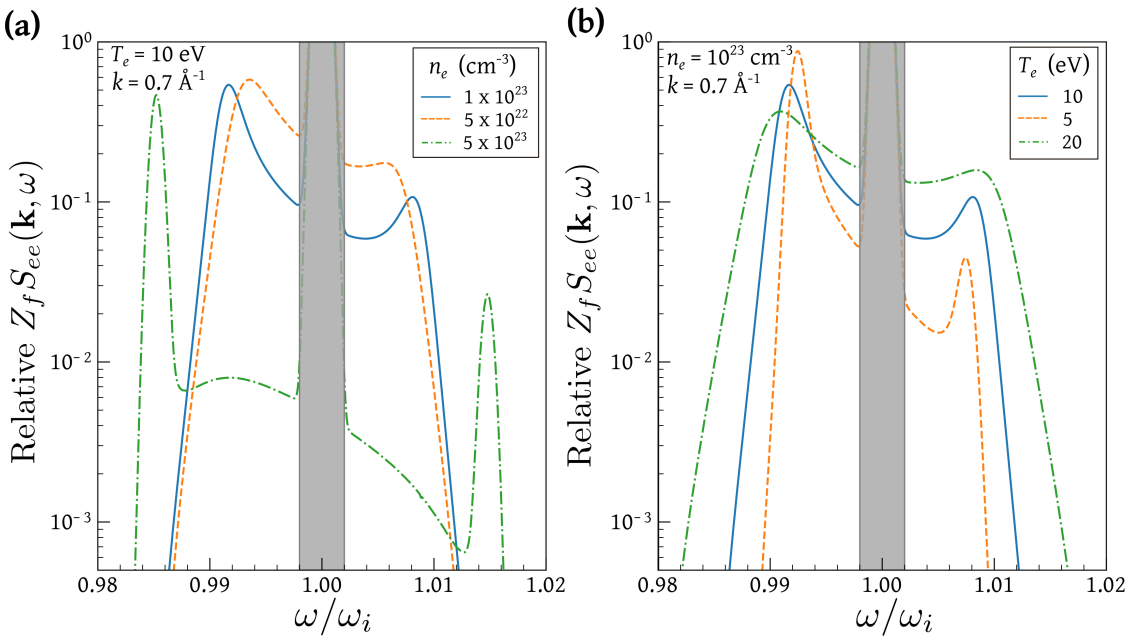

Figure 2.3: Comparison of the collective free-free scattering feature arising from resonance of the electron plasma waves. **(a)** Dependence on electron density for fixed $T_e = 10\,\text{eV}$. **(b)** Dependence on electron temperature for fixed $n_e = 10^{23}\,\text{cm}^{-3}$.

($\Theta \gg 1$), follows the Bohm-Gross dispersion relation [49],

$$\omega_{\text{epw}}^2 = \omega_{pe}^2 + 3k^2 v_{th}^2\,, \tag{2.3.1}$$

where $v_{th} = \sqrt{k_B T_e/m_e}$ is the mean thermal speed of the electrons. In the regime of weak degeneracy ($\Theta \sim 1$), this relation evolves, as demonstrated by Thiele *et al.* in Ref. [50], to,

$$\omega_{\text{epw}}^2 = \omega_{pe}^2 + 3k^2 v_{th}^2 \left(1 + 0.088 n_e \Lambda_e^3\right) + \left(\frac{\hbar k^2}{2m_e}\right)^2 . \tag{2.3.2}$$

As illustrated in Figure 2.3, the dominance of $\omega_{pe}^2 (\propto n_e)$ in determining the position of the EPW resonance is evident. The width of the peaks, reflecting the extent of Landau damping, is heavily influenced by the electron temperature.

In instances where both the red- and blue-shifted plasmon peaks are resolved, an alternative method for determining the electron temperature emerges. This method is independent of a detailed formulation of dissipative processes within the system and is

referred to as the detailed balance relationship [51],

$$\frac{S(\mathbf{k},\omega)}{S(-\mathbf{k},-\omega)} = \exp\left[-\frac{\hbar\omega}{k_B T_e}\right]. \tag{2.3.3}$$

For an isotropic and homogeneous system, $S(-\mathbf{k},-\omega) = S(\mathbf{k},-\omega)$. This relationship highlights the higher propensity for electrons to acquire energy during the scattering process. The availability of lower-energy electron states is comparatively constrained, especially in the context of degenerate plasmas.

2.3.2 Ion-acoustic Wave

In many X-ray Thomson scattering experiments, the ions are frequently treated as static, allowing for a simplified approximation to the ion-ion structure factor [52],

$$S_{ii}(\mathbf{k},\omega) \approx S_{ii}(\mathbf{k})\delta(\omega). \tag{2.3.4}$$

This assumption implies that all scattering within the time scales of the ions is considered elastic. Such a scenario often arises due to the broad source function prevalent in most XRTS experiments. However, in cases where an exceptionally narrow X-ray [53] or optical probe [54] is employed, it becomes possible to resolve the collective behaviour of the ions.

In the low-frequency regime, $\omega \ll \omega_{pi}$, the scattering spectrum results primarily from the Doppler shift due to scattering from electrons that are screening the ions. These scattering features are known as ion-acoustic waves (IAW) and reflect the ion velocity distribution. The resonance associated with these waves occurs at the ion-acoustic frequency, which, in the weak electron-ion coupling limit ($ZT_e \gg T_i$), is given by [55],

$$\omega_{\text{iaw}} = \omega_{ac} \simeq \pm k\sqrt{\frac{Zk_B T_e + 3k_B T_i}{m_i\left(1+k^2\lambda_s^2\right)}}. \tag{2.3.5}$$

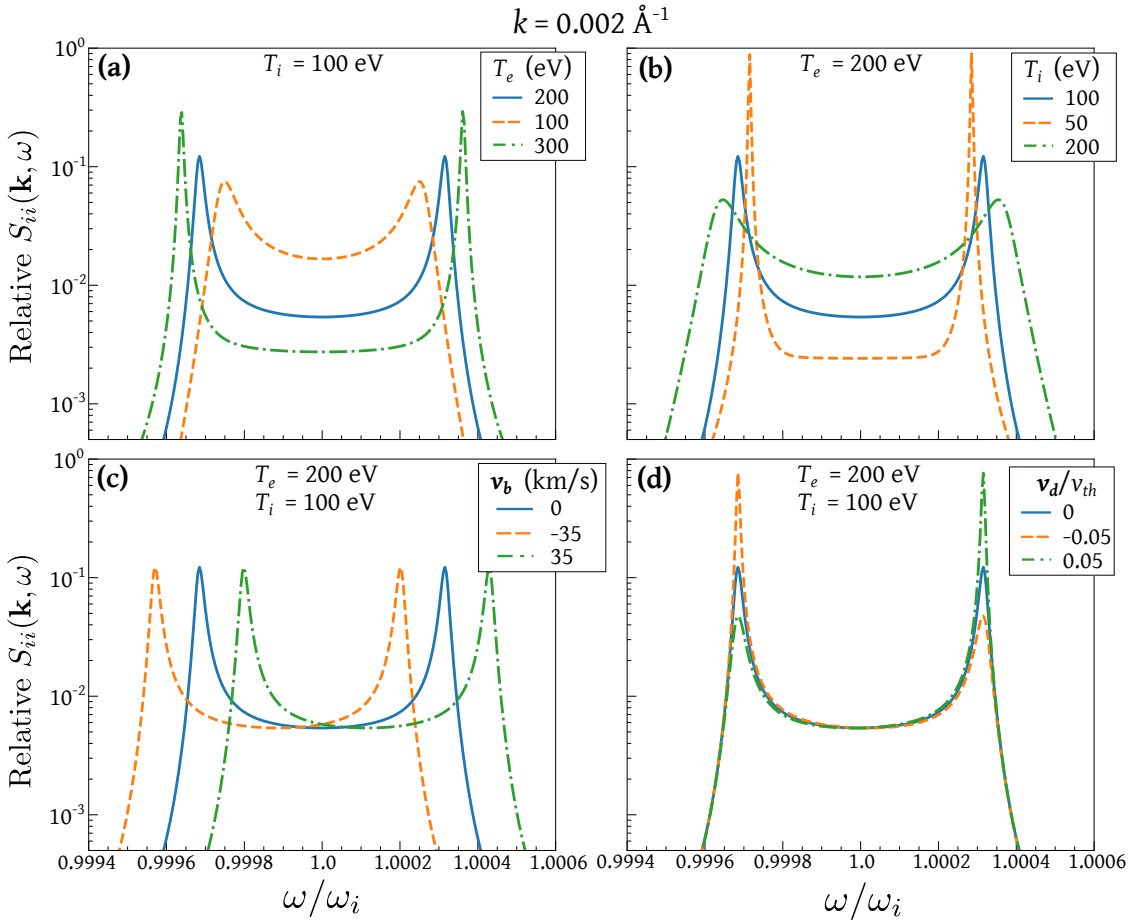

Figure 2.4: Ion-acoustic scattering features for carbon with $Z_f = 4$, $n_e = 10^{21}\,\mathrm{cm}^{-3}$, $\lambda_i = 263.25\,\mathrm{nm}$ **(a)** Shows the variation with electron temperature for a fixed $T_i = 100\,\mathrm{eV}$. **(b)** Variation with ion temperature for a fixed $T_e = 200\,\mathrm{eV}$. **(c)** Variation with bulk velocity, $\mathbf{v_b}$, for a fixed T_e and T_i. **(d)** Variation with drift velocity, $\mathbf{v_d}$, for a fixed T_e and T_i where $v_{th} = \sqrt{k_B T_e/m_e}$.

If $ZT_e < 3T_i$ then the ion-acoustic resonance is strongly damped and typically not resolved. Figures 2.4(a) and (b) illustrate that in instances where the plasma ionisation is known, the frequency shift of the IAW features is roughly dependent on the electron temperature, while their width correlates with the ion temperature.

If a plasma exhibits a bulk velocity, $\mathbf{v_b}$, relative to the scattering wavevector, the observed IAW frequency undergoes an additional Doppler shift,

$$\Delta\omega = \omega_{ac} - \mathbf{k}\cdot\mathbf{v_b}\,. \tag{2.3.6}$$

The effect of this frequency shift is illustrated in Figure 2.4(c).

The final dependence of the ion-acoustic features arises from the relative drift of electrons and ions [55]. The emergence of resonant oscillations, such as ion-acoustic waves, within a plasma, is constrained by electron and ion Landau damping. The degree of damping is directly proportional to the gradient of the velocity distribution functions, assessed at the phase velocity of the waves. When there is a relative drift in the electron velocity, $\mathbf{v_d}$, with respect to the ions, it alters the phase velocity of the waves, consequently diminishing the damping effect on the red- or blue-shifted ion-acoustic peak. In Figure 2.4(d), the impact of no relative drift between electrons and ions is compared to scenarios with positive and negative drifts.

2.4 Non-collective Scattering

The non-collective scattering regime is characterised by $\alpha \ll 1$. In this regime, the incident probe undergoes scattering due to the motions of individual particles, as the length scale probed is smaller than the characteristic screening length. The free-free scattering features, as illustrated in Figure 2.5, reflect the shape of the momentum distribution.

The scattered frequency experiences a Doppler shift from the incident frequency by an amount $\omega_{\text{non-col}}$, which is proportional to the component of the electron velocity in the direction $\mathbf{k}$. This frequency shift arises as a result of two contributions. Firstly, as the electrons observe the incident probe at a Doppler-shifted frequency $\omega' = \omega_i - \mathbf{k}_i \cdot \mathbf{v}$, and secondly due to the electron's velocity component in the observer's direction. Consequently, the frequency shift of a scattered photon by a free electron is given by,

$$\omega_{\text{non-col}} = -\frac{\hbar k^2}{2m_e} \pm \mathbf{k} \cdot \mathbf{v}\,. \tag{2.4.1}$$

The first term in equation 2.4.1 arises from the transfer of momentum during the

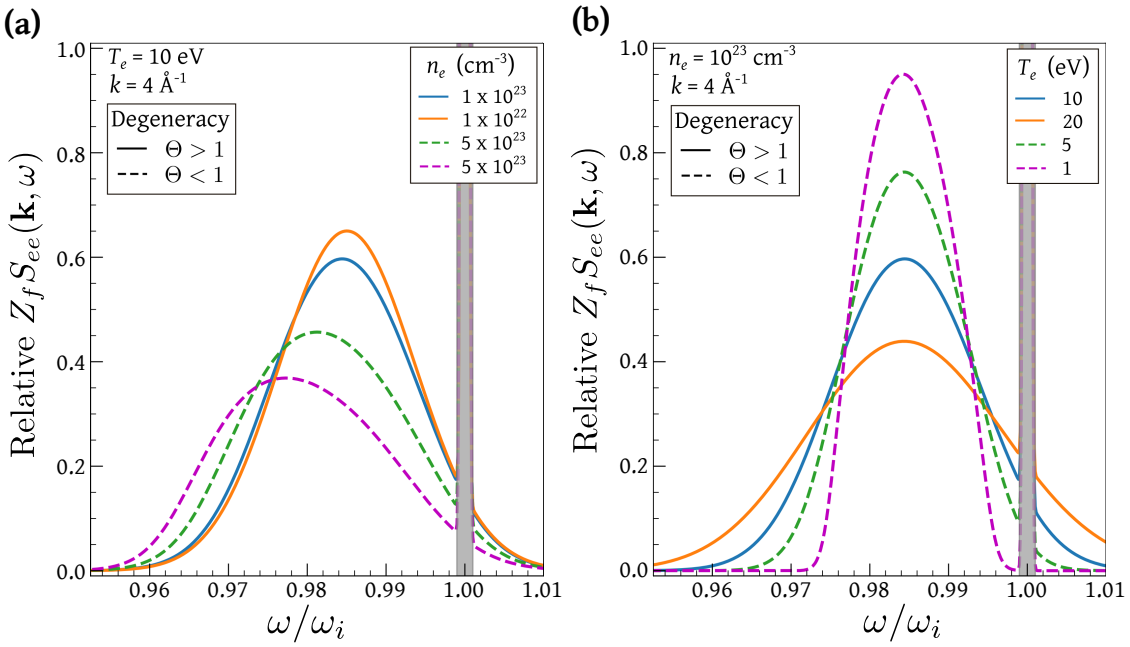

Figure 2.5: Free-free scattering features in the non-collective regime for carbon with $Z_f = 4$ and an incident probe with a photon energy $E_{ph} = 4\,\text{keV}$ **(a)** Variation with electron density for a constant $T_e = 10\,\text{eV}$. The peak of the inelastic feature is given by the Compton shift $\Delta\omega = -\hbar k^2/2m_e$. **(b)** Variation with electron temperature for a constant $n_e = 10^{23}\,\text{cm}^{-3}$. The scattering from degenerate and non-degenerate systems are shown as dashed and solid lines, respectively.

scattering process (recoil effect), which induces the Compton downshift in the scattered radiation. Consequently, non-collective scattering is commonly identified as Compton scattering. Given that k is dependent on ω_{pe}, as demonstrated in equation 2.1.6, for a fixed probe and scattering angle, the Compton downshift is therefore dictated by the electron density.

The second term accounts for the Doppler effect and gives rise to the scattering spectrum's dependence on the electron momentum distribution, $f(\mathbf{p})$. For a system in thermal equilibrium the distribution function is given by either the Fermi-Dirac [56, 57] or Maxwell-Boltzmann distributions,

$$f(\mathbf{p}) \propto \begin{cases} \exp\left(\frac{{p_F}^2 - p^2}{2m_e k_B T_e}\right) & \text{Maxwell-Boltzmann (Non-degenerate)} \\ \left[\exp\left(\frac{p^2 - {p_F}^2}{2m_e k_B T_e}\right) + 1\right]^{-1} & \text{Fermi-Dirac (Degenerate)} \end{cases}, \quad (2.4.2)$$

where $p_F = \hbar k_F$ is the Fermi momentum. For a degenerate system, the width of the spectrum is therefore proportional to the Fermi velocity, $v_F = \sqrt{2E_F/m_e}$ and hence $n_e^{1/3}$. In a non-degenerate plasma, the Compton scattering spectrum will reflect a Maxwell-Boltzmann distribution, and the width will therefore yield a measurement of the electron temperature.

Chapter 3

X-ray Thomson Scattering for Fusion Capsule Diagnostics

The content within this chapter is based on "A case study of using x-ray Thomson scattering to diagnose the in-flight plasma conditions of DT cryogenic implosions", Physics of Plasmas 25, 072703 (2022), Poole *et al.* [58].

3.1 Introduction

As outlined in Section 1.1, the theoretical modelling of the extreme matter properties reached during the implosion of an inertial confinement fusion capsule is a challenging task. This stems from the need to incorporate a quantum mechanical treatment of degenerate electrons, alongside considerations of moderately strongly-coupled ions and intricate many-particle correlations [4, 59–61]. The uncertainty in the equation of state within this regime results in unverified calculations for transport properties, ionisation balance, and energy and temperature equilibration [62–66]. Consequently, experimental validation is vital for benchmarking and developing models that can be integrated into radiation hydrodynamic codes which are utilised for ICF capsule design.

Over the past couple of decades, concerted efforts have been directed towards the development of new diagnostics capable of resolving isolated regions within the imploding capsule. Multi-keV spectrally resolved X-ray Thomson scattering (XRTS) is one of these techniques [51, 67, 68]. This chapter details the case study investigating the feasibility of deploying such a diagnostic in ICF implosion experiments conducted at OMEGA. The analysis is performed by constructing synthetic, spatially integrated, spectra using the collision-radiative code SPECT3D [69], including the X-ray scattering simulator [70], which is a post-processor of the radiation hydrodynamic codes LILAC [71] and DRACO [72].

3.2 Previous Work

The first experimental observation of non-collective, inelastic X-ray scattering from shocked liquid deuterium is discussed in Ref. [25]. This demonstrated the ability to infer critical parameters such as the electron temperature, ionisation and electron density from the elastic (Rayleigh) and inelastic (Compton) components in the scattering spectra in ICF dense matter. However, the scattering data lacked spatial information, and the subsequent analysis failed to isolate contributions from distinct regions.

Spatial temperature and ionisation profiles were determined from a near-solid density foam using a collimated X-ray beam in Ref. [73]. Using the Imaging X-ray Thomson Spectrometer at the OMEGA laser facility [74, 75], this study determined the temperature and ionisation states along multiple positions along the flow axis of the carbon foam. Overall good agreement was found between the experimental data and theoretical predictions with the exception of the high-temperature, low-density rarefaction region of the blast wave.

Simultaneous collective and non-collective scattering data for dynamically compressed deuterium was collected in Ref. [76] using the 2 keV Si Ly-α line. Focusing on compression states with $\rho/\rho_0 \sim 2.8 - 4.05$, this study employed VISAR shock velocity measurements to determine mass density, guided by current equation of state (EOS) data. This diagnostic integration enabled a more refined parameter space restriction when determining ionisation from the XRTS data.

To date, successful experiments at the OMEGA laser facility have provided valuable insights into the conditions of spherical CH implosions [77, 42]. However, no endeavour has yet been undertaken to deploy an XRTS diagnostic on a laser direct-drive ICF implosion of a layered, cryogenic deuterium-tritium (DT) spherical target. In addition, direct measurements of the fuel adiabat (as defined in equation 1.1.9) and densities are not yet achievable, instead they are inferred from the neutron yield and X-ray self-emission [78, 79]. To assess the feasibility of using XRTS, this work focuses on

generating and analysing X-ray scattering data obtained from ICF targets with varying adiabats.

The primary objective of this research was to resolve the in-flight conditions of the DT fuel. This timing is typically defined as when the ablation surface reaches two-thirds of the initial gas radius, $R_{\text{Ablation surface}}/R_{\text{Vapor, initial}} = 2/3$. During this time, Rayleigh-Taylor instabilities are growing on the outer shell surface due to inherent target and laser non-uniformities. One concern as the capsule approaches the end of its acceleration phase is ensuring the integrity of the shell structure. Developing a diagnostic capable of inferring the density and temperature of the shell during this critical stage therefore holds significant value for informing future capsule designs.

3.3 Proposed Experimental Setup

As detailed in Chapter 2, X-ray Thomson scattering is a powerful diagnostic tool used to determine plasma conditions when their densities exceed the critical density, $n_c = \epsilon_0 m_e \omega^2/e^2$, of optical probes. However, due to its low scattering cross-section, the first consideration when proposing an XRTS experiment is ensuring the scattered signal can be observed above background noise. For a probe laser, with energy E_L, incident on a foil backlighter, generating X-rays with an efficiency η_x, the total number of photons in the free-free (inelastic) scattering feature, N_{scatt}, can be estimated as [51]

$$N_{\text{scatt}} = \left(\frac{E_L}{h\nu}\eta_x\right)\left(\frac{\Omega_{\text{plasma}}}{4\pi}\eta_{\text{att}}\right)\left(\frac{n_e\sigma_{\text{Th}}\ell}{(1+\alpha)^2}\right), \tag{3.3.1}$$

where η_{att} is the attenuation of the probe X-rays through the dense plasma, Ω_{plasma} is the solid angles subtended by the plasma, α is the scattering parameter (equation 2.2.6) and ℓ is the path length of the photons through the plasma.

For the in-flight plasma conditions investigated, the scattering fraction, $n_e\sigma_{\text{Th}}\ell$, is approximately equal to 10^{-4}, where representative values for the compressed shell have

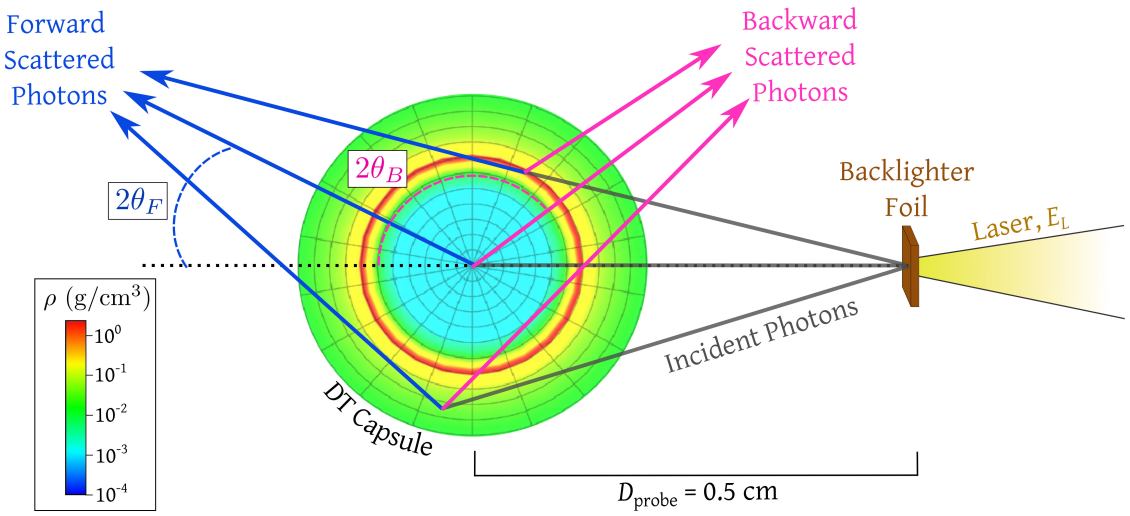

Figure 3.1: A sketch of the proposed experimental setup, with a laser of energy E_L incident on a backlighter target, producing X-rays with a conversion efficiency of η_x. The scattering X-rays are shown incident on the 3-D inferred density profile from SPECT3D using the 1-D simulation data produced by the LILAC code. Schematic of the scattering events, recorded on the detector by SPECT3D, from different zones throughout the implosion are shown. The scattering geometry is demonstrative and not drawn to scale.

been taken as $n_e \sim 10^{23}$ cm^{-3} and $\ell \sim 75$ μm. This small scattering fraction presents a challenge when fielding XRTS on a cryogenic implosion due to the significant self-emission from the plasma.

A key benefit of fielding XRTS as a plasma diagnostic is that it has two distinct scattering regimes, the collective and the non-collective. In the non-collective regime, the scattered power spectrum reflects the electron velocity distribution, making it sensitive to T_e. In contrast, the collective scattering regime reflects the collective motion of the electrons, which provides information on n_e. Designing an experiment where both regimes are recorded can therefore reduce uncertainty on the inferred conditions.

To model the X-ray emissivity, a 1 kJ laser with a 10 ps pulse and a source diameter of 50 μm is assumed to be incident on a backlighter foil, producing a Gaussian X-ray source. The conversion efficiency is estimated as $\eta_x = 0.01\%$ [80], and the spectral spread of the X-rays have a full width at half maximum (FWHM) of 10 eV. The backlighter foil is placed 0.5 cm away from the imploding target. Such a close backlighter

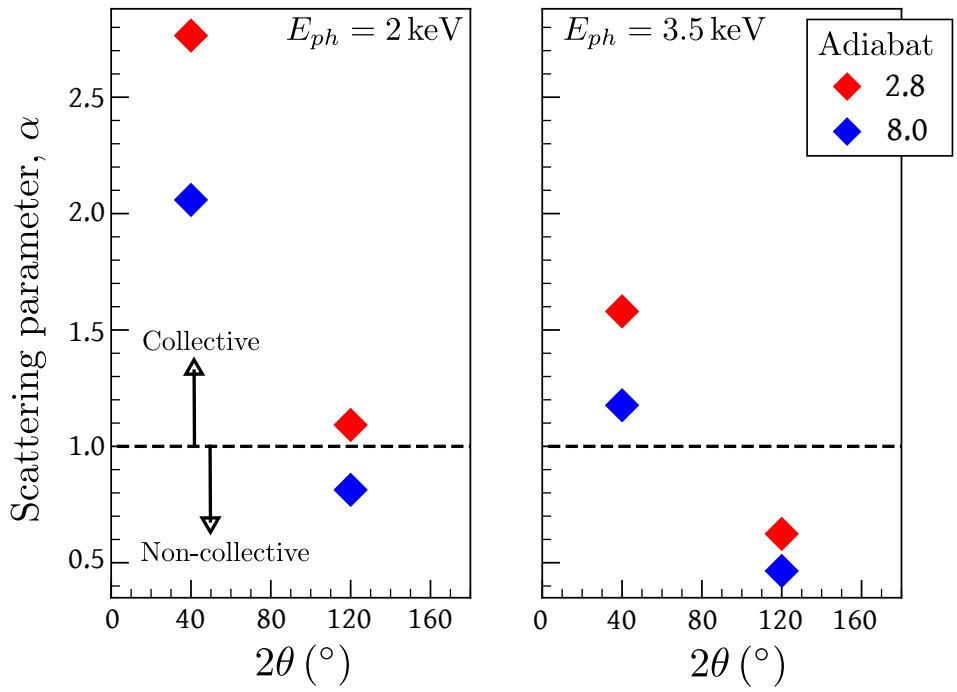

Figure 3.2: Scattering parameters, α, as calculated for the densest zone in the compressed DT shell for each scattering angle and probe energy with the two extreme adiabats as discussed in Section 3.5. A dashed line is shown at $\alpha = 1$ which is the approximate separation of collective, $\alpha > 1$, and non-collective, $\alpha \leq 1$, scattering.

distance is possible due to the development of a fast target positioner (FASTPOS) in cryogenic implosions by Stoeckl *et al.* [81]. The demonstrative scattering geometry is illustrated in Figure 3.1. With these laser and plasma parameters, using equation 3.3.1, the total number of scattered photons is $\sim 3 \times 10^7$. The forward scattering was collected at $2\theta_F = 40^\circ$ and the backward scattering at $2\theta_B = 120^\circ$.

Two experimental setups were investigated, one with an X-ray probe energy of $E_{ph} = 2\,\text{keV}$ and the other with $E_{ph} = 3.5\,\text{keV}$. Previous experiments conducted at OMEGA have successfully radiographed cryogenic implosions using a crystal imaging system with a silicon He_α backlighter at $\sim 1.865\,\text{keV}$ [82]. This backlighter has reported X-ray efficiencies similar to those considered in this work, though over a 20 ps pulse [80]. Alternate X-ray sources that could be used include Cl K_α at $\sim 2.62\,\text{keV}$ and Cl Ly-α at $\sim 2.96\,\text{keV}$ [83].

The scattering regimes observed by each detector for the in-flight conditions are

shown in Figure 3.2. By selecting multiple probes, one can investigate how the inferred conditions vary depending on the chosen photon energy. These two energies were chosen as each retain one detector in the collective and the other in the non-collective regime. It is important to note that the α-values shown in Figure 3.2 are calculated for the densest region in the compressed DT shell. As the conditions within the capsule implosion are inhomogeneous, these values are not representative of the scattering observed from the ICF capsule as a whole. To ascertain the overall scattering signal observed by each detector, the fully integrated scattering spectra must be calculated.

3.4 Obtaining simulated spatially integrated spectra

The cryogenic DT implosion plasma conditions were calculated using the LILAC code for 1-D simulations and the DRACO code for 2-D simulations. The LILAC code is a 1-D spherical Lagrangian, radiation-hydrodynamics code [71] that simulates symmetric, laser direct-drive implosions. It includes laser ray-tracing with an inverse bremsstrahlung model that can also account for cross-beam energy transfer (CBET) [84]. LILAC also includes a nonlocal thermal transport model that uses a simplified Boltzmann equation with a Krook collision term [85], multi-group radiation diffusion, and a first-principles equation-of-state (FPEOS) model [86, 87] and opacity (FPOT) model [88] derived from molecular dynamics methods.

In comparison, DRACO is an arbitrary Lagrangian–Eulerian (ALE) code employing a second-order accurate Winslow rezoning algorithm [89, 90]. It uses a 3-D ray-based inverse bremsstrahlung energy deposition model for laser drive and includes CBET. Similar to LILAC it uses FPEOS and FPOT for material models, but uses the implicit Schurtz–Nicolai–Busquet (iSNB) for nonlocal electron heat-transport model [91].

The inhomogenity of the plasma produced in an ICF implosion yields diverse scattering signals from various regions within the plasma. The capability to simulate fully spatially integrated spectra, while considering plasma opacity and self-emission, is cru-

cial for determining, for a specific scattering geometry, the dominant scattering features. This provides invaluable insights for experimental designs.

SPECT3D is a spectroscopy code produced by Prism Computational Sciences which post-processes hydrodynamics code output and simulates high-resolution spectra and images for LTE and non-LTE plasmas in 1-D, 2-D, and 3-D geometries [69]. It computes a variety of diagnostic signatures that can be compared with experimental measurements including: time-resolved and time-integrated spectra, space-resolved spectra and streaked spectra. In a SPECT3D simulation, the radiation incident at a detector is computed by solving the radiative transfer equation along a series of lines-of-sight (LOSs) through the plasma grid. At each plasma volume element along a LOS, the frequency-dependent absorption and emissivity of the plasma is calculated. The scattering cross-section is computed using local values of the plasma conditions based on the formalism originally developed in Refs. [52, 40]. Scattered X-ray photons are added to the local source function, allowing SPECT3D to utilise the same algorithms as it uses for plasma self-emission. It is assumed that the radiation from a non-monochromatic, isotropically emitting point-like X-ray source is scattered within each volume element of the SPECT3D spatial grid. The source is specified by its photon-energy-dependent intensity and location in 3-D space. The intensity of the radiation from the source is adjusted for each volume element based on the distance to the source. It includes attenuation due to plasma absorption and the change in the solid angle. The radiation flux at each pixel in the detector plane is calculated by integrating the scattered radiation along each LOS. The scattering angle is computed for each volume element based on the LOS and the line that connects the volume element centre and the source [70].

An important part of this work involved the development with Prism of an additional feature to SPECT3D which allows for selected plasma cells to be excluded from contributing to the scattered signal. This enables the contribution of specified plasma regions to the total scattered spectrum to be isolated. Models for computing

self-emission and absorption coefficients remain the same in each zone regardless of whether they have been excluded from the scattering calculation. By comparing the spectrum from isolated regions to the fully integrated spectrum, a potential dominant contributor can be identified. For XRTS, as shown in equation 3.3.1, the fraction of scattered photons is dependent on n_e. At the in-flight stage of an ICF implosion, the compressed DT shell has the highest n_e. The DT shell is therefore expected to dominate the overall scattering signal, and the inferred plasma parameters should be representative of this region.

At present, SPECT3D does not incorporate any detector considerations into the modelled scattering signal (see Appendix A for further information on using XRTS in SPECT3D). To transform it into a synthetic scattering signal, first the number of detected photons in the free-free scattering feature is calculated as [92],

$$N_{\mathrm{d}} = N_{\mathrm{scatt}} \times \left(\frac{\Omega_{\mathrm{det}}}{4\pi} R_{\mathrm{crystal}} \eta_d \right) = N_{\mathrm{scatt}} \times \Gamma_{\mathrm{det}} \,, \tag{3.4.1}$$

where Γ_{det} is the fraction of detected photons determined by R_{crystal} and η_d which are the crystal reflectivity and the detector efficiency, respectively. The solid angle of a detector with a crystal of length w placed a distance D_{crystal} from the target can be approximated as,

$$\Omega_{\mathrm{det}} \approx \frac{w}{D_{\mathrm{crystal}}} \sin\theta_0 \,, \tag{3.4.2}$$

where θ_0 is the incident Bragg angle on the crystal. For this work, a $\Gamma_{\mathrm{det}} \sim 10^{-5}$ is assumed which gives $N_{\mathrm{d}} \sim 300$ for the in-flight conditions. With currently available spectrometers, such as ZSPEC at the OMEGA laser facility [93], a detector efficiency of $\Gamma_{\mathrm{det}} \sim 10^{-6}$ can be readily achieved. Although this efficiency would generate a marginally detectable signal, boosting the captured photon fraction is within reach. One approach involves utilising a disposable X-ray crystal closer to the imploding capsule, minimising distance-related losses. Alternatively, next-generation detectors with

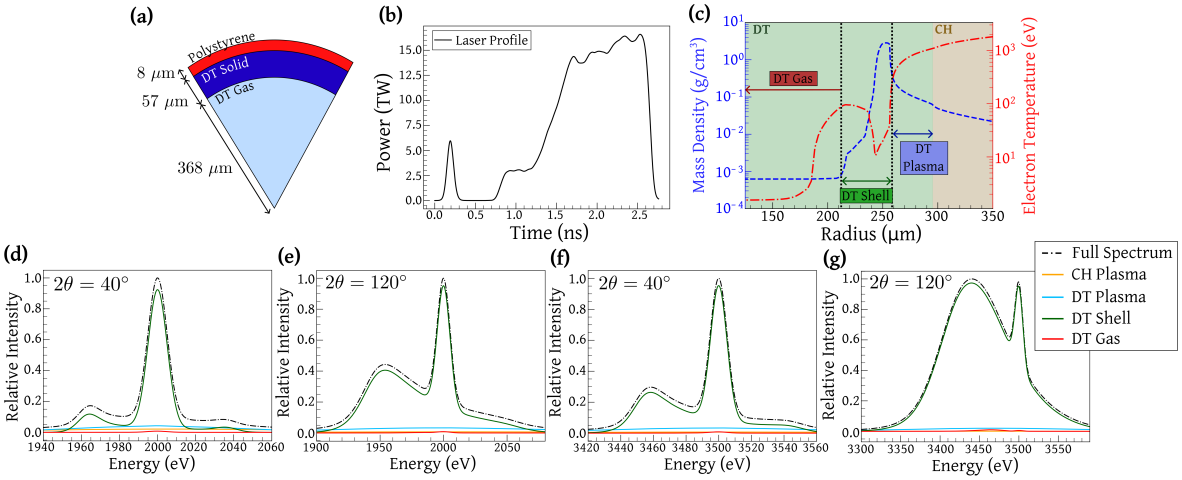

Figure 3.3: **(a)** Simulated design for a target with an in-flight adiabat of 2.8. The target is compressed with the laser profile shown in **(b)**. **(c)** Density and electron temperature conditions in the ICF implosion across the shock wave (propagating to the left) when $R_{\text{Ablation surface}}/R_{\text{Vapor, initial}} = 2/3$, $t = 2215\,\text{ps}$, as determined by the LILAC code for the target. The scattering contributions from the DT in the unshocked fuel (DT Gas), compressed shell (DT Shell) and coronal plasma (DT Plasma) have been isolated and compared to the fully integrated spectrum. For a 2 keV probe, the contribution from each region of the plasma to the overall scattering spectrum is shown for both the forward (40°), **(d)**, and backward (120°) scattering regime, **(e)**. The same breakdown of the plasma has been performed with a 3.5 keV energy probe in **(f)** and **(g)**.

superior quantum efficiency could offer a significant leap in sensitivity.

Furthermore, synthetic experimental noise was incorporated into the spectra. This involved applying Poisson statistics, which estimates the noise as $\sim 1/\sqrt{N_t}$, where N_t is the total number of photons per spectral resolution element, including self-emission. The details of each study conducted are detailed in the subsequent sections.

3.5 Resolving extreme adiabats from 1-D simulations

The initial exploration in this feasibility study focused on 1-D simulations of two extreme target adiabats. The target chosen for the high adiabat design was used in the first phase of the performance optimisation campaign conducted at OMEGA. Whilst subsequent target designs in this campaign have since set the record neutron yield on OMEGA [94], the target selected for this study remains a good design reference point

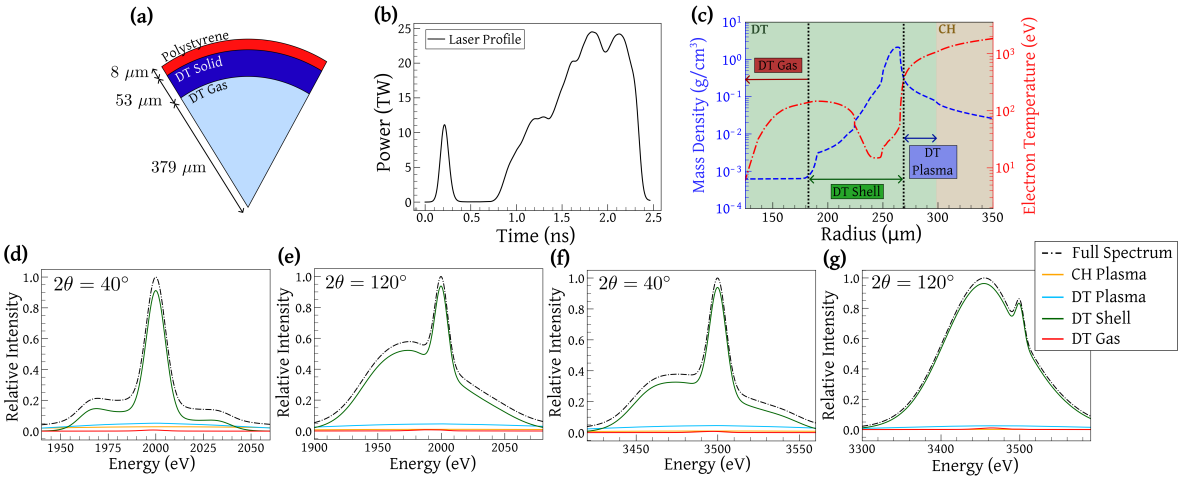

Figure 3.4: As with Figure 3.3 but for an ICF capsule with an in-flight adiabat of 8.0 at $t = 1901$ ps.

for a stable implosion. The lower adiabat target design used was part of a campaign to probe performance right below an observed 'stability cliff' [15] that is still considered in modern implosion designs on OMEGA. The details of the two targets chosen for this investigation are shown in Figures 3.3 and 3.4 with in-flight adiabats of 2.8 and 8.0, respectively.

The total scattering signal for each detector is shown as a dashed black line in (d)-(g) of each of these figures. At the in-flight stage, the capsule implosion can be divided into four primary regions; the DT gas, the compressed DT shell, the DT coronal plasma, and the CH coronal plasma. Utilising the new feature in SPECT3D, the breakdown of the spectral contribution from each of these regions is shown in comparison to the overall scattering signal. As predicted, the spectrum recorded by each detector is dominated by the contribution from the compressed DT shell.

Following the detector assumptions detailed in section 3.4, approximately 3 photons/eV contribute to the inelastic scattering feature. Over the timescale of the X-ray pulse, this signal is observed above the continuum emission for each detector as shown in Figure 3.5. Assuming a spectral resolution of 3 eV/bin, this provides an inelastic signal of ~ 9 photons/bin.

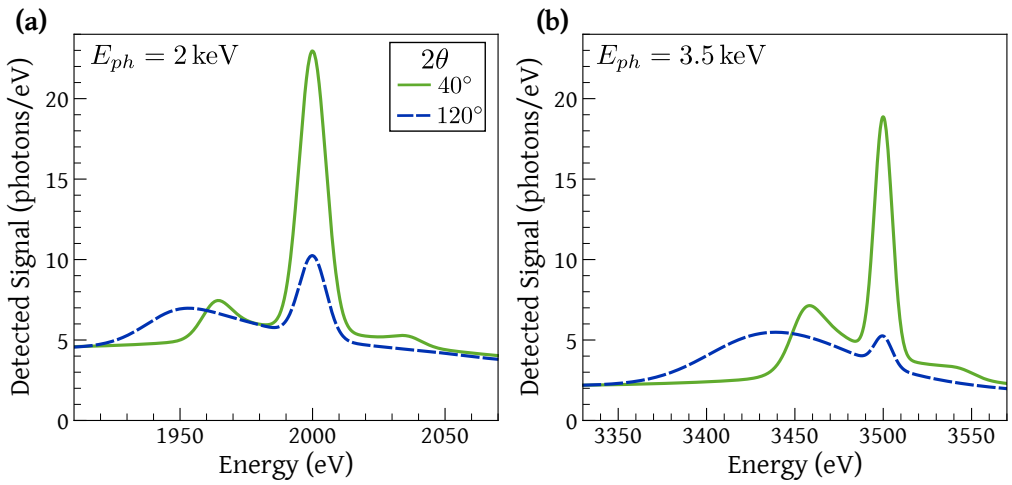

Figure 3.5: Total detected signal per eV, where Γ_{det} is assumed to be 10^{-5}, integrated over the time of the X-ray laser pulse = 10 ps. The signal is shown for the target with an adiabat of 2.8 with **(a)** 2 keV and **(b)** 3.5 keV incident photon energies.

The resultant scattering spectra, where the continuum emission has been removed and synthetic experimental noise added, are shown in Figure 3.6. These figures demonstrate that for experimental conditions with identical scattering setups, the two extreme adiabat targets considered here produce notably differing scattering spectra. In the forward detector, using a 2 keV probe (shown in Figure 3.6(a)), the plasmon scattering from both adiabat's is observed. However, with the 3.5 keV probe (shown in Figure 3.6(b)), the forward inelastic scattering from the high-adiabat is dominated by Compton scattering. This is evidenced by the broadening of the inelastic peak and the loss of a forward shifted plasmon peak. This change in scattering features is evidence of its higher electron temperature and lower density.

3.5.1 Analysing spatially integrated XRTS

To extract the plasma conditions by fitting the spatially integrated simulated spectra, the inverse problem instability must first be addressed. This implies that a measured spectrum can be fitted equally well by a range of different conditions [95]. Bayesian inference, using Markov-Chain Monte Carlo (MCMC) to sample the multidimensional

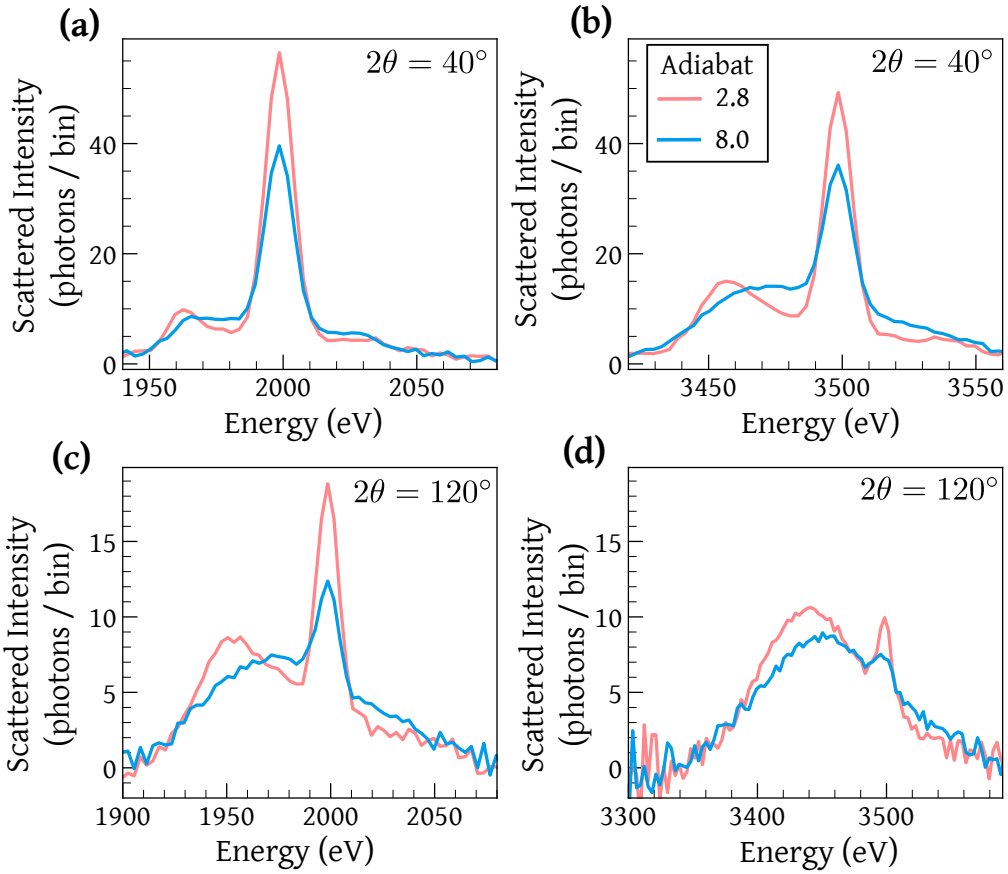

Figure 3.6: Synthetic experimental X-ray scattering data produced with SPECT3D using 1-D LILAC simulations, assuming 3 eV/bin and Poisson statistics to simulate noise. **(a)**, **(b)**: Forward scattering spectra using a 2 keV and a 3.5 keV probe, respectively. **(c)**, **(d)**: Backward scattering spectra using a 2 keV and a 3.5 keV probe, respectively.

space, is a robust approach for exploring the behaviour of the complex multi-parameter simulations [96] (see Appendix B for further details).

Accurately modelling the inhomogeneous plasma poses a challenge. Ideally multiple plasma regions would be assumed, though fitting them with MCMC brings complications. To avoid regions overlapping, their parameter spaces would need to be restricted, preventing where they can explore during the MCMC analysis. However, such restrictions would ultimately bias the converged conditions. The MCMC exploration conducted in this work therefore assumed only two weighted uniform plasma regions, one containing DT and the other CH. This raises a critical question: can a single-region model provide meaningful insights into the complex, inhomogeneous reality?

The MCMC analysis was setup to explore the ionisation, temperature and density that best fit the forward and backward scattering spectra individually. The parameter space for the DT region assumed a uniform distribution with linear sampling for the electron temperature, $1 \leq T_e(\text{eV}) \leq 10^3$ and ionisation, $0 \leq \bar{Z} \leq 1$ (where $\bar{Z} = (Z_D + Z_T)/2$). A logarithmic sampling was taken for the electron density, $10^{20} \leq n_e(\text{cm}^{-3}) \leq 5 \times 10^{24}$. A large sampling space was used to reduce bias on the converged conditions.

The MCMC code determines the likelihood of finding a specific set of parameters, $\Psi(T_e, n_e, \bar{Z})$, given the synthetic experimental spectrum, $I_{\text{exp}}(\omega)$, at each step using Bayesian inference,

$$P(\Psi|I_{\text{exp}}) = \frac{P(I_{\text{exp}}|\Psi)P(\Psi)}{P(I_{\text{exp}})}\,. \tag{3.5.1}$$

Here $P(\Psi)$ is the prior distribution of possible parameters, $P(I_{\text{exp}})$ is the marginal likelihood of the observed data over all possible parameters and $P(I_{\text{exp}}|\Psi)$ is the likelihood of finding $I_{\text{exp}}(\omega)$ given the input parameters, Ψ. The forward model likelihood, $P(I_{\text{exp}}|\Psi) = e^{-\beta_{\text{cost}}}$, is a user defined function that gives an acceptance percentage for each Ψ. The cost function, β_{cost}, is selected such that the range of converged MCMC fits fall within the experimental noise of $I_{\text{exp}}(\omega)$.

A standard cost function determines the maximum error between the MCMC fitted spectrum, $I_{\text{fit}}(\omega)$, and the synthetic experimental spectrum as,

$$\beta_{\text{cost}} = \max\left[\frac{I_{\text{fit}}(\omega) - I_{\text{exp}}(\omega)}{\sqrt{2}\sigma}\right]^2. \tag{3.5.2}$$

The factor σ is the standard deviation representative of the noise of the synthetic scattering spectrum. Whilst a cost function such as the sum of squares can result in an overall tighter range of accepted MCMC fits to $I_{\text{exp}}(\omega)$, this method assumes a perfect fitting model which can lead to high confidence in false results [95].

For certain spectra, such as those collected by the forward scattering detector, the

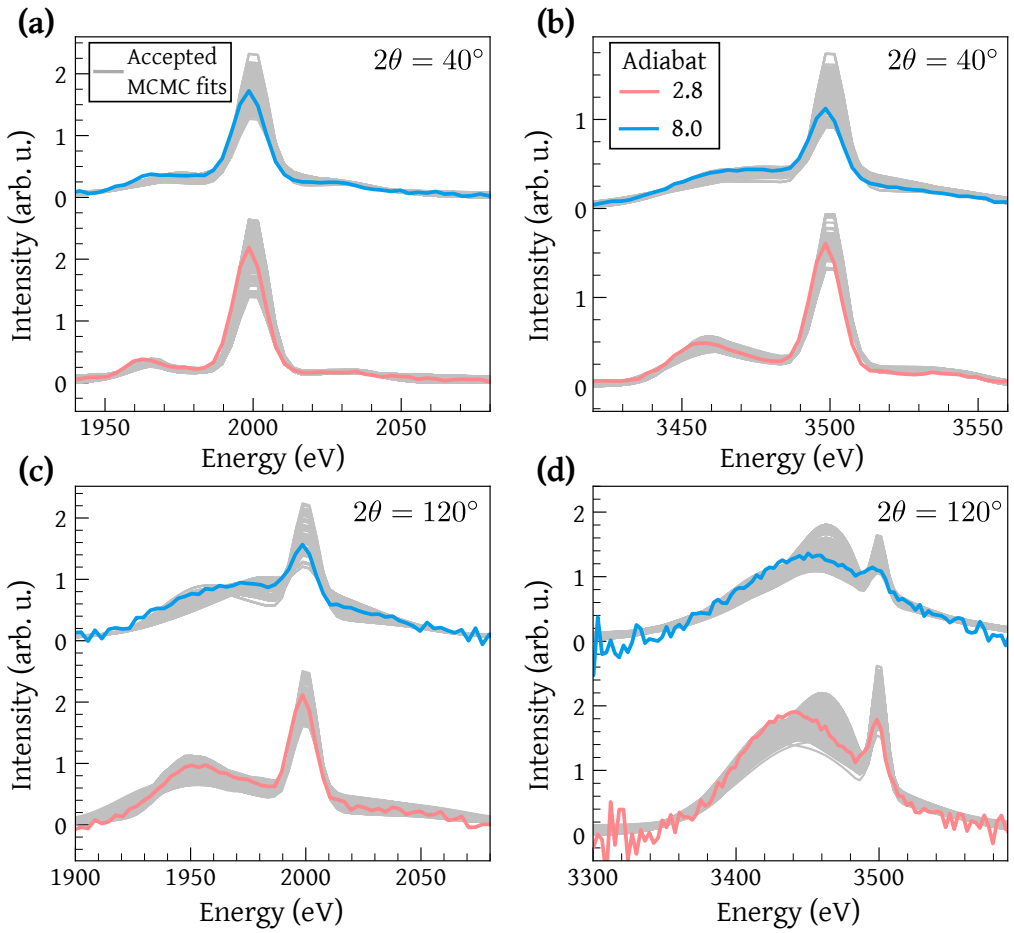

Figure 3.7: The range of accepted MCMC fits, shown in grey, for each simulated scattering spectrum as illustrated in Figure 3.6.

cost function in equation 3.5.2 can preferentially fit the more intense elastic scattering signal. In cases such as these, a 'percentage' cost function is used instead,

$$\beta_{\text{cost}} = \max\left[\frac{I_{\text{fit}}(\omega) - I_{\text{raw}}(\omega)}{I_{\text{raw}}(\omega)}\frac{1}{\sqrt{2}\sigma}\right]^2. \tag{3.5.3}$$

This more evenly weights the fitting of both the elastic and inelastic peaks. For any cost function, the value of σ is typically not known *a priori*. It is chosen for each MCMC exploration such that the synthetic scattering signal falls comfortably within the spread of the accepted fits. Examples of the range of accepted MCMC fits are shown in Figure 3.7. While each synthetic scattering spectrum may not precisely align with the range of MCMC fits, this discrepancy is an inherent outcome of modelling an inhomogeneous

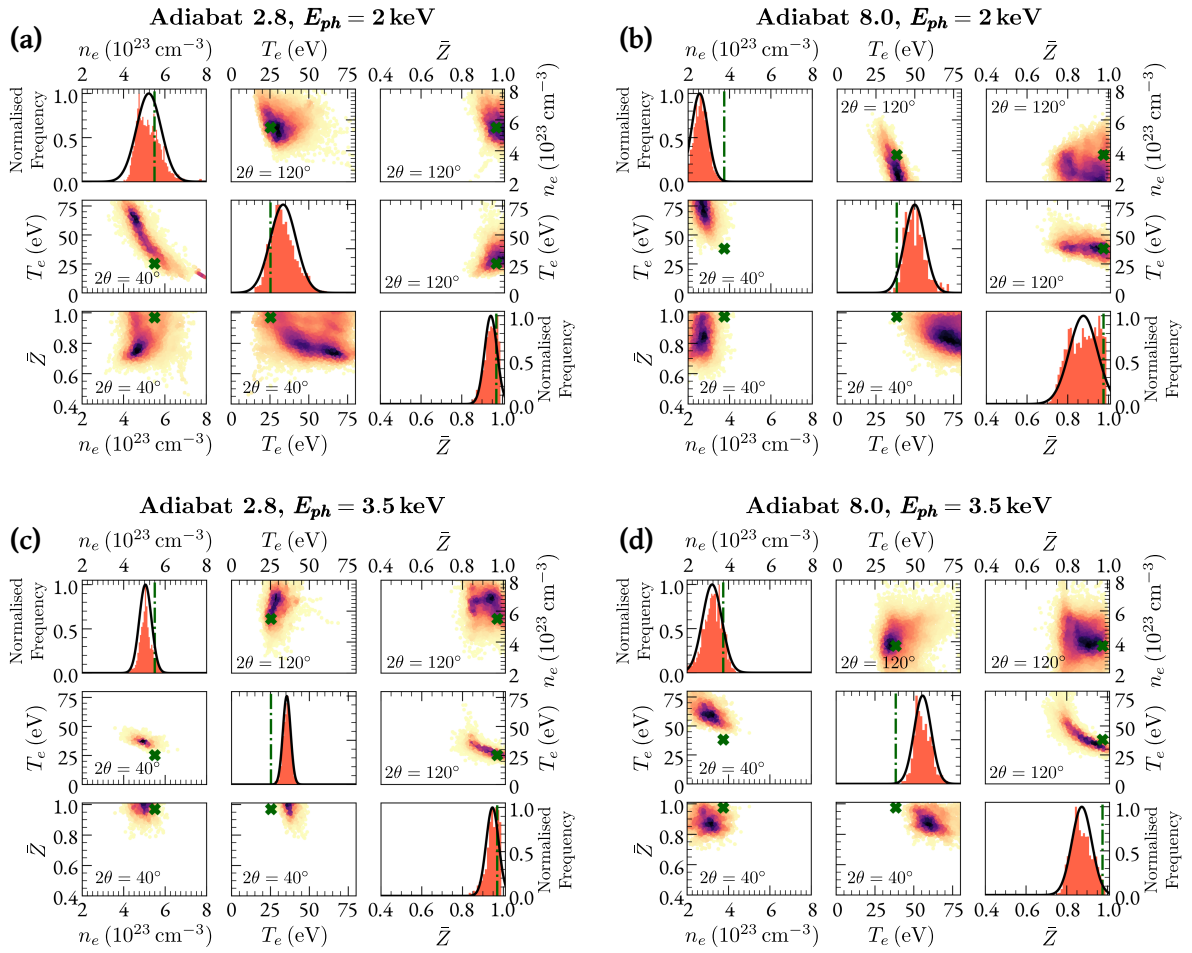

Figure 3.8: Converged parameters from MCMC exploration fitting the synthetic scattering spectra. Variation in DT plasma parameters from; **(a)** 2.8 adiabat and 2 keV probe, **(b)** 8.0 adiabat and 2 keV probe, **(c)** 2.8 adiabat and 3.5 keV probe, and **(d)** 8.0 adiabat and 3.5 keV probe. The scatter plots show the correlation between each DT parameter. The lower quadrant scatter plots are from fitting the 40° scattering data, whilst the upper quadrant shows the 120° scattering data. The scatter plots have been coloured to represent the spatial density of points. The diagonal plots show the combined histograms for each parameter from both the scattering regimes. Superimposed on each histogram is a normal distribution of the fits. The mass-averaged parameter values from the LILAC 1-D simulations are highlighted as a green dashed line or cross.

scattering event using a single uniform plasma region.

To analyse the MCMC data, the DT parameters were plotted on a combined matrix shown in Figure 3.8. The scatter plots for each scattering angle are shown separately and have been coloured to represent the spatial density of points. In Figure 3.8, the histograms along the diagonal are the combined histograms for both the forward and

backward scattering parameters. The mean and standard deviation on each parameter is determined by then fitting a normal distribution to the histograms.

To determine the effectiveness of using a single uniform plasma region to represent the inhomogeneous conditions, the MCMC parameters are compared to the mass-weighted parameters from the 1-D LILAC simulations. The mass-weighted simulation values are calculated using,

$$\langle \mathrm{F} \rangle = \frac{\sum F_i \rho_i 4\pi r_i^2 \mathrm{d}r_i}{\sum \rho_i 4\pi r_i^2 \mathrm{d}r_i}\,, \tag{3.5.4}$$

where F_i is the desired parameter in zone i. The mass-weighted parameters are determined for each region of the implosion. It can be seen in Table 3.1 that the converged MCMC conditions are in close agreement with the mass-weighted parameters from the compressed DT shell. As discussed previously, this was an expected result, as the high density and relative homogeneity of the compressed DT shell region meant it dominated the observed scattering features.

The MCMC analysis on the forward scattering spectra tend to converge around lower densities, higher temperatures and broader ionisations. This results in either broader or slightly skewed distributions on the combined DT parameters. The differing numerical convergence occurs due to the broadening of the observed plasmon scattering

Table 3.1: Comparison of the DT plasma conditions found at MCMC convergence, as illustrated in Figure 3.8, with the LILAC 1-D simulations' mass-weighted values. The MCMC reported errors are the 1σ standard deviations from the histogram normal distributions.

DT Parameter	$\mathbf{T_e}$ (eV)	$\mathbf{n_e}$ (cm^{-3})	$\bar{\mathbf{Z}}$
Adiabat 2.8			
Simulation	25	5.5×10^{23}	0.97
MCMC 2 keV	33 ± 8	$(5.2 \pm 0.6) \times 10^{23}$	0.94 ± 0.03
MCMC 3.5 keV	35 ± 3	$(5.0 \pm 0.3) \times 10^{23}$	0.95 ± 0.03
Adiabat 8.0			
Simulation	38	3.7×10^{23}	0.97
MCMC 2 keV	50 ± 6	$(2.6 \pm 0.4) \times 10^{23}$	0.88 ± 0.07
MCMC 3.5 keV	56 ± 6	$(3.2 \pm 0.5) \times 10^{23}$	0.87 ± 0.05

peaks. This broadening is a result of the relatively wide X-ray source FWHM and contributions from the lower density regions of the compressed shell producing non-collective Compton scattering features. In this 1-D case, information on the compressed DT shell can be obtained focusing solely on the backward scattering. As illustrated in the parameter density maps in Figure 3.8, analysis focusing solely on the backward scattering would result in closer agreement with the simulation's mass-averaged electron temperature.

The MCMC analysis reveals limited information about the CH plasma. This is because its lower density compared to the DT shell, as demonstrated earlier, makes it negligible in shaping the observed scattering feature. Consequently, it contributes minimally to the overall signal, resulting in a significantly low weighting within the MCMC analysis. This, in turn, prevents convergence on meaningful CH plasma conditions.

3.6 Extending to 2-D simulations

On many ICF implosions, conducted both at the National Ignition Facility and OMEGA, asymmetries in the capsule convergence have been observed to severely affect the overall target performance [97, 98]. These asymmetries can arise as a result of imperfections in the laser drive and target. They are characterised by their Legendre mode number $l = 2\pi R/\lambda_p$, where the perturbation wavelength λ_p is measured relative to the initial target radius R. A low mode perturbation is therefore a result of a large-scale feature compared to R, such as a misaligned drive beam. Perturbations can be amplified by the growth of hydrodynamic instabilities, degrading the performance of the ICF implosion [99].

The limitations of 1-D simulations in capturing hydrodynamic instabilities necessitates a more advanced approach to understand their impact on the scattering spectrum and inferred plasma conditions. Figure 3.9 illustrates the impact of extending to 2-D simulations which incorporate some of these instabilities into the simulated dynamics.

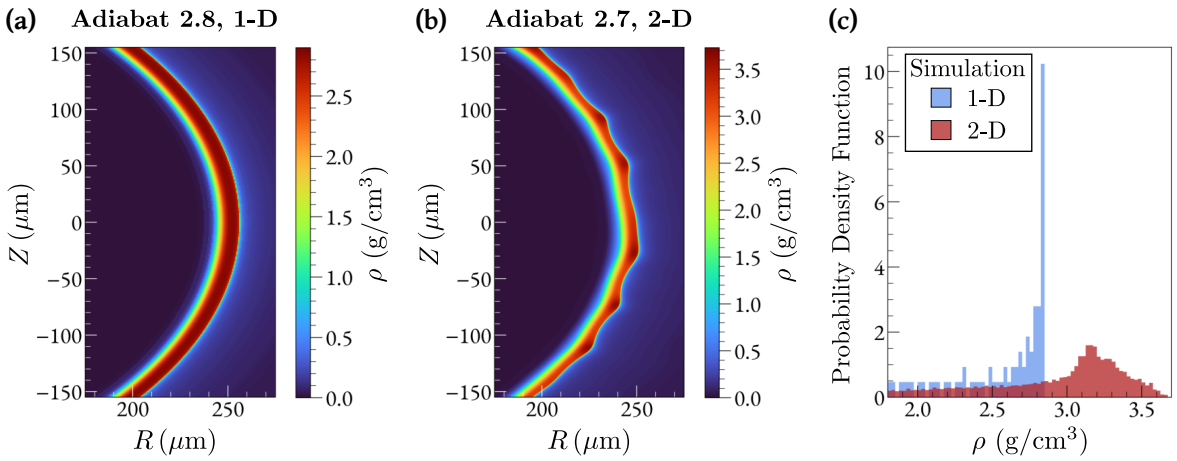

Figure 3.9: 2-D mass-density profiles of the compressed DT shells at two-thirds compression for similar adiabat cases using 1-D, **(a)**, and 2-D, **(b)**, models. The 1-D adiabat is as described in Figure 3.3 and the 2-D adiabat is as described in Figure 3.10. **(c)** The probability density function of the mass density within the compressed DT shell for both the 1-D (in blue) and 2-D (in red) cases.

The inclusion of 2-D effects diminishes the uniformity of the in-flight compressed shell. This effectively disperses the DT mass over a broader range, significantly increasing the volume of dense material encountered by the probing X-rays. Such a deviation from the ideal, comparatively homogeneous 1-D scenario can affect the MCMC convergence around representative conditions, as a broader range of plasma conditions are influencing the observed scattering spectra.

The 2-D simulations used in this investigation were run assuming full smoothing by spectral dispersion imprint up to Legendre mode 50, allowing for the growth of high mode perturbations. The targets modelled in the 2-D simulations were chosen to imitate the in-flight adiabat conditions from section 3.5. An additional target with and in-flight adiabat of 5.4 was studied to provide a bench-mark for distinguishing closer adiabats. The target designs and in-flight conditions are illustrated in Figures 3.10, 3.11 and 3.12. To determine the mass-weighted parameters from the 2-D simulations, equation 3.5.4 is altered to,

$$\langle \mathrm{F} \rangle = \frac{\sum F_i \rho_i 2\pi r_i A_i}{\sum \rho_i 2\pi r_i A_i}\,, \tag{3.6.1}$$

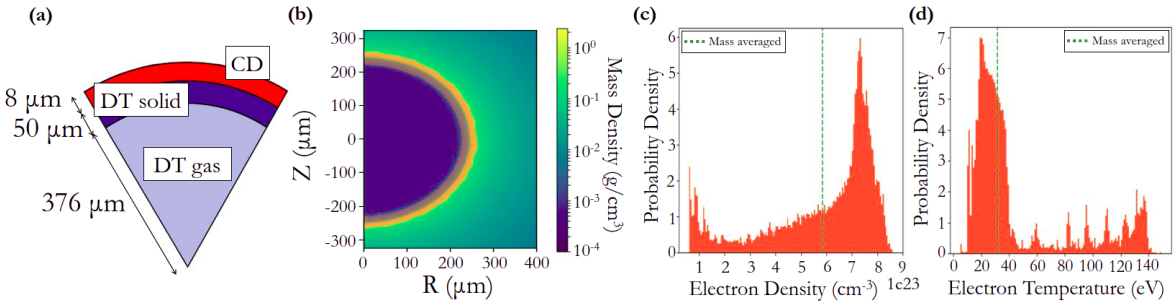

Figure 3.10: **(a)** Simulated target design, with an adiabat of 2.7. **(b)** 2-D mass density conditions in the ICF implosion at two-thirds compression, $t = 2121$ ps, as determined by the DRACO code for the target. The region of the compressed DT shell is highlighted in orange. The dark blue encapsulated within this region is the forming DT hot spot. The hot DT coronal plasma surrounds the shell and the low density mass beyond that is the CD plasma. For the compressed shell region, the distribution of the electron density and electron temperature are shown in plots **(c)** and **(d)**, respectively. The corresponding mass averaged quantities are shown as green dashed lines.

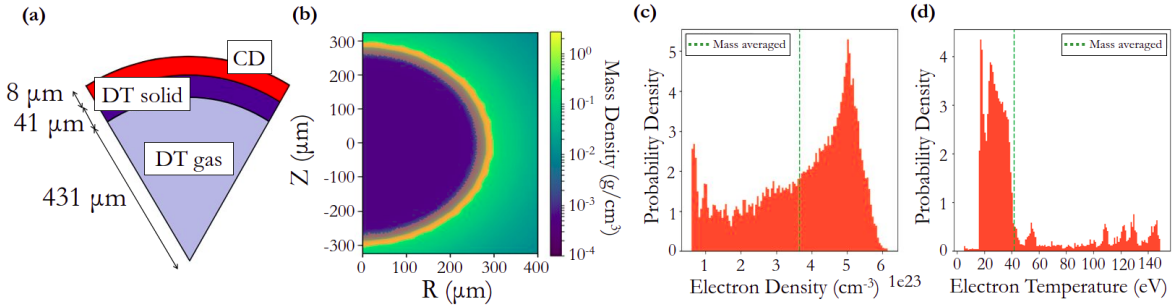

Figure 3.11: As with Figure 3.10 but with an ICF capsule with an adiabat of 5.4 and at $t = 1640$ ps.

where A_i is the area of cell i.

The interpretation of scattering data produced by the 2-D simulations poses a challenge due to the wide range of electron densities within the compressed shell. As shown by equation 2.2.9, the scattering parameter $\alpha \propto \sqrt{n_e}$. At relatively constant electron temperatures, the presence of a significant portion of low-density plasma leads to non-collective scattering observed in the forward detector. This effect can be mitigated by opting for X-ray probes with lower photon energies. The 2-D analysis therefore focuses on the use of the 2 keV X-ray probe, as explored in section 3.5, and yields MCMC convergences depicted in Figure 3.13.

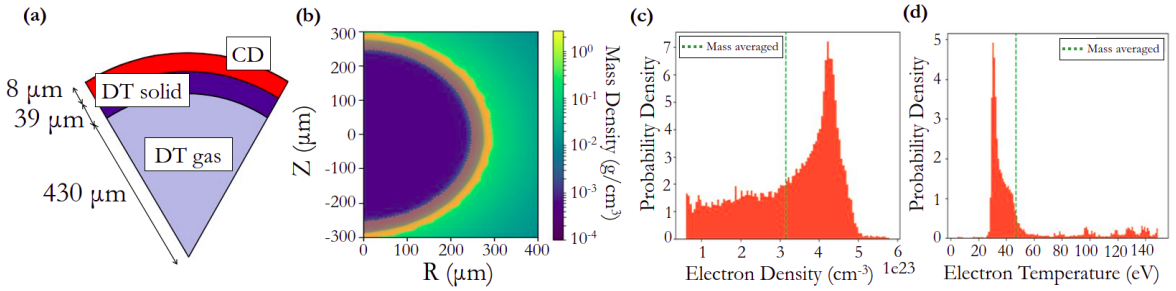

Figure 3.12: As with Figure 3.10 but with an ICF capsule with an adiabat of 8.8 and at $t = 164\,\text{ps}$.

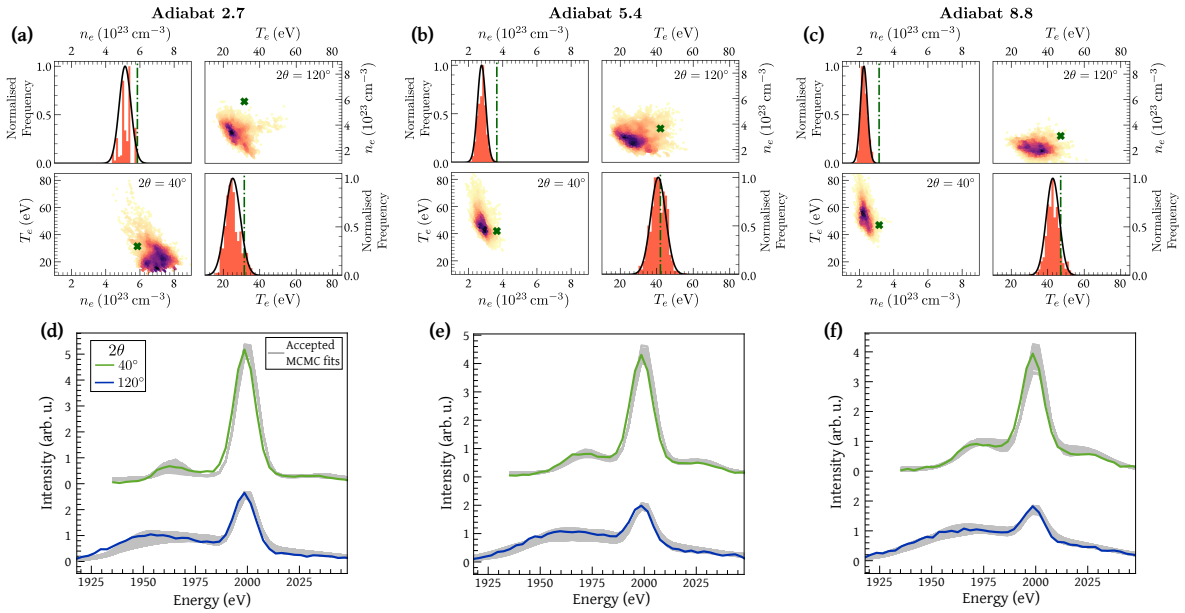

Figure 3.13: MCMC convergence of electron density and temperature for 2-D simulations using a 2 keV probe. The variation in DT plasma parameters are shown for; **(a)** 2.7 adiabat, **(b)** 5.4 adiabat, and **(c)** 8.8 adiabat. The form of the matrix plots are as in Figure 3.8. Below each matrix the corresponding accepted MCMC fits for the forward and backward scattering are shown compared to the corresponding synthetic simulated spectrum.

For the higher adiabat targets, the forward detector converges around lower densities, indicating a discernible mixture of collective and non-collective scattering features. In contrast, the 2.7 adiabat target, which has the narrowest density distribution, converges around higher densities for the forward scattering. As detailed in section 2.3.1, the position of the collective scattering peaks is correlated with the plasma frequency, $\omega_{pe} \propto \sqrt{n_e}$. Consequently, a plasma with higher electron density produces a plasmon

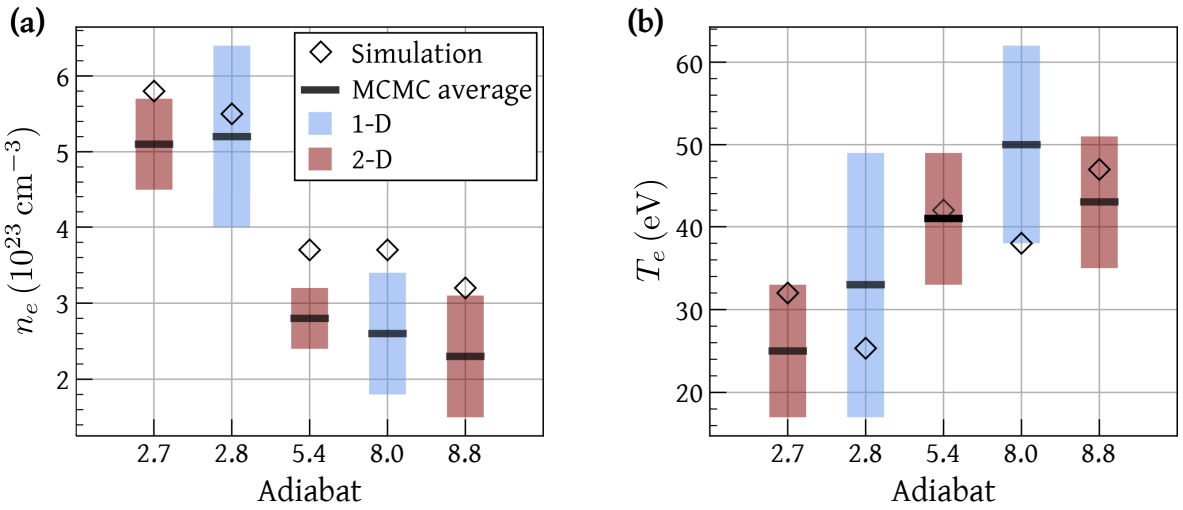

Figure 3.14: Comparison of MCMC parameter convergence for electron density, **(a)**, and electron temperature, **(b)** using 1-D, in blue, and 2-D, in red, simulations with a 2 keV X-ray probe. The error bars shown are the 2σ errors from the normal distribution fit to the MCMC histograms. The mass-averaged compressed shell values determined from each simulation are indicated as black diamonds.

scattering peak at a greater energy shift from the elastic signal. As illustrated in Figure 3.10(c), a significant portion of the compressed shell has an electron density in the range of $6 - 8 \times 10^{23}\,\mathrm{cm}^{-3}$. This region produces the inelastic scattering peak $\sim 40\,\mathrm{eV}$ from the central energy in the forward detector. It is therefore not surprising that the MCMC analysis on the forward scattering for this target converges around densities

Table 3.2: Comparison of the DT plasma conditions found at MCMC convergence, as illustrated in Figure 3.13, with the DRACO 2-D simulations' mass-weighted values. The MCMC reported errors are the 1σ standard deviations from the histogram normal distributions.

DT Parameter	$\mathbf{T_e}$ (eV)	$\mathbf{n_e}$ (cm^{-3})	$\bar{\mathbf{Z}}$
Adiabat 2.7			
Simulation	32	5.8×10^{23}	0.97
MCMC 2 keV	25 ± 4	$(5.1 \pm 0.3) \times 10^{23}$	0.91 ± 0.05
Adiabat 5.4			
Simulation	42	3.7×10^{23}	0.98
MCMC 2 keV	41 ± 4	$(2.8 \pm 0.2) \times 10^{23}$	0.92 ± 0.04
Adiabat 8.8			
Simulation	47	3.2×10^{23}	0.99
MCMC 2 keV	43 ± 4	$(2.3 \pm 0.2) \times 10^{23}$	0.95 ± 0.03

corresponding to these values, rather than the mass-averaged electron density.

To assess the effectiveness of the XRTS technique developed in this chapter for discerning plasma conditions within the in-flight compressed shell of ICF targets with varying adiabats, Figure 3.14 illustrates the range of converged MCMC parameters. For both the 1-D and 2-D simulations, a noticeable disparity emerges in the inferred electron density between low and high adiabat targets. Although the shift in electron temperature across the adiabat range is not as pronounced, this technique adeptly captures the trend of resolving higher temperatures for higher adiabats. It is worth noting that the converged temperatures, particularly for the 1-D simulations, may be improved by focusing solely on the backward scattering analysis.

3.7 Constraints at Peak Compression

Developing a diagnostic capable of probing the conditions at peak compression in an ICF implosion would unlock invaluable insights into achieving ignition. Current diagnostics such as neutron scattering can measure the hydrodynamic properties of the dense DT fuel, though they remain sensitive to the inferred ion temperature in the shell [78]. However, implementing a Thomson scattering diagnostic at peak compression presents challenges not encountered at the in-flight times investigated above. At this stage, core temperatures within the ICF capsule can exceed several keV, generating significant self-emission that a fielded X-ray source must overcome to yield a discernible scattering signal. In addition, as illustrated in Figure 3.15, regions of high density are no longer constrained to the compressed shell. To identify the plasma within the compressed shell, a density constraint of $\rho > \rho_{\max}/e$ has been applied. Unlike the in-flight stage, the observed scattering signal will therefore be a composite from multiple regions, complicating data interpretation.

In Figure 3.15, the hot spot of the depicted target exhibits a mass-averaged electron temperature of $\sim 3000\,\mathrm{eV}$. This causes a significant influx of background photons

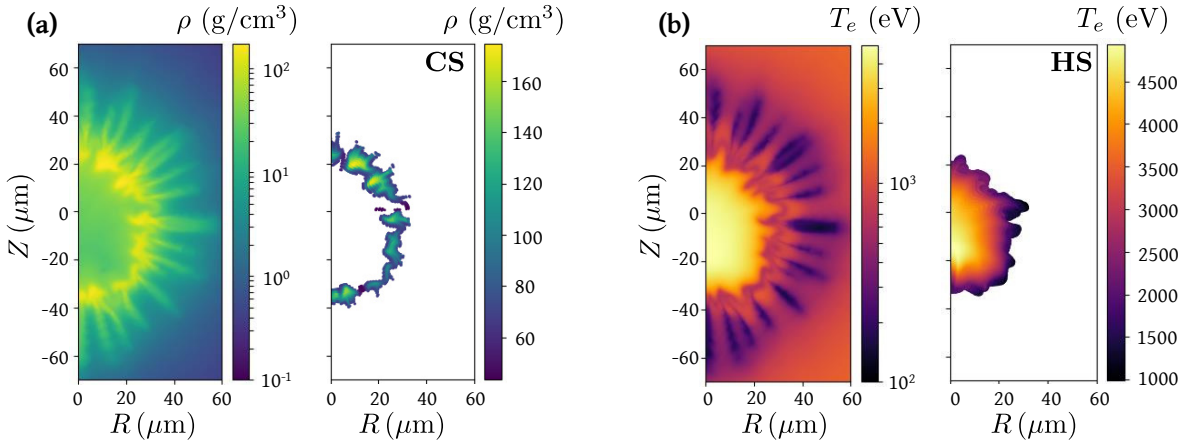

Figure 3.15: 2-D density, **(a)**, and temperature, **(b)**, conditions at peak compression, $t = 2120\,\text{ps}$, from the target shown in Figure 3.11. On the right of each plot, the parameters within the compressed shell or hot spot are isolated.

spanning the energy spectrum of existing X-ray sources at OMEGA. Consequently, addressing the demand for implementing XRTS at peak compression necessitates exploring novel, higher energy sources. However, the higher energy of X-ray photons required to overcome self-emission renders it unfeasible to employ a detector in the collective regime.

One source considered in this work was an X-ray Free Electron Laser (XFEL) [100]. XFELs have proven their efficacy in various experiments by delivering high-resolution X-ray scattering. The distinct advantages that make it such an appealing source for diagnosing plasma conditions during peak compression include the production of narrow-bandwidth, high-energy photons, and the ability to focus coherent X-rays precisely over a limited area. Assuming a 50 fs X-ray pulse with 11 keV photons and a FWHM of 10 eV, the total energy incident on the plasma was 100 μJ with a spot size of 80 μm. This spot size was chosen so the incident X-rays encapsulate the entirety of the compressed shell which, as illustrated in Figure 3.15, has a radius just under 40 μm. However, the detector is still assumed to observe the full scale of the imploding capsule.

If Γ_{det} is, as before, assumed to be 10^{-5}, the total signal observed by the forward scattering detector is shown in Figure 3.16(a). The signal-to-noise ratio is ~ 1.2 across

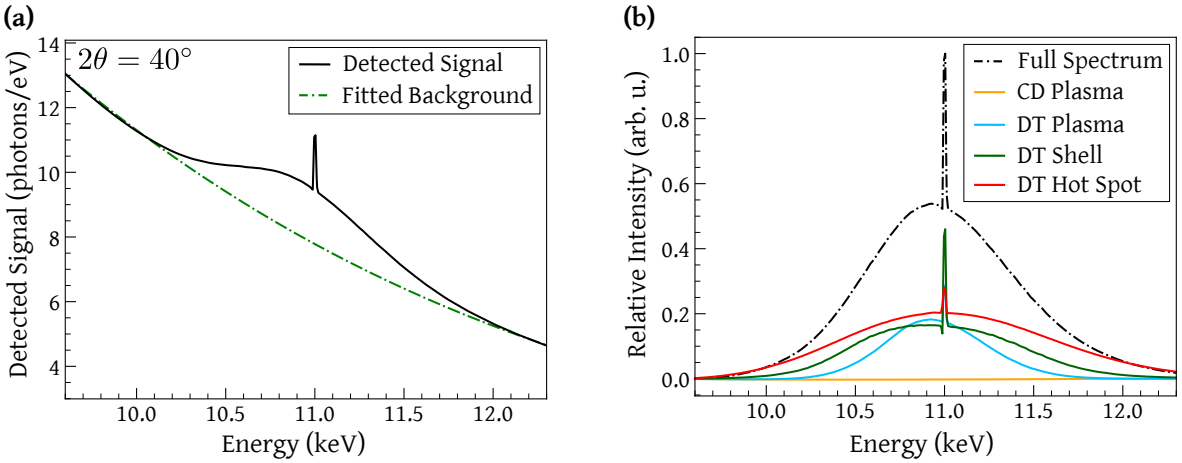

Figure 3.16: **(a)** Detected signal integrated over the time of the XFEL source, 50 fs, and where Γ_{det} is assumed to be 10^{-5}. **(b)** Breakdown of regional contribution to the total scattering signal.

the time length of the laser probe with a couple of thousand photons contributing to the total inelastic signal. In comparison, the inelastic scattering observed on the backward scattering detector is an order of magnitude smaller.

In Figure 3.16(b), the contribution from each distinct region of the plasma is compared to the overall scattered signal. Unlike the in-flight case, the heightened densities throughout the capsule result in the hot spot, compressed shell, and DT coronal plasma contributing nearly equally to the signal. Analysing the data as performed in the in-flight cases, where a single uniform DT plasma region is assumed, would therefore be inappropriate at peak compression. Instead, a multi-region plasma must be considered, necessitating constraints between these distinct regions, as discussed previously. Relying solely on the analysis of this XRTS signal would therefore prove challenging and potentially introduce biases into the results.

To mitigate parameter bias, one approach could involve deploying XRTS during both the two-thirds and peak compression phases of the implosion. Figure 3.17 presents a comparative analysis of conditions during the in-flight and peak compression stages, simulated using the 1-D LILAC simulation code, across varying target adiabats. The simulated targets all contained a CD ablator, DT ice and DT fuel layer with varying

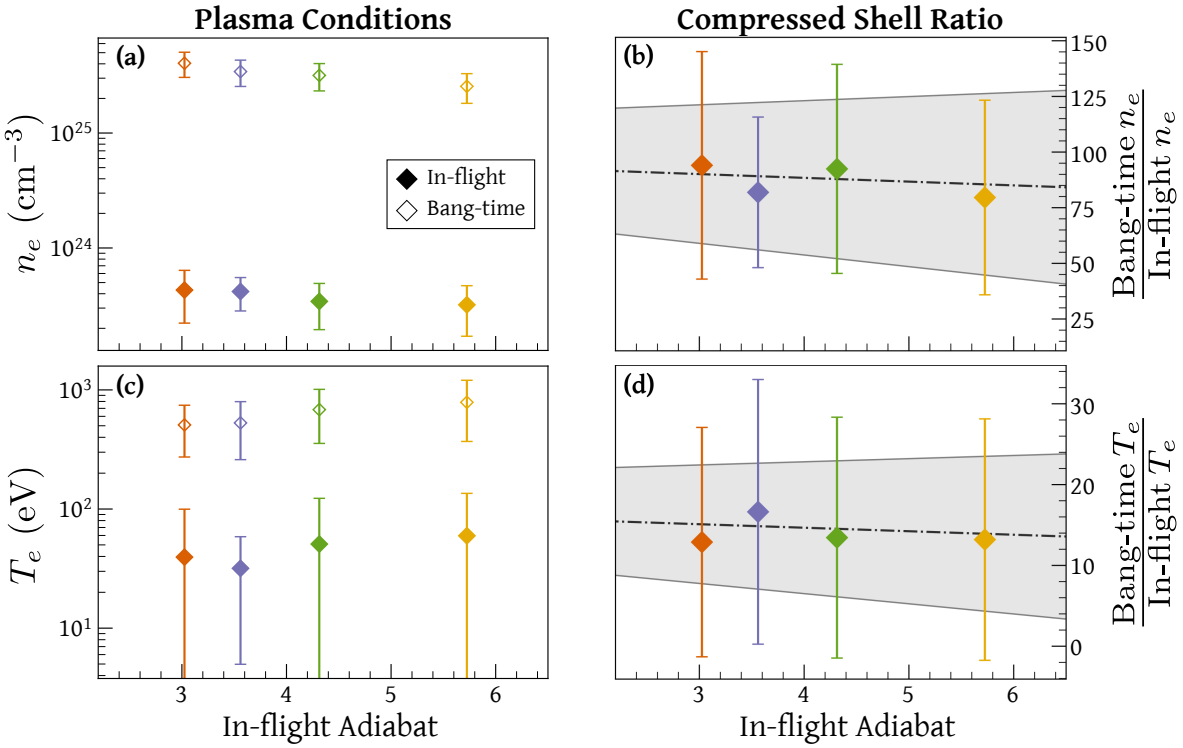

Figure 3.17: Comparison of the electron density, **(a)** and **(b)**, and electron temperature, **(c)** and **(d)**, at two-thirds and peak compression of 1-D LILAC ICF simulations. On the right panel, a linear fit to their relationship is shown as a black dash-dotted line with an error margin indicated in grey.

thicknesses to alter the measured in-flight adiabat. The mean values represent the mass-weighted conditions within the compressed shell, and the quoted error is determined as its variance. Across the target adiabats, an approximate linear trend is noticeable between the peak compression (bang-time) and in-flight conditions. This observed comparability suggests that deploying XRTS at both time points may prove instrumental in constraining parameters within the compressed shell at peak compression.

Future investigations into peak compression XRTS could also explore the prospect of integrating the potential scattering signal with alternative diagnostic techniques, such as neutron spectroscopy [101, 102], to assist in distinguishing between the hot spot and the compressed shell conditions.

3.8 Conclusions

This chapter has demonstrated the potential offered by the development of an X-ray Thomson scattering diagnostic platform for cryogenic inertial confinement fusion implosions in resolving the in-flight compressed shell conditions. Spatially-integrated XRTS spectra were calculated for 1-D and 2-D simulated conditions of low and high adiabat, deuterium-tritium (DT) cryogenic implosions at two-thirds convergence.

Markov-Chain Monte Carlo analysis was conducted for two different scattering setups, yielding valuable information on the compressed shell conditions. The spectral resolution in spatially integrated measurements was exploited to discriminate between different regions in the plasma. The optimal approach for resolving the compressed shell plasma conditions, using a realistic laser probe from OMEGA EP, involved performing MCMC analysis on spectra generated using a low-energy X-ray probe, specifically at 2 keV. This methodology successfully achieved the overarching goal of distinguishing between high and low adiabat implosion conditions, using both 1-D and 2-D simulations. Enhanced agreement between MCMC parameters and simulations could be attained by employing a narrower bandwidth (FWHM < 10 eV) probe beam. This adjustment would render the forward inelastic scattering signal more sensitive to electron density, a feasibility achievable with a Free Electron Laser.

The analysis of potential scattering signals from peak compression, utilising an XFEL, revealed an equal influence from the three distinct DT plasma regions. Consequently, to mitigate analytical bias, independent sources of constraint on the DT parameters would be essential. The observed relationship between the in-flight and peak compression conditions indicates that in-flight data could serve as a valuable means to constrain the compressed shell conditions.

In addition, research and development on a spectrometer to optimise the detection of the XRTS signal is required to meet the constraints shown within this chapter.

Chapter 4

Experimental Probing of Warm Dense Matter Silicon at 100 GPa

The content within this chapter is based on "Multimessenger measurements of the static structure of shock-compressed liquid silicon at 100 GPa", Physical Review Research 6, 023144 (2024), Poole *et al.* [103].

4.1 Introduction

Over the last few decades, high-energy density facilities have generated sufficiently long-lived warm dense matter sates, enabling the deployment of advanced diagnostic suites [104–106]. Notably, the Linac Coherent Light Source's X-ray free electron laser has facilitated high-resolution X-ray scattering measurements for probing the electronic and atomic structure of high-pressure states [100, 107]. However, XFELs face limitations in compression capabilities and achievable WDM volumes, hindering the creation of macroscopic homogeneous conditions. At kJ- to MJ-class laser facilities, conditions expected in both Jovian planet interiors [108] and fusion ignition capsules [22] can be generated. Accurately determining pressure, density, and temperature within these complex states of matter remains challenging without employing molecular-dynamic simulations in the data analysis. Furthermore, limitations in applying standard model approximations at high pressures make equation-of-state development [4, 109] costly.

At such laser-facilities, diagnostic access can be comparatively constrained and probing shock-compressed matter has often been limited to single diagnostics e.g. X-ray Thomson scattering [25, 76, 110, 111] or X-ray diffraction (XRD) [112–115] for measuring the electronic and atomic structures, or impedance matching techniques via a velocity interferometry system for any reflector (VISAR) [116]. Initial efforts to combine scattering and velocimetry observations to infer WDM conditions were undertaken

by Falk *et al.* [117], though this required fielding each diagnostic on separate shots. These efforts highlight the critical need for platforms equipped with multiple *in situ* probing diagnostics.

In the work detailed within this chapter, an experimental platform was designed to investigate the extreme states of matter generated at high-power laser facilities. This demonstrates a crucial step forward in the endeavour to directly measure pressure, density and temperature of WDM through a multi-messenger approach. The simultaneous *in situ* structure characterisation provides a unique tool for controlling diagnostic biases, measurement uncertainties, and selecting models. Reverse Monte Carlo techniques were employed to determine the shock-compressed conditions via measurement of liquid scattering [95, 118]. For this study, silicon was chosen due to its importance in the understanding of planetary interiors [119, 120], for its use as a dopant to ablators in inertial confinement fusion target designs [121, 122] and to mitigate laser-imprint effects on multi-layer targets [123, 124].

4.2 Experimental Setup

The experiments were conducted at the OMEGA-EP laser facility at the Laboratory for Laser Energetics [126]. A $51\,\mu$m thick poly-crystalline silicon sample was shock-compressed to $\sim 100\,$GPa using a single drive laser beam delivering $\sim 440\,$J over $10\,$ns with a $\sim 1.1\,$mm diameter distributed phase plate. The drive laser was incident on a $11\,\mu$m polystyrene (C_8H_8) ablator at a $19.3°$ angle with respect to the target normal. The ablator was fixed to the front of the silicon sample using a thin layer of glue ($< 1\,\mu$m). Three additional beams were tightly focused on a $12.5\,\mu$m thick copper backlighter with an areal size of $4\,\text{mm}^2$, generating a $1\,$ns pulse of copper He-alpha X-rays centred at $E \sim 8.4\,$keV [127]. The X-ray source was placed $\sim 17\,$mm away from the silicon sample.

The experimental configuration devised to probe the structure of WDM silicon at

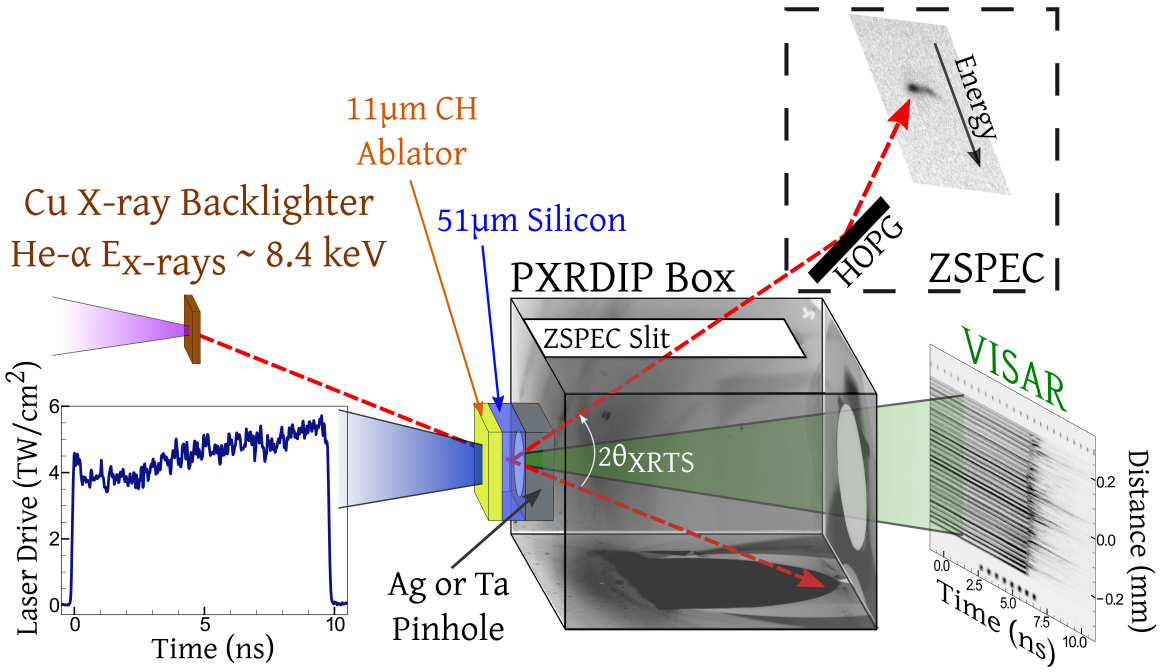

Figure 4.1: Experimental setup at the OMEGA-EP laser facility. The silicon target is mounted on the front of the PXRDIP box [125] with a 100 μm thick, 0.5 mm diameter silver or tantalum pinhole. A single beam drives the CH-Si target with a tailored pulse as shown in the inset figure. The remaining three lasers generate copper He-α X-rays. The red dashed lines represent the scattered X-ray paths that are collected by the X-ray Thomson scattering and X-ray diffraction image plates. The raw data shown were collected from s30967. NB: Not drawn to scale.

OMEGA-EP is shown in Figure 4.1. It employed a variation of the powder X-ray diffraction image plate (PXRDIP) setup [114]. This consists of an enclosed box which holds the X-ray sensitive Fujifilm BAS-MS image plates (IP's) [128] on each inner surface. Each image plate is filtered with 12.5μm copper and 25μm Kapton. A circular hole is cut in the rear of the box to allow diagnostic access for the VISAR laser.

Due to spatial constraints the X-ray diffraction only accessed momentum transfers up to $k \sim 4\,\text{Å}^{-1}$ at 8.4 keV. To extend the capabilities of the PXRDIP diagnostic, OMEGA's Bragg crystal spectrometer (ZSPEC) was added to measure scattering at high momentum transfer, and is capable of resolving the electronic structure of sufficiently ionized systems. The ZSPEC consists of a 25 mm × 50 mm highly-oriented pyrolitic graphite (HOPG) crystal with a radius of curvature of 27 mm, and was placed

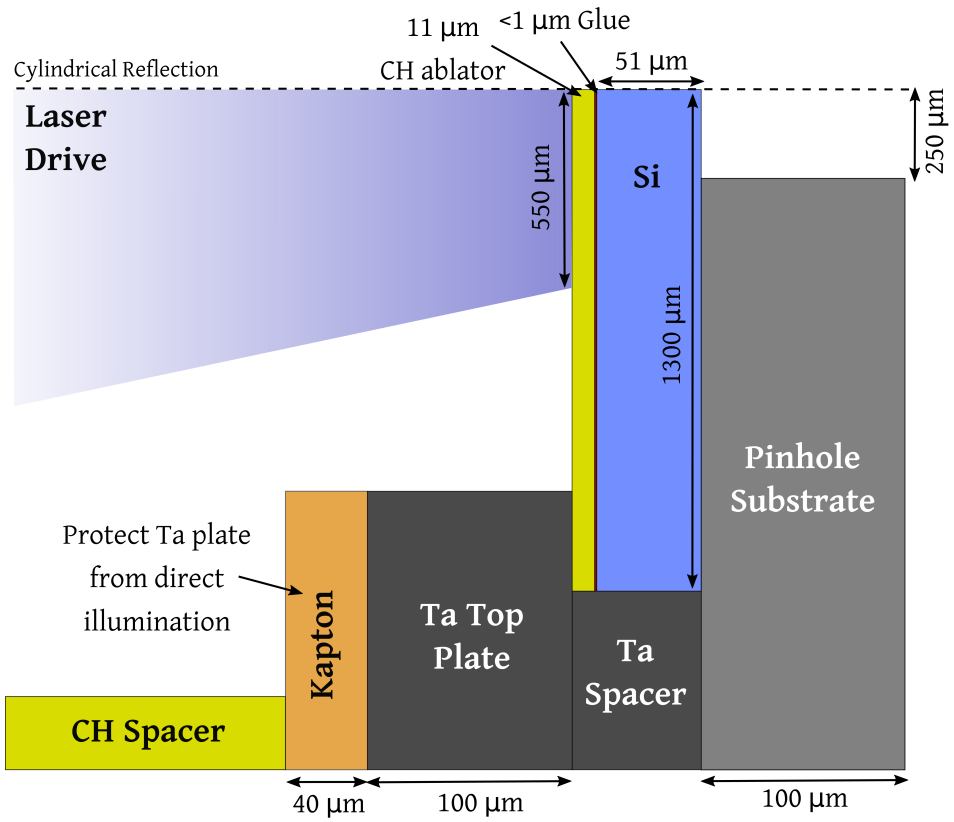

Figure 4.2: Target sample mounted to the front of the PXRDIP enclosure. The target is cylindrically symmetric with a total depth of 2 mm and width of 10 mm. NB: Not drawn to scale.

12.8 cm after the sample. As shown in the top inset in Figure 4.1, the ZSPEC was fielded out of perfect von-Hamos focusing meaning the X-rays were spectrally dispersed on a curve.

The silicon sample, illustrated in detail in Figure 4.2, was fitted to the front of the PXRDIP enclosure on top of a 0.5 mm diameter silver or tantalum collimating aperture pinhole. The pinhole restricts the diagnostics' line-of-sight to the central planar shock region. These pinhole materials were chosen to ensure no fluorescence within the ZSPEC energy range, and to reduce interference between the pinhole and silicon Bragg peaks on the PXRDIP.

4.3 Shock-breakout Measurements using VISAR

Velocity interferometry is a well-characterised diagnostic in the study of high-energy-density matter [129]. Through the use of a coherent laser and interferometers it produces a 1-D image of the shock spatial profile which can be used to measure shock and particle velocity. The OMEGA facility uses a frequency-doubled Nd-YAG laser ($\lambda = 532\,\text{nm}$) to produce a 50 ns pulse which is reflected from the back of the shock-compressed target. This reflection is transmitted through a Mach-Zehnder interferometer which splits the light down two paths, one containing a chosen UV-grade fused silica delay etalon which induces a known time delay, τ. An etalon of index n ($n = 1.4607$ for fused silica) and thickness h will produce a time delay of $\tau = (2h/c)(n - 1/n)$. When these two optical paths are recombined, their interference term is constructed from the optical fields reflected from the target at time t and $t - \tau$. At points of constructive interference a fringe is formed. The time history of the fringe pattern is recorded on an optical streak camera which enables transit-time measurements with $\sim 1 - 2\%$ accuracy. The observed fringe shift, $F(t)$, describes the change in phase difference at time t from the initial phase difference. Given a known velocity sensitivity, i.e. a measure of the velocity per fringe (VPF), the fringe shift is used to measure the time-resolved shock velocity, $D(t)$, of the reflecting surface via $D(t - \tau/2) = (\lambda/2\tau)F(t)$. The VPF can be

Table 4.1: Experimental parameters for all the shocked-compressed silicon shots including the total incident energy of the shock-compression drive laser, E_{drive}. The quoted silicon, h_{Si}, and ablator, h_{CH}, thicknesses are the nominal material values.

Shot	$h_{\text{CH}}\,(\mu\text{m})$	$h_{\text{Si}}\,(\mu\text{m})$	$E_{\text{drive}}\,(\text{J})$	$t_{\text{drive}}\,(\text{ns})$	$t_{\text{SBO}}\,(\text{ns})$
Shock-compressed conditions					
30964	11 ± 2	51 ± 1	441.3	-0.049 ± 0.025	5.35 ± 0.04
30967	11 ± 2	51 ± 1	429.0	-0.15 ± 0.025	6.22 ± 0.06
33538	11 ± 2	51 ± 1	437.9	-0.002 ± 0.025	5.20 ± 0.04
33541	11 ± 2	51 ± 1	422.5	0.014 ± 0.025	4.91 ± 0.03

calculated as $VPF = \lambda/\left[2\tau(1+\delta)\right]$, where δ (≈ 0.0318) is a corrective term accounting for chromatic dispersion within the fused silica etalon.

To optimise the spatial and temporal resolution, the etalon thickness and streak camera sweep rate is selected based on the predicted shock velocity, which for the conditions investigated here was $\sim 10\,\mathrm{km/s}$. The chosen etalon thickness was $40.034\,\mathrm{mm}$, giving a velocity sensitivity of $VPF = 1.24\,\mathrm{km/s}$, with a sweep speed of $15\,\mathrm{ns}$. The magnification gave a $500\,\mu\mathrm{m}$ field of view of the target which covered the space open to the pinhole.

As silicon is opaque to the VISAR wavelength ($\lambda = 532\,\mathrm{nm}$) at the investigated conditions, direct measurements of shock and particle velocity are only made achievable by employing witness materials and pressure windows. A witness material, such as α-quartz, has well-characterised properties within the investigated regime and is commonly placed adjacent to the primary target material. This placement allows the witness to serve as a reference for impedance matching calculations. However, introducing these materials is unsuitable for scattering measurements due to the significant contamination they can cause, making it difficult to isolate the scattering signal from the liquid. Instead, the VISAR was used to measure the shock-breakout (SBO) time, t_{SBO}, from the rear of the sample. The total shock time through both the CH ablator and silicon sample is $t = t_{\mathrm{SBO}} - t_{\mathrm{drive}}$, where t_{drive} is the measured laser driver timing. This total time can be related to the shock speeds in the silicon and CH via,

$$t = \frac{h_{\mathrm{Si}}}{D_{\mathrm{Si}}} + \frac{h_{\mathrm{CH}}}{D_{\mathrm{CH}}}\,, \tag{4.3.1}$$

where h_{Si} and h_{CH} are the silicon and CH thicknesses, respectively. The measured timings and target thicknesses for each shock-compressed experiment are listed in Table 4.1.

As a direct measurement of particle velocity, U, cannot be obtained on each shot,

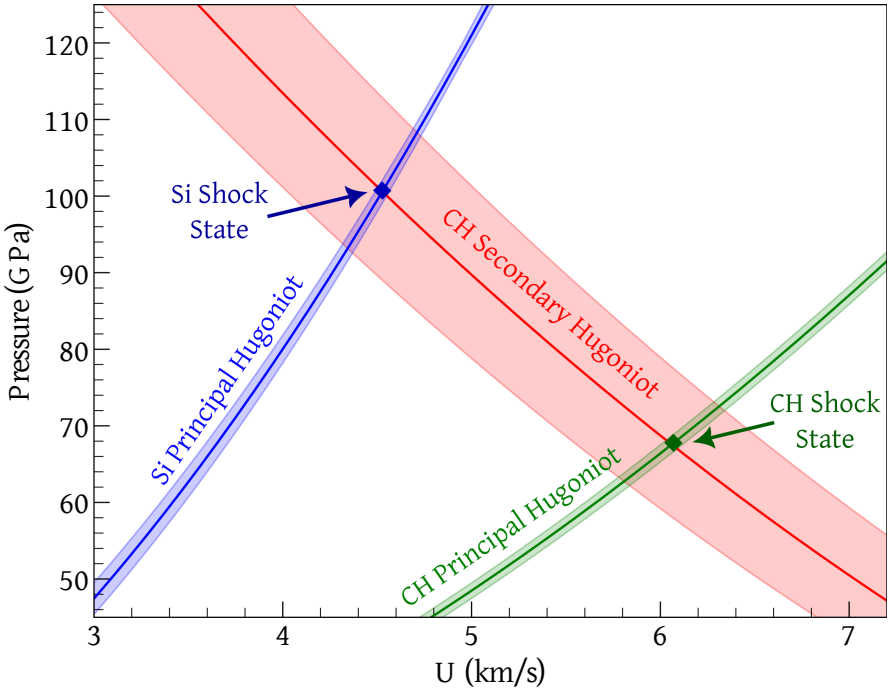

Figure 4.3: Impedance matching calculation for s30967 using the principal Hugoniot for silicon from Ref. [116] and CH from Ref. [130] in blue and green, respectively. The intercept of the secondary CH Hugoniot provides the corresponding silicon shock state. The lighter red error shown on the secondary Hugoniot captures the Hugoniot uncertainties for each material and the shock-breakout timing, t_{SBO}, uncertainty.

previous experimental data [116] is used to infer the silicon velocity,

$$D_{\mathrm{Si}} = 10.3(\pm 0.1) + 1.8(\pm 0.1)\,[U - 4.95]\ . \tag{4.3.2}$$

This is valid for $4 < U\ (\mathrm{km/s}) < 6.5$ and is based on the explosively driven data collected by Pavlovski in Ref. [131]. The corresponding linear relationship used for the CH ablator is [130],

$$D_{\mathrm{CH}} = 21.029(\pm 0.057) + 1.305(\pm 0.015)\,[U - 14.038]\ . \tag{4.3.3}$$

These equations are used alongside the Rankine-Hugoniot relations, which are derived from the conservation of mass, momentum and energy across a shock front, to infer the

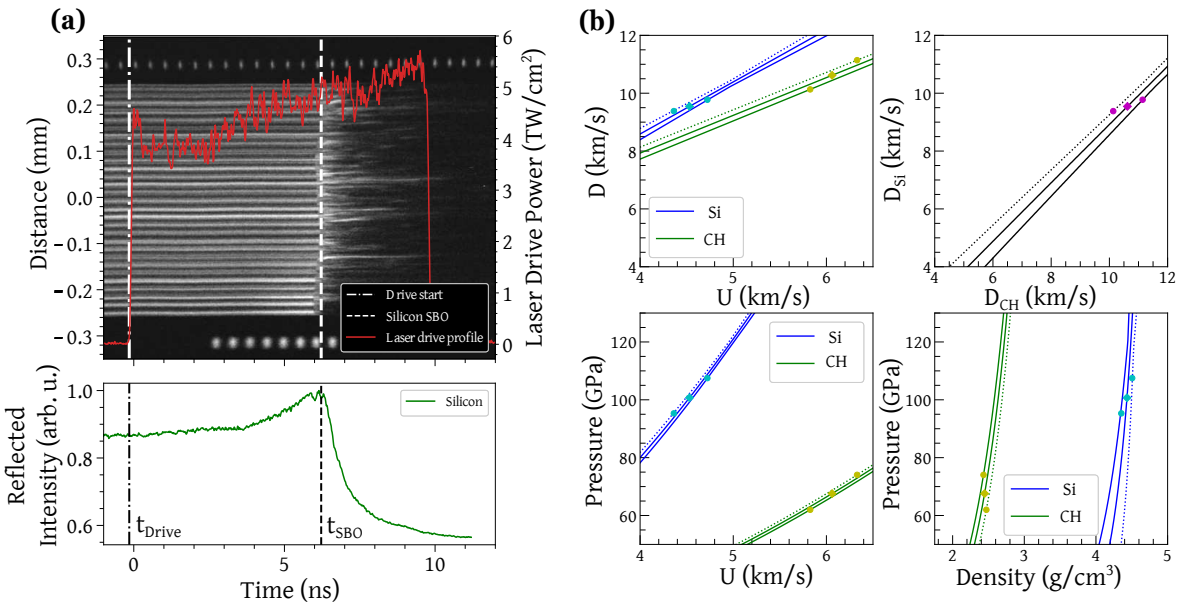

Figure 4.4: **(a)** Raw VISAR data from s30967. The fringes are reflected from the rear of the 51 μm thick Si sample. Superimposed in red is the laser drive power. The integrated VISAR intensity is projected underneath. The time of shock-breakout, t_{SBO}, is determined as the point at which there is a sharp gradient decline in reflected VISAR signal. **(b)** Impedance matching CH and Si shock conditions, using equations 4.3.2, 4.3.3 and 4.3.4, to find (shown in the upper right quadrant) the linear relationship between D_{CH} and D_{Si}. The statistical errors arising from the CH and Si model uncertainties are shown throughout as fainter green and blue lines, respectively. The appropriate shock speed for each material (highlighted as a magenta diamond) is found by substituting the D_{CH}-D_{Si} relation into equation 4.3.1. The corresponding 1σ error due to both model and experimental uncertainties are shown as magenta circles. This information is carried through the remaining plots to find the corresponding P-ρ space for CH and Si.

post-shock P-ρ state,

$$P = P_0 + \rho_0 D U \quad , \quad \rho = \frac{\rho_0 D}{D - U} \, , \tag{4.3.4}$$

where $P_0 \approx 0\,\mathrm{GPa}$ and $\rho_0 = 2.329\,\mathrm{g/cm^3}$ are the pre-shock conditions. This impedance matching calculation is illustrated in Figure 4.3. As the shock crosses the interface between the CH ablator and the higher-impedance silicon crystal, a shock is reflected back into the CH. The particle velocity and pressure across the interface between the now shocked silicon and double shocked CH is 'impedance matched'. The silicon and CH shock states are therefore given by the blue and green dots in Figure 4.3, respectively.

The total shock state uncertainty includes the measured error on t_{SBO}. An example of the VISAR diagnostic analysis for s30967 is shown in Figure 4.4. The inferred silicon shock speed, pressure and density for each shock-compressed experiment are listed in Table 4.2.

These conditions are compared to HELIOS 1-D simulations which utilised SESAME-EOS [132] and the drive laser profile. To match the t_{SBO} measured with the VISAR diagnostic, the drive laser energy is scaled by a factor $\mathcal{S}_d$. The scaling factors for each experiment are listed in Table 4.2. An example of the mass density through the target is shown in Figure 4.5(a). The simulations emphasise the non-uniformity of the conditions within the silicon during the X-ray scattering event, which is highlighted in orange. The simulated shock speed through the silicon is determined by tracking the mass density gradient. An example of this shock tracking is shown as a thick red line in Figure 4.5(a). As detailed in Table 4.2, the silicon shock speeds, D_{Si}, inferred from the VISAR transit time are in close agreement with the HELIOS simulations. This gives confidence in the utilised impedance matching technique detailed above.

The simulated mass-averaged plasma conditions, $\langle X \rangle_m$ (where X is a plasma parameter), within the silicon during the X-ray probe were calculated as the mass-weighted average in space and averaged over the probe duration in time [68]. This is determined

Table 4.2: Comparison of the inferred plasma conditions for each shot using Rankine-Hugoniot relations, on the left, and the Si mass-averaged conditions from HELIOS simulations during the scattering event on the right. The drive laser energy scaling factor, $\mathcal{S}_d$, is listed for each simulation.

Shot	$\mathbf{D_{Si}}$ (km/s)	**P** (GPa)	$\boldsymbol{\rho}$ (g/cm^3)	$\mathbf{D_{Si}}$ (km/s)	**P** (GPa)	$\boldsymbol{\rho}$ (g/cm^3)	$\mathcal{S}_\mathbf{d}$
	VISAR Transit Time			**HELIOS Simulations**			
30964	11.4 ± 0.3	146 ± 9	4.54 ± 0.07	10.9 ± 0.2	70 ± 7	3.3 ± 0.2	0.60
30967	9.5 ± 0.2	101 ± 6	4.43 ± 0.08	9.4 ± 0.1	48 ± 4	3.2 ± 0.1	0.41
33538	11.7 ± 0.3	155 ± 10	4.56 ± 0.07	11.6 ± 0.2	81 ± 10	3.3 ± 0.2	0.87
33541	12.4 ± 0.2	178 ± 10	4.60 ± 0.07	12.0 ± 0.2	82 ± 10	3.2 ± 0.2	1.00

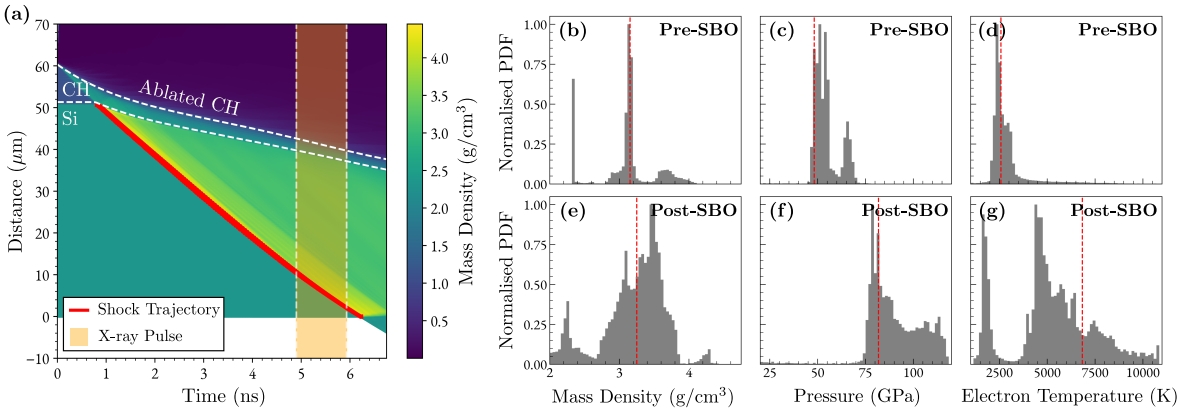

Figure 4.5: **(a)** Eulerian HELIOS 1-D simulation, produced by scaling the drive laser profile to match the measured t_{SBO}, for s30967. The silicon shock trajectory is shown as a thick red line and the timing of the X-ray laser pulse is highlighted in orange. The subsequent histograms show the normalised probability distribution functions (PDFs) of the silicon conditions during the X-ray scattering event as predicted by the HELIOS simulations. The vertical red dashed lines are their respective mass-averaged values, $\langle X \rangle_m$. **(b)**, **(c)** and **(d)** show the density, pressure and T_e, respectively, for s30967, taken before shock-breakout. **(e)**, **(f)** and **(g)** as above for s33538, taken after shock-breakout.

as,

$$\langle X \rangle_m (t) = \frac{\sum_i V_i(t)\rho_i(t)X_i(t)}{\sum_i V_i(t)\rho_i(t)}, \tag{4.3.5}$$

$$\begin{aligned} \langle X \rangle_m &\equiv \langle \langle X \rangle_m (t) \rangle_t \\ &= \frac{\sum_{j_{\min}}^{j_{\max}} \langle X \rangle_m (t_j) t_j}{\Delta t_{\mathrm{xray}}}, \end{aligned} \tag{4.3.6}$$

where $V_i(t)$ is the volume in the i-th cell at time t and $\Delta t_{\mathrm{xray}} \approx 1\,\mathrm{ns}$ is the X-ray pulse time length. The inferred P-ρ states for each shot are listed in Table 4.2. These mass-averaged values are compared to the overall parameter distributions during the X-ray scattering event in Figure 4.5. In the pre-shock-breakout data the sharp peaks corresponding to the low density region indicate the presence of ambient silicon.

4.4 Spectrally resolved X-ray scattering

To record the spectrally dispersed X-ray Thomson scattering, OMEGA's Bragg crystal spectrometer, called the zinc-spectrometer (ZSPEC) as it was designed to be focused on the zinc He-α emission at 9 keV, was used. The central Bragg angle was 13.2° with an spectral range of ±2.5°. Its image plate was protected by a 5 mm beryllium filter and mounted 13.1 cm from the crystal. As previously discussed, this meant that the ZSPEC was fielded out of perfect von-Hamos focusing, resulting in the spectrally resolved X-rays being scattered on to a cone. This deliberate defocusing can enhance the expected spatial resolution of the diagnostic. Had the ZSPEC been fielded in-focus, the anticipated spatial resolution would have been $\sim 50\,\mu$m/pixel, with the pixel size on the image plate being 50 μm. However, the chosen defocusing improves this spatial resolution to $\sim 45\,\mu$m/pixel.

In the raw intensity image shown in Figure 4.6(a), the X-ray scattering cone is highlighted in black and the scattered photon energy, E_{ph}, increases to its point. The dispersion of the ZSPEC is [133] $\Delta E/\Delta x \sim 7$ eV/pixel. To extract the spectrally re-

Table 4.3: Experimental X-ray scattering parameters for all investigated shots, including the total optical laser energy incident on the copper X-ray backlighter foil, E_{xray}.

Shot	$2\theta_{\text{XRTS}}$ (°)	Pinhole	E_{xray} (J)	t_{xray} (ns)	t_{SBO} (ns)	L_{coh}
Background target - No Silicon						
30970	70	Ta	3760.7	-	-	260 ± 9
Ambient conditions						
30968	70	Ta	3618.6	-	-	430 ± 10
Shock-compressed conditions						
30964	95	Ta	3707.5	5	5.35 ± 0.04	615 ± 10
30967	70	Ta	3908.4	4.8	6.22 ± 0.06	580 ± 10
33538	70	Ag	3778.3	5	5.20 ± 0.04	875 ± 20
33541	98	Ag	3835.0	5	4.91 ± 0.03	534 ± 8

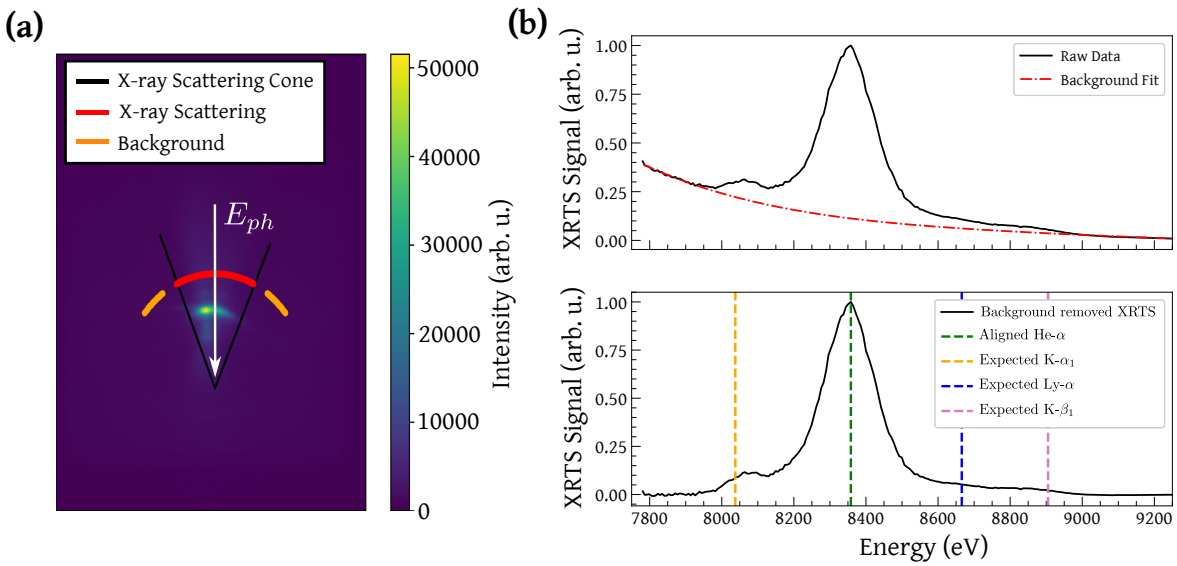

Figure 4.6: **(a)** Raw intensity of calibration s33544 where the copper foil was placed in the target holder of the PXRDIP box. **(b)** In the top plot the XRTS spectrum extracted after integrating along each energy arc is shown. A further polynomial background fit (red dash-dotted line) is subtracted from the overall signal to produce the spectrum in the lower plot. The energy axis is calibrated to the Cu He-alpha peak. The expected positions of the remaining Cu transitions are shown as vertical dashed lines.

solved spectrum, the total scattering signal along each energy arc is determined. The pixels falling along an arc, such as those highlighted in red in Figure 4.6(a), have an average pixel background value (determined from the orange arcs which fall outside of the X-ray scattering cone) removed, and are then summed. This gives an integrated scattering signal, $I(x)$, for a given spatial position x on the IP. The spectrum is converted from spatial to energy space using,

$$I(E) = \frac{hc}{2d}\csc\left[\tan^{-1}\left(\frac{I(x) + D_c\sin\theta_0 + D_{ip}\sin\theta_0}{D_{ip}\cos\theta_0 + D_c\cos\theta_0}\right)\right] \equiv \frac{hc}{2d}\csc\left[\tan^{-1}(\psi)\right]$$
$$= \frac{hc}{2d}\sqrt{1+\frac{1}{\psi^2}}\,, \tag{4.4.1}$$

where $2d = 0.67\,\text{nm}$ is the HOPG lattice spacing, $D_c = 12.8\,\text{cm}$ is the distance from the source to the HOPG crystal, $D_{ip} = 13.1\,\text{cm}$ is the distance from the HOPG crystal to the IP, and $\theta_0 = 13.2°$ is the central Bragg angle on the crystal. In the upper plot

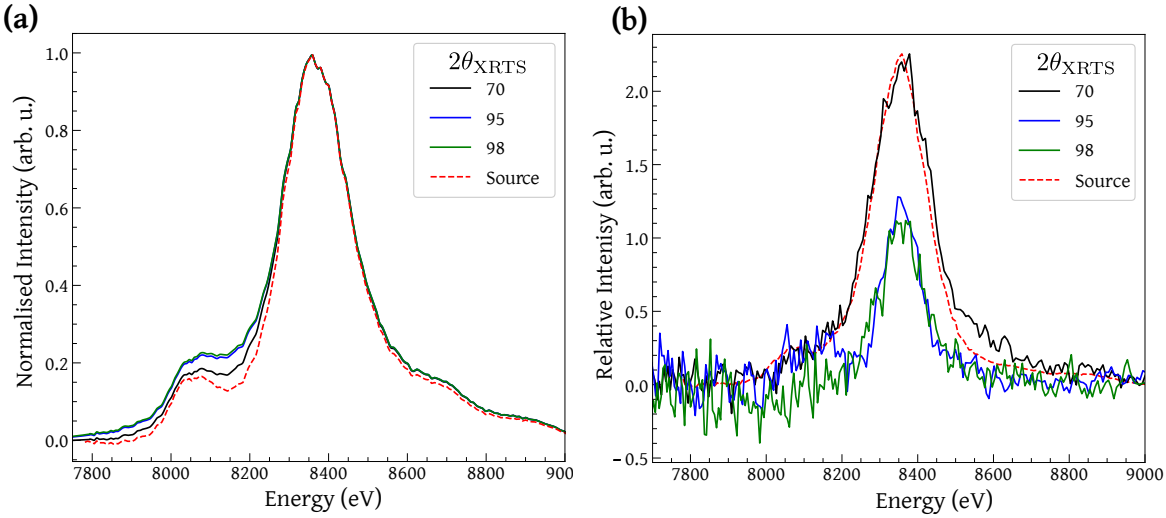

Figure 4.7: **(a)** Predicted spectrally resolved X-ray scattering signal using the measured source function (as described in Figure S1b of Supplementary Material) and the resolved shock-compressed conditions, $\rho = 4.6\,\mathrm{g/cm^2}$, $T = 6900\,\mathrm{K}$ and $Z = 1.5$. **(b)** Comparison of the spectrally resolved XRTS signal for the post-SBO shots where $V_\mathrm{l}/V_\mathrm{s} > 0.9$. The source function is scaled to the $\theta_{\mathrm{XRTS}} = 70°$ scattering signal and is shown as a red dashed line.

of Figure 4.6(b), the XRTS spectrum from the copper X-ray source is shown. After a further polynomial fit to the background is removed, the total background removed spectrally resolved X-ray scattering spectrum is given in the lower plot of Figure 4.6(b). The energy calibration is performed by aligning the peak signal with the Cu He-α transition at 8.358 keV. It can be seen in the lower plot that the remaining expected Cu transitions align with the lower intensity peaks observed on the spectrum.

The expected ionisation within the shock-compressed liquid silicon is $Z \sim 1.5$. As illustrated in Figure 4.7(a), this relatively low ionisation would not produce a significant increase in the inelastic scattering signal at each $2\theta_{\mathrm{XRTS}}$ scattering location. This signal increase was not observed on the experimental data, shown in Figure 4.7(b), above the source and diagnostic noise. The spectrally resolved X-ray scattering can therefore not be used independently to extract the shock-compressed conditions, but can be qualitatively combined with the X-ray diffraction information.

To compare the XRTS to the angularly resolved X-ray diffraction signal, the XRTS

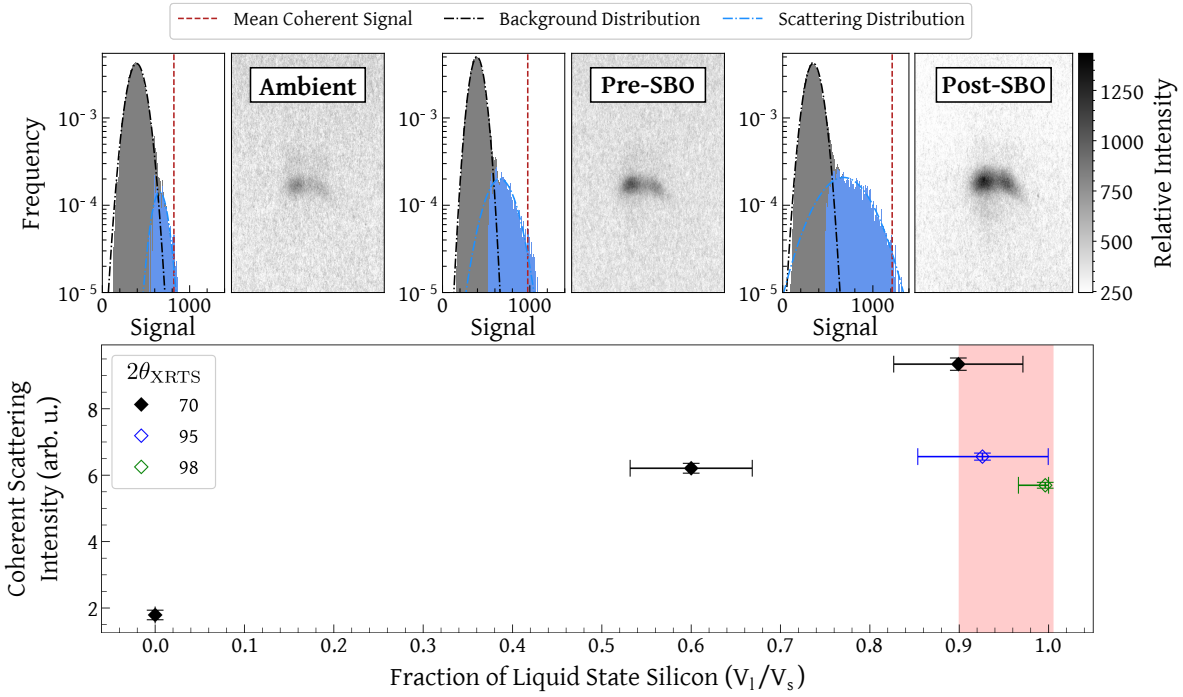

Figure 4.8: The XRTS signal intensities focused around the coherent scattering arc for ambient s30968 **(a)**, pre-SBO s30967 **(b)** and post-SBO s33538 **(c)** at $2\theta_{\mathrm{XRTS}} = 70°$. The raw scattering image is shown on the right of each plot and their corresponding scattering signal histograms are shown on the left. Each histogram in grey is the total observed signal intensity distribution with the black dash-dotted Gaussian fits being dominated by the background signal. The overlaid blue histograms are the isolated scattering signal distributions after the background Gaussian has been removed. The red dashed lines are the mean coherent signal intensities, L_{coh}. **(d)** Relative intensity of the elastic XRTS signal ($\propto S_{ii}$) against the fraction of liquid silicon, $V_{\mathrm{l}}/V_{\mathrm{s}}$, for all $2\theta_{\mathrm{XRTS}}$. Highlighted in red are the shots taken after shock-breakout. For these shots the liquid fraction is greater than ~ 0.9 and the scattering is assumed to be only from liquid silicon. The liquid fraction of the unfilled diamond points at 95° and 98° are determined from HELIOS simulations (where $T_e > 0.145\,\mathrm{eV}$) due to insufficient ambient data at these scattering locations.

must be spectrally integrated to give $I(k) = \sum_\omega I(k,\omega)$. However, as only the coherent scattering signal is clearly observed over the background noise, an integration over all ω-space cannot be performed. Additionally, using the peak intensity of the spectrally resolved signals shown in Figure 4.7(b) as a measurement of their relative coherent scattering signal, L_{coh}, would introduce significant uncertainty due to the compounded error of isolating the X-ray scattering cone and from the integration methods performed over each energy arc. Instead, as demonstrated in Figure 4.8, their L_{coh} are determined

by removing fitted background Gaussian distributions from the overall signal intensities - isolating the target scattering. The signals are corrected for filtering, polarisation, backlighter distance and relative thickness of the silicon seen by the X-ray source. The subsequent Gaussian fits to these scattering histograms yields, $L_{\mathrm{coh}} = (\mu_s + 2\,\sigma_s) - \mu_b$, where s and b denote the Gaussian distributions to the scattering and background signals, respectively. The coherent scattering intensities are listed in Table 4.3. For the ambient s30968, where $2\theta_{\mathrm{XRTS}} = 70°$, the Ta Bragg peak from the (112) lattice plane is resolved by the XRTS. This pinhole scattering signal is isolated from the silicon scattering by subtracting the XRTS coherent signal from the reference s30970, where only the Ta pinhole was loaded in the target holder.

Additionally, the fraction of shocked (fluid) material within the probe volume can be inferred by comparing the scattering data obtained with varying time delays between the drive laser and X-ray probe. As the volume of liquid silicon increases, the elastic scattering signal recorded on the XRTS, fielded in-between Bragg peaks, becomes more intense. By comparing the L_{coh} of ambient and shocked silicon, information on the fraction of shocked (fluid) silicon within the probe volume is obtained. Using a simple scattering model as described by Pelka *et al.* [134], which is based on the approach of Chihara [41], the time-averaged volume fraction of liquid (l) to solid (s) silicon present during the scattering event is calculated as,

$$\frac{V_l}{V_{\mathrm{s}}} = \frac{L^l_{\mathrm{coh}}}{L^s_{\mathrm{coh}}}\,\frac{S^s_{\mathrm{tot}}}{S^l_{\mathrm{tot}}} = \frac{L^l_{\mathrm{coh}}}{L^s_{\mathrm{coh}}}\,\frac{Z_{Si}\left[1 - I_{\mathrm{coh}}(k)/Z^2_{Si}\right]}{I_{\mathrm{coh}}(k)S_{ii}(k)}\,, \tag{4.4.2}$$

where S_{tot} are the static structure factors and $Z_{\mathrm{Si}} = 14$ is the nuclear charge. As shown in Figure 4.8, the volume fraction for the shock-compressed silicon states was found to be $V_l/V_s > 0.6$.

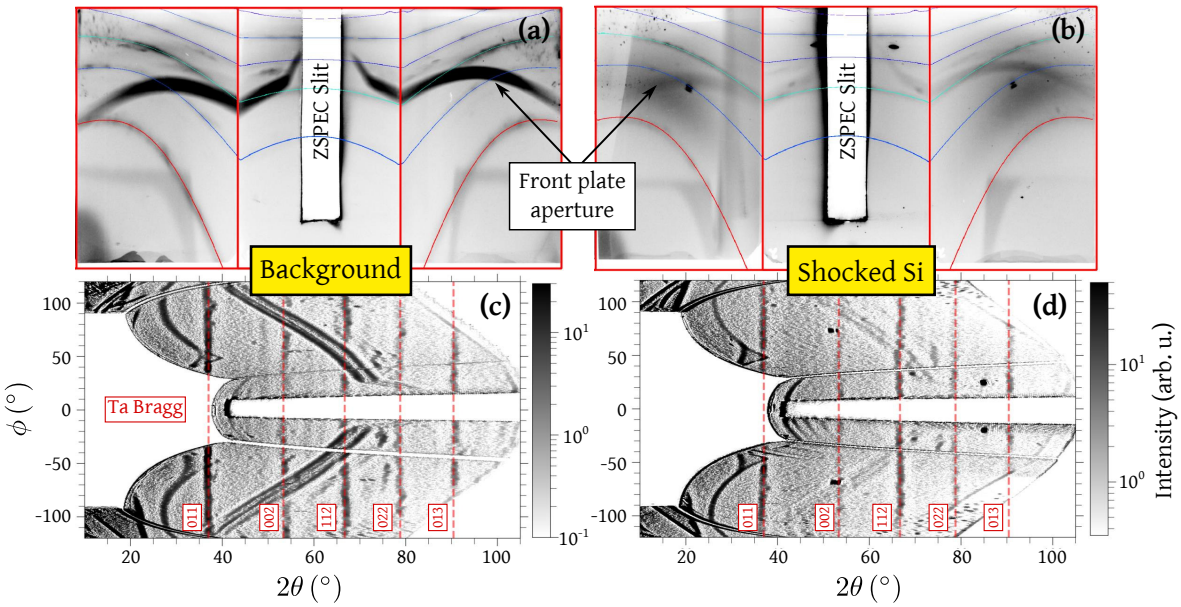

Figure 4.9: **(a)** and **(b)**: Raw images plates for background s30970 and shocked silicon s30967, respectively. The lines shown are the Bragg diffraction peaks of the Ta pinhole which are used to calibrate the geometry of the PXRDIP box. Their corresponding warped 2θ-ϕ signals at the pinhole position are shown in **(c)** and **(d)**, respectively. The scattering distributions for the pinhole used a SNIP background removal process [125] which enhances sharp peaks, improving signal-to-background ratios.

4.5 Extracting Liquid Angularly resolved scattering

At the investigated conditions, as further confirmed by the XRTS analysis, silicon is expected to be in the fluid state, which occurs when dynamically compressed above 30 GPa [135, 107]. Whilst liquid silicon scattering, up to 30 GPa, has been previously observed at XFELs [107] and synchrotrons [135], extracting the contribution from low-Z liquids at high-power laser facilities is experimentally challenging due to limited X-ray source brightness, the presence of fluorescence, spurious scattering from the pinhole, and X-ray emission in the drive ablation plasma. Whilst the PXRDIP platform has successfully been used to provide information on crystal structure of solids [112], including ramp-compressed silicon [115], the extraction of liquid scattering requires careful consideration of each background contribution.

Using Lawrence Livermore National Laboratory's AnalyzePXRDIP procedure [125],

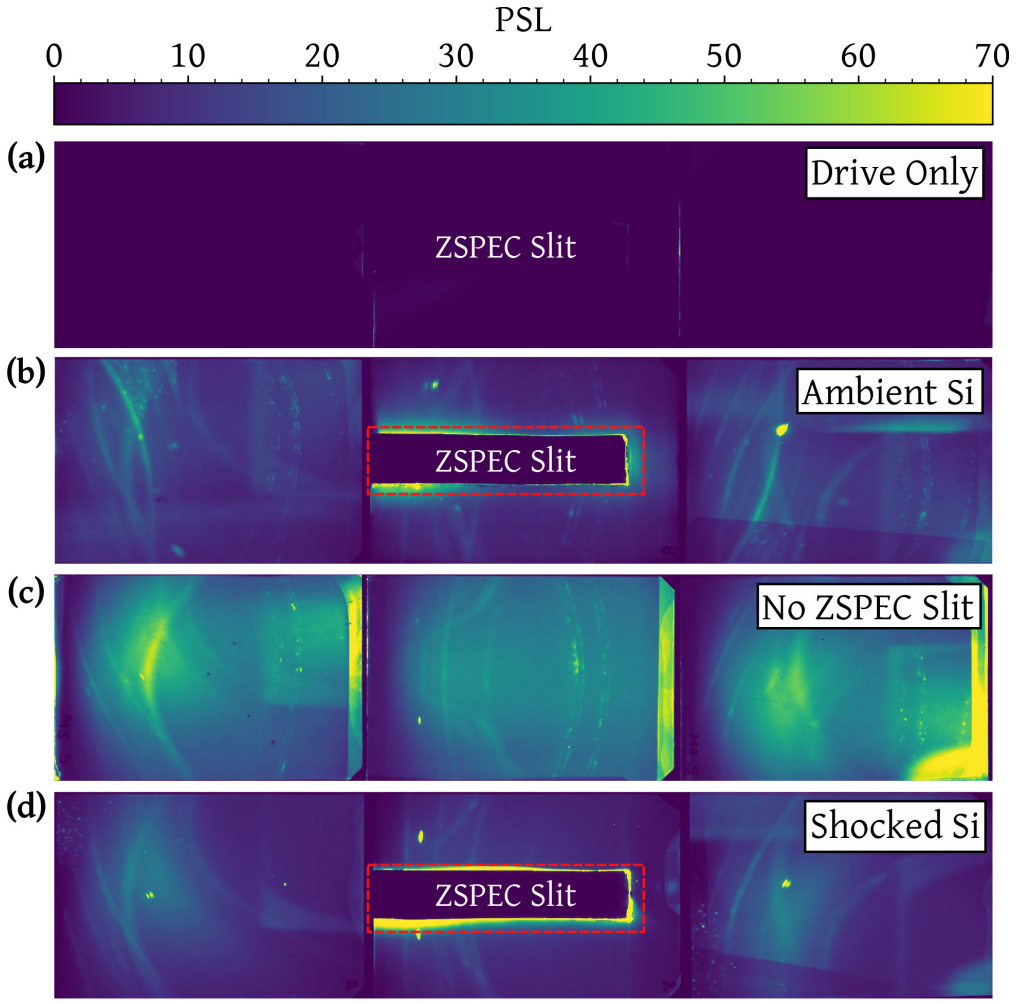

Figure 4.10: Comparison of raw PXRDIP data for **(a)** drive only s30966, **(b)** ambient Si s30968, **(c)** s33539 which used an Ag pinhole and removed the ZSPEC access slit, and **(d)** s30967. The only contamination from the X-ray lasers is highlighted within the red dashed box around the ZSPEC slit in (d). This area is excluded in subsequent analysis. The higher signal level in s30968, and s33539 compared to s30967, is a result of a reflection off a Cu filter placed at the bottom of the PXRDIP box.

the raw X-ray diffraction image plates, shown in Figures 4.9(a) and (b), are warped into 2θ-ϕ by using the tantalum pinhole Bragg peaks as calibrants. The pinhole calibration for each shot is shown in (c) and (d). To isolate the liquid silicon scattering, the background signal must be removed from the shocked data. Whilst a variant of the Statistics-sensitive Non-linear Iterative Peak-clipping (SNIP) algorithm is often used to isolate signal from the background in PXRDIP scattering data [125], this process is only appropriate when dealing with sharp Bragg peaks, such as shown in Figure

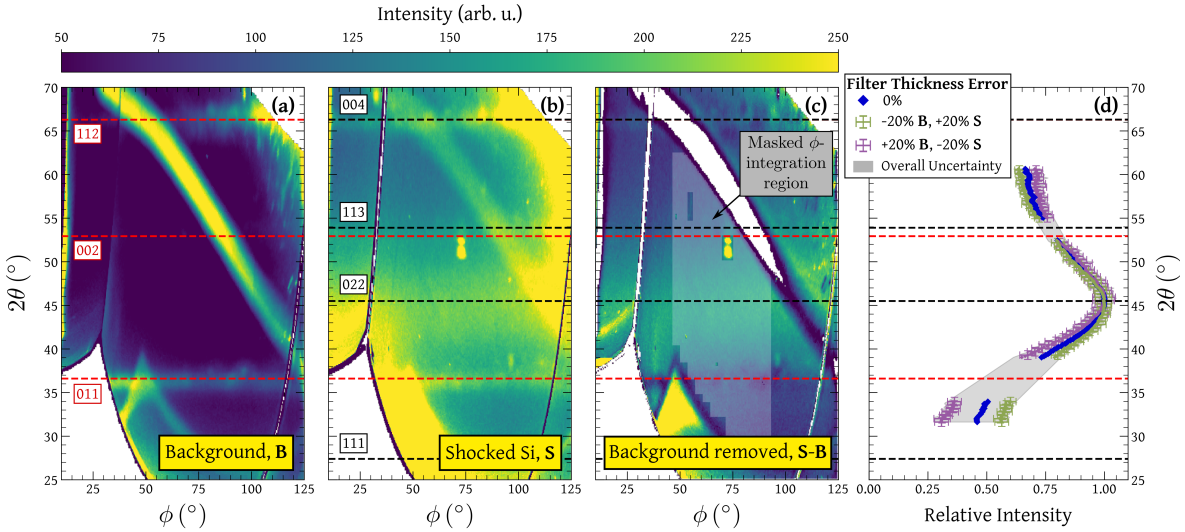

Figure 4.11: **(a)** and **(b)**: The warped, intensity corrected signals at the sample position for background s30970 and shocked silicon s30967, respectively. The superimposed red and black dashed horizontal lines are the calibrated 2θ Bragg diffraction peaks of the Ta pinhole and the expected ambient silicon peaks, respectively. **(c)** Shocked Si scattering after background removal. Artifacts from this removal process are seen at the edges of the image plates. The region selected for ϕ-integration is highlighted in grey. **(d)** Shown in blue, the partial-ϕ integration of (c) to obtain the liquid scattering signal in 2θ. The purple and green lines show the effect filter thickness uncertainties have on the inferred liquid shape. The overall signal uncertainty is taken over the grey shaded region.

4.9. To quantify the background signal a series of shots were performed to isolate each contributor. Firstly, in s30966, as shown in Figure 4.10(a), the signal intensity recorded on the IP's when only the drive laser was present (i.e. no X-ray probe) was measured. At the investigated pressure, this was found to be negligible in comparison to the data collected with X-ray scattering events. Secondly, the signal contamination from the addition of the ZSPEC line-of-sight slit in the PXRDIP box was investigated in s33539, shown in Figure 4.10(b), by removing the slit. The only contamination region was found to be around the access slit. Finally, comparison of the scattering recorded on the PXRDIP using an ambient silicon sample (e.g. s30968) versus for a reference s30970, where the silicon sample was removed, showed the dominant background scattering contributor to be the pinhole. Subsequent analysis therefore utilises s30970 as the background reference.

The scattering for the background s30970 and shocked s30967 shown in Figure 4.11 (a) and (b), respectively, are obtained by accounting for the filtering (12.5 μm Cu and 25 μm Kapton), incident solid angle, polarisation ($(1+\cos^2 2\theta)/2$) and the attenuation of the scattered X-rays. The background subtracted shocked signal is shown in Figure 4.11(c). Contamination at the edge of the IP's means a full integration in ϕ-space cannot be performed. The partial-ϕ integration region, highlighted in grey, therefore focuses on the IP centre, and excludes the 2θ regions around the Ta Bragg peaks. The resultant liquid scattering signal is shown in blue in Figure 4.11(d).

The 12.5 μm Cu and 25 μm Kapton filters used for the PXRDIP IP's have a 20% thickness uncertainty. Propagating this error through the background removal process results in the purple and olive plots shown in (d). The intensity error of each signal is given by the standard deviation from the mean signal along the ϕ integration. As scattering at high-k was not recorded, their absolute signal intensity is not applicable and they are normalised to their broad liquid scattering peak around 45°. This process demonstrates the effect filter uncertainties have on the overall shape of the liquid scattering feature. The total liquid scattering signal, $I_{\mathrm{liq}}(k)$, therefore encapsulates the region highlighted in grey. A 2θ error of $\sim 0.5°$ is taken to be the average deviation of the observed pinhole Bragg peaks from their expected values.

At high momentum transfers the liquid scattering signal is the result of coherent, $I_{\mathrm{coh}}(k)$, incoherent, $I_{\mathrm{incoh}}(k)$, and multiple, $I_{\mathrm{m}}(k)$, scattering events. As the silicon thickness is small relative to its attenuation length, $I_{\mathrm{m}}(k)$ is assumed to be negligible. The experimentally measured $I_{\mathrm{liq}}(k)$ is therefore related to the normalised ion-ion structure factor, $S_{\mathrm{ii}}(k)$, via [136, 137],

$$\frac{I_{\mathrm{liq}}(k)}{\gamma} \equiv I_{\mathrm{scal}}(k) = I_{\mathrm{coh}}(k)\left[S_{\mathrm{ii}}(k) - 1\right] + \left[I_{\mathrm{coh}}(k) + I_{\mathrm{incoh}}(k)\right], \tag{4.5.1}$$

where $I_{\text{coh}}(k) = |f_i(k) + q(k)|^2$, with $f_i(k)$ the form factor of the tightly bound electrons and $q(k)$ that of the free electrons that follow the ion motion [41]. Here, $I_{\text{incoh}}(k)$ is obtained using the tabulated values from Ref. [138] and $I_{\text{coh}}(k)$ is simulated using the multi-component scattering spectra (MCSS) code [139], which for a given set of parameters, $\Psi(\rho, T, Z)$, produces a theoretical diffraction signal, $I_{\text{fit}}(k)$. The factor γ is a scaling constant defined such that $I_{\text{scal}}(k \to \infty) = I_{\text{coh}}(k) + I_{\text{incoh}}(k)$. To experimentally obtain γ, momentum transfers in excess of 10 Å^{-1} are required, a regime not currently accessible at high-power laser facilities. Instead the experimental signal is scaled to the simulated fit using,

$$I_{\text{scal}}(k) = I_{\text{liq}}(k) \times \Gamma \frac{I_{\text{fit}}^{\text{max}}}{I_{\text{liq}}^{\text{max}}}, \tag{4.5.2}$$

where Γ is a free random Gaussian scalar with a standard deviation equal to the noise of the raw data, and $I_{\text{fit}}^{\text{max}}$ and $I_{\text{liq}}^{\text{max}}$ are the peak values in the MCSS fit and raw X-ray scattering data, respectively.

The large parameter space, $\Psi(\rho, T, Z)$, is explored using a Markov-Chain Monte Carlo (MCMC) procedure similar to that outlined in Chapter 3 [95, 58]. This determines the likelihood of a set of parameters producing the experimental spectrum based on an acceptance percentage $P\left[I_{\text{scal}}(k)|\Psi\right] = \text{e}^{-\beta_{\text{cost}}}$ with

$$\beta_{\text{cost}} = \max\left[\frac{I_{\text{fit}}(k) - I_{\text{scal}}(k)}{\sqrt{2}\sigma\Sigma}\right]^2, \tag{4.5.3}$$

where Σ is the error on I_{scal}, and $\sigma = 0.5$ is a scalar chosen to allow acceptance freedom within data uncertainty. The investigated parameter space assumed a uniform distribution with linear sampling for the density, $2.33 \leq \rho\,(\text{g/cm}^3) \leq 6$, ionisation, $0 \leq Z \leq 14$, and temperature, $10^3 \leq T_e = T_i\,(\text{K}) \leq 1.1 \times 10^4$.

Simulating $S_{\text{ii}}(k)$, however, is subject to model biases and requires appropriate selection of electron and ion interactions. An important factor to consider when determining

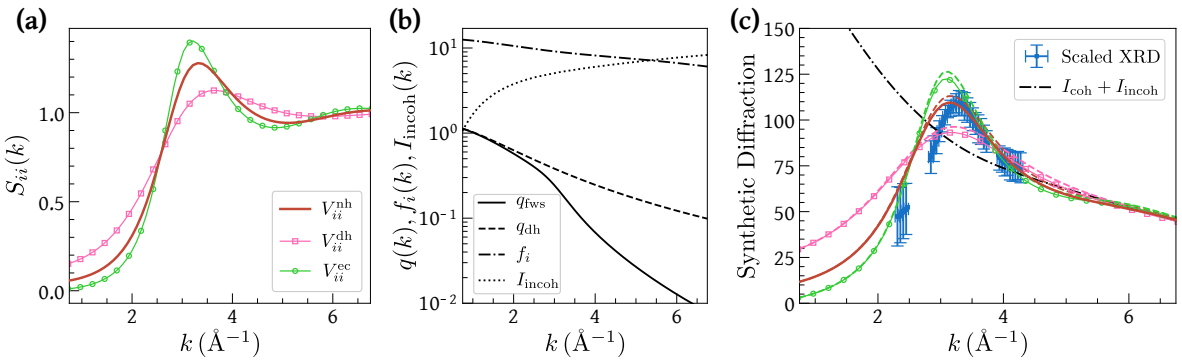

Figure 4.12: **(a)** Ion-ion structure factors, $S_{ii}(k)$, for each $V_{ii}(k)$ for a silicon sample at $\rho = 4.6\,\mathrm{g/cm}^3$, $Z = 1.3$ and $T = 5300\,\mathrm{K}$. **(b)** Comparison of the tabulated incoherent scattering signal I_{incoh} [138], the bound electron form factor, $f_i(k)$, and the screening cloud, $q(k)$, produced with Debye-Hückel and finite-wavelength screening models. **(c)** The synthetic diffraction signals produced with each $V_{ii}(k)$, $q(k)$, $f(k)$ and I_{incoh}, as shown in (a) and (b), compared to the scaled experimental scattering signal. For this representative plot, the scaling parameter, Γ, from equation 4.5.2 was chosen using the NH I_{fit} (solid red curve).

such models is the effect of inter-particle correlations. This can be estimated by the coupling parameters given in equations 1.1.3 and 1.1.6. For the conditions expected in the shock-compressed silicon, $\Gamma_{aa} > 1$ and $\Gamma_{ei} < 1$. As the electron-ion correlations are relatively weak, a linear response approximation to the screening cloud is justified, and a Coulomb interaction between the electrons and ions is assumed,

$$V_{ei}(k) \approx \frac{Ze^2}{\epsilon_0 k^2}\,. \tag{4.5.4}$$

Model sensitivities for producing synthetic X-ray scattering signals using MCSS are illustrated in Figure 4.12. This demonstrates how the dominant contributor to the synthetic scattering signal is the chosen ion-ion interaction potential, $V_{ii}(k)$. The screening cloud models, $q(k)$, as shown in Figure 4.12(c), cannot be differentiated within the measured experimental error. Previous work has demonstrated that at large momentum transfers in high-density matter the screening has deviated from the simple Debye-Hückel (DH) model as a result of finite-wavelength screening (FWS) [64]. The FWS screening cloud model is therefore chosen for the subsequent MCMC analysis.

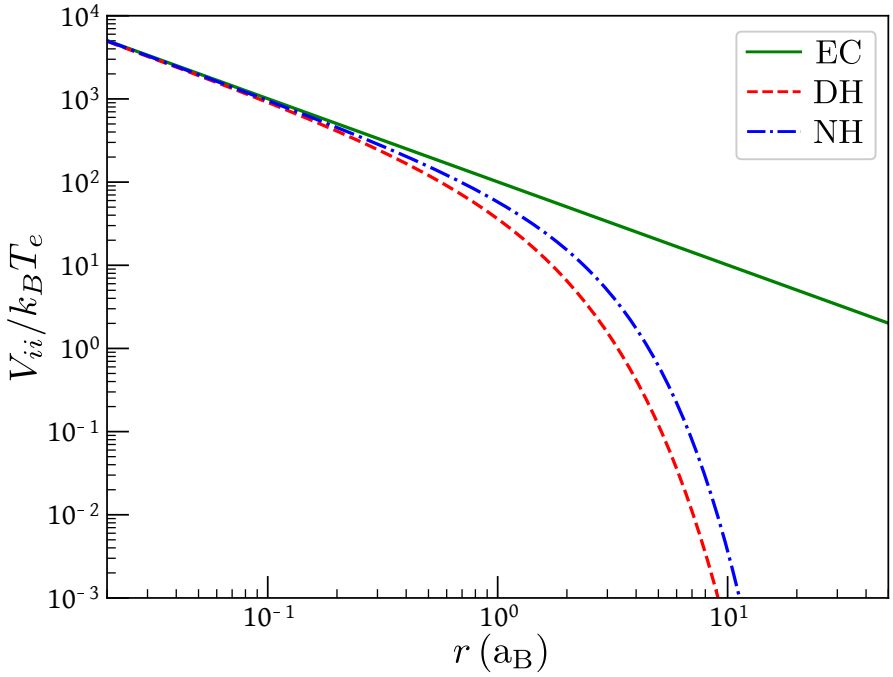

Figure 4.13: Comparison of the ion-ion interaction potentials, $V_{ii}(r)$, using the effective Coulomb (EC), Debye-Hückel (DH) and non-linear Hulthén (NH) models. The models are produced for a silicon sample at $\rho = 4.6\,\mathrm{g/cm^3}$, $T = 5300\,\mathrm{K}$ and $Z = 1.3$.

In the partially ionised, low density state, the ion-ion interaction potential is commonly modelled using Debye-Hückel [44]. This work compares the DH model with the bare (unscreened) effective Coulomb (EC) interaction and a model non-linear Hulthén (NH) interaction [140]; the latter approximately describes screening beyond the DH approach. The potentials for each V_{ii} are illustrated in Figure 4.13 and are given by,

$$V_{ii}^{\mathrm{ec}}(r) = -\frac{Z^2e^2}{4\pi\epsilon_0 r}\,, \tag{4.5.5}$$

$$V_{ii}^{\mathrm{dh}}(r) = V_{ii}^{\mathrm{ec}}(r)\,\mathrm{e}^{-\kappa_e r}\,, \tag{4.5.6}$$

$$V_{ii}^{\mathrm{nh}}(r) = V_{ii}^{\mathrm{ec}}(r)\,\frac{\kappa_e r}{\mathrm{e}^{\kappa_e r}-1}\,, \tag{4.5.7}$$

where κ_e is the inverse screening length (equation 2.2.7).

The subsequent range of accepted fits after MCMC convergence using the non-linear Hulthén V_{ii} model are shown in grey in Figure 4.14. The post-shock breakout

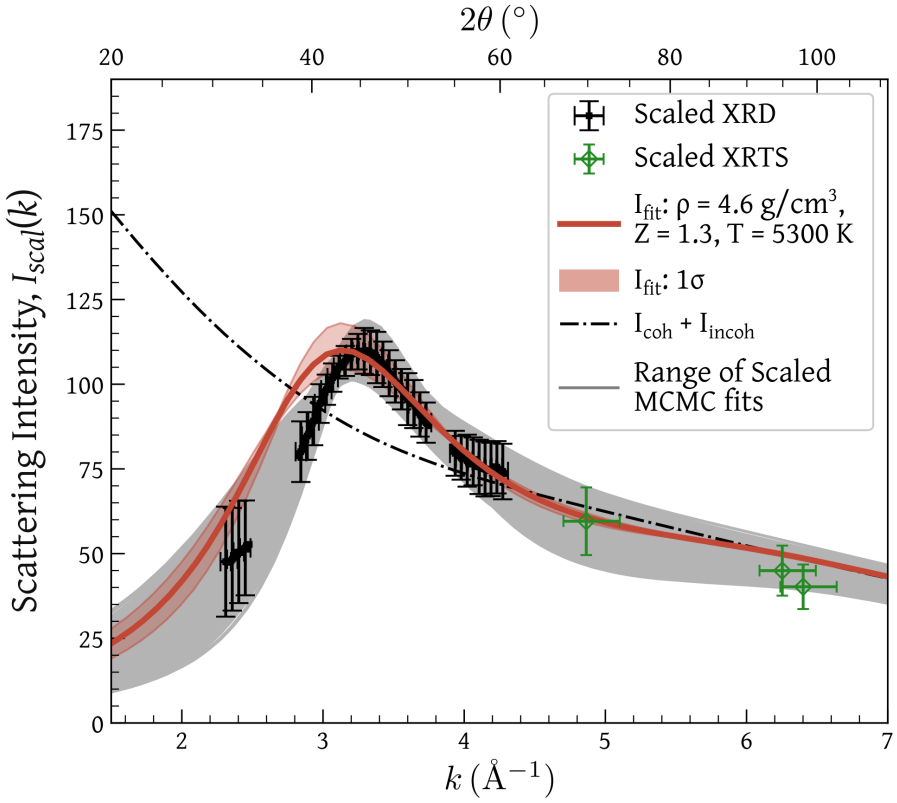

Figure 4.14: The liquid silicon scattering signal, $I_{\text{scal}}(k)$, (in black) is shown scaled to the theoretical signal, $I_{\text{fit}}(k)$, (thick red line) produced by the combined VISAR and converged MCMC conditions using the non-linear Hulthén model, given in Table 4.4. The 1σ error of $I_{\text{fit}}(k)$ is shaded in red. The dash-dotted black line shows $I_{\text{coh}} + I_{\text{incoh}}$ for these values. The broad range of accepted MCMC fits (in grey) are scaled to the mean $I_{\text{fit}}(k)$ signal.

XRTS data shots (s30964, s33538 and s33541) – where the fraction of liquid silicon is greater than ~ 0.9 – are compared in green to the diffuse angularly resolved scattering recorded on s30967, extending the effective k range. These L_{coh} signals are scaled by fitting the value at $2\theta_{\text{XRTS}} = 70°$ to the range of accepted MCMC fits. As only the coherent contribution is resolved using ZSPEC, this fitting procedure uses the MCMC fits, I_{fit}, prior to adding the incoherent scattering contribution, I_{incoh}. The higher $2\theta_{\text{XRTS}}$ signals are then determined by their scattering intensity relative to the 70° data. The total signal errors are compounded by their respective coherent scattering uncertainties and the scaling error of L_{coh} at 70°. While these points were not included

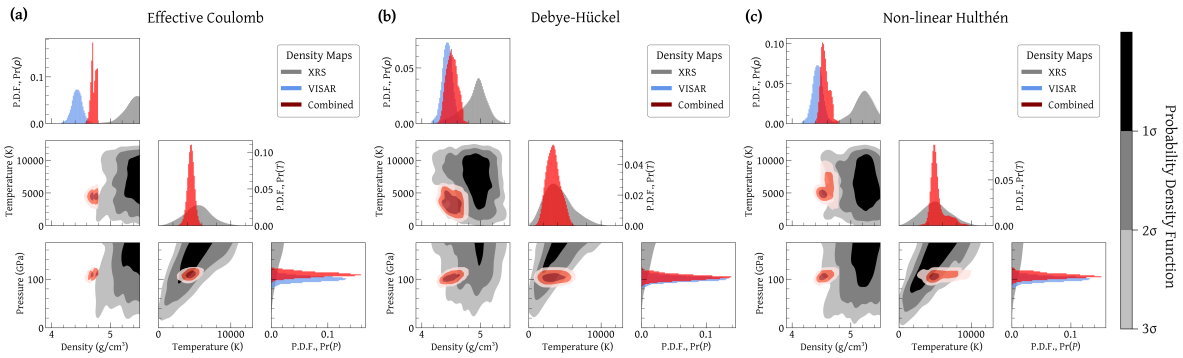

Figure 4.15: Probability density functions for the liquid silicon density, pressure and temperature state using the effective Coulomb **(a)**, Debye-Hückel **(b)** and non-linear Hulthén **(c)** $V_{ii}(k)$ models. The lower quadrant plots compare the 1, 2 and 3σ parameter correlations for the MCMC converged X-ray scattering analysis (grey heat maps) and the combined density functions (red heat maps). The diagonal histograms show the probability densities for each parameter. The VISAR distributions are added in blue for density and pressure.

in the MCMC fitting process due to the lack of an absolute signal intensity calibration between XRD and XRTS, they nonetheless exhibit good agreement with the results.

Under conditions of strongly coupled ions and degenerate electrons, where screening is expected to be significant, the total plasma pressure can be determined from the converged parameters using the 'two-fluid' framework discussed by Vorberger *et al.* [141, 142]. Details of this model are described in Appendix C. The resultant probability distribution functions for the liquid scattering analysis are shown in grey in Figure 4.15.

4.6 Combining VISAR and XRD Analysis

The information on the shock-compressed conditions obtained using the concurrent VISAR and X-ray scattering diagnostics can be combined to find the mutually agreed parameter space. Given the VISAR and MCMC P-ρ probability density functions, their subsequent joint probability is defined as,

$$\mathrm{Pr}_j(\rho, P) = \frac{\mathrm{Pr}_m(\rho, P) \times \mathrm{Pr}_v(\rho, P)}{\sum_{\rho,P} \left[\mathrm{Pr}_m(\rho, P) \times \mathrm{Pr}_v(\rho, P)\right]} \,. \tag{4.6.1}$$

These 2-D combined density functions are shown as red heat maps in the lower left plots in Figure 4.15.

Unlike the VISAR diagnostic, the MCMC convergence of the X-ray scattering analysis is dependent not only on pressure and density, but also on temperature. The combined $\Pr(P, \rho)$ can therefore be propagated into temperature space. This re-distributes the X-ray scattering $\Pr(P, \rho, T)$ to penalise where the density and pressure disagree with VISAR. However, as VISAR provides no direct measurement of temperature, its 3-D density function is defined such that $\Pr_v(\rho, P, T_i) \equiv \Pr_v(\rho, P, T_j)$, where $i(\neq j)$ describes a position along the temperature axis. By using equation 4.6.1, the 2-D phase space for pressure and temperature can subsequently be found as,

$$\Pr_j(P, T) = \frac{\sum_\rho \Pr_j(\rho, P, T)}{\sum_{P,T} \left[\sum_\rho \Pr_j(\rho, P, T)\right]} . \tag{4.6.2}$$

This process can be repeated in the ionisation space. The resultant combined probability distribution functions are used to find the combined 1σ errors of each parameter, i.e. $\Pr_j(\rho)$. These are listed in Table 4.4. The simulated X-ray diffraction fits, I_{fit}, produced

Table 4.4: Comparison of the liquid silicon conditions within 1σ for the X-ray scattering MCMC convergence and the combined VISAR state using each ion-ion interaction potential.

$\mathbf{V_{ii}(k)}$	$\boldsymbol{\rho}$ (g/cm^3)	**P** (GPa)	**T** (K)	$\bar{\mathbf{Z}}$
MCMC Convergence				
EC	5.5 ± 0.2	200 ± 60	6600 ± 2900	1.3 ± 0.3
DH	4.9 ± 0.2	250 ± 90	6900 ± 3000	3 ± 1
NH	5.2 ± 0.2	190 ± 60	6500 ± 3000	1.5 ± 0.4
MCMC and VISAR Combined				
EC	4.72 ± 0.05	110 ± 5	4500 ± 500	1.01 ± 0.03
DH	4.51 ± 0.09	104 ± 6	3400 ± 1000	1.5 ± 0.1
NH	4.56 ± 0.07	106 ± 6	5300 ± 1100	1.26 ± 0.04

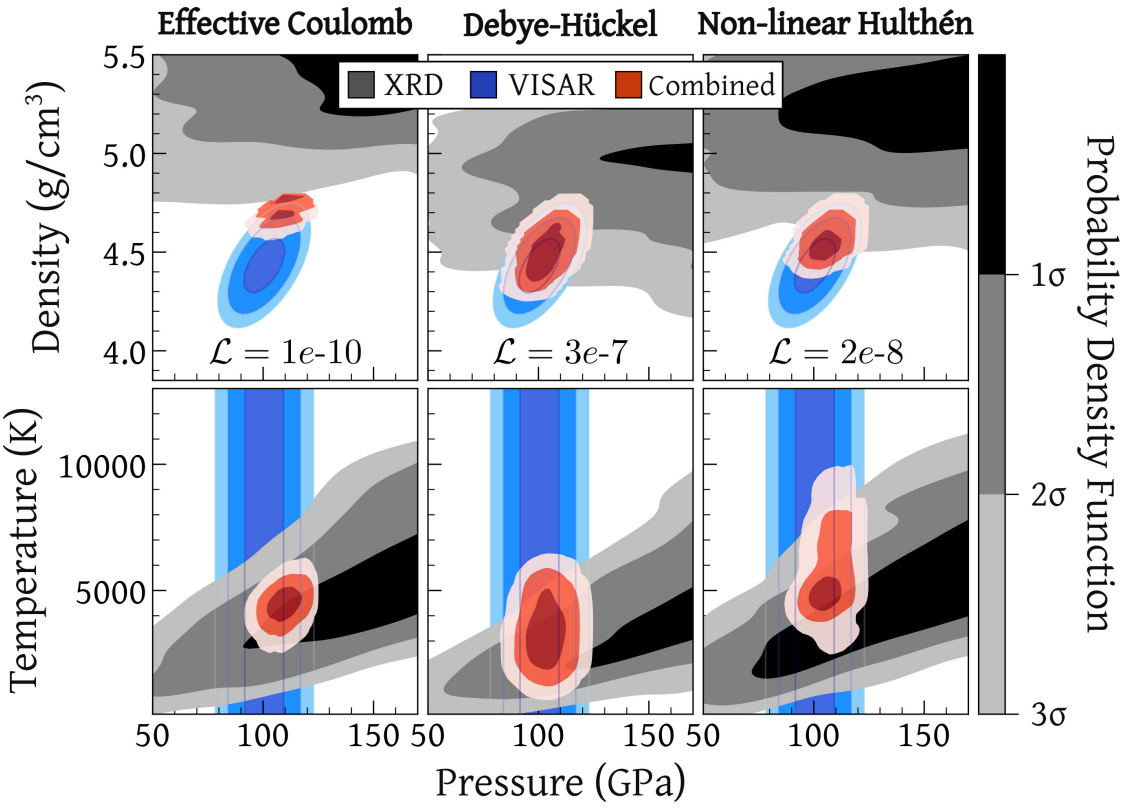

Figure 4.16: Probability density functions in the P-ρ and P-T phase for VISAR (blue heat maps) and X-ray scattering (grey heat maps) analysis using each V_{ii}. The corresponding joint distributions are superimposed as red heat maps. In the upper grid the likelihood, as defined in equation 4.6.3, of each V_{ii} is shown.

by the conditions inferred when combining VISAR and the non-linear Hulthén MCMC convergence are shown in red in Figure 4.14. A detailed comparison of the converged probability density functions $\Pr(P, \rho)$ and $\Pr(P, T)$, for each ion-ion potential model, are shown in Figure 4.16.

The likelihood of each ion-ion potential model given the VISAR information can be defined as the sum of its joint probability distribution,

$$\mathcal{L}\left(V_{ii}|\text{VISAR}\right) = \sum_{\rho,P} \Pr_m(P,\rho) \times \Pr_v(P,\rho)\,, \tag{4.6.3}$$

where m and v denote the X-ray diffraction MCMC and VISAR probability density functions, respectively. These likelihoods are indicated in the upper grid of Figure 4.16.

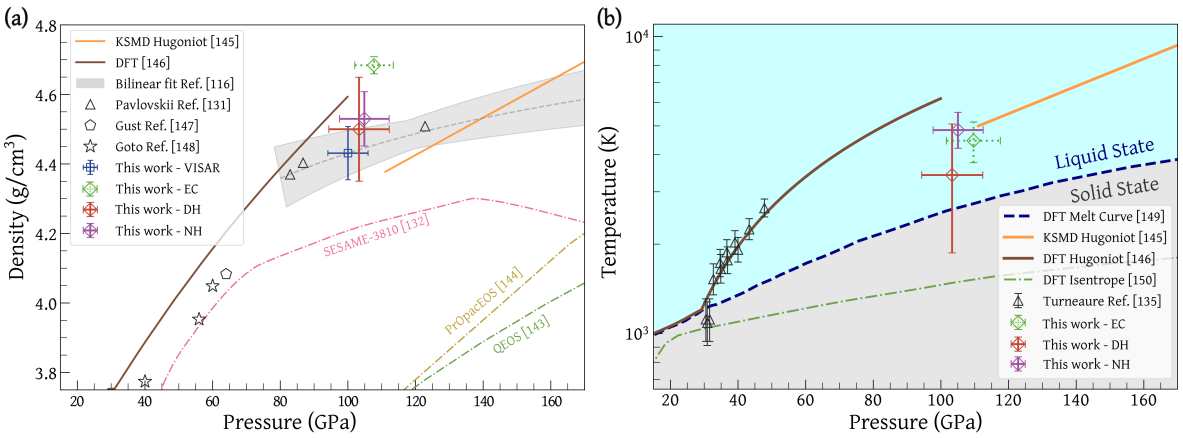

Figure 4.17: **(a)** The principal silicon Hugoniot where this work is compared to SESAME-3810, [132], quotidian equation-of-state (QEOS) [143], PrOpacEOS [144], *ab initio* Kohn-Sham DFT molecular-dynamics (KSMD) [145], principle Hugoniot from DFT [146], and previous experimental work collected via conservation methods [131, 147, 148]. The bilinear fit [116] used to infer particle velocity is shown as a filled grey bar. **(b)** The silicon pressure-temperature phase diagram comparing the combined 1σ error for each V_{ii} to the measured and predicted melt curve [149], the DFT isentrope [150] and previous shocked silicon experiments [135] where the temperature was inferred using molecular dynamics [151].

They show that comparatively, the effective-Coulomb model is a poor representation of the liquid silicon state. This is expected as it does not account for screening effects.

The limited observed overlap between the VISAR and XRD PDFs can be attributed to various factors. Firstly, each diagnostic is sensitive to distinct aspects of the shock-compressed conditions, leading to differences in their observed distributions. Moreover, it is worth noting that the VISAR Hugoniot measurement is derived from data collected in Ref. [131] where no experimental uncertainty was provided. Consequently, this results in a narrower uncertainty on the VISAR PDF. However, this constraint may be refined should more experimental silicon Hugoniot information in this regime become available, or if advancements are made in experimental platforms that allow for the inclusion of witnesses and pressure windows without contaminating the observed liquid scattering. Secondly, the relative simplicity of the screening models investigated in the X-ray scattering data implies that they are not absolute representations of the underlying physics. While more refined models may be attainable through the utilisa-

tion of density function theory (DFT) simulations [152, 153], such methodologies are computationally expensive and introduce varying degrees of complexity in the models.

Despite these uncertainties, there are parameter spaces common to both diagnostics. By combining their PDFs, we can achieve a more comprehensive understanding of the shock-compressed conditions by constraining the XRD parameter search to those consistent with the pressure-density Hugoniot relation established by the VISAR measurement. Furthermore, a discernible difference in the conditions inferred utilising each screening model can still be observed.

In Figure 4.17 the VISAR and MCMC combined 1σ P-ρ and P-T for each ion-ion potential model are plotted on silicon's principal Hugoniot. Despite having the closest agreement with VISAR in P-ρ, the temperature predicted by the commonly used Debye-Hückel model falls below the Hugoniot state. Instead we find the implementation of a Hulthén potential [140], which estimates non-linear screening regimes beyond DH, better describes the thermodynamic conditions. This experimental platform therefore demonstrates the capability to effectively distinguish between screening models, which is essential for accurately predicting material behaviour under extreme conditions.

4.7 Conclusions

This chapter presents detailed insights into the extreme states of matter generated at high-power laser facilities. While previous investigations on liquid silicon have been confined to pressures around $\sim 50\,\mathrm{GPa}$ [107, 135], this study explores higher pressures by leveraging multiple *in situ* diagnostics in conjunction with MCMC analysis. This approach effectively mitigates diagnostic biases and yields uncertainties on the shock-compressed state that are comparable to previous experimental endeavours, without the reliance on EOS models.

Furthermore, the synergistic integration of various diagnostics facilitated the discernment of distinct static screening models. The results revealed the necessity of

incorporating screening beyond the linear Debye-Hückel approach, advocating for the adoption of a Hulthén potential to achieve alignment between the measured liquid silicon state and Hugoniot predictions.

Future endeavours could aim to develop an experimental platform conducive to the inclusion of witnesses without impeding liquid scattering measurements. Such a platform would enable direct Hugoniot measurements, thereby refining the uncertainty associated with the VISAR result, which presently relies on previous data.

Nevertheless, the development of this platform and the analytical methodology presented represent crucial steps toward advancing our understanding of the structure of high-energy density matter produced at high-power laser facilities. These efforts pave the way for further exploration and deeper insights into the fundamental properties of extreme states of matter.

Chapter 5

Investigating the Characteristics of Turbulent Plasmas through Optical Thomson Scattering

5.1 Introduction

A comprehensive understanding of the processes governing magnetic field generation and amplification within turbulent plasmas is crucial for interpreting observations of magnetic fields throughout the universe [154, 155]. While many physical processes, such as the Biermann battery mechanism [156], are posited to generate seed magnetic fields in initially unmagnetised plasmas, their predicted field strengths in astrophysical settings significantly underestimate observed values [157–159]. Instead, the stochastic motions inherent in turbulent plasmas, appear to stretch and fold an initially weak magnetic field until it reaches a dynamically significant level.

The amplification of this weak magnetic field can be described in two distinct phases. Initially, during what is termed the kinematic phase, the magnetic energy undergoes exponential growth. This phase concludes when the magnetic energy reaches approximate equipartition with the kinetic energy at the dissipation scale. Subsequently, beyond this point, the magnetic energy undergoes sustained growth during the non-linear phase until it eventually reaches saturation, roughly one outer-scale eddy-turnover time later. The magnetic energy is now a fraction of the total kinetic energy of the fluid motions. This phenomenon is referred to as the turbulent dynamo mechanism for magnetic field amplification [160, 161].

A stochastic field is characterised by its inherently random behaviour, showcasing a broad spectrum of values across both time and space. These stochastic motions and magnetic fields are pervasive in plasma physics, arising from an array of diverse mechanisms including fluid instabilities and micro-instabilities. Within a plasma, the velocity, $\mathbf{u}(\mathbf{x}, t)$, and magnetic, $\mathbf{B}(\mathbf{x}, t)$, fields at a given position $\mathbf{x}$ and time t are

defined as the sum of their mean and stochastic components,

$$\mathbf{u}(\mathbf{x},t) = \bar{\mathbf{u}}(\mathbf{x},t) + \delta\mathbf{u}(\mathbf{x},t)\,, \tag{5.1.1}$$

$$\mathbf{B}(\mathbf{x},t) = \bar{\mathbf{B}}(\mathbf{x},t) + \delta\mathbf{B}(\mathbf{x},t)\,. \tag{5.1.2}$$

These fluctuating fields are defined such that their spatial average is $\langle\delta\mathbf{u}\rangle = 0$. If the characteristic scale ℓ over which the fluctuating fields vary is substantially smaller than the scale $\bar{l}$ characterising the variation of mean fields, then the spatial average can be established over an intermediate scale l, which satisfies $\ell \ll l \ll \bar{l}$.

The fluctuation dynamo has long be predicted to prevail in instances where a dynamically significant field is present, which is characterised by the strength of the root-mean-square fluctuations,

$$u_{\rm rms} \equiv \left\langle \delta\mathbf{u}^2 \right\rangle^{1/2}\,, \tag{5.1.3}$$

$$B_{\rm rms} \equiv \left\langle \delta\mathbf{B}^2 \right\rangle^{1/2}\,, \tag{5.1.4}$$

A dynamically significant field is defined as $B_{\rm rms} \sim u_{\rm rms}\sqrt{\mu\rho}$, where μ is the magnetic permeability, signifying a state where the magnetic energy approaches equipartition with the energy of turbulent motions. This criterion is established by evaluating the magnetic Reynolds number, which estimates the relative influences of magnetic induction ($\nabla\times(\mathbf{u}\times\mathbf{B})$) versus magnetic diffusion ($\eta\nabla^2\mathbf{B}$),

$${\rm Rm} \equiv \frac{u_{\rm rms}L}{\eta}\,. \tag{5.1.5}$$

Here, L is the length scale of driving stochastic motions with characteristic velocity $u_{\rm rms}$, and η is the resistivity of the plasma. When ${\rm Rm} \ll 1$, diffusive processes smooth out field non-uniformities. Conversely, when ${\rm Rm} \gg 1$, the inductive term dominates, and the field lines move with the flow. This condition facilitates the stretching of field

lines, potentially leading to amplification.

If the magnetic Reynolds number surpasses some critical threshold, $\mathrm{Rm_c}$, the fluctuation dynamo can operate; otherwise, magnetic fields decay diffusively. The precise value of this threshold depends on the Mach number ($\mathcal{M} = u_{\mathrm{rms}}/c_s$), the driving mechanism of the stochastic motions, and the magnetic Prandtl number of the plasma,

$$\mathrm{Pm} \equiv \frac{\mathrm{Rm}}{\mathrm{Re}} = \frac{\nu}{\eta}\,, \tag{5.1.6}$$

where $\mathrm{Re} \equiv u_{\mathrm{rms}} L/\nu$ is the fluid Reynolds number and ν is the kinematic viscosity. These Reynolds numbers are associated with the length scale L of the largest eddies, with characteristic velocities u_{rms}. The rate at which these eddies fragment into smaller ones is dictated by their turnover rate $\gamma_L \sim u_{\mathrm{rms}}/L$, which correlates with the rate at which field lines are stretched by motions with characteristic scales L. Assuming Kolmogorov scaling for velocities on length scales ℓ ($u_\ell \sim u_{\mathrm{rms}}\,(\ell/L)^{1/3}$), the rate of field line stretching can be shown to satisfy $\gamma_\ell \propto \ell^{-2/3}$. This relationship highlights that field line stretching happens most rapidly at small scales. Consequently, dominant field growth occurs initially at the resistive scale ℓ_η, defined as the length scale where $\ell_\eta \sim \eta/u_{\ell_\eta}$.

In the regime where $\mathrm{Pm} \gg 1$, the resistive scale is significantly smaller than the viscous dissipation scale, $\ell_\eta \ll \ell_\nu \sim \nu/u_{\ell_\nu}$. Although motions at these scales remain random, they exhibit spatial smoothness. The field growth rate, γ_b, is therefore driven by viscosity-dominated turbulence and is determined as the turnover rate of eddies at the viscous dissipation scale, $\gamma_b \sim \mathrm{Re}^{1/2} u_{\mathrm{rms}}/L$. When $\mathrm{Pm} \gtrsim 1$ the resistive scale is $\ell_\eta \sim \eta/u_{\ell_\nu}$, and magnetic fluctuations at this scale grow exponentially, at a rate proportional to the characteristic turnover rate of motions at the viscous scale, $\gamma_b \sim u_{\ell_\nu}/\ell_\nu$. However, in the vicinity of $\mathrm{Pm} \simeq 1$, the scaling has shown to deviate to asymptotic behaviour [162].

Comparatively, in the $\mathrm{Pm} \ll 1$ regime, the resistive scale is characterised by $\ell_\eta \sim \eta/u_{\ell_\eta}$, and the stochastic fluid motion driving dynamo action adopts a chaotic nature. However, achieving dynamo action in this scenario demands a significantly higher critical magnetic Reynolds number compared to the $\mathrm{Pm} \gtrsim 1$ case. When $\mathrm{Rm} \gg \mathrm{Rm}_c$, the dynamo growth rate is estimated as the characteristic turnover rate on the resistive scale $\gamma_b \sim \mathrm{Rm}^{1/2} u_{\mathrm{rms}}/L$ [163, 164].

Comprehensive understanding of the intricacies of the fluctuation dynamo requires experimental exploration in conjunction with simulation endeavours. Quantifying the properties of the fluctuation dynamo necessitates experimental techniques capable of measuring plasma conditions and magnetic field growth rates. This experimental characterisation, employing techniques such as scattering, radiography and emissivity measurements, is used both to detect the presence of dynamo action and to infer transport properties such as ν and η.

In this chapter, reverse Monte Carlo techniques are employed to infer the temperatures and densities of turbulent plasmas utilising optical Thomson scattering (OTS). Although Thomson scattering directly probes plasma properties, it has been observed

Table 5.1: Governing motions of dynamo action in different Prandtl number (equation 5.1.6) regimes.

Prandtl Number	**Resistive scale**	**Driving motion**
$\mathrm{Pm} \gg 1$	$\ell_\eta \ll \ell_\nu \sim \nu/u_{\ell_\nu}$	Viscosity-dominated turbulence. Stochastic motions exhibit spatial smoothness. Magnetic field growth determined by turnover rate of eddies at ℓ_ν
$\mathrm{Pm} \gtrsim 1$	$\ell_\eta \sim \eta/u_{\ell_\nu}$	Similar to $\mathrm{Pm} \gg 1$ case though the growth rate behaviour changes as the $\mathrm{Pm} \simeq 1$ threshold is reached
$\mathrm{Pm} \ll 1$	$\ell_\eta \sim \eta/u_{\ell_\eta}$	Resistivity-dominated turbulence. Stochastic motions adopt chaotic nature. Higher Rm_c required for dynamo action. Magnetic field growth governed by Rm.

to introduce perturbative heating effects [165]. The conditions observed via OTS are therefore compared with X-ray emissivity data, a passive diagnostic approach. This comparative analysis not only facilitates a deeper understanding of diagnostic methodologies but also offers insights into effectively characterising the properties of turbulent plasmas.

5.2 Previous Work

Experimental investigations into turbulent dynamo phenomena have been undertaken through the use of high-power laser facilities. Initially, work at the Vulcan laser facility demonstrated the turbulent amplification of magnetic fields by directing a laser-produced shock through a plastic mesh [166]. This process yielded a turbulent plasma characterised by a magnetic Prandtl number of Pm $\sim 10^{-4}$ and a magnetic Reynolds number of approximately unity. The exploration of higher Prandtl regimes, which requires sufficiently large magnetic Reynolds numbers, necessitated the development of a platform capable of generating turbulent plasmas at higher-power laser facilities [167].

Subsequently, evidence of the fluctuation dynamo in turbulent plasmas with Rm $\sim$ 600 and Pm < 1, was successfully demonstrated at the OMEGA laser facility [168]. Here, ten long-pulse laser beams were directed at two opposing chlorine-doped plastic foils, generating supersonic jets that passed through asymmetric grids before colliding, creating a turbulent plasma. More recently, experiments conducted at the National Ignition Facility (NIF) replicated the generation of a turbulent plasma, akin to the methodology outlined in Ref. [168], achieving a Pm ≈ 12 [169]. The magnetic fields generated on this platform were $B_{\mathrm{rms}} \sim 800\,\mathrm{kG}$, more than 6 times those produced on the equivalent OMEGA platform in Ref. [168]. In this regime, where the electron Larmor radius ($\propto B_{\mathrm{rms}}^{-1}$) is smaller than the mean free path ($\propto T_e^2/n_e$), X-ray emissivity data observed the presence of localised temperature gradients for a dynamically significant time. This observation indicated a remarkable suppression of thermal heat

conduction, amounting to a reduction by two orders of magnitude.

However, this X-ray emissivity data does not directly measure local temperature and density conditions. For this purpose, diagnostics such as Thomson scattering are essential. Previous work conducted at OMEGA utilised a 2ω ($\lambda_i = 526.5\,\mathrm{nm}$) laser to collect spatially-resolved optical Thomson scattering, temporally-integrated over the 1 ns pulse length [165]. Utilising the temperatures derived from the OTS analysis, the magnetic Prandtl number was determined as $\mathrm{Pm} \sim 2.7$. However, notable observations indicated significant heating effects within the scattering volume due to the Thomson laser beam. This heating influences the inferred Prandtl number as $\mathrm{Pm} \propto T_i^{5/2} T_e^{3/2}$. To address this effect, this chapter details an experimental campaign identical to that in Ref. [165], but employing a temporally-resolved, spatially-integrated Thomson probe.

5.3 Experimental Setup

The experiments conducted at the OMEGA laser facility at the Laboratory for Laser Energetics [74] employed the experimental setup depicted in Figure 5.1. The laser drive beams, directed onto each 50 μm thick CH foil, initiate the formation of supersonic plasma jets that propagate toward their respective polyimide grids. The intentional offset between these grids introduces an asymmetry between the counter-propagating jets, which subsequently collide in the centre approximately 25 ns after the onset of the driving laser pulses. The initial asymmetry in the plasma-jet density and flow profiles induces significant shearing motions in the interaction region. This, in turn, facilitates Kelvin-Helmholtz instabilities, giving rise to significant stochasticity in the flow profile of the developing interaction region. Within the interaction region, the density and temperature are markedly higher than those of the individual plasma jets. This, coupled with a reduction in characteristic speeds (u_{rms}), results in subsonic stochastic motions within the turbulent plasma, $\mathcal{M} \approx 0.5$.

To comprehensively characterise the turbulent plasma, a synergistic approach utilis-

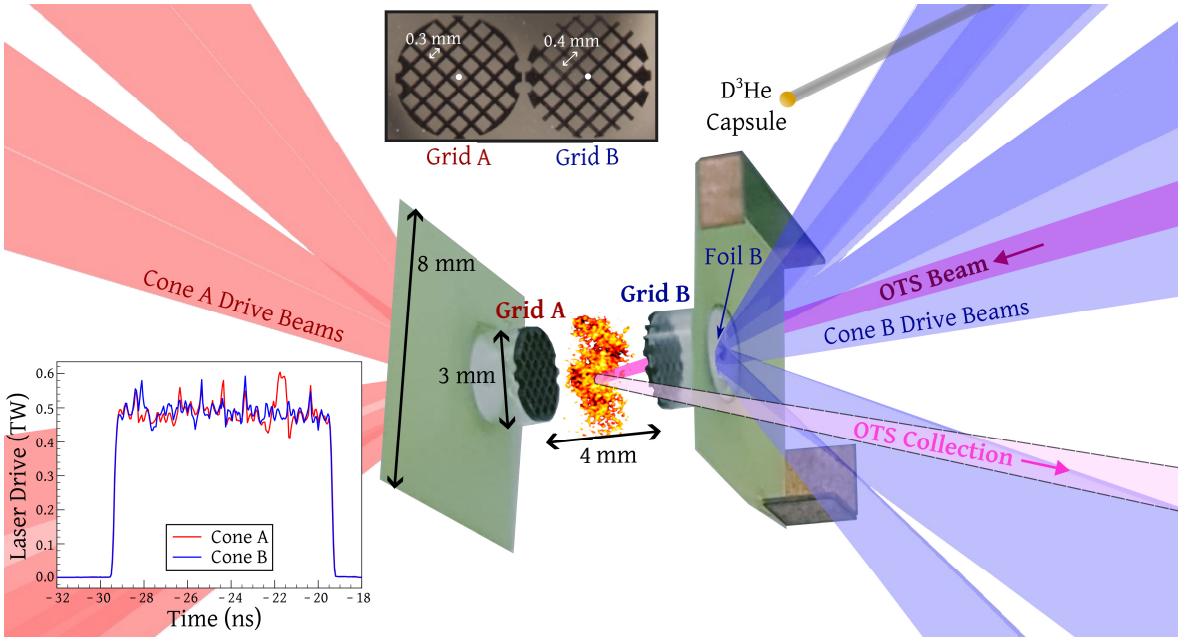

Figure 5.1: Experimental setup at the OMEGA laser facility. The pictured target consists of two cones, labelled A and B, each with a CH (50% C, 50% H) plastic foil attached to its rear. The laser drive incident on each foil, shown in the inset plot, is composed of ten 1 ns, 500 J UV (351 nm) beams staggered to deliver a 10 ns flat pulse shape. Attached to the front of each foil are 230 μm thick and 3 mm diameter annular CH washers with a central 400 μm hole. On the front of each cone, polyimide grids are attached using CH cans. The grids, shown in detail in the top image, are 250 μm thick with 300 μm holes and 100 μm wires. The grids are offset such that grid A has a hole in its centre whilst grid B has crossing wires. The separation between the grids is 4 mm, making the total separation between each CH foil 8 mm. The 4ω (263.25 nm) Thomson scattering beam, as indicated in pink on the right, probes on the central 50 μm diameter turbulent plasma. The intersection between the OTS probe beam and collection volume (shown in light pink) denotes the cylindrical scattering volume. NB: Not drawn to scale.

ing multiple diagnostic techniques is required. For quantifying the generated magnetic fields, a proton-imaging diagnostic was employed by fielding a D^3He capsule 1 cm from the centre of the interaction region. The capsule, with a diameter of 420 μm, consisted of 2 μm of SiO_2 and was filled with 18 atm D^3He gas (6 atm D_2 and 12 atm ^3He). It was imploded using seventeen 500 J UV beams, each with a 1 ns pulse length and a 1.82 mm defocus. The subsequent DD and D^3He fusion reactions generated $\sim 10^8$ 3.0 MeV and 14.7 MeV protons, respectively. Previous experimental work on such capsule implosions

have demonstrated an up-shift in the mean proton energy to 3.3 MeV and 15.0 MeV [170].

The fusion protons uniformly propagate outward from the capsule implosion, with a finite fraction traversing the turbulent plasma and ultimately reaching a CR-39 detector [171] positioned 27 cm from the target centre. The detector is designed such that the 3.3 MeV protons are stopped in the first layer and the 15.0 MeV protons in the second. With no heating effects from the Thomson scattering probe, the measured magnetic field strength in the turbulent plasma is $B_{\text{rms}} \sim 50\,\text{kG}$ [172, 165].

In addition, each experimental shot employed X-ray emission and optical Thomson scattering diagnostics, timed independently from the proton-imaging. Detailed explanations of these techniques are provided in the subsequent sections.

5.4 Optical Thomson Scattering Analysis

To characterise the properties of the turbulent plasma, as depicted in Figure 5.1, a 4ω, $\lambda_i = 263.25\,\text{nm}$, OTS probe was focused on the central $50\,\mu\text{m}$ diameter interaction region. The Thomson scattering diagnostic on OMEGA, as illustrated in Figure 5.2, comprises a reflective collection system coupled to an ion-acoustic and electron plasma wave spectrometer system. The collection telescope is positioned to collect the $2\theta = 59.9^\circ$ scattering, and is constructed using an $f/10$ off-axis section of a traditional $f/1.25$ Schwarzschild objective [173]. This configuration results in a collected angular spread,

$$\Delta(2\theta) = 2\tan^{-1}\left(\frac{1}{2\times f\text{-number}}\right) = 5.7^\circ. \tag{5.4.1}$$

The ion-acoustic features are measured using a 1 m Czerny-Turner spectrometer equipped with a 3600 groves/mm diffraction grating which is coupled to a Rochester optical streak system (ROSS) [173]. This IAW spectrometer covers a spectral window of 4 nm, resulting in a measured spectral resolution of 0.02 nm. The pulse front tilt

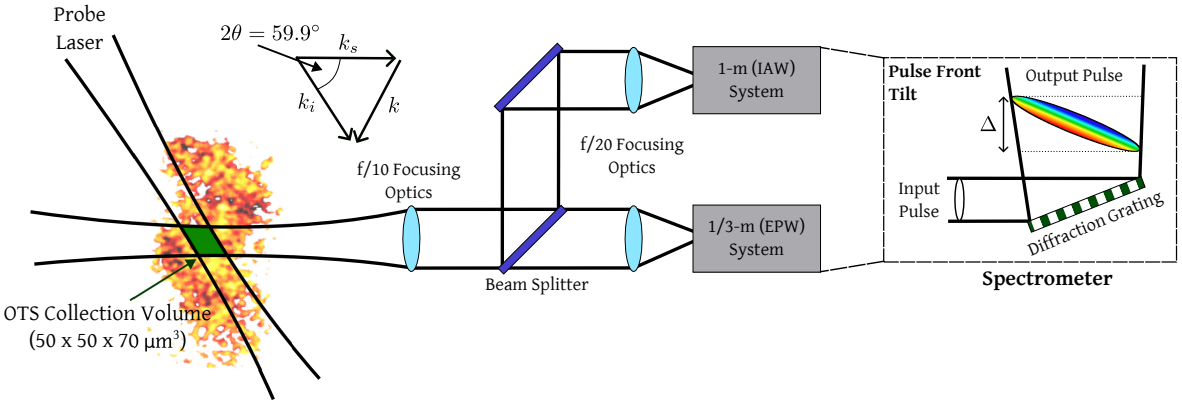

Figure 5.2: Schematic of the optical Thomson scattering diagnostic configuration on OMEGA [54]. As illustrated on the far right, the chosen diffraction grating in the IAW and EPW spectrometers introduces a pulse front tilt as a result of an increased path difference Δ [174].

introduced by the IAW spectrometer sets a limiting temporal resolution of 0.2 ns [174]. For the electron plasma feature measurements, a 0.3 m spectrometer with a diffraction grating of 1200 grooves/mm, is coupled to a second ROSS. This EPW spectrometer records a spectral window of 40 nm with a resolution of 0.5 nm. The EPW spectrometer introduces a pulse front tilt with a corresponding temporal resolution of 0.02 ns. The overall EPW temporal resolution is ultimately constrained by the streak camera, with $\Delta t \sim 0.03$ ns.

5.4.1 Ion-acoustic wave

As discussed in Section 2.3.2, the ion-acoustic wave scattering features can provide detailed information on the electron and ion temperature. The scattering signal observed by the IAW streak camera is dependent on its source function, $\Sigma(\omega)$, and the turbulent plasma's structure factor,

$$I(\mathbf{k}, \omega) \propto \Sigma(\omega) \times S(\mathbf{k}, \omega)\,. \tag{5.4.2}$$

As detailed in Figure 5.3 the IAW source function is found to be well fitted by a Gaussian function with a FWHM ≈ 0.03 nm.

Illustrated in Figure 5.4 is an instance of the time-resolved scattering signal ob-

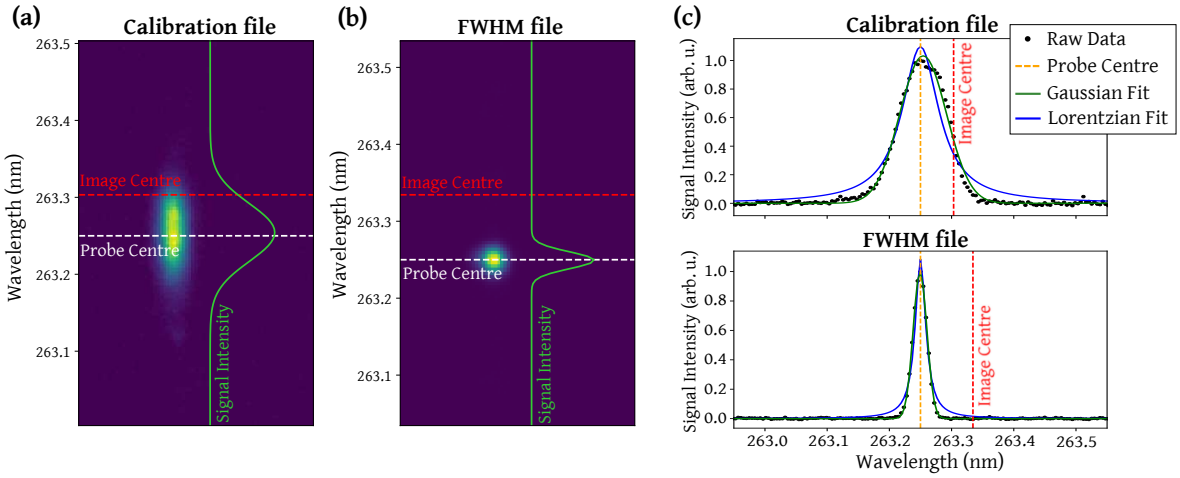

Figure 5.3: **(a)** Calibration of the IAW streak to locate the 4ω probe centre, $\lambda_i = 263.25\,\text{nm}$. **(b)** Source function, $\Sigma(\omega)$, to determine full width at half maximum. **(c)** Representative Gaussian and Lorentzian fits to the spectra shown in (a) and (b). The IAW source function is assumed to be Gaussian with a FWHM of 0.03 nm.

served with a 1 ns pulse length Thomson scattering probe at 31 ns after the onset of the driving laser pulses. To isolate the scattering signal, a time-averaged background signal, taken after the Thomson probe, is subtracted from the scattering data. Using the IAW temporal resolution of 0.2 ns, Figure 5.4(c) demonstrates an example of the time-averaged signal extracted at a specific time step.

The structural characteristics of the ion-acoustic resonances are primarily influenced by the electron temperature, ion temperature and the bulk fluid velocity $\mathbf{v_b}$. During the OTS measurement, the bulk fluid velocity undergoes variations due to stochastic motions within the scattering volume, deviating from a constant value. This variability manifests in the IAW scattering signal as broadening of the resonant peaks, a phenomenon not adequately captured by simply increasing the ion temperature, as depicted in Figure 5.5. To account for the impact of velocity gradients, an isotropic and normally distributed velocity fluctuation is assumed with a mean bulk velocity of $\bar{v}_b \equiv \hat{\mathbf{k}} \cdot \bar{\mathbf{v}}_\mathbf{b}$ and a standard deviation of $\Delta v_b \sim v_{rms}$. The total structure factor for the

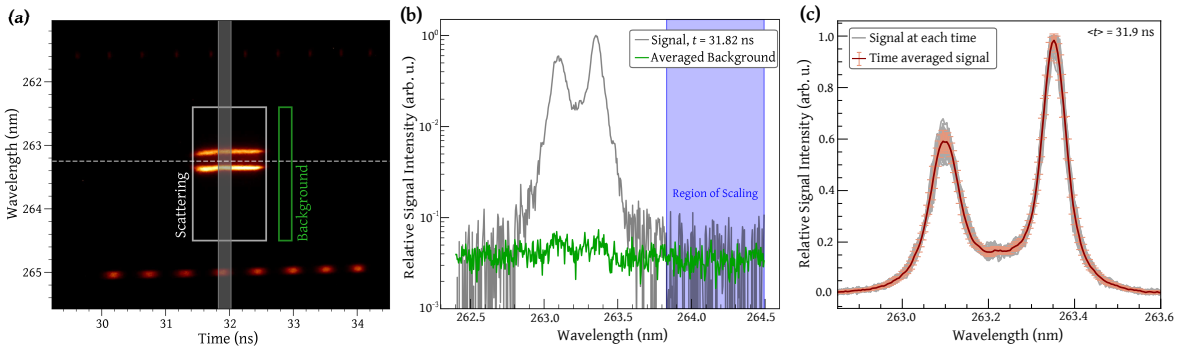

Figure 5.4: **(a)** Spectrally-resolved IAW feature. The scattering signal is isolated with the white box and the background signal is extracted from within the green box. **(b)** The time-averaged background signal, shown in green, is scaled to an example data signal, shown in grey, and subtracted. **(c)** The time-averaged scattering signal for the highlighted region in (a) is taken as the mean of each contributing background-removed signal (shown in grey). The signal error is given by the standard deviation.

IAW feature is therefore expressed by [165],

$$S(\mathbf{k},\omega) \approx \frac{\sqrt{3}}{\sqrt{\pi}\Delta\bar{v}_b}\int \mathrm{d}u \exp\left[-\frac{3\,(u-\bar{v}_b)^2}{\Delta {v_b}^2}\right] \times S(\mathbf{k},\omega,u)\,, \tag{5.4.3}$$

where u is the explored velocity space. To streamline the analytical process and reduce computational expenses associated with explicitly determining each structure factor, an effective approximation can be employed,

$$S(\mathbf{k},\omega,u) \approx S(\mathbf{k},\omega-\delta\omega,\bar{v}_b)\,, \tag{5.4.4}$$

where $\delta\omega = k(\bar{v}_b - u)$. The structure factor $S(\mathbf{k},\omega)$ for some given conditions is assessed using a Thomson scattering simulator developed on the formalism in Refs. [175, 176]. The red fit in Figure 5.5 demonstrates that introducing a normally distributed velocity range provides a robust fit to the observed scattering signal, effectively capturing the variations present in the bulk fluid velocity.

To explore the multi-parameter space, MCMC analysis is employed. At each time step, the observed IAW signal, $I_{\mathrm{raw}}(\omega)$, is fitted under the assumption of a uniform distribution with linear sampling for electron and ion temperatures ($10 < T\,(\mathrm{eV}) < 550$),

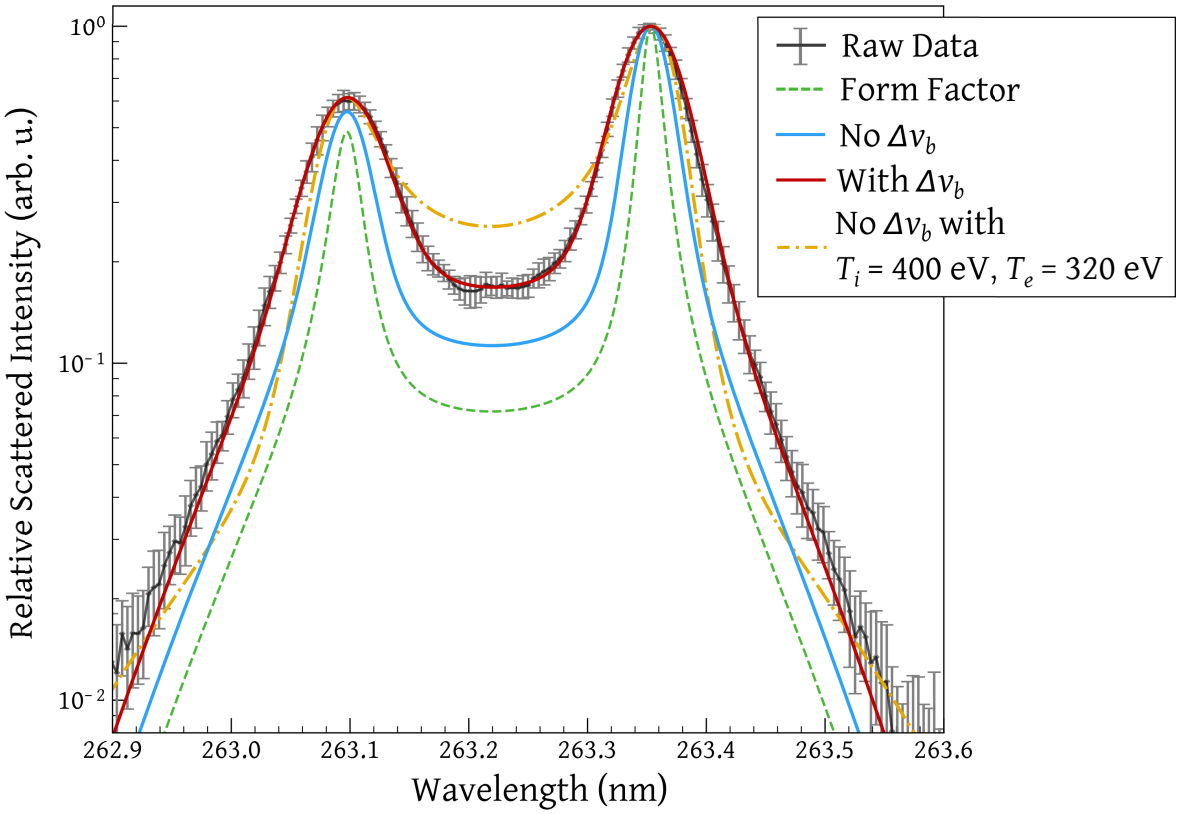

Figure 5.5: Demonstrative fitting of the IAW signal shown in Figure 5.4(c). The form of $S(\mathbf{k},\omega)$ for a fully ionised CH plasma with $T_e = 400\,\text{eV}$ and $T_i = 200\,\text{eV}$ is shown as a dashed green line. This $S(\mathbf{k},\omega)$ is then coupled with the source function, $\Sigma(\omega)$, to produce the solid blue fit. Introducing a velocity gradient Δv_b to this fit transforms it to the solid red line. An example fit at a higher ion temperature with no velocity gradient is shown as a yellow dash-dotted line. The electron density is assumed as $n_e = 5e20\,\text{cm}^{-3}$ throughout.

the average bulk velocity ($-300 < \bar{v}_b\,(\text{km/s}) < 300$), and the bulk velocity gradient ($0 < \Delta v_b\,(\text{km/s}) < 200$). Additionally, the exploration extends to include drift velocity v_d ($0 < v_d\,(\text{km/s}) < 1000$) and electron density. Due to the comparatively weaker dependence of IAW features on electron density, a more stringent constraint is imposed on its linear sampling, ensuring a range of $5e19 < n_e\,(\text{cm}^{-3}) < 5e20$. This constraint is applied to minimise the computational time of exploring a parameter space that exerts minimal influence on the resulting spectrum.

The MCMC code evaluates the acceptance percentage of each fit, $I_{\text{fit}}(\omega)$, with a

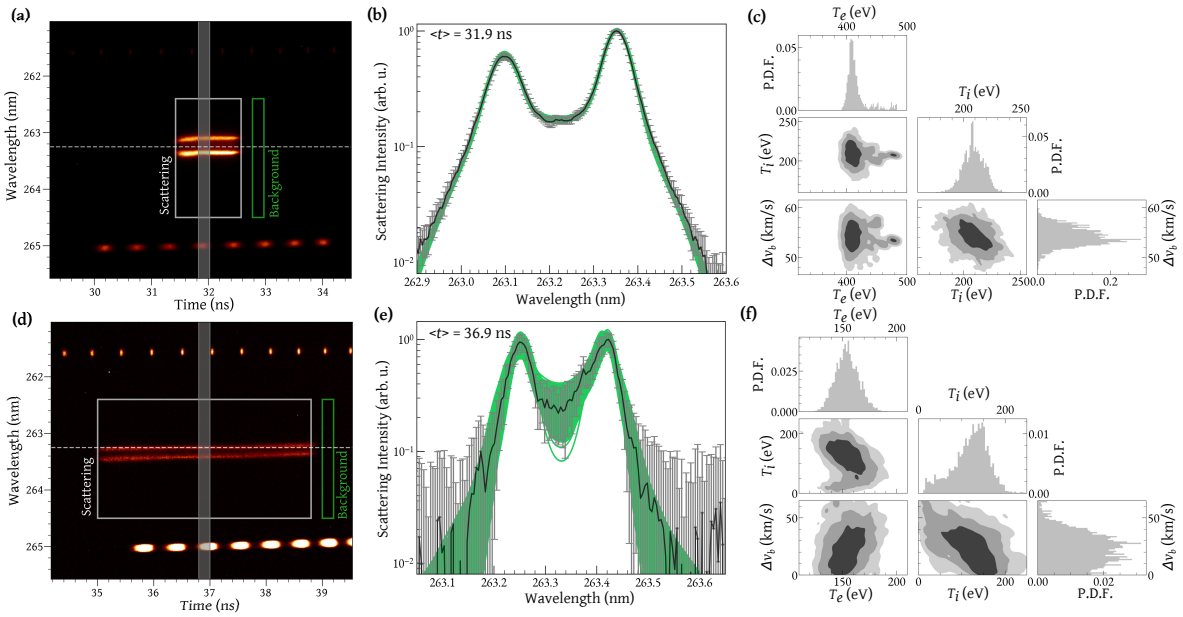

Figure 5.6: **(a)** Temporally-resolved IAW signal as shown in Figure 5.4(a). **(b)** The range of converged MCMC fits, shown in green, is compared to the time-step highlighted in grey in (a). **(c)** Corresponding parameter probability density functions for the fits shown in (b). The lower quadrant plots compare the 1, 2 and 3σ parameter correlations and the diagonal histograms show the probability densities for each parameter. **(d)-(f)** As above but for a 3.7 ns Thomson scattering probe.

cost function defined as,

$$\beta_{\text{cost}} = \max_{\omega'<1}\left[\frac{I_{\text{fit}}(\omega') - I_{\text{raw}}(\omega')}{I_{\text{raw}}(\omega')}\frac{1}{\sqrt{2}\sigma}\right]^2 + \max_{\omega'>1}\left[\frac{I_{\text{fit}}(\omega') - I_{\text{raw}}(\omega')}{I_{\text{raw}}(\omega')}\frac{1}{\sqrt{2}\sigma}\right]^2, \quad (5.4.5)$$

where $\omega' = \omega/\omega_i$. This cost function is therefore designed to assess the appropriateness of the fit to both the red- and blue-shifted IAW features. This ensures that the fitting process does not favour the more intense Doppler shifted peak, providing a comprehensive assessment of the fit across the entire spectrum.

Figure 5.6 demonstrates the range of accepted fits and their corresponding converged parameter spaces for both a 1 ns and a 3.7 ns pulse length OTS probe, each with a total energy of ~ 40 J. Notably, the observed scattering signal for the 3.7 ns probe exhibits lower intensity, resulting in greater uncertainty in the data signal. This increased uncertainty manifests as a broader convergence of T_i and Δv_b, as these two parameters

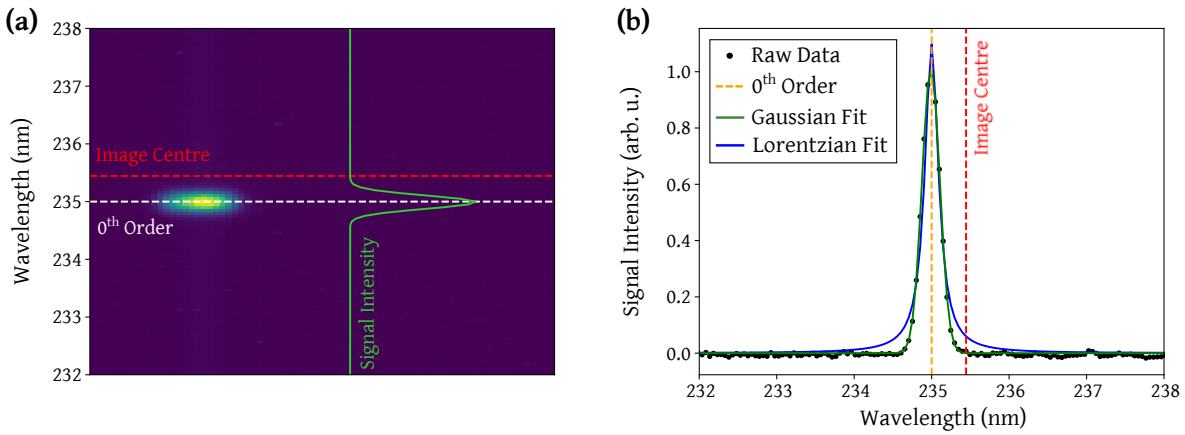

Figure 5.7: **(a)** Source function and calibration of the EPW streak to locate the 0^{th} order scattering at 235 nm. **(b)** Representative Gaussian and Lorentzian fits to the spectrum shown in (a). The EPW source function is assumed to be Gaussian with a FWHM of 0.3 nm.

collectively adapt to encompass the breadth of the IAW peaks.

5.4.2 Electron plasma wave

The plasmon scattering signal observed by the EPW streak is also reliant on the formulation presented in equation 5.4.2. As illustrated in Figure 5.7, the EPW source function is accurately represented by a Gaussian with a FWHM ≈ 0.3 nm. The characteristics of the plasmon scattering structure factor, as detailed in equation 2.3.2, predominantly depend on the electron density and electron temperature.

The resolved EPW signal corresponding with the shot illustrated in Figure 5.4 is shown in Figure 5.8. A similar background removal process is performed, employing the lower wavelength as a scaling region. This scaling approach prevents any potential contamination from the EPW feature, which extends from its peak resonance, λ_{epw}, to $\lambda_i = 263.25\,\text{nm}\cdot$ Given the relatively minor pulse front tilt induced in the EPW streak, a reduced binning strategy is applied to compute the time-averaged signal at each time step.

In many instances, the EPW features are effectively characterised by simply fitting electron temperature and electron density conditions. Under such circumstances, the

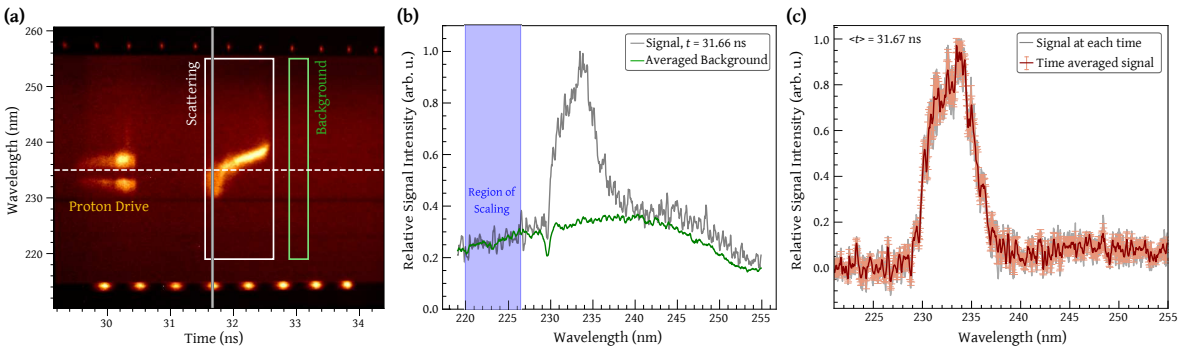

Figure 5.8: **(a)** Spectrally-resolved EPW feature from the same shot shown in Figure 5.4. The scattering signal is isolated with the white box and the background signal is extracted from within the green box. **(b)** The time-averaged background signal, shown in green, is scaled to an example data signal, shown in grey, and subtracted. **(c)** The time-averaged scattering signal for the highlighted region in (a) is taken as the mean of each contributing background-removed signal (shown in grey). The signal error is given by the standard deviation.

width of the EPW peak is governed by the electron temperature. However, as evidenced, particularly during the early times of the OTS probe in Figure 5.8(a), there is a broadening of the EPW signal that cannot be adequately explained solely by a temperature measurement. Similar to the bulk velocity influence on the IAW signal, the presence of density fluctuations within the scattering volume contributes to the observed broadening of the EPW signal. Much like the IAW, the impact of density gradients can be accommodated by assumed an isotropic and normally distributed density fluctuation with a mean of $\bar{n}_e$ and a standard deviation of Δn_e. The total structure for the EPW feature is therefore expressed as [165],

$$S(\mathbf{k},\omega) \approx \frac{1}{\sqrt{\pi}\Delta n_e} \int \mathrm{d}n \exp\left[-\frac{(n-\bar{n}_e)^2}{{\Delta n_e}^2}\right] \times S(\mathbf{k},\omega,n)\,, \tag{5.4.6}$$

where n is the explored density space.

There is, however, no effective approximation for relating the structure factor at each investigated density. Consequently, each $S(\mathbf{k},\omega,n)$ must be explicitly calculated, resulting in a computationally demanding process to determine equation 5.4.6 with the required resolution. To address this challenge, the EPW structure is instead evaluated

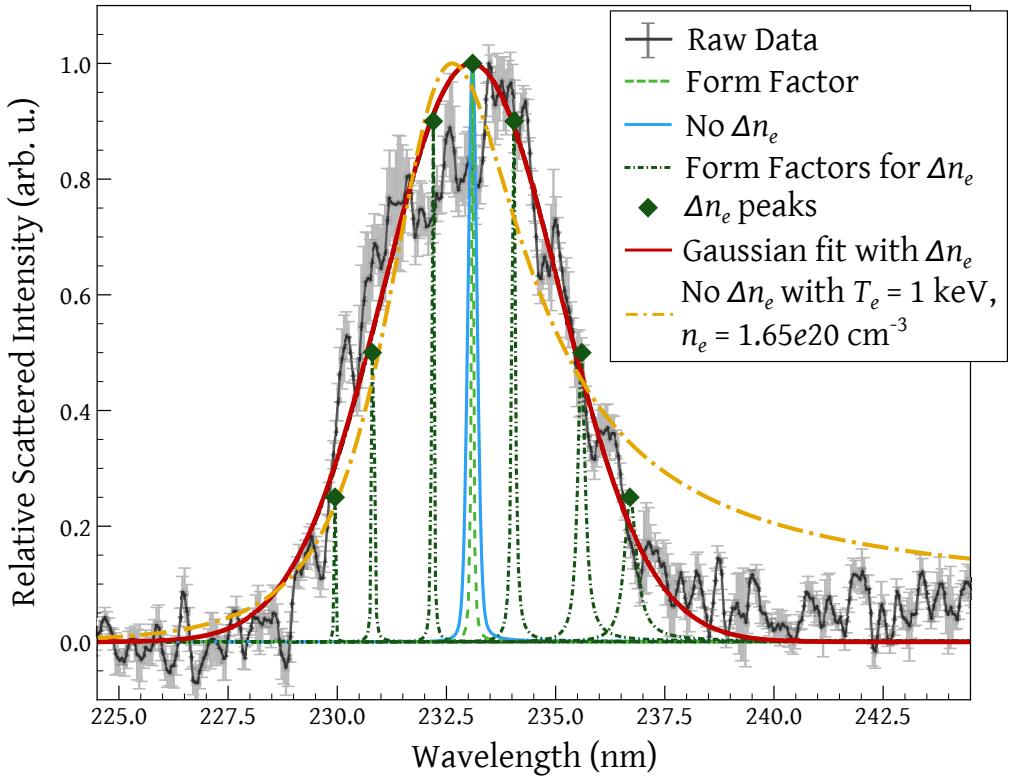

Figure 5.9: Demonstrative fitting of the EPW signal shown in Figure 5.8(c). The form of $S(\mathbf{k}, \omega)$ for a fully ionised CH plasma with $T_e = 400\,\text{eV}$ and $n_e = 2.35e20\,\text{cm}^{-3}$ is shown as a light dashed green line. This $S(\mathbf{k}, \omega)$ is then coupled with the source function to produce the solid blue fit. The incorporation of a density gradient Δn_e necessitates the computation of form factors across a representative density range, depicted by dark dash-dotted green lines. A Gaussian fit to the peak of each form factor, illustrated as green diamonds, is followed by the integration with the source function, resulting in the generation of the solid red line. An example fit at a higher electron temperature with no density gradient is shown as a yellow dash-dotted line. The ion temperature is assumed as $T_i = 200\,\text{eV}$ throughout.

at a representative range of densities sampled from the normal density fluctuation distribution. Subsequently, a Gaussian function is fitted to the peak position of the EPW feature for each calculated $S(\mathbf{k}, \omega, n)$. This Gaussian fit is then compared to the experimental signal. It is important to note that while the Gaussian fit may not perfectly capture the entirety of the EPW signal, it offers a satisfactory description of the observed signal whilst ensuring that computational costs remain manageable, allowing for effective exploration of the parameter space. An example of this fitting procedure is illustrated in Figure 5.9.

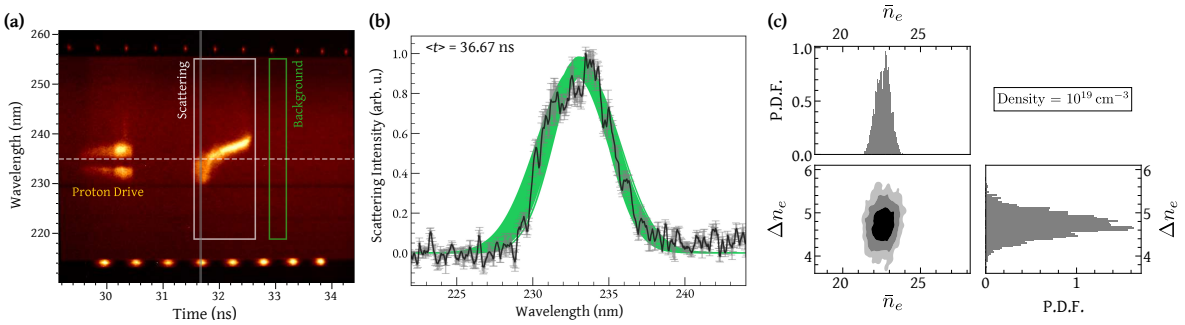

Figure 5.10: **(a)** Temporally-resolved EPW signal as shown in Figure 5.8(a). **(b)** The range of converged MCMC fits, shown in green, is compared to the time-step highlighted in grey in (a). **(c)** Corresponding parameter probability density functions for the fits shown in (b). The lower quadrant compares the 1, 2 and 3σ parameter correlations and the diagonal histograms show the probability densities for each parameter. The electron density values are given in $10^{19}\,\mathrm{cm}^{-3}$.

In contrast to the diagnostic comparisons outlined in Chapters 3 and 4, the MCMC exploration of the EPW parameter space is not conducted in isolation from the IAW analysis. This integration is necessitated by the collective influence of electron temperature and density fluctuations, which contribute to the broadening of the EPW feature. Therefore, to accurately extract information on the density gradients, it is essential to utilise an independent constraint on the temperature conditions, as provided by the IAW analysis.

At each time step, the observed EPW signal, $I_{\mathrm{raw}}(\omega)$, is fitted using MCMC assuming a uniform distribution with logarithmic sampling for the electron density ($1e19 < \bar{n}_e\,(\mathrm{cm}^{-3}) < 5e20$) and density gradient ($1e18 < \Delta n_e\,(\mathrm{cm}^{-3}) < 3e20$). The exploration of electron and ion temperatures assumes a linear sampling, constrained by the mean, $\bar{T}_{\mathrm{iaw}}$, and standard deviation, $\sigma_{T_{\mathrm{iaw}}}$, derived from the IAW analysis at the corresponding time. The temperature exploration is therefore defined as, $-2\sigma_{T_{\mathrm{iaw}}} < T - \bar{T}_{\mathrm{iaw}} < 2\sigma_{T_{\mathrm{iaw}}}$. This restricted exploration meant that there was no convergence in the temperature space. Therefore, only the density results are presented for the EPW MCMC analysis.

The MCMC code evaluates the acceptance percentage of each fit, $I_{\mathrm{fit}}(\omega)$, with a

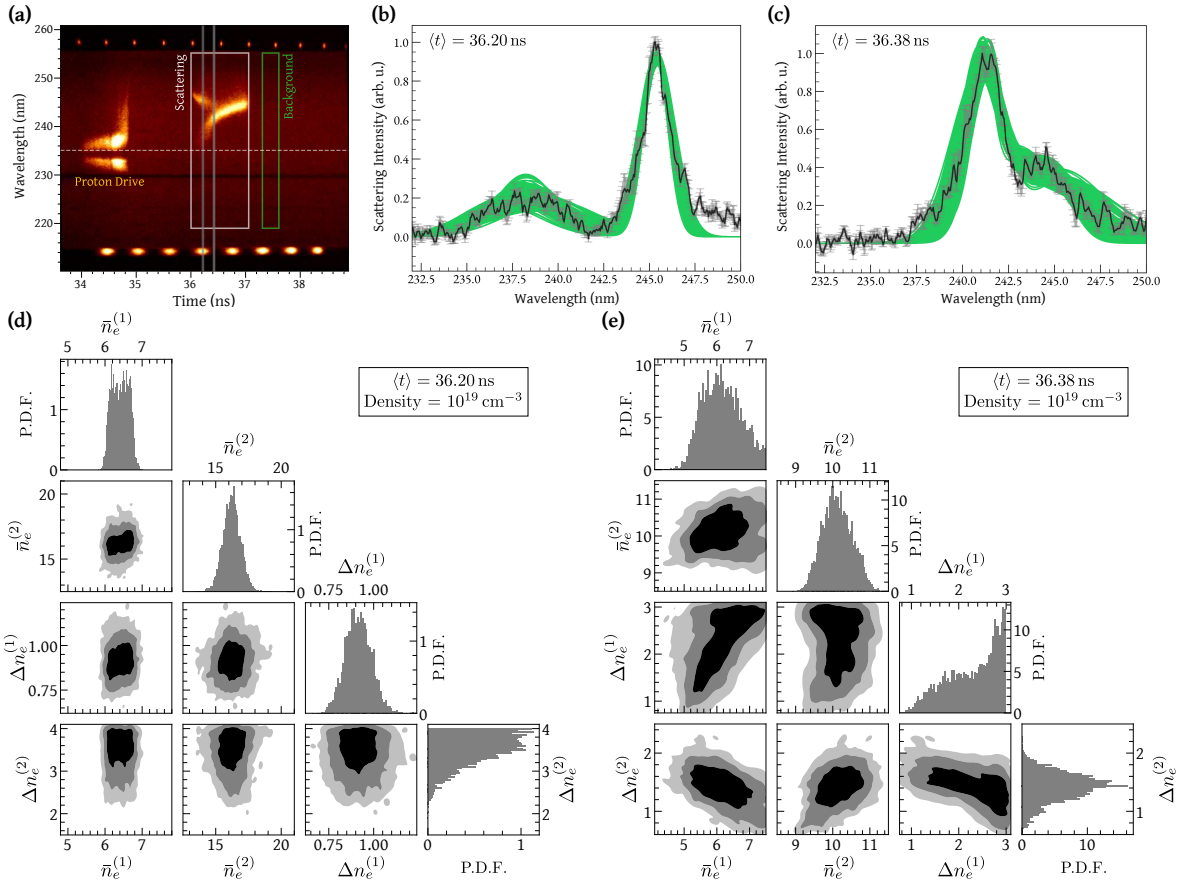

Figure 5.11: **(a)** Temporally-resolved EPW signal for a Thomson probe at $t_{\text{ots}} = 36\,\text{ns}$. A double EPW feature is observed at early times. **(b)** The range of converged MCMC fits, shown in green, is compared to the first time-step highlighted in grey in (a). **(c)** As in (b) for the later time-step highlighted in grey in (a). **(d)** Corresponding parameter probability density functions for the fits shown in (b). The lower quadrant compares the 1, 2 and 3σ parameter correlations and the diagonal histograms show the probability densities for each parameter. The lower and higher density fitting regions are delimited with a (1) and (2), respectively. The electron density values are given in $10^{19}\,\text{cm}^{-3}$. **(e)** As in (d) for the fits shown in (c).

cost function defined as,

$$\beta_{\text{cost}} = \sum_{\omega'} \left[\frac{I_{\text{fit}}(\omega') - I_{\text{raw}}(\omega')}{\sqrt{2}\sigma} \right]^2, \tag{5.4.7}$$

where ω' encapsulates the region where $I_{\text{fit}}(\omega') > 0.15 \times \max\left[I_{\text{fit}}(\omega)\right]$. Whilst a soft boundary cost function, similar to the one employed for the IAW feature, was explored, it became apparent that the convergences tended to favour fitting the lower wavelength region. This tendency can be attributed to the inherent limitations of using a Gaussian function, which fails to accurately capture the lower wavelength tail, to describe the observed EPW feature. Therefore a cost function which assessed the overall fit to the scattering signal above 15% was found to produce a more appropriate range of accepted fits, such as illustrated in Figure 5.10.

Since the EPW signal is comparatively weaker than the IAW, successful observation occurred only in two of the investigated shots. The second EPW signal, which probed the turbulent plasma at a later time, revealed a double feature at the onset of the Thomson probe, as illustrated in Figure 5.11. The presence of this double feature is attributed to the Thomson probe initially scattering from the edge of the interaction region, which is at a lower density. As the probe heats the plasma, the interaction region begins to expand into the Thomson scattering volume and an increasing scattering signal is observed from the higher density interaction region.

Within this region, obtaining good fits to the EPW feature required fitting two weighted plasma conditions. Although these conditions are assumed to be at the same temperature, they are independently fitted for $\bar{n}_e$ and Δn_e. To prevent the crossing over of the two conditions, tighter restrictions were imposed on their density explorations. As a consequence of these restrictions, the probability density functions of the converged parameters, as shown in Figures 5.11(d) and (e), do not consistently resemble normal distributions. Whilst this form of convergence is less than ideal, it becomes inevitable

in fittings of this nature where the conditions are closely situated and their respective scattering signals, especially at later times, are intertwined.

The electron density information inferred from the electron plasma wave analysis can subsequently be used to improve the accuracy of the X-ray emission analysis.

5.5 X-ray Emission Analysis

An X-ray framing camera (XRFC) was fielded perpendicular to the colliding jets to measure the spatially-resolved X-ray emission profile. The configuration consisted of a pinhole array situated 91.4 mm from the target centre and a charge-coupled device (CCD) camera placed a further 182.9 mm away, resulting in a 2× magnification. The pinhole array comprised two pinholes, each with a diameter of 50 μm and spaced 6 mm apart. This arrangement produced two distinct images on the CCD camera which were recorded on separate strips. Each strip had a time-gating of 1 ns and were timed dependently.

The emission observed by the XRFC is used to infer the spatially-resolved line-of-sight-averaged density-weighted electron temperature profile [169]. At the expected densities and temperatures ($n_e \sim 10^{20}\,\mathrm{cm}^{-3}$, $T_e \gtrsim 50\,\mathrm{eV}$) the plasma can be assumed to be fully ionised, and the X-ray emission is therefore dominated by free-free Bremsstrahlung radiation. Assuming a thermal distribution of particles, the spectral density, $\epsilon_\omega^{\mathrm{ff}}$, for a CH plasma is dependent on [177],

$$\epsilon_\omega^{\mathrm{ff}} \propto Z_{\mathrm{eff}}\, n_e^2\, T_e^{-\frac{1}{2}} \exp\left(-\frac{\hbar\omega}{k_B T_e}\right) . \tag{5.5.1}$$

where the effective ionisation $Z_{\mathrm{eff}} = (Z_C^2 + Z_H^2)/(Z_C + Z_H) \approx 5.3$. Since the plasma in the interaction region is optically thin to X-rays detected by the XRFC, the measured

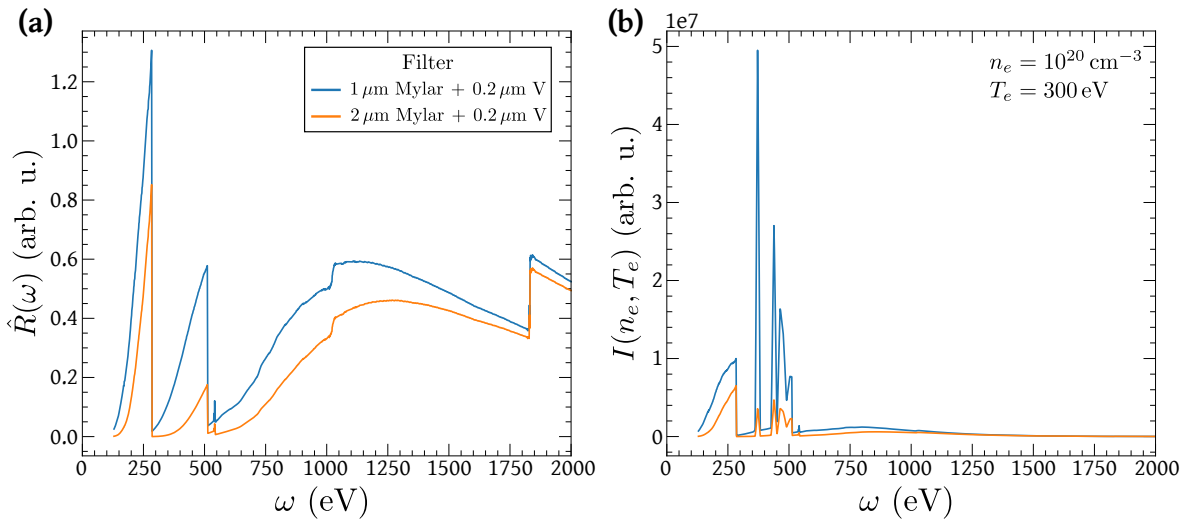

Figure 5.12: **(a)** Frequency-sensitive response of the XRFC for each filter. The detector response is found by multiplying the filter transmissions by the microchannel plate (MCP) response [178]. **(b)** Expected frequency-resolved signal measured by the XRFC for a plasma at $n_e = 10^{20}\,\mathrm{cm}^{-3}$ and $T_e = 300\,\mathrm{eV}$. The X-ray spectrum is simulated using SPECT3D [69] and PrOpacEOS tables with non-local thermodynamic equilibrium atomic transitions. This means that the atomic level populations are determined by solving a coupled set of atomic rate equations, such as collisional ionisation and excitation, spontaneous emission and radiative recombination.

intensity, $I(n_e, T_e)$, on the CCD camera therefore satisfies,

$$I(n_e, T_e) \propto \int \mathrm{d}s\, n_e^2\, T_e^{-\frac{1}{2}} \int \mathrm{d}\omega\, \hat{R}(\omega) \exp\left(-\frac{\hbar\omega}{k_B T_e}\right), \tag{5.5.2}$$

where the signal is integrated along the line-of-sight, $\mathrm{d}s$, and $\hat{R}(\omega)$ denotes the frequency-dependent response of the XRFC [178]. An example of the frequency-resolved intensity for one set of plasma conditions is shown in Figure 5.12.

To infer information about the temperature profile of the turbulent plasma, unique filters were applied to the two pinholes of the framing camera. Consequently, at each time instance, the distinct attenuation of the X-ray plasma emission facilitated the characterisation of the electron temperature. This is achieved by determining the ratio

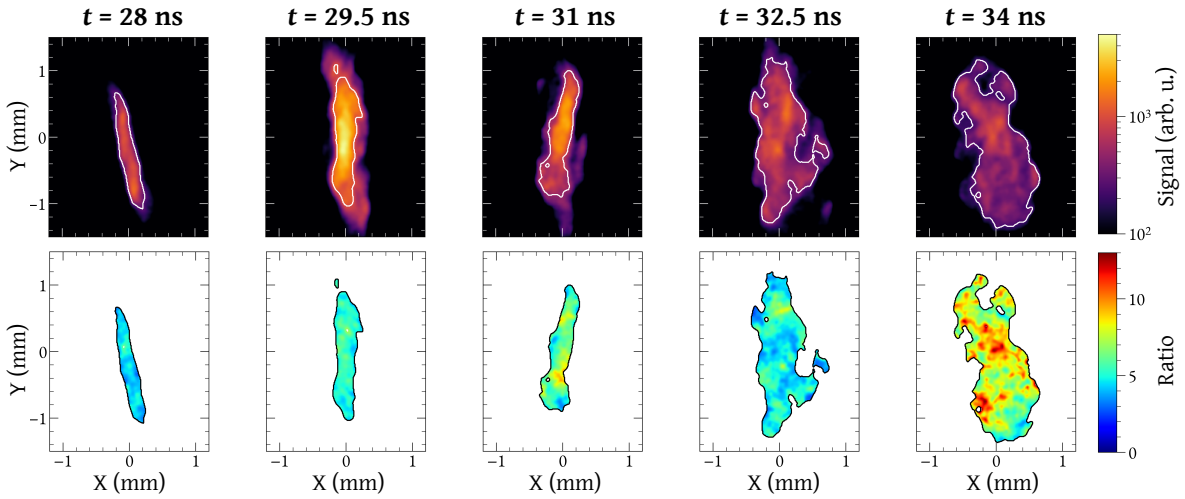

Figure 5.13: Evolution of the plasma within the interaction region as observed by the 1 ns time-gated X-ray framing camera. The top row shows the emission data recorded by the thinner filter pack (1 μm Mylar + 0.2 μm vanadium). The plasma region, denoted as a white boundary in each image, where the signal is $> 0.2 \times I_{\max}$, is isolated via a 2-D Gaussian window function. The bottom row shows the corresponding ratio maps, as defined in equation 5.5.3.

between the observed intensity at each discrete spatial location,

$$\mathcal{R}(n_e, T_e) = \frac{I_1(n_e, T_e)}{I_2(n_e, T_e)} \,. \tag{5.5.3}$$

The ratio is defined such that $I_1(n_e, T_e)$ represents the intensity from the thinner filter pack, composed of 1 μm Mylar and 0.2 μm vanadium, and $I_2(n_e, T_e)$ is produced by the thicker filter pack, composed of 2 μm Mylar and 0.2 μm vanadium.

To overlay the X-ray emission profiles from each distinct filter, a 2-D Gaussian smoothing function with a FWHM of 50 μm is first applied to each image. This is set by the spatial resolution of the XRFC in the used configuration. The most probable point of overlap between the emission profiles of each filter is then determined using a cross-correlation function of the normalised intensities in space,

$$\mathcal{C}(x, y) = \left(\frac{I_1(x, y)}{\bar{I}_1} \right) * \left(\frac{I_2(x, y)}{\bar{I}_2} \right) \,. \tag{5.5.4}$$

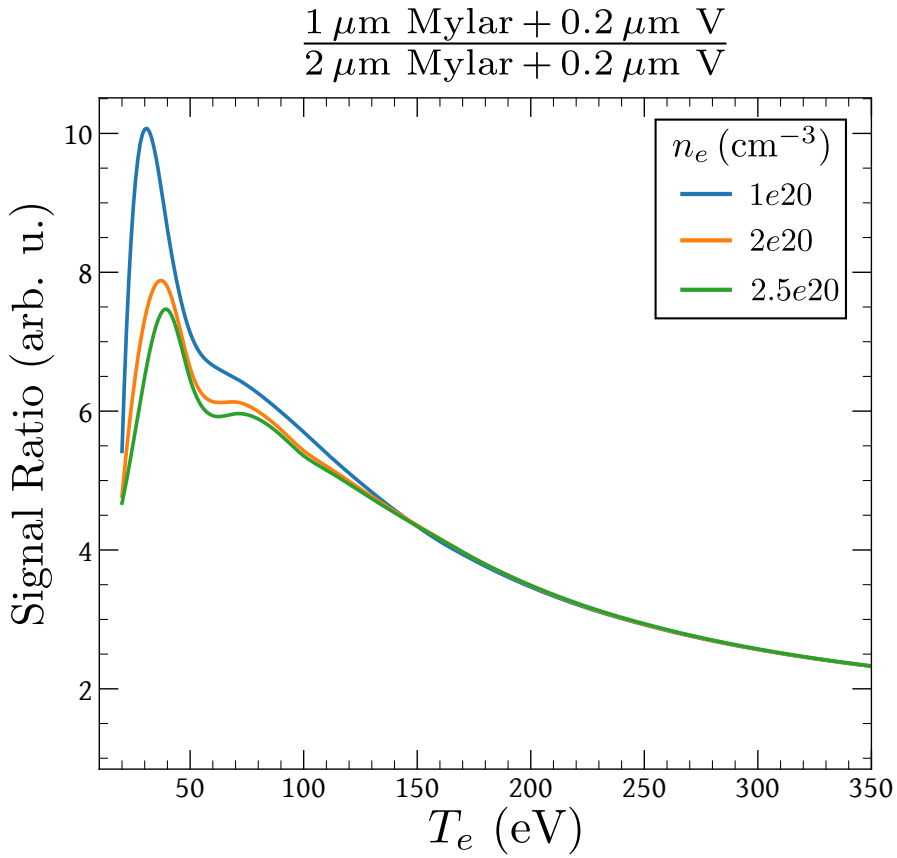

Figure 5.14: X-ray ratio curves, as defined by equation 5.5.5, for a 1 μm Mylar + 0.2 μm vanadium and 2 μm Mylar + 0.2 μm vanadium filter pack. The effect of the chosen electron density on the resultant ratio curve is shown for three different densities.

Here, the intensity signals are normalised to ensure equal weighting between the two images. Once the two emission profiles are spatially superimposed, the ratio map, as defined in equation 5.5.3, can be calculated. The emission region below 20% of the maximum signal intensity is excluded from the subsequent ratio maps shown in Figure 5.13. These regions, on the edge of the interaction plasma, are excluded as their lower signal results in a larger uncertainty in their ratio value and because they will be at a lower density than the bulk plasma in the centre, meaning they would require a different ratio curve.

To infer temperature information from the produced ratio maps, the frequency-resolved signal measured by the XRFC, as shown in Figure 5.12(b), is determined for a range of temperatures and densities. By assuming a fixed density, the ratio curve is

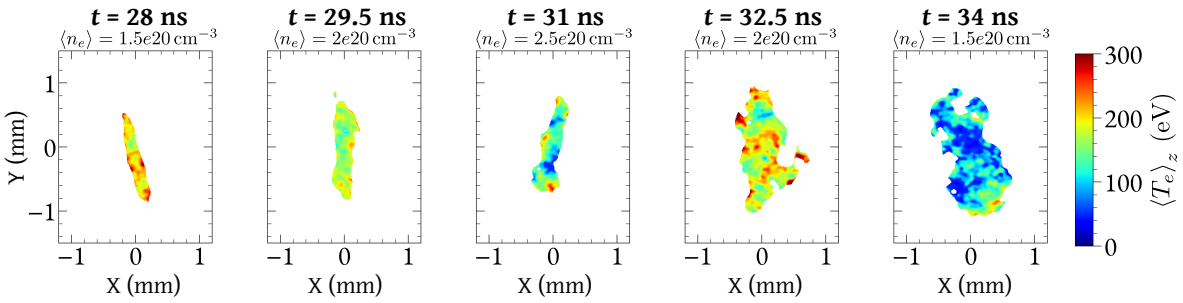

Figure 5.15: The inferred spatially-resolved line-of-sight-averaged density-weighted electron temperature profile, $\langle T_e \rangle_z$, for the ratio maps shown in Figure 5.13 using ratio curves such as shown in Figure 5.14.

given by,

$$R(T_e) = \frac{\int \mathrm{d}\omega \, I_1(\omega, T_e)}{\int \mathrm{d}\omega \, I_2(\omega, T_e)} \,. \tag{5.5.5}$$

Figure 5.14 shows the calculated ratio curves for the selected filter pack across various electron densities. As the chosen electron density significantly influences the ratio curve, having an independent measure of plasma density, such as Thomson scattering, is vital for reducing uncertainties.

An ideal ratio curve has its peak at the lowest expected temperature within the plasma, and a direct correlation between ratio and temperature. However, in the calculated ratio curves, particularly at the higher electron densities, a secondary peak becomes apparent around $T_e \sim 80\,\mathrm{eV}$. Below this threshold the ratio value does not have a direct one-to-one relationship with temperature, leading to a notable uncertainty in the temperature estimation within this range. This lower temperature range is therefore excluded from the final temperature distributions.

However, in order to calibrate the ratio curves with the inferred ratio maps, it is necessary to utilise the lower temperature region as the maximum value of the ratio curve is required. This calibration process takes into account the uncertainty in the filter thicknesses. Each filter material has a thickness uncertainty of $\sim 20\%$, while the vanadium coating has an uncertainty of $\sim 10\%$. To determine the actual thickness from the shot day, the X-ray emission data captured at the latest time is utilised, where the

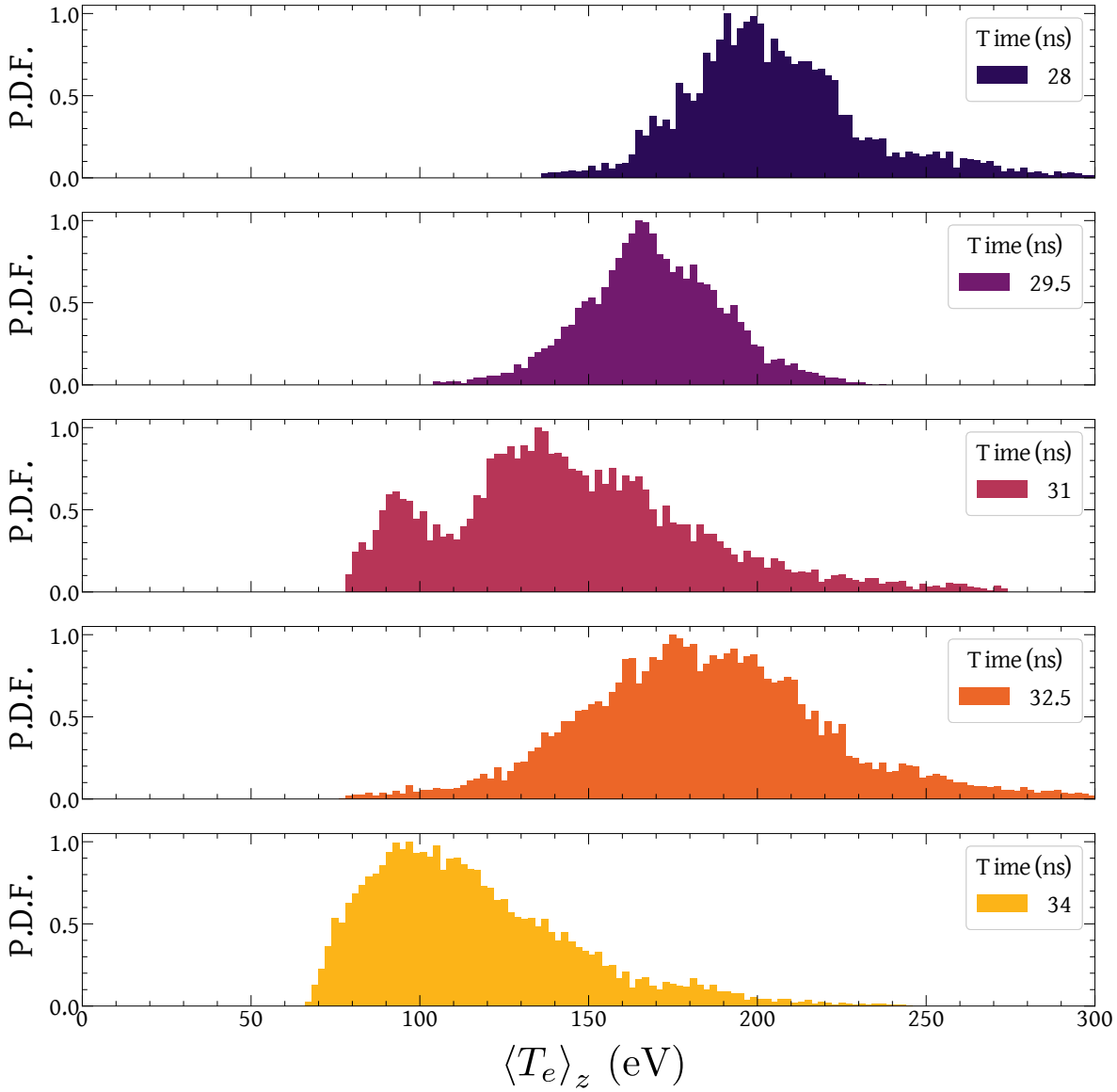

Figure 5.16: The normalised probability density functions of $\langle T_e \rangle_z$ from the 2-D maps shown in Figure 5.15. The low temperature region, below the secondary peak in the ratio curve, has been excluded.

plasma will be coolest and the ratio value at a maximum, as illustrated in Figure 5.13. By examining the various potential thicknesses, the most probable filter thickness is identified by aligning the peak value in the ratio curve with the corresponding peak value in the ratio map. The filter thicknesses are determined to be 0.85 μm and 2 μm of Mylar in the thin and thick filter packs, respectively, with a 0.21 μm vanadium coating.

The resulting 2-D line-of-sight-averaged density-weighted electron temperature profiles, $\langle T_e \rangle_z$, are shown in Figure 5.15. The average electron density assumed for each ratio map is listed above each figure. The corresponding temperature distributions are illustrated in Figure 5.16, where the lower temperature region, $T_e \lesssim 80\,\text{eV}$, has been excluded.

5.6 Plasma Heating from the Thomson Probe

In Figure 5.17, a comprehensive comparison of the plasma conditions as observed by the Thomson scattering probe and X-ray framing camera are illustrated for the shots listed in Table 5.2. These conditions are also compared to three-dimensional radiation-magnetohydrodynamic FLASH simulations [179, 168]. It should be noted that, in all the investigated shots, the XRFC observed the turbulent plasma prior to the Thomson probe.

Table 5.2: Experimental timings for the start of the X-ray framing camera, t_{xrfc}, and Thomson probe, t_{ots}. The duration, Δt_{ots}, and energy, E_{ots}, of the Thomson probe are also listed.

Shot	t_{xrfc} (ns)	t_{ots} (ns)	Δt_{ots} (ns)	E_{ots} (J)
104468	31.0	34.5	1	26.1
104469	29.5	33.0	1	33.4
104470	28.0	31.5	1	32.3
104471	32.5	36.0	1	31.7
104476	34.0	35.0	3.7	37.9

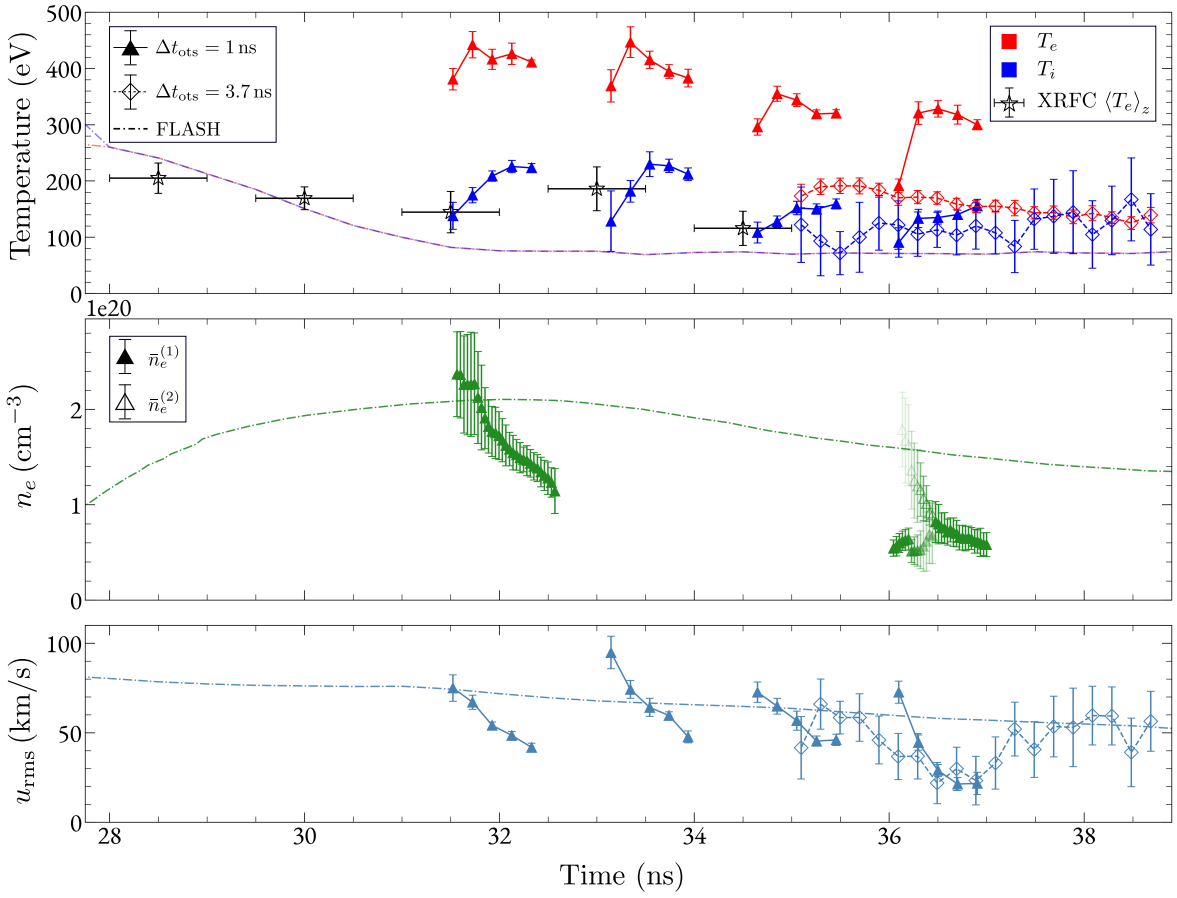

Figure 5.17: Converged plasma conditions from Thomson scattering analysis for the shots listed in Table 5.2 compared to the X-ray emission analysis and FLASH simulations. The temperature and velocity information is obtained from the IAW fitting and the density from the EPW. The quoted error on the mean electron density, $\bar{n}_e$, is $\Delta n_e + \sqrt{\sigma^2_{\bar{n}_e} + \sigma^2_{\Delta n_e}}$. In the later EPW shot, within the region where two weighted plasma regions are fitted, both conditions are shown with a visibility equal to their respective relative weighting.

The data presented reveals a significant disparity in temperature estimations, with the 4ω Thomson scattering probe indicating markedly higher temperatures compared to those observed by the XRFC or predicted by the FLASH simulations. This discrepancy provides compelling evidence of the perturbative heating effects of the Thomson probe.

To further investigate the heating effect of the Thomson probe, the OTS data collected on shot 104470, where $t_{\text{ots}} = 31.5\,\text{ns}$, is utilised. The internal thermal energy density of the plasma can be approximated as,

$$\epsilon_{\text{th}} = \epsilon_{\text{th}}^{e} + \epsilon_{\text{th}}^{i} \approx \frac{3 n_e k_B}{2} \left(T_e + \frac{T_i}{\langle Z \rangle} \right) , \tag{5.6.1}$$

where the average ionisation $\langle Z \rangle = n_e / n_i \approx 3.5$, and e and i denote the electrons and ions, respectively. At the onset of the Thomson probe, the temporal evolution of the electrons' internal thermal energy can be approximated as,

$$\frac{\partial}{\partial t} \epsilon_{\text{th}}^{e} \approx Q_{\text{heat}} \, , \tag{5.6.2}$$

where Q_{heat} is the heating of the electrons induced by the Thomson probe,

$$Q_{\text{heat}} = \kappa_a I_{\text{ots}} = \kappa_a \left(\frac{E_{\text{ots}}}{\Delta t_{\text{ots}} A_{\text{T}}} \right) . \tag{5.6.3}$$

Here, E_{ots} is the energy of the scattering probe over the Thomson area, $A_{\text{T}} \approx (50 \times 70)\,\mu\text{m}^2$. The absorption coefficient, κ_a, of the Thomson probe is well approximated by inverse Bremsstrahlung absorption in a fully ionised plasma,

$$\kappa_a = \frac{16\pi\sqrt{2\pi} e^6}{3c \left(4\pi\epsilon_0 \sqrt{m_e k_B} \right)^3} \frac{Z_{\text{eff}}\, n_e^2 \log\Lambda}{T_e^{3/2} \omega_i^2 \sqrt{1 - \omega_{pe}^2/\omega_i^2}} \, , \tag{5.6.4}$$

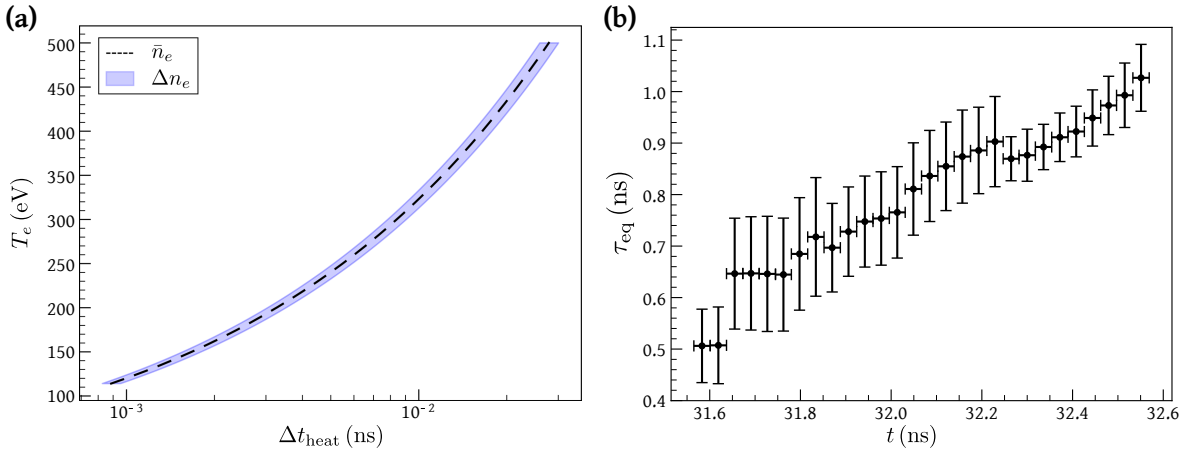

Figure 5.18: **(a)** Rate of electron heating by inverse Bremsstrahlung absorption, equation 5.6.6, as a function of electron temperature. The mean electron density is taken as $2.4 \times 10^{20}\,\text{cm}^{-3}$ with an error of $2 \times 10^{19}\,\text{cm}^{-3}$. **(b)** Evolution of the carbon ion temperature equilibration time with the electrons, as given by equation 5.6.7, over the duration of the Thomson probe.

where the Coulomb logarithm is given by [165],

$$\log\Lambda = 23.5 - \log\frac{\sqrt{n_e\left[\text{cm}^{-3}\right]}}{\left(T_e\,[\text{eV}]\right)^{5/4}} - \sqrt{10^{-5} + \frac{\left(\log T_e\,[\text{eV}] - 2\right)^2}{16}}\,. \tag{5.6.5}$$

The proportional relationship of the absorption coefficient to $T_e^{-3/2}$ implies that lower energy electrons are preferentially heated, contributing to the process of bringing the turbulent plasma closer to thermodynamic equilibrium.

By rearranging equation 5.6.2, the internal electron energy at early times can be approximated as,

$$\epsilon^e_{\text{th}}(t) \approx \epsilon^e_{\text{th}}(t = t_{\text{ots}}) + Q_{\text{heat}}\Delta t_{\text{heat}}\,. \tag{5.6.6}$$

This form of the equation provides insight into the rate of Bremsstrahlung heating of the electrons at the onset of the Thomson probe, $\Delta t_{\text{heat}} \gtrsim \epsilon^e_{\text{th}}(t = t_{\text{ots}})/Q_{\text{heat}}$. Prior to the Thomson probe, the electrons and ions can be assumed to be in equilibrium. The electron temperature at $t = t_{\text{ots}}$ can therefore be approximated by the initial temperature observed for the ions, which closely aligns with the $\langle T_e \rangle_z$ distributions

derived from the XRFC analysis.

The dependency of Δt_{heat} on electron temperature is illustrated in Figure 5.18(a), showing that at the initiation of the Thomson probe, the rate of Bremsstrahlung heating is $\Delta t_{\text{heat}} \gtrsim 1\,\text{ps}$. This rapid electron heating explains why the initial T_e inferred by the OTS analysis is significantly higher than its unperturbed value, given the inherent temporal resolution of the IAW is 200 ps. Conversely, the ions will equilibrate with the electrons on a timescale given by their rate of collisions,

$$\tau_{\text{eq}} = \frac{(4\pi\epsilon_0)^2\, 3 m_e m_i}{8\sqrt{2\pi} e^4 Z_i^2 n_e \log\Lambda} \left(\frac{k_B T_e}{m_e} + \frac{k_B T_i}{m_i} \right)^{3/2} . \tag{5.6.7}$$

Given the significantly smaller mass of hydrogen (m_i^H) to carbon (m_i^C) ions, this equilibration time is primarily governed by the behaviour of the carbon atoms. The temporal evolution of τ_{eq} throughout the Thomson probe is illustrated in Figure 5.18(b), indicating an equilibration of $\sim 0.5\,\text{ns}$ at early times. Consequently, the heating of the ions progresses at a substantially slower pace compared to the electrons, allowing for its discernment over the duration of the Thomson probe.

By the second time step resolved by the ion-acoustic wave data ($\Delta t \sim 400\,\text{ps}$), the electron temperature has peaked whilst the electron density has remained relatively constant. This constancy in density indicates that, at this stage, cooling effects resulting from the expansion of the heated volume can be disregarded. Consequently, the temporal evolution of the internal energy, as described by equation 5.6.2, can now be expressed as,

$$\frac{\partial}{\partial t} \epsilon_{\text{th}}^e \approx Q_{\text{heat}} + Q_{\text{rad}} - Q_{\text{ei}} - Q_{\text{e}} \,. \tag{5.6.8}$$

The second term on the right-hand side of equation 5.6.8 accounts for X-ray emission, primarily dominated by free-free Bremsstrahlung radiation,

$$Q_{\text{rad}} = \frac{16\sqrt{2\pi k_B} e^6}{3\hbar \left(4\pi\epsilon_0 c \sqrt{m_e}\right)^3} Z_{\text{eff}} \sqrt{T_e}\, n_e^2 g_{ff} \,, \tag{5.6.9}$$

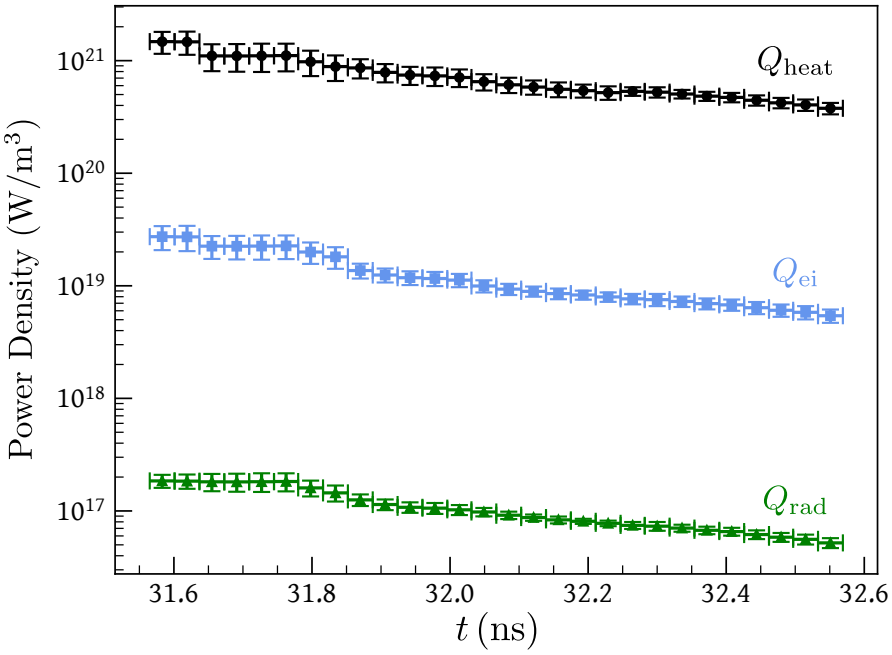

Figure 5.19: Relative strength of the heating (black), electron-ion equilibration (blue) and Bremsstrahlung radiation (green) contributions to equation 5.6.8.

where the velocity-averaged Gaunt factor $g_{ff} \approx 1.2$. The third term, Q_{ei}, denotes the electron-ion balance, representing the energy exchange between electrons and ions through collision processes,

$$Q_{\text{ei}} = \frac{3 n_e k_B}{2\tau_{\text{eq}}} \left(T_e - T_i\right) . \tag{5.6.10}$$

The relative contribution of each term to the change in the electrons' internal thermal energy is shown in Figure 5.19. This illustrates that both the Bremsstrahlung radiation and electron-ion balance terms are comparatively small compared to the heating induced by the Thomson probe.

The final term in equation 5.6.8 is a result of the heat flux, $\mathbf{q_e}$, within the Thomson scattering volume,

$$Q_{\text{e}} = -\nabla \cdot \mathbf{q_e} = -\nabla \cdot \left(-\kappa_c \nabla T_e\right) . \tag{5.6.11}$$

Assuming Spitzer thermal conductivity [180], the coefficient of heat conduction is ap-

proximated by,

$$\kappa_c \approx \frac{3}{2} n_e k_B \chi_s \,, \tag{5.6.12}$$

where the thermal diffusivity is [30],

$$\chi_s = 2.1 \times 10^{13} \frac{T_e^{5/2}}{Z_{\rm eff} n_e \log \Lambda} \,. \tag{5.6.13}$$

The timescale over which the heat front generated by the Thomson probe propagates can be estimated as, $\tau_\chi \sim A_T/\chi_s \approx 20\,\text{ps}$. This timescale is compared to the dynamical timescale, $\tau_{\rm D}$, during which the plasma expands due the presence of a pressure gradient. Assuming the heat front travels at the sound speed of the plasma, given by,

$$c_s = \sqrt{\frac{k_B \left(\langle Z \rangle T_e + 5T_i/3 \right)}{\langle m_i \rangle}} \,, \tag{5.6.14}$$

the expansion timescale can be approximated as $\tau_{\rm D} \sim 2r_{\rm T}/c_s \approx 300\,\text{ps}$. This order of magnitude difference in timescales justifies neglecting expansion cooling effects during the initial half of the Thomson probe.

Assuming cylindrical symmetry equation 5.6.11 can be expressed as,

$$Q_{\rm e} \approx \frac{\mathcal{C}}{r} \frac{\partial}{\partial r} \left(r T_e^{5/2} \frac{\partial T_e}{\partial r} \right) \,, \tag{5.6.15}$$

where the constant $\mathcal{C} = \kappa_c / T_e^{5/2}$. To estimate the magnitude of the temperature gradient, ΔT_e, over the Thomson heating region $\Delta r = r_{\rm T} \approx 25\,\mu\text{m}$, equation 5.6.15 is simplified to,

$$Q_{\rm e} \approx \frac{\mathcal{C}}{\Delta r^2} \left(T_e^{5/2} \Delta T_e \right) \Big|_{r=r_{\rm T}} \,. \tag{5.6.16}$$

Here, the temperature at the Thomson volume boundary is approximated as,

$$T_e\left(r = r_{\mathrm{T}}\right) \approx \frac{T_e\left(r = 0\right) + T_i\left(r = 0\right)}{2}\,. \tag{5.6.17}$$

The second time step in the IAW data marks a transition point. The electrons have reached their peak temperature due to the heating from the Thomson probe, while the cooling expansion phase has yet to fully commence. At this juncture, the plasma heating has therefore reached an equilibrium with conduction. Assuming a momentary negligible change in the internal electron thermal energy, $\partial\epsilon^e_{\mathrm{th}}/\partial t \sim 0$, substituting equation 5.6.16 into equation 5.6.8 provides an estimate on the temperature gradient induced by the Thomson heating. The temperature gradient over the Thomson beam is $\Delta T_e \sim -200\,\mathrm{eV}$.

Beyond this stage, the adiabatic expansion of the heated Thomson volume must be considered alongside the spatial evolution of the internal electron thermal energy. Equation 5.6.8 is therefore extended to,

$$\frac{\partial}{\partial t}\epsilon^e_{\mathrm{th}} + \mathbf{u_e}\nabla\cdot\epsilon^e_{\mathrm{th}} \approx Q_{\mathrm{heat}} + Q_{\mathrm{rad}} - Q_{\mathrm{ei}} - Q_{\mathrm{e}} - \frac{5}{2}p_e\nabla\cdot\mathbf{u_e}\,, \tag{5.6.18}$$

where $p_e = 2\epsilon^e_{\mathrm{th}}/3$ is the electron pressure, and $\mathbf{u_e}$ is the fluid velocity. Notably, the spatial information on the internal thermal energy, which will have both density and temperature dependants, was not obtained with the data presented here. Therefore, forthcoming experiments are planned to acquire spatially-resolved Thomson scattering data with a short pulse length, $\Delta t_{\mathrm{ots}} \approx 100\,\mathrm{ps}$, to reduce the temporal integration.

The heating effect induced by the Thomson probe is also evident in the proton radiography data illustrated in Figure 5.20. Without the Thomson probe, by $t \approx 31\,\mathrm{ns}$ the plasma has cooled, causing a significant drop in the magnetic Reynolds number, Rm. The relatively homogeneous proton flux data shown in Figure 5.20(b) indicates a decay in the magnetic fields, suggesting that Rm has fallen below the critical Reynolds

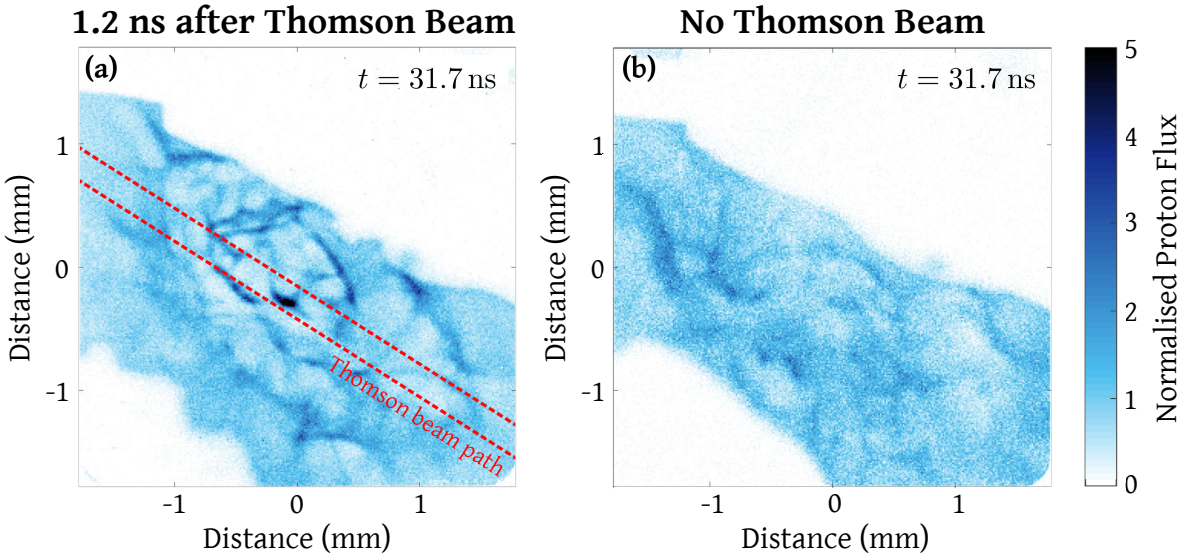

Figure 5.20: Raw 15 MeV proton flux images taken at $t = 31.7$ ns. Larger amplitude proton flux inhomogeneities are observed in the data taken 1.2 ns after the end of the Thomson probe, **(a)**, as opposed to the same time with no Thomson probe, **(b)**. The path of the Thomson beam is indicated in (a) with red-dashed lines.

number, $\mathrm{Rm_c}$, rendering the turbulent dynamo inactive. Conversely, with the influx of the Thomson beam prior to the proton radiography, Figure 5.20(a) exhibits greater fluctuations in the proton flux. This observation implies that the Thomson heating has elevated the magnetic Reynolds number to $\mathrm{Rm} > \mathrm{Rm_c}$, thereby enabling the turbulent dynamo to operate once again.

5.7 Turbulent plasma generated at the NIF

To further investigate the properties of turbulent plasmas, a platform able to generate stronger magnetic fields is required. This is performed by replicating the platform shown in Figure 5.1 on the National Ignition Facility at Lawrence Livermore National Laboratory. The NIF experimental platform, identical to that detailed in Ref. [169], used two doped, 100 μm thick, polystyrene foils (48.3% C, 49.6% H, 1.2% O, 0.6% N, 0.1% Mn, 0.1% Co). Each foil was ablated using 48 frequency-tripled ($\lambda = 351\,\mu$m) laser beams with a 1 mm spot diameter. The total laser illuminated onto each disk was

$\sim 125\,\mathrm{kJ}$ over a 15 ns square pulse length. The polyimide grids which generated the asymmetry between the counter-propagating plasma jets had 300 μm holes and 300 μm thick wires.

The turbulent plasma was observed by a gated X-ray detector (GXD), oriented perpendicular to the propagating jets. This detector comprised of an X-ray framing camera, differential filtering and a pinhole array. The X-ray framing camera employed 4-strips, each with a time gating of 100 ps, and implemented differential filtering to capture the X-ray emission profile at two distinct times. The pinhole array consisted of four 25 μm diameter pinholes, staggered to prevent image overlap onto the four camera strips. The array was positioned to enable a $2\times$ magnification of the interaction plasma. A 1 μm thick copper filter covered half of the camera and two staggered pinholes, while a 2 μm thick vanadium filter covered the remaining pinholes.

Previous experiments using the NIF's dynamo platform demonstrated a strong suppression of heat conduction within a turbulent plasma where $\mathrm{Rm} \approx 3500$ [169]. This suppression was attributed to the existence of substantial temperature fluctuations, occurring on a scale of $\sim 50\,\mu$m, as observed in the line-of-sight-averaged density-weighted electron temperature distribution captured by the GXD. However, for a comprehensive understanding of the thermal conduction suppression, direct measurements of the local temperature fluctuations are required. This is achieved through the measurement of time-resolved ion-acoustic and electron plasma wave scattering, using an optical Thomson scattering 3ω ($\lambda_i = 351\,\mathrm{nm}$) probe.

5.7.1 Optical Thomson scattering

The OTS probe consisted of a beam quad which was positioned equidistant from each grid and situated 500 μm away from the centre of the plasma interaction region. Each beam had a 150 μm diameter focus and delivered $\sim 30\,\mathrm{J/ns}$ over a 15 ns square pulse length. The total area of plasma illuminated by the OTS quad was therefore $\sim 300\times$

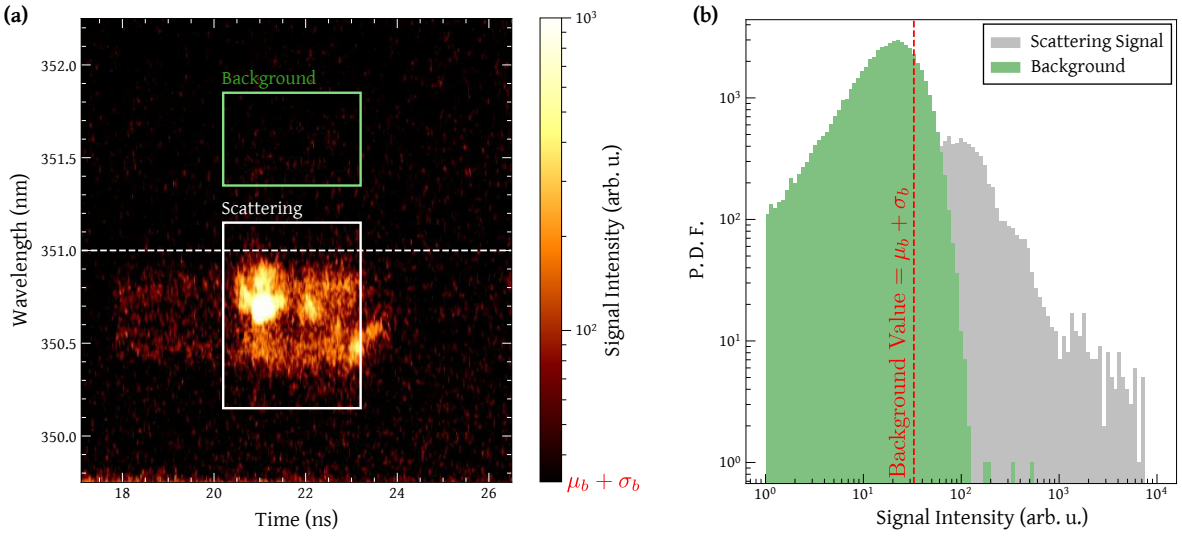

Figure 5.21: **(a)** Spectrally and temporally-resolved ion-acoustic wave scattering feature observed for the NIF turbulent plasma. The scattering signal is indicated within the white box and a mean background value, $\mathcal{B} = \mu_b + \sigma_b$, is extracted from within the green box. **(b)** Probability distribution functions of the signal intensity within the scattering signal box, shown in grey, and the background box, shown in green. The background value, indicated with a dashed red line, is taken as the mean plus one standard deviation of the background distribution.

$300\,\mu\text{m}^2$. The Thomson scattering was collected at $2\theta = 44.3°$, with an angular spread of $\Delta(2\theta) \approx 10°$. The OTS probe was timed to start at $t_{\text{ots}} = 18\,\text{ns}$ after the drive lasers, 2 ns prior to the expected collision of the jets and subsequent formation of the turbulent region.

The ion-acoustic wave scattering observed over the 15 ns probe is illustrated in Figure 5.21, with the scattering region highlighted by a white box. Despite the OTS probe remaining on beyond the point where the scattering signal disappears ($t \gtrsim 23\,\text{ns}$), the presence of increasing density fluctuations within the plasma refract the Thomson probe away from the scattering volume, ultimately leading to its disappearance from the diagnostic observation. The observed IAW signal, depicted in Figure 5.21(a) with a logarithmic scale, is predominately weak except for a few discernible bright hot spots. Given this characteristic, employing a background removal process similar to the one performed on the OMEGA platform in section 5.4.1 is not suitable here. Instead, a

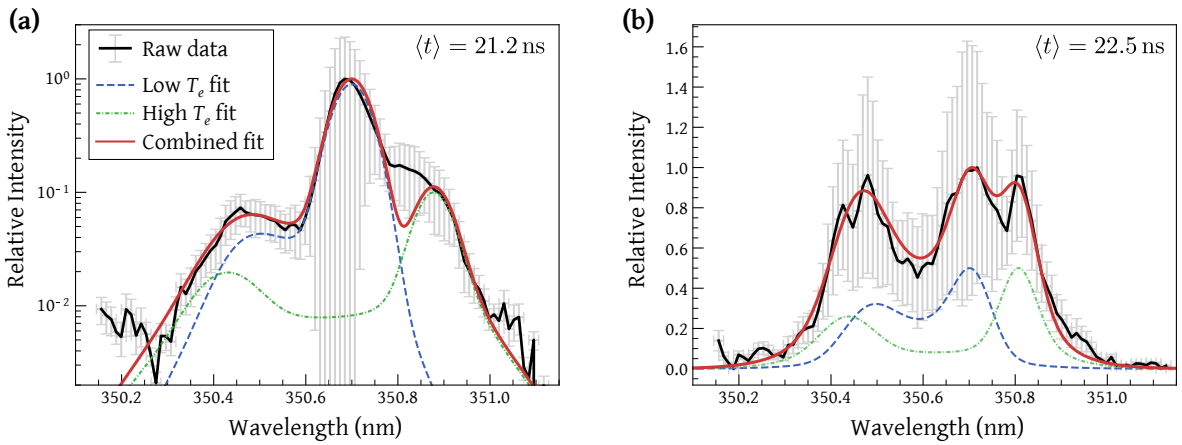

Figure 5.22: The early, **(a)**, and late, **(b)**, temporally-integrated IAW scattering features for the data shown in Figure 5.21. Each time step is fit assuming two plasma conditions, one with a high (green dash-dotted line) and the other a low (blue dashed line) electron temperature. The fitted conditions are listed in Table 5.3. These two IAW features are combined to produce the red line fit which is compared to the raw data in black.

mean background value, determined away from the IAW feature as illustrated in Figure 5.21(b), is subtracted from the entire scattering feature.

As a result of the low signal, a large temporal integration is required to improve the signal-to-noise. The IAW feature is therefore separated into two time steps, each with a temporal integration of $\Delta t \approx 1.2$ ns. The signal at each time is shown in Figure 5.22. Despite the inherent error in each signal, valuable insights into the temperature fluctuations within the scattering volume can still be obtained. Utilising MCMC analysis in this scenario is not suitable, mainly owing to the sub-optimal signal level but also due to the diverse range of plasma conditions contributing to the overall signal. In contrast to the OMEGA turbulent plasma, the NIF IAW structure factor can not be well described by the straightforward addition of velocity or temperature gradients. This complexity arises from the uncertainty regarding whether the temperature distribution adheres to a normal, isotropic distribution.

Instead of employing MCMC analysis and parameter gradients, the IAW analysis focuses on the objective of demonstrating the presence of a substantial temperature

variation within the Thomson scattering region. Consequently, an effective approach involves fitting a weighted combination of two distinct plasma conditions: one with the electron temperature set to its lowest feasible value and another where it is set to its highest. The IAW scattering features produced by these two conditions at each time step are illustrated in Figure 5.22 and their corresponding parameters listed in Table 5.3.

This analysis of the IAW feature effectively demonstrates that a broad range of electron temperatures are present within the Thomson scattering volume. During the early time period, the mean electron temperature is $\bar{T}_e = 790\,\text{eV}$ with a distribution of $\Delta T_e = 1020\,\text{eV}$. In contrast, during the later stage, the mean electron temperature decreases to $\bar{T}_e = 575\,\text{eV}$ with a distribution of $\Delta T_e = 610\,\text{eV}$. These mean electron temperatures are subsequently used in the electron plasma wave analysis.

The corresponding EPW signal is illustrated in Figure 5.23. Although the background could be removed from the EPW signal by fitting a broadband blackbody emission at each time, it is apparent in Figure 5.23(a) that the signal sensitivity across wavelength is not normalised, resulting in a streaked appearance. To address this issue, an alternative approach is employed whereby a background signal over time is determined by averaging across a low-wavelength scattering region, beyond the observed EPW scattering feature. This λ-averaged background signal is then scaled to

Table 5.3: Fitted parameters of the high and low T_e conditions for the early and late time ion-acoustic wave scattering features as shown in Figure 5.22.

Parameter	$\langle \mathbf{t} \rangle = \mathbf{21.2\,ns}$		$\langle \mathbf{t} \rangle = \mathbf{22.5\,ns}$	
	Low $\mathbf{T_e}$	**High $\mathbf{T_e}$**	**Low $\mathbf{T_e}$**	**High $\mathbf{T_e}$**
T_e (eV)	280	1300	270	880
T_i (eV)	200	600	330	390
$\bar{v}_b$ (km/s)	460	430	470	400
Ratio	0.1	0.9	0.5	0.5
n_e (cm^{-3})	2×10^{20}		2×10^{20}	

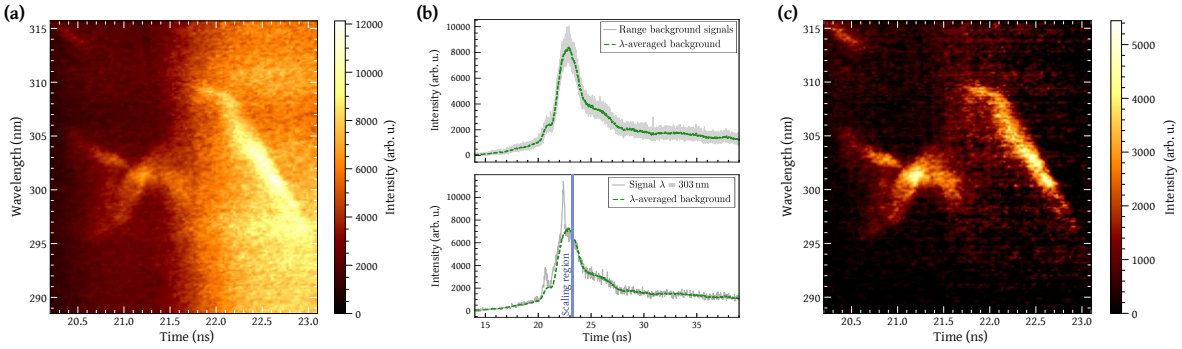

Figure 5.23: **(a)** The corresponding electron plasma wave scattering feature observed for the same shot as shown in Figure 5.21. **(b)** The upper panel depicts the temporal uniform background signal (represented by the dashed green line), derived through the averaging of background signals at low-λ. The lower panel shows the process of scaling this λ-averaged background signal, using the highlighted blue region, to the scattering signal at a specific wavelength. **(c)** The final EPW scattering signal is found by performing the background removal process demonstrated in (b) across all wavelengths.

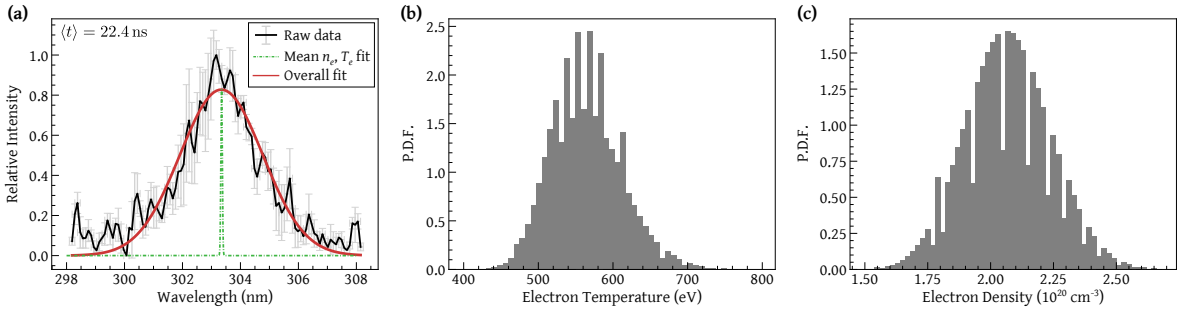

Figure 5.24: **(a)** The temporally-integrated EPW scattering feature at one time step for the data shown in Figure 5.21. The EPW feature resulting from the mean $\bar{T}_e$, $\bar{n}_e$ conditions is illustrated as a dash-dotted green line. By fitting a Gaussian, shown as a red line, to the raw data the distribution of contributing electron temperatures, **(b)**, and densities, **(c)**, can be found by assuming the pressure, $\bar{P} \propto \bar{T}_e \bar{n}_e$, remains constant.

the scattering at each wavelength, as illustrated in Figure 5.23(b), and subtracted. The resulting EPW signal is shown in Figure 5.23(c).

The electron plasma wave scattering feature exhibited good signal-to-noise, facilitating the application of the temporal integration, set by the streak camera, of $\Delta t = 0.1$ ns. An example of the inferred EPW signal at one time step is shown in Figure 5.24(a). Despite the range of plasma conditions produced, it is evident that the EPW structure derived from a single set of conditions falls short of capturing the observed signal's breadth. In the same figure, a green dash-dotted line is shown as an example of the

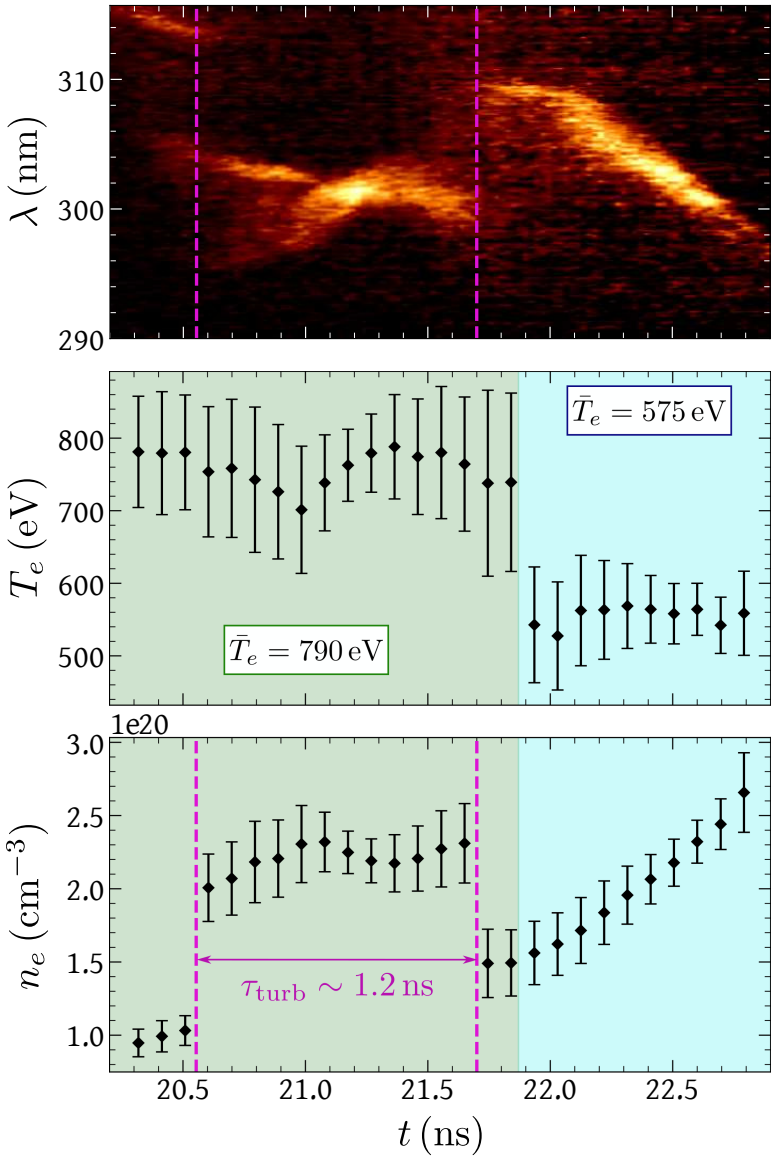

Figure 5.25: Distribution of electron temperatures and electron densities, inferred from the EPW data. The region utilising the early time IAW fit is highlighted in green, and the late time in blue. The turbulent structure time scale, τ_{turb}, indicated in pink, is measured as the persistence of one of the density structures.

scattering signal produced by a single set of plasma conditions. For simplicity, the signal $I_{\mathrm{epw}}(n_e, T_e)$ can effectively be treated as a delta function at $\lambda_{\mathrm{epw}}(n_e, T_e)$ (see equation 2.3.2).

To determine the range of conditions required within the scattering volume to generate the observed EPW signal at each time step, the mean electron temperature infor-

mation obtained from the IAW analysis, $\bar{T}_e$, is utilised. Assuming that the condition $\bar{T}_e$ represents the bulk average temperature and is the primary contributor to the EPW signal, the corresponding electron density, $\bar{n}_e$, required to produce the scattering signal at the peak intensity wavelength can be determined. Subsequently, as the turbulent plasma can assumed to be isobaric, a mean pressure is determined as $\bar{P} \approx k_B \bar{T}_e \bar{n}_e$. The assumption of an isobaric plasma is supported by the X-ray emission data. The presence of a broad distribution of temperature fluctuations on the scale lengths of $\sim 100\,\mu$m would not be evident if the plasma were not isobaric.

To mitigate the impact of random noisy fluctuations in the signal influencing the inferred parameter distributions, a Gaussian is initially fit to the raw data. Finally, the distribution of electron temperatures and densities required to produce the Gaussian fit of the EPW signal can be found by ensuring the pressure remains constant. Figures 5.24(b) and (c) show examples of the resulting distributions at one time step. Extending this analysis across the entirety of the observed EPW scattering produces the temperature and density distributions shown in Figure 5.25.

A prominent feature observable in both the raw EPW data and the inferred electron density distributions is a distinct 'jump'-like behaviour. This rapid change in density can be associated with the time for turbulent structures to persist. Given the measured time scale for a turbulent structure, $\tau_{\text{turb}} \approx 1.2\,$ns, and considering the Thomson scale $L_{\text{T}} \approx 300\,\mu$m, an approximate value for the turbulent velocity within the Thomson volume can be determined as $u_{\text{rms}} \sim L_{\text{T}}/\tau_{\text{turb}} \approx 250\,$km/s. This is notably higher than that observed in the OMEGA turbulent plasma where $u_{\text{rms}} \sim 70\,$km/s, as illustrated in Figure 5.17.

5.7.2 Gated X-ray detector

The GXD analysis for the NIF turbulent plasma follows a procedure similar to the one outlined in Section 5.5. The X-ray detector, depicted in Figure 5.26(a), captured the

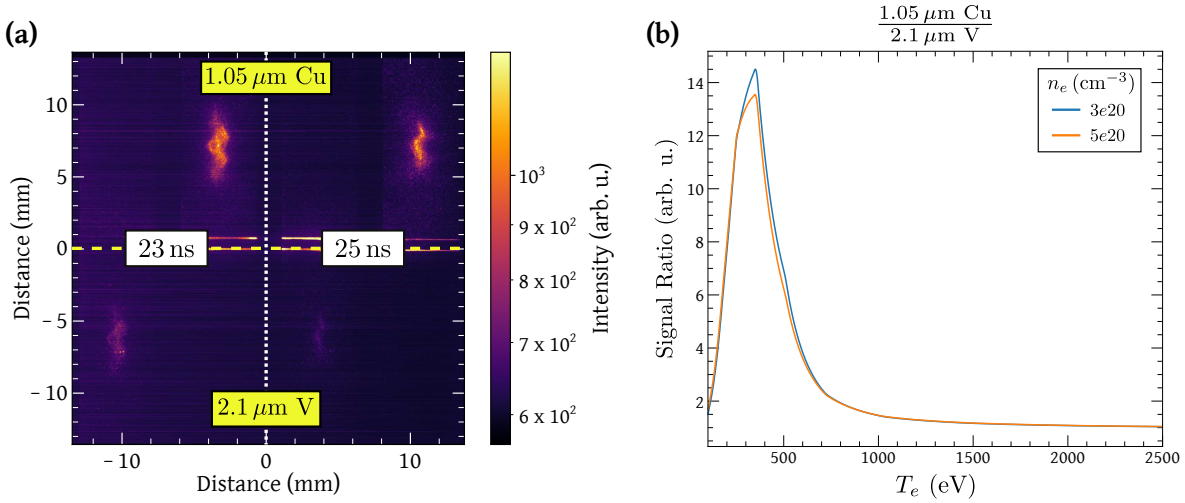

Figure 5.26: **(a)** Raw gated X-ray detector from the NIF platform. The two X-ray framing camera strips on the left on the image were taken at 23 ns, whilst the other two were taken at 25 ns. The top half of the framing camera was covered with 1.05 μm copper and the bottom half with 2.1 μm vanadium. **(b)** X-ray ratio curves, as defined by equation 5.5.5, for a 1.05 μm copper and 2.1 μm vanadium filter pack. The relatively small effect of the chosen electron density on the resultant ratio curve is shown for two different densities.

plasma's X-ray emission at 23 ns and 25 ns. At these later times, however, the electron plasma wave scattering is no longer observable within the Thomson scattering volume due to the increased density gradients. It is therefore not possible to directly infer the mean electron density in the plasma at these times.

Nevertheless, at 23 ns, the EPW analysis indicates a gradual increase in electron density towards 3×10^{20} cm^{-3}. Figure 5.26(b) shows ratio curves for the 1.05 μm copper and 2.1 μm vanadium filter pack corresponding to two predicted densities. Remarkably, these ratio curves exhibit minimal sensitivity to density variations. Given its proximity to the EPW data, subsequent analysis primarily concentrates on the 23 ns time step.

Unlike the X-ray framing camera analysis performed on the OMEGA platform, the NIF gated X-ray detector requires a more careful background removal process. This requirement arises due to the presence of streaking, hot-spots, and a distinct background signal associated with each filter at both time steps. The method for isolating the plasma interaction region using the copper and vanadium filters at 23 ns is detailed in

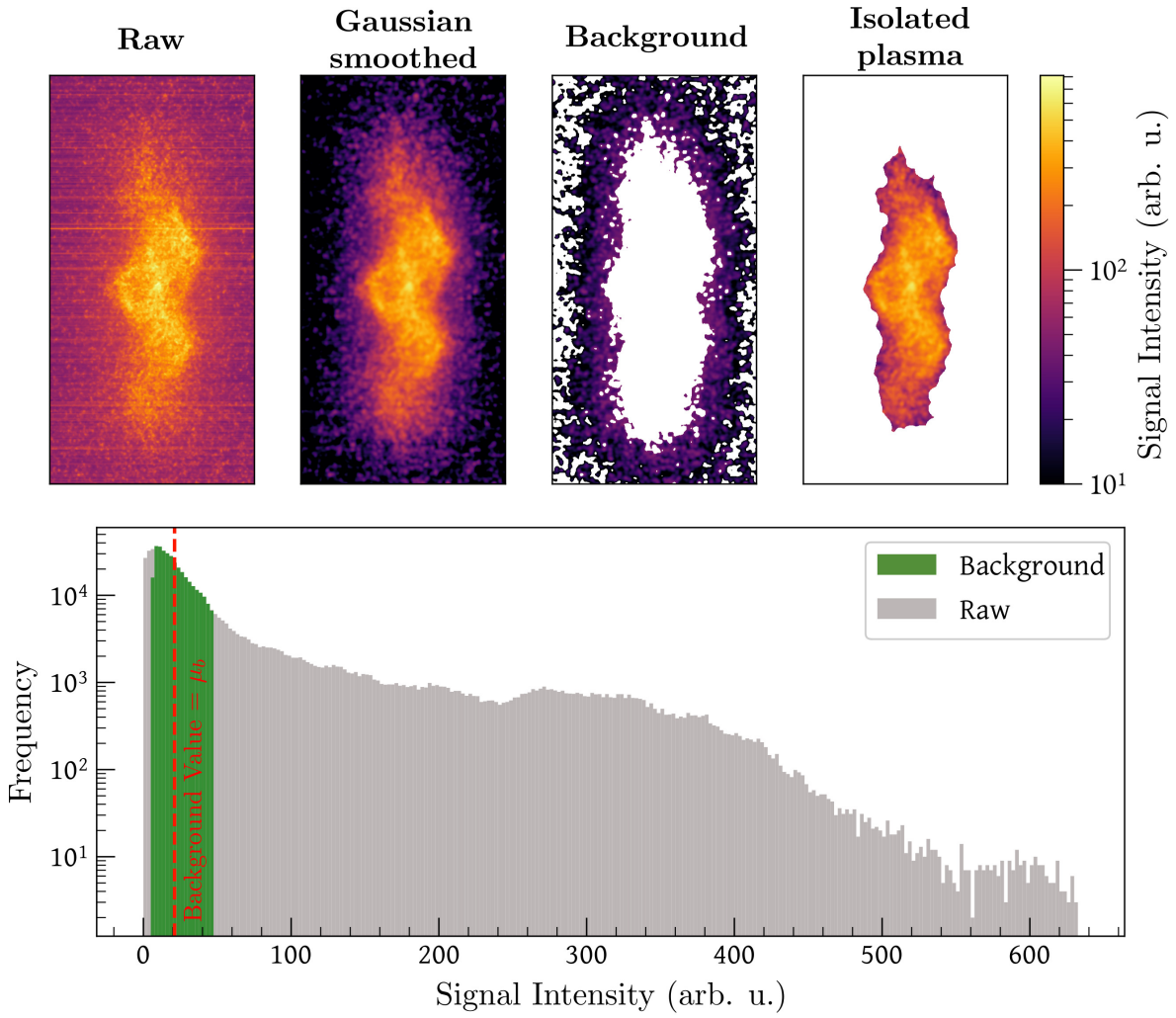

Figure 5.27: Background removal process for isolating the X-ray emission observed by the 1.05 μm copper filter at 23 ns. The raw image is transformed into the second panel by having a 2-D Gaussian smoothing function with a FWHM of 50 μm applied and a horizontal kernel to remove the streaked background. In the third panel the background emission around the plasma interaction region is isolated as the lower 10% of the observed signal. As shown as a red vertical line in the lower panel, a mean background value, μ_b, is then subtracted from the Gaussian smoothed image. In the fourth panel the plasma interaction region is isolated using a 2-D Gaussian window function.

Figures 5.27 and 5.28, respectively. Subsequently, these two images are overlaid using the cross-correlation function defined by equation 5.5.4.

The resulting ratio map is shown in Figure 5.29(b). To infer the line-averaged mass-weighted electron temperature map, the ratio curve corresponding to a mean electron

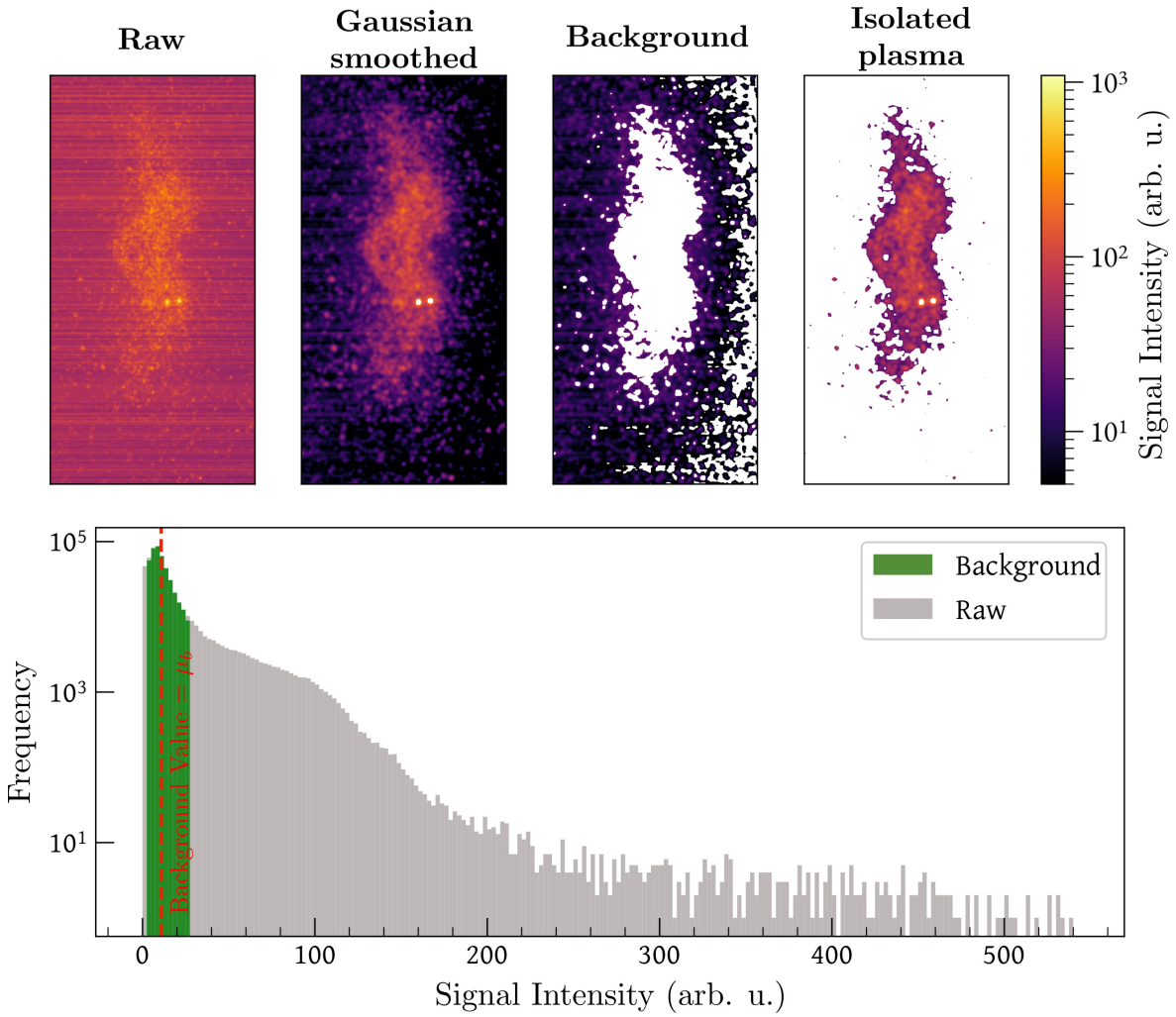

Figure 5.28: Utilising the background removal process outlined in Figure 5.27, the X-ray emission observed by the 2.1 μm vanadium filter at 23 ns is isolated. Additionally, the raw image undergoes outlier removal to eliminate the two hot-spots situated at the centre of the interaction region, which would effect the subsequent analysis.

density of $3 \times 10^{20}\,\mathrm{cm}^{-3}$ is utilised. The resulting temperature distribution is shown in Figure 5.30(a) and compared to data reported in Ref. [169] and distributions derived from conduction-on and conduction-off FLASH simulations. Despite employing the same experimental platform, the inferred distributions exhibit substantial disparities. This discrepancy is attributed to the chosen X-ray framing camera filter pack. As shown in Figure 5.30(b), the polyimide-vanadium filter pack utilised in Ref. [169] has a much gentler gradient, thereby increasing its sensitivity to higher plasma temperatures. In contrast, the copper-vanadium filter pack employed in this data exhibits limited

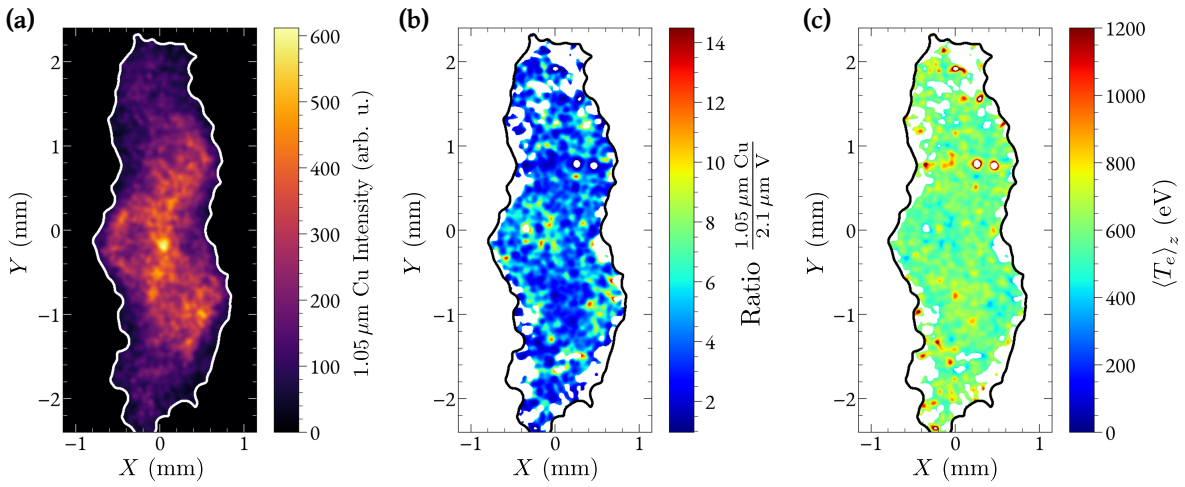

Figure 5.29: **(a)** X-ray emission image observed by the gated X-ray detector using a 1.05 μm copper filtering at $t = 23$ ns. The isolated plasma region is highlighted within the white boundary. **(b)** The ratio of the X-ray emission for the 1.05 μm copper and 2.1 μm vanadium filter pack. **(c)** Two-dimensional map of the electron temperature averaged over the line of sight, $\langle T_e \rangle_z$. This is produced using the ratio curve as shown in Figure 5.26(b) with $\bar{n}_e = 3 \times 10^{20}\,\mathrm{cm}^{-3}$.

sensitivity to plasma conditions surpassing 1000 eV.

Furthermore, both temperature distributions closely resemble their corresponding synthetic $\langle T_e \rangle_z$ distributions derived from the FLASH simulation with the conduction turned off. This highlights that the X-ray emission analysis serves merely as a metric for inferring the temperature distributions and does not yield absolute values. Hence, it is critical to utilise diagnostics such as Thomson scattering to obtain direct temperature measurements. The electron temperature range inferred from the late-time ion-acoustic wave data is indicated as a grey bar in Figure 5.30(a). While this range appears to encompass the temperatures observed by the copper-vanadium filter pack, it is important to note that the Thomson probe only observes a limited region of the plasma. Consequently, there may be higher temperature regions not captured by the Thomson scattering. Additionally, the low-temperature range observed in the OTS data cannot be inferred from the gated X-ray detector data, as both ratio curves exclude the $T_e \lesssim 400$ eV range. Nevertheless, the agreement between the FLASH conduction-off and experimental temperature distributions derived utilising each filter pack are indicative

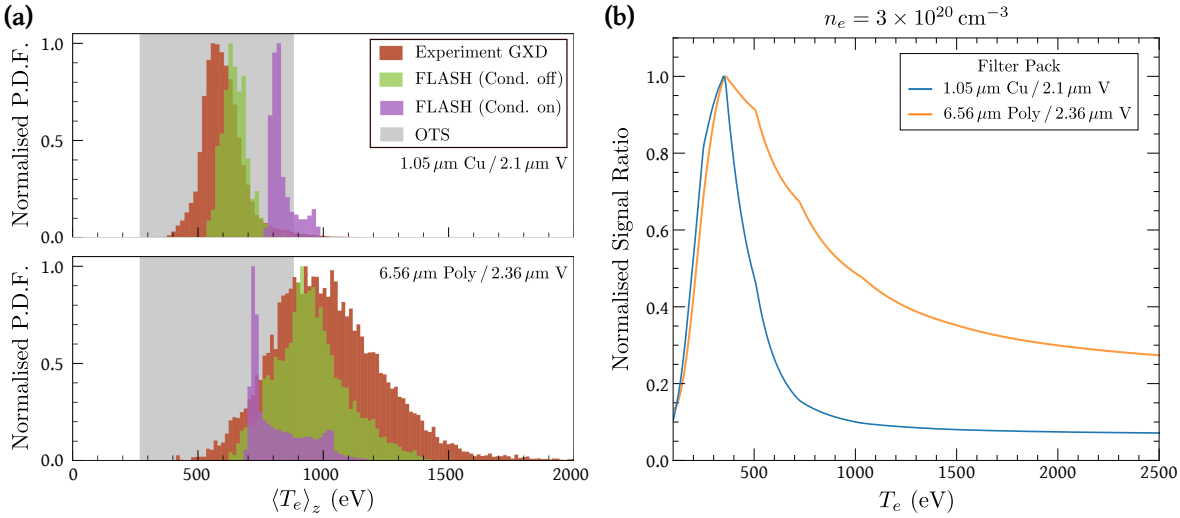

Figure 5.30: **(a)** The normalised probability density functions of $\langle T_e \rangle_z$ from the 2-D maps produced utilising the copper-vanadium (Figure 5.29(c)) and polyimide-vanadium (Ref. [169]) filter packs, shown in the upper and lower panels, respectively. Both are compared with analogous distributions derived from the conduction-on (green histograms) and conduction-off (purple histograms) FLASH simulations. The FLASH simulations are post-processed to infer synthetic $\langle T_e \rangle_z$ maps for each filer pack. The region highlighted in grey corresponds to the T_e range inferred by the late-time ion-acoustic wave scattering. **(b)** Normalised ratio curves of the X-ray emission, with $\bar{n}_e = 3{\times}10^{20}\,\mathrm{cm}^{-3}$, for the copper-vanadium filter pack utilised here, and the polyimide-vanadium filter pack from Ref. [169].

of the NIF platform being in a regime where thermal conduction is suppressed.

5.7.3 OMEGA vs NIF

The turbulent plasma conditions, as inferred through the optical Thomson scattering analysis, for both the OMEGA and NIF platforms are summarised in Table 5.4. These values are representative and focus on the early time Thomson probing, where the unperturbed electron temperature is assumed to be equivalent to the early time ion temperature.

As previously discussed, the Thomson probe induced perturbative heating on the OMEGA platform. However, this same level of perturbation was not evident on the NIF platform. Instead, analysis from the NIF ion-acoustic wave scattering indicated a cooling trend of the plasma over the observed timescale of scattering. This disparity in

heating effects on the two platforms can be attributed to two factors. Firstly, the reduced intensity of the NIF Thomson probe, I_{ots}, and secondly, the NIF plasma's higher electron temperature, which effectively reduces the inverse Bremsstrahlung absorption coefficient, κ_a.

The persistence of the temperature and density fluctuations within the Thomson scattering volume on the NIF platform, indicates a regime where thermal conduction has been suppressed. This suppression can be assessed by initially calculating the Spitzer thermal diffusivity, as defined in equation 5.6.13. In the absence of conduction suppression, any temperature gradients within the Thomson volume (ignoring Thomson heating effects) would be expected to dissipate over a timescale $\tau_\chi \sim A_{\text{T}}/\chi_s$. As

Table 5.4: Experimental parameters for the OMEGA and NIF turbulent plasma platforms as derived through this chapter. It should be noted that the OMEGA Thomson probe focused on the centre of the interaction region, whilst the NIF probe was focused 500 μm from the centre. The average timing of this data is $\langle t \rangle = 31.5$ ns and $\langle t \rangle = 21.2$ ns for the OMEGA and NIF platforms, respectively.

Parameter	**OMEGA**	**NIF**
Thomson parameters		
λ_{ots} (nm)	263.25	351
L_{T} (μm)	50	300
I_{ots} (W/cm^2)	9×10^{14}	1×10^{14}
Plasma parameters		
T_e (eV)	150	790
n_e (cm^{-3})	2×10^{20}	2×10^{20}
Z_{eff}	5.3	5.7
u_{rms} (km/s)	70	250
Inferred parameters		
κ_a (cm^{-1})	3.9	0.8
χ_s (cm^2/s)	0.1×10^6	6.5×10^6
τ_χ (ns)	0.2	0.1
Péclet	0.2	0.1
Magnetic Prandtl	0.02	6.8

indicated in Table 5.4, this timescale is expected to be $100 - 200\,\mathrm{ps}$ for the NIF and OMEGA plasma, respectively. The OMEGA X-ray emission data corroborates this expectation, as it only observes temperature variations of $\sim 30\,\mathrm{eV}$ over a temporal integration of 1 ns. This temperature variation closely mirrors that observed in the ion temperature during the initial 200 ps of the Thomson probe.

However, significant temperature fluctuations persist in both the NIF X-ray emission data and over the duration of the Thomson probe. This discrepancy with the expected dissipation timescale strongly implies that thermal conduction has indeed been suppressed. As demonstrated in Figure 5.25, turbulent structures within the NIF Thomson scattering volume persisted over a timescale $\tau_{\mathrm{turb}} \sim 1.2\,\mathrm{ns}$. This indicates a reduction in the effective conductivity, χ, by a factor of $\chi/\chi_s \sim \tau_\chi/\tau_{\mathrm{turb}} \lesssim 0.1$.

This suppression is further supported by evaluating the dimensionless Péclet number, which describes the ratio between convection and conduction processes within the Thomson scale, L_{T},

$$\mathrm{Pe} = \frac{u_{\mathrm{rms}} L_{\mathrm{T}}}{\chi_s}\,. \tag{5.7.1}$$

Given that conduction is not the dominant process in the NIF plasma, the Péclet number must be greater than unity. However, under the assumption of Spitzer conductivity, the Péclet number is $\mathrm{Pe} \sim 0.1$. Consequently, the extent of thermal conductivity suppression is estimated as $\chi/\chi_s \lesssim \mathrm{Pe} \sim 0.1$.

A less conservative approach to assess this suppression involves calculating the conduction timescale, τ_χ, based on the length scale of localised hot and cold patches in the gated X-ray detector, $\ell_{\mathrm{T}} \lesssim 100\,\mu\mathrm{m}$. Since these patches are still observable at 23 ns (approximately 3 ns after the jet collision and subsequent generation of the turbulent plasma), they must have persisted for a dynamical time $\tau_{\mathrm{turb}} \sim L/c_s \approx 4\,\mathrm{ns}$, where $L \sim 1\,\mathrm{mm}$ is the spatial extent of the interaction region. This approach yields a thermal conductivity suppression of $\chi/\chi_s \lesssim 0.004$.

5.8 Conclusions

This chapter has detailed the inference of turbulent plasma characteristics generated by experimental platforms at both the OMEGA and NIF laser facilities. The conditions were determined utilising both temporally-resolved optical Thomson scattering and the spatially-resolved X-ray emission data. Significant heating induced by the Thomson probe was observed on the OMEGA platform, an effect not observed at the NIF attributed to its substantially lower heating power (approximately two orders of magnitude less than that at OMEGA). This finding highlights the intricate interplay between diagnostic observations and their potential perturbative effects on the experimental system.

By integrating temporally-resolved ion-acoustic and electron plasma wave scattering data with MCMC analysis, the local plasma characteristics prior to perturbative heating effects could be inferred. As a result, the magnetic Prandtl numbers obtained differ from previous work conducted on identical experimental platforms. On the NIF platform, $\mathrm{Pm} \sim 6.8$, roughly half that reported in Ref. [169]. However, it is important to acknowledge that the Thomson probe only observed a $\sim 300\,\mu$m region of the plasma. Considering the plasma's inherent inhomogeneity, as evidenced by the X-ray emission data, there may by regions with higher temperatures and, consequently, larger Prandtl numbers.

On the OMEGA platform, the magnetic Prandtl number was estimated as $\mathrm{Pm} \sim 0.02$, a significant two orders of magnitude smaller than the value reported in Ref. [165]. This disparity can be partially attributed to the timing of the data acquisition. In Ref. [165], the data captured the turbulent plasma conditions at $t = 27\,$ns, when the plasma is considerably hotter compared to the $t = 31.5\,$ns observation presented in this work. The Thomson heating does, however, induce an increase in the magnetic Prandtl number, reaching a peak of around $\mathrm{Pm} \sim 0.2$. This notable discrepancy in the Prandtl number before and after the Thomson beam heating can have significant implications

concerning the growth rates of the magnetic field.

Research on the turbulent dynamo platform remains ongoing, with future endeavours focusing on resolving the spatial evolution of heat front propagation induced by the Thomson probe on the OMEGA platform. Additionally, forthcoming experiments on the NIF are planned to enhance the signal-to-noise ratio of the ion-acoustic wave scattering, paving the way for the implementation of a more robust analytical procedure than the one outlined in this work. These developments hold promise for improving the characterisation of inferred experimental conditions and furthering the understanding of the mechanics behind the turbulent dynamo effect.

Chapter 6

Conclusion

6.1 Summary

This thesis has presented the development of diagnostic analysis for inferring temperature and density conditions across diverse experimental platforms. The research focused on integrating Thomson scattering with various experimental techniques to enhance diagnostic capabilities.

Chapter 3 explored the feasibility of utilising a dual-channel X-ray Thomson scattering diagnostic platform for a direct-drive fusion implosion. This was achieved by generating synthetic forward and backward spatially-integrated XRTS spectra using both 1-D and 2-D cryogenic simulations. The focus of this chapter was on resolving the in-flight conditions of targets with varying adiabats, which is a crucial design parameter in the development of ICF capsules. The integration of an X-ray scattering model with Markov-Chain Monte Carlo analysis yielded valuable information regarding the compressed shell's inhomogeneous conditions. Despite challenges posed by reduced shell uniformity in 2-D simulations, leading to increased electron density distributions, this methodology successfully distinguished between high and low adiabat implosion conditions. Furthermore, this research highlighted the considerations involved in the preparation of experimental campaigns and emphasised the significance of such endeavours in advancing our understanding of ICF processes.

The first experimental data was presented in Chapter 4. This campaign developed a novel experimental platform to investigate the equation-of-state of high-energy density matter produced at high-power laser facilities. By leveraging *in situ* scattering and velocimetry diagnostics, in conjunction with MCMC analysis, this study inferred the pressure, density and temperature state of liquid silicon at 100 GPa. Furthermore, the synergistic integration of these diagnostics facilitated the discernment of distinct

static screening models. The results revealed the necessity of incorporating non-linear screening beyond the Debye-Hückel approach to achieve alignment between the shock-compressed state and Hugoniot predictions. These findings emphasised the complex dynamics underlying the behaviour of high-energy density matter, and the role that models can play on the inferred conditions.

Finally, Chapter 5 detailed the diagnostic approaches utilised to infer the characteristics of turbulent plasmas. This chapter focused on two experimental campaigns, conducted on the OMEGA and NIF laser facilities. Comparison between the spatially-resolved X-ray emission data and temporally-resolved optical Thomson scattering elucidated the significant heating induced by the Thomson probe on the OMEGA platform. Nevertheless, by integrating MCMC analysis with the ion-acoustic and electron plasma wave scattering data, the local plasma characteristics prior to perturbative heating effects could be inferred. Consequently, the magnetic Prandtl numbers obtained through this approach differ from those reported in previous studies conducted on identical experimental platforms. This chapter therefore highlighted the intricate interplay between diagnostic observations and their potential perturbative effects on the experimental system, emphasising the necessity of leveraging multiple diagnostic to garner a comprehensive understanding of plasma behaviour.

6.2 Future Research Paths

This thesis has demonstrated the critical significance of leveraging experimental measurements of thermodynamic conditions to benchmark theoretical models. Such analysis serves as the basis for advancing our understanding of the interactions and behaviours inherent in high-energy density matter. In future work, there are several avenues in which this research can be extended.

Chapter 3 illustrated the challenges associated with resolving an observable X-ray Thomson scattering spectrum above the self-emission of a fusion implosion. Addressing

this challenge would necessitate research and development efforts focused on enhancing spectrometer capabilities. In particular as limited diagnostic access on a full-scale direct-drive inertial confinement fusion implosion poses a significant obstacle to fielding a spectrometer sufficiently close to the capsule. Therefore, exploring alternate X-ray sources with higher fluence than those investigated in this research would also be valuable. This is particularly true if the relatively weaker collective scattering features are to be resolved.

Enhancements in X-ray spectrometer design would also significantly benefit the research conducted in Chapter 4. In this work, substantial challenges pertaining to signal-to-noise ratio in the spectrally-resolved X-ray scattering inhibited its use as an independent measure of the shock-compressed conditions. This challenge was further compounded by the relatively broad bandwidth of the X-ray source employed. To extend this platform to investigate phenomena like ionisation potential depression, leveraging the X-ray Thomson scattering measurement becomes crucial. Furthermore, to explore materials at higher pressures, a substantially higher fluence X-ray source would be necessary to overcome self-emission and observe liquid scattering signals. Although the presented work did investigate silicon at 750 GPa, no observations were made above the target fluorescence. Therefore, improving the X-ray spectrometer efficiency and enhancing the X-ray source is imperative.

Additionally in Chapter 4, a re-design of the experimental platform to accommodate the employment of witnesses without impeding the liquid scattering signal would be invaluable. This modification would facilitate direct measurements of the shocked material's Hugoniot state, reducing reliance on previous data and decreasing uncertainty in inferring the pressure-density state via velocimetry measurements.

In the near future, several experimental campaigns are planned to advance the characterisation of turbulent plasmas, as detailed in Chapter 5. Initially, a campaign is scheduled on the National Ignition Facility to replicate the experiment outlined in

this chapter, with a focus on enhancing signal acquisition in the ion-acoustic wave scattering. This endeavour aims to facilitate a more robust analysis of the temperature distribution within the Thomson scattering volume and potentially reduce the required temporal integration for the IAW data. Additionally, the gated X-ray detector will utilise the polyimide-vanadium filter pack, enabling direct comparison with previous work. It will also capture the plasma X-ray emission earlier in time when the Thomson scattering signal is still observable. Furthermore, this platform will be applied to a pure CH target, where thermal conduction suppression is expected to be significantly reduced.

On the OMEGA turbulent dynamo platform, future work aims to mitigate the heating effects of the Thomson probe by employing an initial heating laser prior to the Thomson analysis. Elevating the temperature of the turbulent plasma will diminish the thermal absorption coefficient, thus reducing the perturbative effects of the Thomson probe. The Thomson scattering will observe the spatial evolution of the heat front propagation induced by the heating laser, by observing the plasma at increased time delays. As this Thomson scattering will be temporally-integrated, the pulse length is reduced to a minimum of 100 ps. These experiments, based on the framework outlined in this thesis, will contribute to enhancing our understanding of the fundamental physical processes governing the turbulent dynamo phenomenon.

References

[1] A. Benuzzi-Mounaix, S. Mazevet, A. Ravasio, T. Vinci, A. Denoeud, M. Koenig, N. Amadou, E. Brambrink, F. Festa, A. Levy, M. Harmand, S. Brygoo, G. Huser, V. Recoules, J. Bouchet, G. Morard, F. Guyot, T. Resseguier, K. Myanishi, N. Ozaki, F. Dorchies, P. M. Gaudin, J. Leguay, O. Peyrusse, O. Henry, S. Raffestin, D. Pape, R. Smith, and R. Musella. "Progress in warm dense matter study with applications to planetology". *Physica Scripta*, T161:014060, 2014.

[2] T. G. Sharp and P. S. Decarli. "Shock effects in meteorites", 2006.

[3] R. S. Craxton, K. S. Anderson, T. R. Boehly, V. N. Goncharov, D. R. Harding, J. P. Knauer, R. L. McCrory, P. W. McKenty, D. D. Meyerhofer, J. F. Myatt, A. J. Schmitt, J. D. Sethian, R. W. Short, S. Skupsky, W. Theobald, W. L. Kruer, K. Tanaka, R. Betti, T. J. B. Collins, J. A. Delettrez, S. X. Hu, J. A. Marozas, A. V. Maximov, D. T. Michel, P. B. Radha, S. P. Regan, T. C. Sangster, W. Seka, A. A. Solodov, J. M. Soures, C. Stoeckl, and J. D. Zuegel. "Direct-drive inertial confinement fusion: A review". *Physics of Plasmas*, 22(11):110501, 2015.

[4] S. X. Hu, L. A. Collins, T. R. Boehly, Y. H. Ding, P. B. Radha, V. N. Goncharov, V. V. Karasiev, G. W. Collins, S. P. Regan, and E. M. Campbell. "A review on ab initio studies of static, transport, and optical properties of polystyrene under extreme conditions for inertial confinement fusion applications". *Physics of Plasmas*, 25(5):056306, 2018.

[5] M. Landeau, A. Fournier, H.-C. Nataf, D. Cébron, and N. Schaeffer. "Sustaining earth's magnetic dynamo". *Nature Reviews Earth & Environment*, 3(4):255–269, 2022.

[6] J. Badro, A. S. Côté, and J. P. Brodholt. "A seismologically consistent compositional model of earth's core". *Proceedings of the National Academy of Sciences*, 111(21):7542–7545, 2014.

[7] F. Soubiran, B. Militzer, K. P. Driver, and S. Zhang. "Properties of hydrogen, helium, and silicon dioxide mixtures in giant planet interiors". *Physics of Plasmas*, 24(4):041401, 2017.

[8] G. A. de Wijs, G. Kresse, L. Vočadlo, D. Dobson, D. Alfe, M. J. Gillan, and G. D. Price. "The viscosity of liquid iron at the physical conditions of the earth's core". *Nature*, 392(6678):805–807, 1998.

[9] T. Guillot. "Interiors of giant planets inside and outside the solar system". *science*, 286(5437):72–77, 1999.

[10] O. A. Hurricane, P. T. Springer, P. K. Patel, D. A. Callahan, K. Baker, D. T. Casey, L. Divol, T. Döppner, D. E. Hinkel, M. Hohenberger, L. F. Berzak Hopkins, C. Jarrott, Kritcher, S. Le Pape, S. Maclaren, L. Masse, A. Pak, J. Ralph, C. Thomas, P. Volegov, and A. Zylstra. "Approaching a burning plasma on the nif". *Physics of Plasmas*, 26(5):052704, 2019.

[11] S. Rightley and S. D. Baalrud. "Kinetic model for electron-ion transport in warm dense matter". *Physical Review E*, 103(6):063206, 2021.

[12] Wikipedia. "Nuclear fusion". Available at: `https://en.wikipedia.org/wiki/Nuclear_fusion`, (Accessed: 5th April 2024).

[13] V. N. Goncharov, T. C. Sangster, T. R. Boehly, S. X. Hu, I. V. Igumenshchev, F. J. Marshall, R. L. McCrory, D. D. Meyerhofer, P. B. Radha, W. Seka, S. Skupsky, C. Stoeckl, D. T. Casey, J. A. Frenje, and R. D. Petrasso. "Demonstration of the highest deuterium-tritium areal density using multiple-picket cryogenic designs on omega". *Physical review letters*, 104(16):165001, 2010.

[14] J. Lindl. *Inertial confinement fusion: the quest for ignition and energy gain using indirect drive*. Springer, New York, 1998.

[15] V. N. Goncharov, T. C. Sangster, R. Betti, T. R. Boehly, M. J. Bonino, T. J. B. Collins, R. S. Craxton, J. A. Delettrez, D. H. Edgell, R. Epstein, R. K. Follett, C. J. Forrest, D. H. Froula, V. Y. Glebov, D. R. Harding, R. J. Henchen, S. X. Hu, I. V. Igumenshchev, R. Janezic, J. H. Kelly, T. J. Kessler, T. Z. Kosc, S. J. Loucks, J. A. Marozas, F. J. Marshall, A. V. Maximov, R. L. McCrory, P. W. McKenty, D. D. Meyerhofer, D. T. Michel, J. F. Myatt, R. Nora, P. B. Radha, S. P. Regan, W. Seka, W. T. Shmayda, R. W. Short, A. Shvydky, S. Skupsky, C. Stoeckl, B. Yaakobi, J. A. Frenje, M. Gatu-Johnson, R. D. Petrasso, and D. T. Casey. "Improving the hot-spot pressure and demonstrating ignition hydrodynamic equivalence in cryogenic deuterium–tritium implosions on omega". *Physics of Plasmas*, 21(5):056315, 2014.

[16] R. Betti and O. A. Hurricane. "Inertial-confinement fusion with lasers". *Nature Physics*, 12(5):435–448, 2016.

[17] S. Atzeni and J. Meyer-ter Vehn. *The physics of inertial fusion: beam plasma interaction, hydrodynamics, hot dense matter*, volume 125. OUP Oxford, 2004.

[18] O. L. Landen, D. T. Casey, J. M. DiNicola, T. Döppner, E. P. Hartouni, D. E. Hinkel, L. F. B. Hopkins, M. Hohenberger, A. L. Kritcher, S. L. Pape, B. J. MacGowan, S. Maclaren, K. D. Meaney, M. Millot, P. K. Patel, J. Park, L. A. Pickworth, H. F. Robey, J. S. Ross, S. T. Yang, A. B. Zylstra, K. L. Baker, D. A. Callahan, P. M. Celliers, M. J. Edwards, O. A. Hurricane, J. D. Lindl, J. D. Moody, J. Ralph, V. A. Smalyuk, C. A. Thomas, B. M. V. Wonterghem, and C. R. Weber. "Yield and compression trends and reproducibility at nif". *High Energy Density Physics*, 36:100755, 2020.

[19] K. Anderson and R. Betti. "Laser-induced adiabat shaping by relaxation in inertial fusion implosions". *Physics of Plasmas*, 11(1):5–8, 2004.

[20] J. Melvin, H. Lim, V. Rana, B. Cheng, J. Glimm, D. H. Sharp, and D. C. Wilson. "Sensitivity of inertial confinement fusion hot spot properties to the deuterium-tritium fuel adiabat". *Physics of Plasmas*, 22(2):022708, 2015.

[21] T. R. Dittrich, O. A. Hurricane, D. A. Callahan, E. L. Dewald, T. Döppner, D. E. Hinkel, L. F. B. Hopkins, S. L. Pape, T. Ma, J. L. Milovich, J. C. Moreno, P. K. Patel, H.-S. Park, B. A. Remington, J. D. Salmonson, and J. L. Kline. "Design of a high-foot high-adiabat icf capsule for the national ignition facility". *Physical review letters*, 112(5):055002, 2014.

[22] H. Abu-Shawareb, R. Acree, P. Adams, J. Adams, B. Addis, R. Aden, P. Adrian, B. Afeyan, M. Aggleton, L. Aghaian, et al. "Lawson criterion for ignition exceeded in an inertial fusion experiment". *Physical review letters*, 129(7):075001, 2022.

[23] V. Gopalaswamy, C. A. Williams, R. Betti, D. Patel, J. P. Knauer, A. Lees, D. Cao, E. M. Campbell, P. Farmakis, R. Ejaz, K. S. Anderson, R. Epstein, J. Carroll-Nellenbeck, I. V. Igumenshchev, J. A. Marozas, P. B. Radha, A. A. Solodov, C. A. Thomas, K. M. Woo, T. J. B. Collins, S. X. Hu, W. Scullin, D. Turnbull, V. N. Goncharov, K. Churnetski, C. J. Forrest, V. Y. Glebov, P. V. Heuer, H. McClow, R. C. Shah, C. Stoeckl, W. Theobald, D. H. Edgell, S. Ivancic, M. J. Rosenberg, S. P. Regan, D. Bredesen, C. Fella, M. Koch, R. T. Janezic, M. J. Bonino, D. R. Harding, K. A. Bauer, S. Sampat, L. J. Waxer, M. Labuzeta, S. F. B. Morse, M. Gatu-Johnson, R. D. Petrasso, J. A. Frenje, J. Murray, B. Serrato, D. Guzman, C. Shuldberg, M. Farrell, and C. Deeney. "Demonstration of a hydrodynamically equivalent burning plasma in direct-drive inertial confinement fusion". *Nature Physics*, pages 1–7, 2024.

[24] A. Zylstra, A. Kritcher, O. Hurricane, D. Callahan, J. Ralph, D. Casey, A. Pak, O. Landen, B. Bachmann, K. Baker, et al. "Experimental achievement and signatures of ignition at the national ignition facility". *Physical Review E*, 106(2): 025202, 2022.

[25] S. P. Regan, K. Falk, G. Gregori, P. B. Radha, S. X. Hu, T. R. Boehly, B. J. B. Crowley, S. H. Glenzer, O. L. Landen, D. O. Gericke, T. Döppner, D. D. Meyerhofer, C. D. Murphy, T. C. Sangster, , and J. Vorberger. "Inelastic x-ray scattering from shocked liquid deuterium". *Physical review letters*, 109(26):265003, 2012.

[26] V. Y. Glebov, C. J. Forrest, J. Kendrick, J. P. Knauer, O. M. Mannion, H. McClow, S. P. Regan, C. Stoeckl, B. Stanley, and W. Theobald. "A new neutron time-of-flight detector for yield and ion-temperature measurements at the omega laser facility". *Review of Scientific Instruments*, 93(9):093522, 2022.

[27] J. Kalirai. "Scientific discovery with the james webb space telescope". *Contemporary Physics*, 59(3):251–290, 2018.

[28] J. L. Sievers, R. A. Hlozek, M. R. Nolta, V. Acquaviva, G. E. Addison, P. A. Ade, P. Aguirre, M. Amiri, J. W. Appel, L. F. Barrientos, et al. "The atacama cosmology telescope: Cosmological parameters from three seasons of data". *Journal of Cosmology and Astroparticle Physics*, 2013(10):060, 2013.

[29] J. E. Cross, B. Reville, and G. Gregori. "Scaling of magneto-quantum-radiative hydrodynamic equations: from laser-produced plasmas to astrophysics". *The Astrophysical Journal*, 795(1):59, 2014.

[30] R. P. Drake. *Introduction to high-energy-density physics*. Springer, 2006.

[31] K. Falk. "Experimental methods for warm dense matter research". *High Power Laser Science and Engineering*, 6:e59, 2018.

[32] B. Militzer, W. B. Hubbard, J. Vorberger, I. Tamblyn, and S. A. Bonev. "A massive core in jupiter predicted from first-principles simulations". *The Astrophysical Journal*, 688(1):L45, 2008.

[33] J. Wade and B. J. Wood. "Core formation and the oxidation state of the earth". *Earth and Planetary Science Letters*, 236(1-2):78–95, 2005.

[34] W. B. Hubbard, T. Guillot, J. I. Lunine, A. Burrows, D. Saumon, M. S. Marley, and R. S. Freedman. "Liquid metallic hydrogen and the structure of brown dwarfs and giant planets". *Physics of Plasmas*, 4(5):2011–2015, 1997.

[35] R. J. Hemley and H. K. Mao. "Optical studies of hydrogen above 200 gigapascals: Evidence for metallization by band overlap". *Science*, 244(4911):1462–1465, 1989.

[36] P. Dalladay-Simpson, R. T. Howie, and E. Gregoryanz. "Evidence for a new phase of dense hydrogen above 325 gigapascals". *Nature*, 529(7584):63–67, 2016.

[37] R. P. Dias and I. F. Silvera. "Observation of the wigner-huntington transition to metallic hydrogen". *Science*, 355(6326):715–718, 2017.

[38] E. Gregoryanz, C. Ji, P. Dalladay-Simpson, B. Li, R. T. Howie, and H.-K. Mao. "Everything you always wanted to know about metallic hydrogen but were afraid to ask". *Matter and Radiation at Extremes*, 5(3):038101, 2020.

[39] O. Klein and Y. Nishina. "On the scattering of radiation by free electrons according to dirac's new relativistic quantum dynamics". *Zeitschrift für Physik*, 52 (11):853–868, 1929.

[40] B. J. B. Crowley and G. Gregori. "X-ray scattering by many-particle systems". *New Journal of Physics*, 15(1):015014, 2013.

[41] J. Chihara. "Interaction of photons with plasmas and liquid metals-photoabsorption and scattering". *Journal of Physics: Condensed Matter*, 12(3): 231, 2000.

[42] L. B. Fletcher, A. L. Kritcher, A. Pak, T. Ma, T. Döppner, C. Fortmann, L. Divol, O. S. Jones, O. L. Landen, H. A. Scott, J. Vorberger, D. A. Chapman, D. O. Gericke, B. A. Mattern, G. T. Seidler, and G. Gregori. "Observations of continuum depression in warm dense matter with x-ray thomson scattering". *Physical review letters*, 112(14):145004, 2014.

[43] E. E. Salpeter. "Electron density fluctuations in a plasma". *Physical Review*, 120 (5):1528, 1960.

[44] P. Debye and E. H"uckel. "Zur theorie der electrolyte". *Phyikalishce Zeitschrift*, 24:185–206, 1923.

[45] L. H. Thomas. "The calculation of atomic fields". In *Mathematical proceedings of the Cambridge philosophical society*, volume 23, pages 542–548. Cambridge University Press, 1927.

[46] E. Fermi. "Statistical method to determine some properties of atoms". *Rend. Accad. Naz. Lincei*, 6(602-607):5, 1927.

[47] G. Gregori, S. H. Glenzer, F. J. Rogers, S. M. Pollaine, O. L. Landen, C. Blancard, G. Faussurier, P. Renaudin, S. Kuhlbrodt, and R. Redmer. "Electronic structure measurements of dense plasmas". *Physics of Plasmas*, 11(5):2754–2762, 2004.

[48] I. Langmuir. "Oscillations in ionized gases". *Proceedings of the National Academy of Sciences*, 14(8):627–637, 1928.

[49] D. Bohm and E. P. Gross. "Theory of plasma oscillations. a. origin of medium-like behavior". *Physical Review*, 75(12):1851, 1949.

[50] R. Thiele, T. Bornath, C. Fortmann, A. Höll, R. Redmer, H. Reinholz, G. Röpke, A. Wierling, S. H. Glenzer, and G. Gregori. "Plasmon resonance in warm dense matter". *Physical Review E*, 78(2):026411, 2008.

[51] S. H. Glenzer and R. Redmer. "X-ray thomson scattering in high energy density plasmas". *Reviews of Modern Physics*, 81(4):1625, 2009.

[52] G. Gregori, S. H. Glenzer, W. Rozmus, R. W. Lee, and O. L. Landen. "Theoretical model of x-ray scattering as a dense matter probe". *Physical Review E*, 67(2): 026412, 2003.

[53] P. Mabey, S. Richardson, T. G. White, L. B. Fletcher, S. H. Glenzer, N. J. Hartley, J. Vorberger, D. O. Gericke, and G. Gregori. "A strong diffusive ion mode in dense ionized matter predicted by langevin dynamics". *Nature communications*, 8(1): 14125, 2017.

[54] R. K. Follett, J. A. Delettrez, D. H. Edgell, R. J. Henchen, J. Katz, J. F. Myatt, and D. H. Froula. "Plasma characterization using ultraviolet thomson scattering from ion-acoustic and electron plasma waves". *Review of Scientific Instruments*, 87(11):11E401, 2016.

[55] D. H. Froula and S. H. Glenzer. *Plasma scattering of electromagnetic radiation*. Elsevier, 2011.

[56] E. Fermi. "Zur quantelung des idealen einatomigen gases". *Zeitschrift für Physik*, 36(11-12):902–912, 1926.

[57] P. A. M. Dirac. "On the theory of quantum mechanics". *Proceedings of the Royal Society of London. Series A, Containing Papers of a Mathematical and Physical Character*, 112(762):661–677, 1926.

[58] H. Poole, R. E. D. Cao, I. Golovkin, T. Walton, S. X. Hu, M. Kasim, S. M. Vinko, J. R. Rygg, V. N. Goncharov, G. Gregori, and S. P. Regan. "A case study of using x-ray thomson scattering to diagnose the in-flight plasma conditions of dt cryogenic implosions". *Physics of Plasmas*, 29(7):072703, 2022.

[59] J. A. Gaffney, S. X. Hu, P. Arnault, A. Becker, L. X. Benedict, T. R. Boehly, P. M. Celliers, D. M. Ceperley, O. Čertík, J. Clérouin, G. W. Collins, L. A. Collins, J.-F. Danel, N. Desbiens, M. W. C. Dharma-wardana, Y. H. Ding, A. Fernandez-Pañella, M. C. Gregor, P. E. Grabowski, S. Hamel, S. B. Hansen, L. Harbour, X. T. He, D. D. Johnson, W. Kang, V. V. Karasiev, L. Kazandjian, M. D. Knudson, T. Ogitsu, C. Pierleoni, R. Piron, R. Redmer, G. Robert, D. Saumon, A. Shamp, T. Sjostrom, A. V. Smirnov, C. E. Starrett, P. A. Sterne, A. Wardlow, H. D. Whitley, B. Wilson, P. Zhang, and E. Zurek. "A review of equation-of-state models for inertial confinement fusion materials". *High Energy Density Physics*, 28:7–24, 2018.

[60] S. X. Hu, B. Militzer, V. N. Goncharov, and S. Skupsky. "Strong coupling and degeneracy effects in inertial confinement fusion implosions". *Physical review letters*, 104(23):235003, 2010.

[61] S. X. Hu. "Continuum lowering and fermi-surface rising in strongly coupled and degenerate plasmas". *Physical review letters*, 119(6):065001, 2017.

[62] C. Wang, Y. Long, X.-T. He, J.-F. Wu, W.-H. Ye, and P. Zhang. "Transport properties of dense deuterium-tritium plasmas". *Physical Review E*, 88(1):013106, 2013.

[63] S. Vinko, O. Ciricosta, and J. Wark. "Density functional theory calculations of continuum lowering in strongly coupled plasmas". *Nature communications*, 5(1): 3533, 2014.

[64] D. A. Chapman, J. Vorberger, L. B. Fletcher, R. A. Baggott, L. Divol, T. Döppner, R. W. Falcone, S. H. Glenzer, G. Gregori, T. M. Guymer, A. L. Kritcher, O. L. Landen, T. Ma, A. E. Pak, and D. O. Gericke. "Observation of finite-wavelength screening in high-energy-density matter". *Nature communications*, 6(1):6839, 2015.

[65] T. G. White, N. J. Hartley, B. Borm, B. J. B. Crowley, J. W. O. Harris, D. C. Hochhaus, T. Kaempfer, K. Li, P. Neumayer, L. K. Pattison, F. Pfeifer, S. Richardson, A. P. L. Robinson, I. Uschmann, and G. Gregori. "Electron-ion equilibration in ultrafast heated graphite". *Physical review letters*, 112(14):145005, 2014.

[66] P. Grabowski, S. Hansen, M. Murillo, L. Stanton, F. Graziani, A. Zylstra, S. Baalrud, P. Arnault, A. Baczewski, L. Benedict, C. Blancard, O. Čertík, J. Clérouin, L. Collins, S. Copeland, A. Correa, J. Dai, J. Daligault, M. Desjarlais, M. Dharma-wardana, G. Faussurier, J. Haack, T. Haxhimali, A. Hayes-Sterbenz, Y. Hou, S. Hu, D. Jensen, G. Jungman, G. Kagan, D. Kang, J. Kress, Q. Ma, M. Marciante, E. Meyer, R. Rudd, D. Saumon, L. Shulenburger, R. Singleton, T. Sjostrom, L. Stanek, C. Starrett, C. Ticknor, S. Valaitis, J. Venzke, and A. White. "Review of the first charged-particle transport coefficient comparison workshop". *High Energy Density Physics*, 37:100905, 2020.

[67] G. Gregori, S. H. Glenzer, K. B. Fournier, K. M. Campbell, E. L. Dewald, O. S. Jones, J. H. Hammer, S. B. Hansen, R. J. Wallace, and O. L. Landen. "X-ray scattering measurements of radiative heating and cooling dynamics". *Physical review letters*, 101(4):045003, 2008.

[68] D. A. Chapman, D. Kraus, A. L. Kritcher, B. Bachmann, G. W. Collins, R. W. Falcone, J. A. Gaffney, D. O. Gericke, S. H. Glenzer, T. M. Guymer, J. A. Hawreliak, O. L. Landen, S. L. Pape, T. Ma, P. Neumayer, J. Nilsen, A. Pak, R. Redmer, D. C. Swift, J. Vorberger, and T. Döppner. "Simulating x-ray thomson scattering signals from high-density, millimetre-scale plasmas at the national ignition facility". *Physics of Plasmas*, 21(8):082709, 2014.

[69] J. J. MacFarlane, I. Golovkin, P. Wang, P. R. Woodruff, and N. A. Pereyra. "Spect3d–a multi-dimensional collisional-radiative code for generating diagnostic signatures based on hydrodynamics and pic simulation output". *High energy density physics*, 3(1-2):181–190, 2007.

[70] I. Golovkin, J. J. MacFarlane, P. Woodruff, I. Hall, G. Gregori, J. Bailey, E. Harding, T. Ao, and S. H. Glenzer. "Simulation of x-ray scattering diagnostics in multi-dimensional plasma". *High Energy Density Physics*, 9(3):510–515, 2013.

[71] J. Delettrez, R. Epstein, M. C. Richardson, P. A. Jaanimagi, and B. L. Henke. "Effect of laser illumination nonuniformity on the analysis of time-resolved x-ray measurements in uv spherical transport experiments". *Physical Review A*, 36(8): 3926, 1987.

[72] P. B. Radha, T. J. B. Collins, J. A. Delettrez, Y. Elbaz, R. Epstein, V. Y. Glebov, V. N. Goncharov, R. L. Keck, J. P. Knauer, J. A. Marozas, F. J. Marshall, R. L. McCrory, P. W. McKenty, D. D. Meyerhofer, S. P. Regan, T. C. Sangster, W. Seka, D. Shvarts, S. Skupsky, Y. Srebro, and C. Stoeckl. "Two-dimensional simulations of plastic-shell, direct-drive implosions on omega". *Physics of Plasmas*, 12(3):056307, 2005.

[73] E. J. Gamboa, P. A. Keiter, R. P. Drake, K. Falk, D. S. Montgomery, and J. F. Benage. "Spatially-resolved x-ray scattering measurements of a planar blast wave". *High Energy Density Physics*, 11:75–79, 2014.

[74] T. R. Boehly, D. L. Brown, R. S. Craxton, R. L. Keck, J. P. Knauer, J. H. Kelly, T. J. Kessler, S. A. Kumpan, S. J. Loucks, S. A. Letzring, F. J. Marshall, R. L. McCrory, S. F. B. Morse, W. Seka, J. M. Soures, and C. P. Verdon. "Initial performance results of the omega laser system". *Optics communications*, 133(1-6): 495–506, 1997.

[75] E. J. Gamboa, C. M. Huntington, M. R. Trantham, P. A. Keiter, R. P. Drake, D. S. Montgomery, J. F. Benage, and S. A. Letzring. "Imaging x-ray thomson scattering spectrometer design and demonstration". *Review of Scientific Instruments*, 83(10):10E108, 2012.

[76] P. Davis, T. Döppner, J. Rygg, C. Fortmann, L. Divol, A. Pak, L. Fletcher, A. Becker, B. Holst, P. Sperling, et al. "X-ray scattering measurements of dissociation-induced metallization of dynamically compressed deuterium". *Nature communications*, 7(1):11189, 2016.

[77] A. L. Kritcher, T. Döppner, C. Fortmann, T. Ma, O. L. Landen, R. Wallace, and S. H. Glenzer. "In-flight measurements of capsule shell adiabats in laser-driven implosions". *Physical Review Letters*, 107(1):015002, 2011.

[78] A. J. Crilly, B. D. Appelbe, O. M. Mannion, C. J. Forrest, V. Gopalaswamy, C. A. Walsh, and J. P. Chittenden. "Neutron backscatter edge: A measure of the hydrodynamic properties of the dense dt fuel at stagnation in icf experiments". *Physics of Plasmas*, 27(1):012701, 2020.

[79] C. Cerjan, P. T. Springer, and S. M. Sepke. "Integrated diagnostic analysis of inertial confinement fusion capsule performance". *Physics of Plasmas*, 20(5): 056319, 2013.

[80] C. Stoeckl, M. Bonino, C. Mileham, S. Regan, W. Theobald, T. Ebert, and S. Sander. "Optimization of a short-pulse-driven si heα soft x-ray backlighter". *High Energy Density Physics*, 41:100973, 2021.

[81] C. Stoeckl, M. Bedzyk, G. Brent, R. Epstein, G. Fiksel, D. Guy, V. N. Goncharov, S. X. Hu, S. Ingraham, D. W. Jacobs-Perkins, R. K. Jungquist, F. J. Marshall, C. Mileham, P. M. Nilson, T. C. Sangster, M. J. Shoup, and W. Theobald. "Soft x-ray backlighting of cryogenic implosions using a narrowband crystal imaging system". *Review of Scientific Instruments*, 85(11), 2014.

[82] C. Stoeckl, R. Epstein, R. Betti, W. Bittle, J. A. Delettrez, C. J. Forrest, V. Y. Glebov, V. N. Goncharov, D. R. Harding, I. V. Igumenshchev, D. W. Jacobs-Perkins, R. T. Janezic, J. H. Kelly, T. Z. Kosc, R. L. McCrory, D. T. Michel, C. Mileham, P. W. McKenty, F. J. Marshall, S. F. B. Morse, S. P. Regan, P. B. Radha, B. Rice, T. C. Sangster, M. J. Shoup, W. T. Shmayda, C. Sorce, W. Theobald, J. Ulreich, M. D. Wittman, D. D. Meyerhofer, J. A. Frenje, M. G. Johnson, and R. D. Petrasso. "Monochromatic backlighting of direct-drive cryogenic dt implosions on omega". *Physics of Plasmas*, 24(5), 2017.

[83] M. K. Urry, G. Gregori, O. L. Landen, A. Pak, and S. H. Glenzer. "X-ray probe development for collective scattering measurements in dense plasmas". *Journal of Quantitative Spectroscopy and Radiative Transfer*, 99(1-3):636–648, 2006.

[84] I. V. Igumenshchev, D. H. Edgell, V. N. Goncharov, J. A. Delettrez, A. V. Maximov, J. F. Myatt, W. Seka, A. Shvydky, S. Skupsky, and C. Stoeckl. "Crossed-beam energy transfer in implosion experiments on omega". *Physics of Plasmas*, 17(12), 2010.

[85] V. N. Goncharov, O. V. Gotchev, E. Vianello, T. R. Boehly, J. P. Knauer, P. W. McKenty, P. B. Radha, S. P. Regan, T. C. Sangster, S. Skupsky, V. A. Smalyuk, R. Betti, R. L. McCrory, D. D. Meyerhofer, and C. Cherfils-Cl'erouin. "Early stage of implosion in inertial confinement fusion: Shock timing and perturbation evolution". *Physics of plasmas*, 13(1):012702, 2006.

[86] S. X. Hu, B. Militzer, V. N. Goncharov, and S. Skupsky. "First-principles equation-of-state table of deuterium for inertial confinement fusion applications". *Physical Review B*, 84(22):224109, 2011.

[87] S. X. Hu, L. A. Collins, V. N. Goncharov, J. D. Kress, R. L. McCrory, and S. Skupsky. "First-principles equation of state of polystyrene and its effect on inertial confinement fusion implosions". *Physical Review E*, 92(4):043104, 2015.

[88] S. X. Hu, L. A. Collins, V. N. Goncharov, T. R. Boehly, R. Epstein, R. L. McCrory, and S. Skupsky. "First-principles opacity table of warm dense deuterium for inertial-confinement-fusion applications". *Physical Review E*, 90(3):033111, 2014.

[89] T. J. B. Collins, C. Stoeckl, R. Epstein, W. A. Bittle, C. J. Forrest, V. Y. Glebov, V. N. Goncharov, D. R. Harding, S. X. Hu, D. W. Jacobs-Perkins, T. Z. Kosc, J. A. Marozas, C. Mileham, F. J. Marshall, S. F. B. Morse, P. B. Radha, S. P. Regan, B. Rice, T. C. Sangster, M. J. S. III, W. T. Shmayda, C. Sorce, W. Theobald, and M. D. Wittmans. "Causes of fuel–ablator mix inferred from modeling of monochromatic time-gated radiography of omega cryogenic implosions". *Physics of Plasmas*, 29(1):012702, 2022.

[90] J. A. Marozas, M. Hohenberger, M. J. Rosenberg, D. Turnbull, T. J. B. Collins, P. B. Radha, P. W. McKenty, J. D. Zuegel, F. J. Marshall, S. P. Regan, T. C. Sangster, W. Seka, E. M. Campbell, V. N. Goncharov, M. W. Bowers, J.-M. G. D. Nicola, G. Erbert, B. J. MacGowan, L. J. Pelz, J. Moody, and S. T. Yang. "Wavelength-detuning cross-beam energy transfer mitigation scheme for direct drive: Modeling and evidence from national ignition facility implosions". *Physics of Plasmas*, 25(5):056314, 2018.

[91] D. Cao, G. Moses, and J. Delettrez. "Improved non-local electron thermal transport model for two-dimensional radiation hydrodynamics simulations". *Physics of Plasmas*, 22(8):082308, 2015.

[92] H. Sawada, S. P. Regan, D. D. Meyerhofer, I. V. Igumenshchev, V. N. Goncharov, T. R. Boehly, R. Epstein, T. C. Sangster, V. A. Smalyuk, B. Yaakobi, G. Gregori, S. H. Glenzer, and O. L. Landen. "Diagnosing direct-drive, shock-heated, and compressed plastic planar foils with noncollective spectrally resolved x-ray scattering". *Physics of Plasmas*, 14(12):122703, 2007.

[93] A. M. Saunders, A. Jenei, T. Döppner, R. W. Falcone, D. Kraus, A. Kritcher, O. L. Landen, J. Nilsen, and D. Swift. "X-ray thomson scattering measurements from hohlraum-driven spheres on the omega laser". *Review of Scientific Instruments*, 87(11):11E724, 2016.

[94] V. Gopalaswamy, R. Betti, J. P. Knauer, N. Luciani, D. Patel, K. M. Woo, A. Bose, I. V. Igumenshchev, E. M. Campbell, K. S. Anderson, K. A. Bauer, M. J. Bonino, D. Cao, A. R. Christopherson, G. W. Collins, T. J. B. Collins, J. R. Davies, J. A. Delettrez, D. H. Edgell, R. Epstein, C. J. Forrest, D. H. Froula, V. Y. Glebov, V. N. Goncharov, D. R. Harding, S. X. Hu, D. W. Jacobs-Perkins, R. T. Janezic, J. H. Kelly, O. M. Mannion, A. Maximov, F. J. Marshall, D. T. Michel, S. Miller, S. F. B. Morse, J. Palastro, J. Peebles, P. B. Radha, S. P. Regan, S. Sampat, T. C. Sangster, A. B. Sefkow, W. Seka, R. C. Shah, W. T. Shmyada, A. Shvydky, C. Stoeckl, A. A. Solodov, W. Theobald, J. D. Zuegel, M. G. Johnson, R. D. Petrasso, C. K. Li, and J. A. Frenje. "Tripled yield in direct-drive laser fusion through statistical modelling". *Nature*, 565(7741):581–586, 2019.

[95] M. Kasim, T. P. Galligan, J. Topp-Mugglestone, G. Gregori, and S. M. Vinko. "Inverse problem instabilities in large-scale modeling of matter in extreme conditions". *Physics of Plasmas*, 26(11):112706, 2019.

[96] C. Andrieu, N. De Freitas, A. Doucet, and M. I. Jordan. "An introduction to mcmc for machine learning". *Machine learning*, 50:5–43, 2003.

[97] H. G. Rinderknecht, D. T. Casey, R. Hatarik, R. M. Bionta, B. J. MacGowan, P. Patel, O. L. Landen, E. P. Hartouni, and O. A. Hurricane. "Azimuthal drive asymmetry in inertial confinement fusion implosions on the national ignition facility". *Physical Review Letters*, 124(14):145002, 2020.

[98] O. M. Mannion, I. V. Igumenshchev, K. S. Anderson, R. Betti, E. M. Campbell, D. Cao, C. J. Forrest, M. G. Johnson, V. Y. Glebov, V. N. Goncharov, V. Gopalaswamy, S. T. Ivancic, D. W. Jacobs-Perkins, A. Kalb, J. P. Knauer, J. Kwiatkowski, A. Lees, F. J. Marshall, M. Michalko, Z. L. Mohamed, D. Patel, H. G. Rinderknecht, R. C. Shah, C. Stoeckl, W. Theobald, K. M. Woo, and S. P. Regan. "Mitigation of mode-one asymmetry in laser-direct-drive inertial confinement fusion implosions". *Physics of Plasmas*, 28(4):042701, 2021.

[99] V. A. Smalyuk, C. R. Weber, O. L. Landen, S. Ali, B. Bachmann, P. M. Celliers, E. L. Dewald, A. Fernandez, B. A. Hammel, G. Hall, A. G. MacPhee,

L. Pickworth, H. F. Robey, N. Alfonso, K. L. Baker, L. F. B. Hopkins, L. Carlson, D. T. Casey, D. S. Clark, J. Crippen, L. Divol, T. D"oppner, M. J. Edwards, M. Farrell, S. Felker, J. E. Field, S. W. Haan, A. V. Hamza, M. Havre, M. C. Herrmann, W. W. Hsing, S. Khan, J. Kline, J. J. Kroll, S. LePape, E. Loomis, B. J. MacGowan, D. Martinez, L. Masse, M. Mauldin, J. L. Milovich, A. S. Moore, A. Nikroo, A. Pak, P. K. Patel, J. L. Peterson, K. Raman, B. A. Remington, N. Rice, M. Schoff, and M. Stadermann. "Review of hydrodynamic instability experiments in inertially confined fusion implosions on national ignition facility". *Plasma Physics and Controlled Fusion*, 62(1):014007, 2019.

[100] L. B. Fletcher, H. J. Lee, T. Döppner, E. Galtier, B. Nagler, P. Heimann, C. Fortmann, S. LePape, T. Ma, M. Millot, A. Pak, D. Turnbull, D. A. Chapman, D. O. Gericke, J. Vorberger, T. White, G. Gregori, M. Wei, B. Barbrel, R. W. Falcone, C.-C. Kao, H. Nuhn, J. Welch, U. Zastrau, P. Neumayer, J. B. Hastings, and S. H. Glenzer. "Ultrabright x-ray laser scattering for dynamic warm dense matter physics". *Nature photonics*, 9(4):274–279, 2015.

[101] A. J. Crilly, B. D. Appelbe, K. McGlinchey, C. A. Walsh, J. K. Tong, A. B. Boxall, and J. P. Chittenden. "Synthetic nuclear diagnostics for inferring plasma properties of inertial confinement fusion implosions". *Physics of Plasmas*, 25(12): 122703, 2018.

[102] O. M. Mannion, A. J. Crilly, C. J. Forrest, B. D. Appelbe, R. Betti, V. Y. Glebov, V. Gopalaswamy, J. P. Knauer, Z. L. Mohamed, C. Stoeckl, J. P. Chittenden, and S. P. Regan. "Measurements of the temperature and velocity of the dense fuel layer in inertial confinement fusion experiments". *Physical Review E*, 105(5): 055205, 2022.

[103] H. Poole, M. K. Ginnane, M. Millot, H. M. Bellenbaum, G. W. Collins, S. X. Hu, D. Polsin, R. Saha, J. Topp-Mugglestone, T. G. White, D. A. Chapman, J. R. Rygg, S. P. Regan, and G. Gregori. "Multimessenger measurements of the static structure of shock-compressed liquid silicon at 100 gpa". *Physical Review Research*, 6(2):023144, 2024.

[104] S. H. Glenzer, L. B. Fletcher, E. Galtier, B. Nagler, R. Alonso-Mori, B. Barbrel, S. Brown, D. A. Chapman, Z. Chen, C. B. Curry, et al. "Matter under extreme conditions experiments at the linac coherent light source". *Journal of Physics B: Atomic, Molecular and Optical Physics*, 49(9):092001, 2016.

[105] M. Koenig, A. Benuzzi-Mounaix, A. Ravasio, T. Vinci, N. Ozaki, S. Pape, D. Batani, G. Huser, T. Hall, D. Hicks, A. MacKinnon, P. Patel, H.-S. Park, T. Boehly, M. Borghesi, S. Kar, and L. Romagnani. "Progress in the study of warm dense matter". *Plasma Physics and Controlled Fusion*, 47(12B):B441, 2005.

[106] K. Wünsch, J. Vorberger, G. Gregori, and D. O. Gericke. "X-ray scattering as a probe for warm dense mixtures and high-pressure miscibility". *Europhysics Letters*, 94(2):25001, 2011.

[107] E. E. McBride, A. Krygier, A. Ehnes, E. Galtier, M. Harmand, Z. Konôpková, H. J. Lee, H.-P. Liermann, B. Nagler, A. Pelka, M. Rödel, A. Schropp, R. F. Smith, C. Spindloe, D. Swift, F. Tavella, S. Toleikis, T. Tschentscher, J. S. Wark, and A. Higginbotham. "Phase transition lowering in dynamically compressed silicon". *Nature Physics*, 15(1):89, 2019.

[108] S. Brygoo, P. Loubeyre, M. Millot, J. R. Rygg, P. M. Celliers, J. H. Eggert, R. Jeanloz, and G. W. Collins. "Evidence of hydrogen- helium immiscibility at jupiter-interior conditions". *Nature*, 593(7860):517–521, 2021.

[109] M. Bonitz, T. Dornheim, Z. A. Moldabekov, S. Zhang, P. Hamann, H. Kählert, A. Filinov, K. Ramakrishna, and J. Vorberger. "Ab initio simulation of warm dense matter". *Physics of Plasmas*, 27(4):042710, 2020.

[110] D. Kraus, D. A. Chapman, A. L. Kritcher, R. A. Baggott, B. Bachmann, G. W. Collins, S. H. Glenzer, J. A. Hawreliak, D. H. Kalantar, O. L. Landen, T. Ma, S. L. Pape, J. Nilsen, D. C. Swift, P. Neumayer, R. W. Falcone, D. O. Gericke, and T. Döppner. "X-ray scattering measurements on imploding ch spheres at the national ignition facility". *Physical Review E*, 94(1):011202(R), 2016.

[111] H. Lee, P. Neumayer, J. Castor, T. Döppner, R. Falcone, C. Fortmann, B. Hammel, A. Kritcher, O. Landen, R. Lee, et al. "X-ray thomson-scattering measurements of density and temperature in shock-compressed beryllium". *Physical review letters*, 102(11):115001, 2009.

[112] A. Lazicki, J. R. Rygg, F. Coppari, R. Smith, D. Fratanduono, R. G. Kraus, G. W. Collins, R. Briggs, D. G. Braun, D. C. Swift, and J. H. Eggert. "X-ray diffraction of solid tin to 1.2 tpa". *Physical review letters*, 115(7):075502, 2015.

[113] F. Coppari, D. Fratanduono, M. Millot, R. Kraus, A. Lazicki, J. Rygg, R. Smith, and J. Eggert. "X-ray diffraction measurements and pressure determination in nanosecond compression of solids up to 600 gpa". *Physical Review B*, 106(13): 134105, 2022.

[114] J. R. Rygg, J. H. Eggert, A. E. Lazicki, F. Coppari, J. A. Hawreliak, D. G. Hicks, R. F. Smith, C. M. Sorce, T. M. Uphaus, B. Yaakobi, and G. W. Collins. "Powder diffraction from solids in the terapascal regime". *Review of Scientific Instruments*, 83(11):113904, 2012.

[115] X. Gong, D. N. Polsin, R. Paul, B. J. Henderson, J. H. Eggert, F. Coppari, R. F. Smith, J. R. Rygg, and G. W. Collins. "X-ray diffraction of ramp-compressed silicon to 390 gpa". *Physical Review Letters*, 130:076101, 2023.

[116] B. J. Henderson, M. C. Marshall, T. R. Boehly, R. Paul, C. A. McCoy, S. X. Hu, D. N. Polsin, L. E. Crandall, M. F. Huff, D. A. Chin, J. J. Ruby, X. Gong, D. E. Fratanduono, J. H. Eggert, J. R. Rygg, and G. W. Collins. "Shock-compressed silicon: Hugoniot and sound speed up to 2100 gpa". *Physical Review B*, 103(9): 094115, 2021.

[117] K. Falk, S. Regan, J. Vorberger, B. Crowley, S. Glenzer, S. Hu, C. Murphy, P. Radha, A. Jephcoat, J. Wark, et al. "Comparison between x-ray scattering and velocity-interferometry measurements from shocked liquid deuterium". *Physical Review E*, 87(4):043112, 2013.

[118] J. Clérouin, N. Desbiens, V. Dubois, and P. Arnault. "Bayesian inference of x-ray diffraction spectra from warm dense matter with the one-component-plasma model". *Physical Review E*, 94(6):061202, 2016.

[119] E. J. Davies, P. J. Carter, S. Root, R. G. Kraus, D. K. Spaulding, S. T. Stewart, and S. B. Jacobsen. "Silicate melting and vaporization during rocky planet formation". *Journal of Geophysical Research: Planets*, 125(2):e2019JE006227, 2020.

[120] K. Hirose, G. Morard, R. Sinmyo, K. Umemoto, J. Hernlund, G. Helffrich, and S. Labrosse. "Crystallization of silicon dioxide and compositional evolution of the earth's core". *Nature*, 543(7643):99–102, 2017.

[121] G. Huser, N. Ozaki, P. Colin-Lalu, V. Recoules, T. Sano, Y. Sakawa, K. Miyanishi, and R. Kodama. "Hugoniot equation of state of si-doped glow discharge polymer and scaling to other plastic ablators". *Physics of Plasmas*, 25(5):052706, 2018.

[122] M. J. Edwards, J. D. Lindl, B. K. Spears, S. V. Weber, L. J. Atherton, D. L. Bleuel, D. K. Bradley, D. A. Callahan, C. J. Cerjan, D. Clark, G. W. Collins, J. E. Fair, R. J. Fortner, S. H. Glenzer, S. W. Haan, B. A. Hammel, A. V. Hamza, S. P. Hatchett, N. Izumi, B. Jacoby, O. S. Jones, J. A. Koch, B. J. Kozioziemski, O. L. Landen, R. Lerche, B. J. MacGowan, A. J. MacKinnon, E. R. Mapoles, M. M. Marinak, M. Moran, E. I. Moses, D. H. Munro, D. H. Schneider, S. M. Sepke, D. A. Shaughnessy, P. T. Springer, R. Tommasini, L. Bernstein, W. Stoeffl, R. Betti, T. R. Boehly, T. C. Sangster, V. Y. Glebov, P. W. McKenty, S. P. Regan, D. H. Edgell, J. P. Knauer, C. Stoeckl, D. R. Harding, S. Batha, G. Grim, H. W. Herrmann, G. Kyrala, M. Wilke, D. C. Wilson, J. Frenje, R. Petrasso, K. Moreno, H. Huang, K. C. Chen, E. Giraldez, J. D. Kilkenny, M. Mauldin, N. Hein, M. Hoppe, A. Nikroo, and R. J. Leeper. "The experimental plan for cryogenic layered target implosions on the national ignition facility—the inertial confinement approach to fusion". *Physics of Plasmas*, 18(5):051003, 2011.

[123] S. X. Hu, G. Fiksel, V. N. Goncharov, S. Skupsky, D. D. Meyerhofer, and V. A. Smalyuk. "Mitigating laser imprint in direct-drive inertial confinement fusion implosions with high-z dopants". *Physical Review Letters*, 108(19):195003, 2012.

[124] G. Fiksel, S. X. Hu, V. A. Goncharov, D. D. Meyerhofer, T. C. Sangster, V. A. Smalyuk, B. Yaakobi, M. J. Bonino, and R. Jungquist. "Experimental reduction of laser imprinting and rayleigh–taylor growth in spherically compressed, medium-z-doped plastic targets". *Physics of Plasmas*, 19(6):062704, 2012.

[125] J. R. Rygg, R. F. Smith, A. E. Lazicki, D. G. Braun, D. E. Fratanduono, R. G. Kraus, J. M. McNaney, D. C. Swift, C. E. Wehrenberg, F. Coppari, M. F. Ahmed,

M. A. Barrios, K. J. M. Blobaum, G. W. Collins, A. L. Cook, P. D. Nicola, E. G. Dzenitis, S. Gonzales, B. F. Heidl, M. Hohenberger, A. House, N. Izumi, D. H. Kalantar, S. F. Khan, T. R. Kohut, C. Kumar, N. D. Masters, D. N. Polsin, S. P. Regan, C. A. Smith, R. M. Vignes, M. A. Wall, J. Ward, J. S. Wark, T. L. Zobrist, A. Arsenlis, and J. H. Eggert. "X-ray diffraction at the national ignition facility". *Review of Scientific Instruments*, 91(4):043902, 2020.

[126] D. D. Meyerhofer, J. Bromage, C. Dorrer, J. H. Kelly, B. E. Kruschwitz, S. J. Loucks, R. L. McCrory, S. F. B. Morse, J. F. Myatt, P. M. Nilson, J. Qiao, T. C. Sangster, C. Stoeckl, L. J. Waxer, and J. D. Zuegel. "Performance of and initial results from the omega ep laser system". In *Journal of Physics: Conference Series*, volume 244, page 032010. IOP Publishing, 2010.

[127] F. Coppari, R. Smith, D. Thorn, J. Rygg, D. Liedahl, R. Kraus, A. Lazicki, M. Millot, and J. Eggert. "Optimized x-ray sources for x-ray diffraction measurements at the omega laser facility". *Review of Scientific Instruments*, 90(12): 125113, 2019.

[128] A. L. Meadowcroft, C. D. Bentley, and E. N. Stott. "Evaluation of the sensitivity and fading characteristics of an image plate system for x-ray diagnostics". *Review of scientific instruments*, 79(11):113102, 2008.

[129] P. M. Celliers and M. Millot. "Imaging velocity interferometer system for any reflector (visar) diagnostics for high energy density sciences". *Review of Scientific Instruments*, 94(1):011101, 2023.

[130] M. A. Barrios, D. G. Hicks, T. R. Boehly, D. E. Fratanduono, J. H. Eggert, P. M. Celliers, G. W. Collins, and D. D. Meyerhofer. "High-precision measurements of the equation of state of hydrocarbons at 1–10 mbar using laser-driven shock waves". *Physics of Plasmas*, 17(5):056307, 2010.

[131] M. N. Pavlovskii. "Formation of metallic modifications of germanium and silicon under shock loading". *Sov. Phys. Solid State*, 9:2514, 1968.

[132] B. I. Bennett, J. D. Johnson, G. I. Kerley, and G. T. Rood. "Recent developments in the sesame equation-of-state library". *Los Alamos National Lab.(LANL), Los Alamos, NM (United States)*, 1978.

[133] A. Pak, G. Gregori, J. Knight, K. Campbell, D. Price, B. Hammel, O. L. Landen, , and S. H. Glenzer. "X-ray line measurements with high efficiency bragg crystals". *Review of Scientific Instruments*, 75(10):3747, 2004.

[134] A. Pelka, G. Gregori, D. O. Gericke, J. Vorberger, S. H. Glenzer, M. M. Günther, K. Harres, R. Heathcote, A. L. Kritcher, N. L. Kugland, B. Li, M. Makita, J. Mithen, D. Neely, C. Niemann, A. Otten, D. Riley, G. Schaumann, M. Schollmeier, A. Tauschwitz, and M. Roth. "Ultrafast melting of carbon induced by intense proton beams". *Physical review letters*, 105(26):265701, 2010.

[135] S. J. Turneaure, S. M. Sharma, and Y. M. Gupta. "Nanosecond melting and recrystallization in shock-compressed silicon". *Physical review letters*, 121(13): 135701, 2018.

[136] J. W. E. Drewitt. "Liquid structure under extreme conditions: high-pressure x-ray diffraction studies". *Journal of Physics: Condensed Matter*, 33(50):503004, 2021.

[137] S. Singh, A. L. Coleman, S. Zhang, F. Coppari, M. G. Gorman, R. F. Smith, J. H. Eggert, R. Briggs, and D. E. Fratanduono. "Quantitative analysis of diffraction by liquids using a pink-spectrum x-ray source". *Journal of Synchrotron Radiation*, 29(4):1033, 2022.

[138] J. H. Hubbell, W. J. Veigele, E. A. Briggs, R. T. Brown, D. T. Cromer, and R. J. Howerton. "Atomic form factors, incoherent scattering functions, and photon scattering cross sections". *Journal of physical and chemical reference data*, 4(3): 471, 1975.

[139] D. A. Chapman. *User Guide and Theoretical Basis for the Multi-Component Scattering Spectra (MCSS) Thomson Scattering Analysis Code (O)*. AWE, 2017.

[140] Y. Varshni. "Eigenenergies and oscillator strengths for the hulthén potential". *Physical Review A*, 41(9):4682, 1990.

[141] J. Vorberger, D. O. Gericke, and W.-D. Kraeft. "The equation of state for hydrogen at high densities". *High Energy Density Physics*, 9(3):448, 2013.

[142] W. Ebeling, H. Reinholz, and G. Röpke. "Hydrogen, helium and lithium plasmas at high pressures". *The European Physical Journal Special Topics*, 229:3403, 2020.

[143] R. M. More, K. H. Warren, D. A. Young, and G. B. Zimmerman. "A new quotidian equation of state (qeos) for hot dense matter". *The Physics of fluids*, 31(10):3059–3078, 1988.

[144] J. MacFarlane, I. Golovkin, and P. Woodruff. "Helios-cr–a 1-d radiation-magnetohydrodynamics code with inline atomic kinetics modeling". *Journal of Quantitative Spectroscopy and Radiative Transfer*, 99(1-3):381–397, 2006.

[145] S. X. Hu, B. Militzer, L. A. Collins, K. P. Driver, and J. D. Kress. "First-principles prediction of the softening of the silicon shock hugoniot curve". *Physical Review B*, 94(9):094109, 2016.

[146] R. Paul, S. Hu, and V. Karasiev. "Crystalline phase transitions and vibrational spectra of silicon up to multiterapascal pressures". *Physical Review B*, 100(14): 144101, 2019.

[147] W. H. Gust and E. B. Royce. "Axial yield strengths and two successive phase transition stresses for crystalline silicon". *Journal of Applied Physics*, 42(5):1897–1905, 1971.

[148] T. Goto, T. Sato, and Y. Syono. "Reduction of shear strength and phase-transition in shock-loaded silicon". *Japanese Journal of Applied Physics*, 21(6A): L369, 1982.

[149] R. Paul, S. X. Hu, and V. V. Karasiev. "Anharmonic and anomalous trends in the high-pressure phase diagram of silicon". *Physical Review Letters*, 122(12):125701, 2019.

[150] R. Paul. Private Communication, 2022.

[151] O. Strickson and E. Artacho. "Ab initio calculation of the shock hugoniot of bulk silicon". *Physical Review B*, 93(9):094107, 2016.

[152] B. Witte, M. Shihab, S. Glenzer, and R. Redmer. "Ab initio simulations of the dynamic ion structure factor of warm dense lithium". *Physical Review B*, 95(14): 144105, 2017.

[153] M. Schörner, M. Bethkenhagen, T. Döppner, D. Kraus, L. B. Fletcher, S. H. Glenzer, and R. Redmer. "X-ray thomson scattering spectra from density functional theory molecular dynamics simulations based on a modified chihara formula". *Physical Review E*, 107(6):065207, 2023.

[154] V. Vacca, M. Murgia, F. Govoni, T. Enßlin, N. Oppermann, L. Feretti, G. Giovannini, and F. Loi. "Magnetic fields in galaxy clusters and in the large-scale structure of the universe". *Galaxies*, 6(4):142, 2018.

[155] E. G. Zweibel and C. Heiles. "Magnetic fields in galaxies and beyond". *Nature*, 385(6612):131–136, 1997.

[156] L. Biermann and A. Schlüter. "Cosmic radiation and cosmic magnetic fields. ii. origin of cosmic magnetic fields". *Physical Review*, 82(6):863, 1951.

[157] K. Subramanian. "From primordial seed magnetic fields to the galactic dynamo". *Galaxies*, 7(2):47, 2019.

[158] D. Ryu, H. Kang, J. Cho, and S. Das. "Turbulence and magnetic fields in the large-scale structure of the universe". *Science*, 320(5878):909–912, 2008.

[159] A. A. Schekochihin and S. C. Cowley. "Turbulence, magnetic fields, and plasma physics in clusters of galaxies". *Physics of Plasmas*, 13(5):056501, 2006.

[160] F. Rincon. "Dynamo theories". *Journal of Plasma Physics*, 85(4):205850401, 2019.

[161] A. A. Schekochihin, S. C. Cowley, S. F. Taylor, J. L. Maron, and J. C. McWilliams. "Simulations of the small-scale turbulent dynamo". *The Astrophysical Journal*, 612(1):276, 2004.

[162] S. Bovino, D. R. Schleicher, and J. Schober. "Turbulent magnetic field amplification from the smallest to the largest magnetic prandtl numbers". *New Journal of Physics*, 15(1):013055, 2013.

[163] A. A. Schekochihin, A. B. Iskakov, S. C. Cowley, J. C. McWilliams, M. R. E. Proctor, and T. A. Yousef. "Fluctuation dynamo and turbulent induction at low magnetic prandtl numbers". *New Journal of Physics*, 9(8):300, 2007.

[164] N. Kleeorin and I. Rogachevskii. "Growth rate of small-scale dynamo at low magnetic prandtl numbers". *Physica Scripta*, 86(1):018404, 2012.

[165] A. F. A. Bott, P. Tzeferacos, L. Chen, C. A. J. Palmer, A. Rigby, A. R. Bell, R. Bingham, A. Birkel, C. Graziani, D. H. Froula, J. Katz, M. Koenig, M. W. Kunz, C. Li, J. Meinecke, F. Miniati, R. Petrasso, H.-S. Park, B. A. Remington, B. Reville, J. S. Ross, D. Ryu, D. Ryutov, F. H. Séguin, T. G. White, A. A. Schekochihin, D. Q. Lamb, and G. Gregori. "Time-resolved turbulent dynamo in a laser plasma". *Proceedings of the National Academy of Sciences*, 118(11): e2015729118, 2021.

[166] J. Meinecke1, H. W. Doyle, F. Miniati, A. R. Bell, R. Bingham, R. Crowston, R. P. Drake, M. Fatenejad, M. Koenig, Y. Kuramitsu, C. C. Kuranz, D. Q. Lamb, D. Lee, M. J. MacDonald, C. D. Murphy, H.-S. Park, A. Pelka, A. Ravasio, Y. Sakawa, A. A. Schekochihin, A. Scopatz, P. Tzeferacos, W. C.Wan, N. C.Woolsey, R. Yurchak, B. Reville, and G. Gregori. "Turbulent amplification of magnetic fields in laboratory laser-produced shock waves". *Nature Physics*, 10 (7):520–524, 2014.

[167] S. A. Muller, D. N. Kaczala, H. M. Abu-Shawareb, E. L. Alfonso, L. C. Carlson, M. Mauldin, P. Fitzsimmons, D. Lamb, P. Tzeferacos, L. Chen, G. Gregori, A. Rigby, A. F. A. Bott, T. G. White, D. Froula, and J. Katz. "Evolution of the design and fabrication of astrophysics targets for turbulent dynamo (tdyno) experiments on omega". *Fusion Science and Technology*, 73(3):434–445, 2018.

[168] P. Tzeferacos, A. Rigby, A. F. A. Bott, A. R. Bell, R. Bingham, A. Casner, F. Cattaneo, E. M. Churazov, J. Emig, F. Fiuza, C. B. Forest, J. Foster, C. Graziani, J. Katz, M. Koenig, C.-K. Li, J. Meinecke, R. Petrasso, H.-S. Park, B. A. Remington, J. S. Ross, D. Ryu, D. Ryutov, T. G. White, B. Reville, F. Miniati, A. A. Schekochihin, D. Q. Lamb, D. H. Froula, and G. Gregori. "Laboratory evidence of dynamo amplification of magnetic fields in a turbulent plasma". *Nature communications*, 9(1):591, 2018.

[169] J. Meinecke, P. Tzeferacos, J. S. Ross, A. F. Bott, S. Feister, H.-S. Park, A. R. Bell, R. Blandford, R. L. Berger, R. Bingham, A. Casner, L. E. Chen, J. Foster, D. Froula, C. Goyon, D. Kalantar, M. Koenig, B. Lahmann, C. Li, Y. Lu, C. A. J. Palmer, R. Petrasso, H. Poole, B. Remington, B. Reville, A. Reyes, A. Rigby, D. Ryu, G. Swadling, A. Zylstra, F. Miniati, S. Sarkar, A. A. Schekochihin, D. Q. Lamb, and G. Gregori. "Strong suppression of heat conduction in a laboratory

replica of galaxy-cluster turbulent plasmas". *Science Advances*, 8(10):eabj6799, 2022.

[170] M. J.-E. Manuel, A. B. Zylstra, H. G. Rinderknecht, D. T. Casey, M. J. Rosenberg, N. Sinenian, C. K. Li, J. A. Frenje, F. H. Séguin, and R. D. Petrasso. "Source characterization and modeling development for monoenergetic-proton radiography experiments on omega". *Review of scientific instruments*, 83(6):063506, 2012.

[171] F. H. Séguin, J. A. Frenje, C. K. Li, D. G. Hicks, S. Kurebayashi, J. R. Rygg, B.-E. Schwartz, R. D. Petrasso, S. Roberts, J. M. Soures, D. D. Meyerhofer, T. C. Sangster, J. P. Knauer, C. Sorce, V. Y. Glebov, C. Stoeckl, T. W. Phillips, R. J. Leeper, K. Fletcher, and S. Padalino. "Spectrometry of charged particles from inertial-confinement-fusion plasmas". *Review of Scientific Instruments*, 74 (2):975–995, 2003.

[172] A. F. A. Bott, C. Graziani, P. Tzeferacos, T. G. White, D. Q. Lamb, G. Gregori, and A. A. Schekochihin. "Proton imaging of stochastic magnetic fields". *Journal of Plasma Physics*, 83(6):905830614, 2017.

[173] J. Katz, R. Boni, C. Sorce, R. Follett, M. J. Shoup, and D. H. Froula. "A reflective optical transport system for ultraviolet thomson scattering from electron plasma waves on omega". *Review of Scientific Instruments*, 83(10):10E349, 2012.

[174] A. Visco, R. P. Drake, D. H. Froula, S. H. Glenzer, and B. B. Pollock. "Temporal dispersion of a spectrometer". *Review of Scientific Instruments*, 79(10):10F545, 2008.

[175] D. E. Evans. "The effect of impurities on the spectrum of laser light scattered by a plasma". *Plasma Physics*, 12(8):573, 1970.

[176] D. E. Evans and J. Katzenstein. "Laser light scattering in laboratory plasmas". *Reports on Progress in Physics*, 32(1):207, 1969.

[177] G. B. Rybicki and A. P. Lightman. *Radiative processes in astrophysics*. John Wiley & Sons, 1991.

[178] G. A. Rochau, J. E. Bailey, G. A. Chandler, T. J. Nash, D. S. Nielsen, G. S. Dunham, O. F. Garcia, N. R. Joseph, J. W. Keister, M. J. Madlener, D. V. Morgan, K. J. Moy, and M. Wu. "Energy dependent sensitivity of microchannel plate detectors". *Review of scientific instruments*, 77(10):10E323, 2006.

[179] P. Tzeferacos, M. Fatenejad, N. Flocke, C. Graziani, G. Gregori, D. Q. Lamb, D. Lee, J. Meinecke, A. Scopatz, and K. Weide. "Flash mhd simulations of experiments that study shock-generated magnetic fields". *High Energy Density Physics*, 17:24–31, 2015.

[180] L. Spitzer Jr and R. Härm. "Transport phenomena in a completely ionized gas". *Physical Review*, 89(5):977, 1953.

[181] Wikipedia. "Metropolis–hastings algorithm". Available at: `https://en.wikipedia.org/wiki/Metropolis%E2%80%93Hastings_algorithm`, (Accessed: 5th April 2024).

[182] S. Groth, T. Dornheim, T. Sjostrom, F. D. Malone, W. M. C. Foulkes, and M. Bonitz. "*Ab initio* exchange-correlation free energy of the uniform electron gas at warm dense matter conditions". *Physical Review Letters*, 119:135001, 2017.

[183] T. Dornheim, Z. A. Moldabekov, and P. Tolias. "Analytical representation of the local field correction of the uniform electron gas within the effective static approximation". *Physical Review B*, 103(16):165102, 2021.

[184] J. Hansen and I. R. McDonald. *Theory of Simple Liquids*. Academic Press, London, 1990.

Appendix A

Using X-ray Scattering in SPECT3D

The spectral radiance of an X-ray source at a brightness temperature T is described by Planck's law,

$$B_\nu(\nu, T) = \frac{2h\nu^3}{c^2} \frac{1}{\exp\left(\frac{h\nu}{k_B T}\right) - 1} \,. \tag{A.0.1}$$

Assuming a Gaussian X-ray source with an incident frequency $\nu_i = c/\lambda_i = E_{ph}/h$, the source function, as illustrated in Figure A.1, is defined as,

$$G_\nu = B_\nu(\nu_i, T) \times \exp\left[-\frac{(\nu - \nu_i)^2}{2\sigma^2}\right] , \tag{A.0.2}$$

where the σ can be found from the defined full-width at half-maximum (FWHM),

$$2\sigma = \frac{\mathrm{FWHM}}{\sqrt{2\ln 2}} \,. \tag{A.0.3}$$

If the X-ray source is placed a distance D_x from the plasma, the solid angle is given by,

$$\Omega_\mathrm{plasma} = \frac{A_\mathrm{plasma}}{D_\mathrm{x}^2} \,, \tag{A.0.4}$$

where A_plasma is the area of plasma the X-ray source is incident on. The total X-ray energy incident on the plasma is therefore,

$$E_\mathrm{in} = \int \mathrm{d}\nu \, G_\nu \times \left(\Omega_\mathrm{plasma} \, A_\mathrm{x} \, t_\mathrm{x}\right) \,, \tag{A.0.5}$$

where t_x and A_x are the pulse length and area of the X-ray source, respectively.

If the X-ray source is produced by a laser incident on a foil, then the required laser energy is,

$$E_\mathrm{L} = \frac{E_\mathrm{in}}{\eta_x \frac{\Omega_\mathrm{plasma}}{4\pi}} \,, \tag{A.0.6}$$

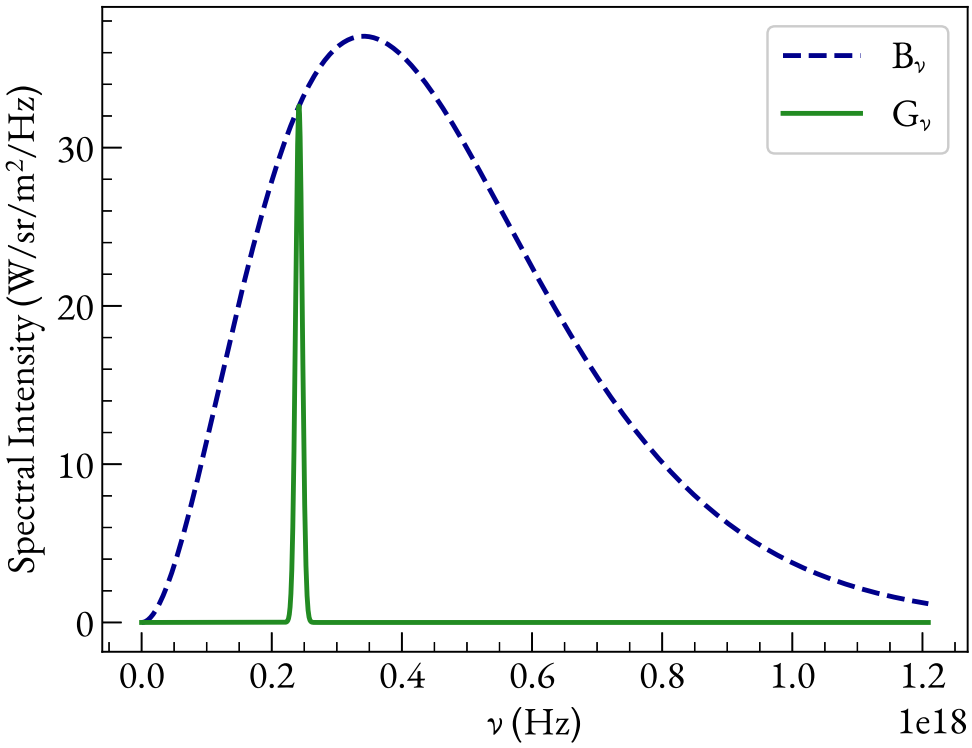

Figure A.1: Spectral intensity of an X-ray source with $E_{ph} = 1000\,\text{eV}$, FWHM $= 50\,\text{eV}$ and source brightness $T = 500\,\text{eV}$.

where ν_x is the X-ray conversion efficiency.

Using a SPECT3D detector placed a distance D_{det} from the plasma, the resultant detected SPECT3D spectral intensity, $W(h\nu) = \text{Wm}^{-2}\text{eV}^{-1}$, can be converted to scattered intensity (photons/eV) via,

$$I(h\nu) = \frac{W(h\nu) t_{\text{X}} A_{\text{X}}}{h\nu e \frac{\Omega_{\text{det}}}{4\pi}}\,, \tag{A.0.7}$$

where the detector solid angle is,

$$\Omega_{\text{det}} = \frac{A_{\text{det}}}{D_{\text{det}}^2}\,, \tag{A.0.8}$$

and A_{det} is the area of the detector where the scattered signal is observed.

Appendix B

Markov-Chain Monte Carlo for Inverse Problem Instability

In experimental data analysis, the inverse problem instability refers to the generation of similar outputs produced by a wide variety of parameter inputs, leading to significant uncertainty in the true parameter space. This challenge is effectively addressed with a Bayesian inference employing Markov-Chain Monte Carlo (MCMC) algorithms, which efficiently sample large dimensional spaces [95]. Bayesian inference implies that the likelihood, P, of encountering a specific set of parameters, Ψ, given an observed outcome I_{exp} is,

$$P(\Psi|I_{\text{exp}}) = \frac{P(I_{\text{exp}}|\Psi)P(\Psi)}{P(I_{\text{exp}})}\,. \tag{B.0.1}$$

Here, $P(\Psi)$ is the prior distribution of possible parameters, $P(I_{\text{exp}})$ is the marginal likelihood of the observed data over all possible parameters and $P(I_{\text{exp}}|\Psi)$ is the likelihood of finding I_{exp} given the input parameters Ψ.

An illustrative depiction of the MCMC algorithms employed to sample the posterior distribution of the parameters is shown in Figure B.1. This methodology offers an efficient means of sampling potential parameters that generate outcomes closely aligned, within a specified uncertainty, with the experimentally observed results. The level of uncertainty is dictated by the forward model likelihood, $P(I_{\text{exp}}|\Psi) = e^{-\beta_{\text{cost}}}$. This cost function is user-defined to establish an acceptance percentage for each Ψ.

A standard likelihood function, commonly referred to as a 'soft-boundary' [95], determines the maximum error between a fitted spectrum, I_{fit}, generated using parameters Ψ, and the experimental results,

$$\beta_{\text{cost}} = \max\left[\frac{I_{\text{fit}}(\omega) - I_{\text{exp}}(\omega)}{\sqrt{2}\sigma}\right]^2. \tag{B.0.2}$$

The factor σ is the standard deviation representative of the experimental noise. Typically, this value is not known *a priori* but chosen to ensure that the range of converged

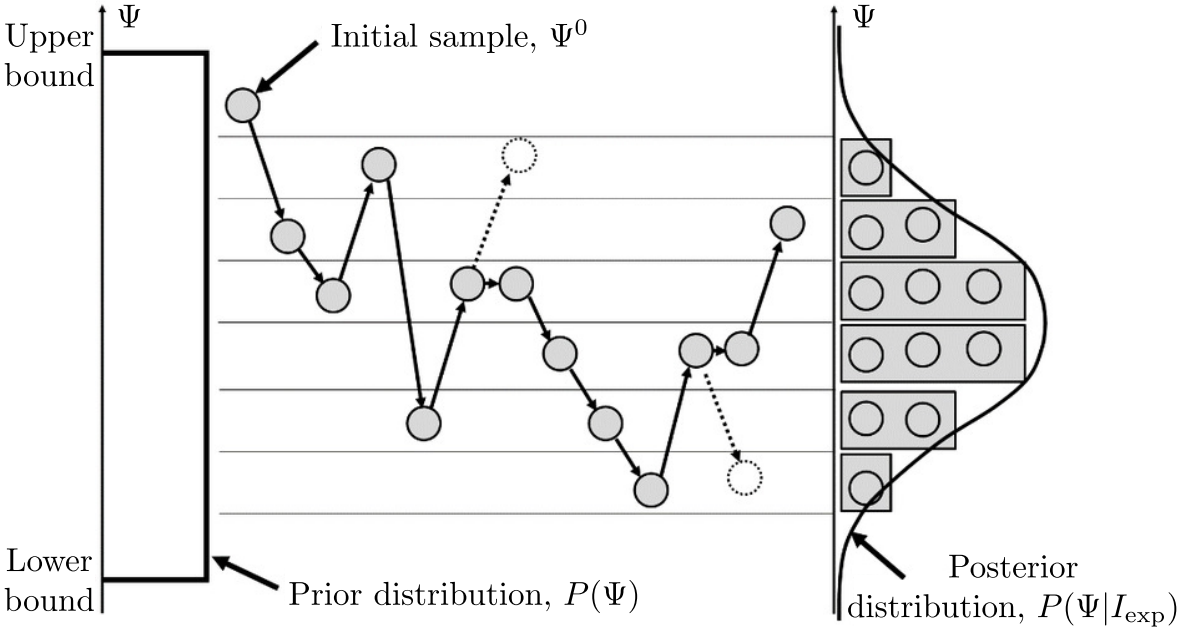

Figure B.1: Adapted from Ref. [181]: Sampling algorithm for a normal one-dimensional posterior probability distribution. The method generates a random walk, or Markov chain, to assess the parameter space Ψ. At each iteration, a new step (going from left to right) is proposed based on the state of the current sample. This proposed step is then either accepted (marked by filled circles) or rejected (denoted by unfilled dashed circles) depending on the value of the probability distribution function at that position. Upon achieving convergence, the parameter posterior distribution, $P(\Psi|I_{\text{exp}})$, exhibits self-similarity.

MCMC fits falls within the experimental uncertainty.

The impact of the chosen σ on the MCMC exploration is demonstrated in Figure B.2. In this illustration, experimental data is generated using a Gaussian function, characterised by $\Psi_{\text{raw}}(\text{Amplitude} = 1, \mu = 0.5, \text{FWHM} = 10)$, compounded with random normal noise with a scale of 0.05. As σ increases, the range of accepted fits and corresponding posterior distributions exhibit a significant broadening. Notably, at $\sigma = 0.1$, the span of fits surpasses the noisy experimental data, indicating a poor convergence to the observed data. Conversely, at $\sigma = 0.005$, the exceptionally narrow range of fits fails to effectively capture the data. Such a small σ consequently yields mean fitting parameters that deviate substantially from the original values, highlighting its inadequate assessment of the noisy data. For σ values on the order of the added experimental

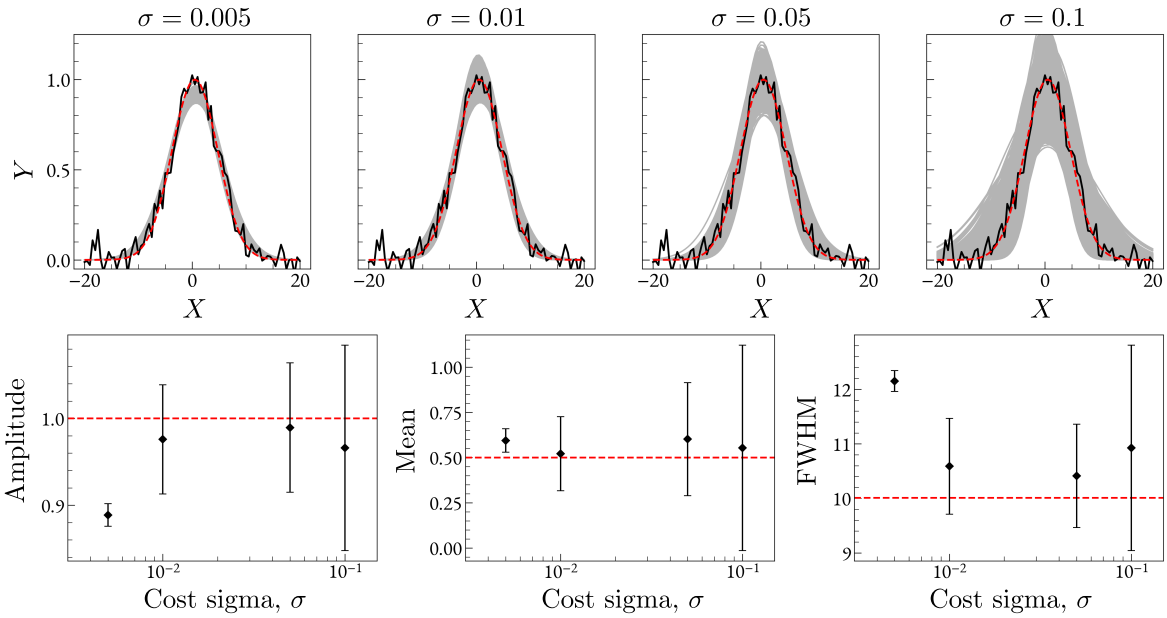

Figure B.2: Effect the chosen sigma cost value has on the converged MCMC parameter space. The upper panel shows the range of converged fits in grey compared to the noisy $I_{\text{exp}}(X)$ data in black. The lower panels show the posterior parameter distributions using each sigma. The original Gaussian fitting parameters, Ψ_{raw}, and spectrum are shown as red dashed lines throughout.

noise ($\sigma = 0.01 - 0.05$), similar fitting and parameter convergences are observed. This demonstrates that within this range, the chosen σ does not significantly impact the quoted parameters.

While employing a cost function such as the sum of squares for the example depicted in Figure B.2 would lead to a tighter convergence around the Ψ_{raw} parameters, it is essential to recognise that such a cost function assumes a perfect fitting model. While this assumption might be suitable in the example case explored here, it often does not hold true for the data presented within this thesis. Utilising such a cost function could therefore potentially yield high confidence in false results, as the fitting model may not adequately account for the complexities and uncertainties inherent in real experimental data. Therefore, cost functions must be selected to align with the characteristics of the actual data being analysed.

Appendix C

Determining Pressure from Static Structure

For general equation of state calculations of a single-temperature plasma, the pressure, P, from the total free energy, F, can be estimated via the Maxwell relation

$$P = \left.\frac{\partial F}{\partial V}\right|_{N,T}, \tag{C.0.1}$$

in which the particle (ion) number, N, and temperature, T, are held constant, and the derivative is taken with respect to the volume, V. This expression can be related in the form of a partial derivative with respect to the mean number density $n = N/V$,

$$P = -n^2 \left.\frac{\partial f}{\partial n}\right|_{T}, \tag{C.0.2}$$

where $f = F/N$ is the free energy per particle. Considering a 'two-fluid' model [141, 142], the total free energy can be decomposed into three contributions; electron f_e, ionic f_i, and electron-ion interactions f_{ei}, i.e.

$$f = f_e + f_i + f_{ei}\,. \tag{C.0.3}$$

This provides the pressure of the plasma according to,

$$\begin{aligned} P = & -n_i^2 \left.\frac{\partial f_e}{\partial n_i}\right|_{T} - n_i^2 \left.\frac{\partial f_{ei}}{\partial n_i}\right|_{T} - n_i^2 \left.\frac{\partial f_i}{\partial n_i}\right|_{T} \\ & = P_e + P_{ei} + P_i\,. \end{aligned} \tag{C.0.4}$$

C.1 Electron-electron contribution

The electronic pressure, P_e, from a density $n_e = n_i/\langle Z_i \rangle$, in which $\langle Z_i \rangle$ is the mean ionisation of the plasma, can be broken down in to a non-interacting, ideal gas-like

contribution, f_e^{id}, and a corrective exchange-correlation contribution arising from the interacting electron gas, f_e^{XC}.

$$\begin{aligned} P_e &= P_e^{\mathrm{id}} + P_e^{XC} \\ &= \langle Z_i \rangle \frac{\mathcal{F}_{3/2}(\eta_e)}{n_e \Lambda_e^3/2} n_i k_{\mathrm{B}} T - n_i^2 \left. \frac{\partial f_e^{\mathrm{XC}}}{\partial n_i} \right|_T , \end{aligned} \tag{C.1.1}$$

where $\Lambda_e = (2\pi\hbar^2/m_e k_{\mathrm{B}} T_e)^{1/2}$ is the thermal de Broglie wavelength, $\mathcal{F}_j$ denotes the complete j^{th} order Fermi-Dirac integral and η_e is the dimensionless chemical potential of the free electrons,

$$\eta_e = \mathcal{F}_{1/2}^{-1} \left[\frac{n_e \hbar^3}{2} \left(\frac{2\pi}{m_e k_{\mathrm{B}} T_e} \right)^{3/2} \right] . \tag{C.1.2}$$

The exchange-correlation can be approximated using a finite difference and Groth *et al.* [182] parametric representation of f_e^{XC},

$$\begin{aligned} P_e^{\mathrm{XC}} &\approx - n_i^2 \frac{f_e^{\mathrm{XC}}(n_i(1+\delta), T) - f_e^{\mathrm{XC}}(n_i(1-\delta), T))}{n_i(1+\delta) - n_i(1-\delta)} \\ &= - \frac{n_i}{2\delta} \left[f_e^{\mathrm{XC}}(n_i(1+\delta), T) - f_e^{\mathrm{XC}}(n_i(1-\delta), T)) \right] . \end{aligned} \tag{C.1.3}$$

C.2 Electron-ion contribution

The pressure contribution arising from electron-ion interactions is determined in linear response,

$$P_{ei} = - \frac{n_i^2}{4\pi^2} \frac{\partial}{\partial n_i} \left(\int_0^\infty \mathrm{d}k \, k^2 \, \chi_{ee}(k, 0) \left[V_{ei}^{\mathrm{eff}}(k) \right]^2 \right) \Big|_T , \tag{C.2.1}$$

where the electron-ion interaction is taken as Coulombic using Z_i^*, the effective ion charge 'seen' by the free electrons,

$$V_{ei}(k) \approx - 4\pi \frac{Z_i^* e^2 k_{\mathrm{C}}}{k^2} , \tag{C.2.2}$$

and the static electron density response function, $\chi_{ee}(k,0)$, is taken in the random phase approximation (RPA). The static electron density response function can therefore be written,

$$\begin{aligned}\chi_{ee}(k,0) &= \frac{\Pi^0_{ee}(k,0)}{1 - V_{ee}(k)[1 - G_{ee}(k,0)]\Pi^0_{ee}(k,0)} \\ &\equiv \frac{\Pi^{\mathrm{SLFC}}_{ee}(k,0)}{1 - V_{ee}(k)\Pi^{\mathrm{SLFC}}_{ee}(k,0)}\,, \qquad \text{(C.2.3)}\\ \Pi^{\mathrm{SLFC}}_{ee}(k,0) &= \frac{\Pi^0_{ee}(k,0)}{1 + V_{ee}(k)G_{ee}(k,0)\Pi^0_{ee}(k,0)}\,, \qquad \text{(C.2.4)}\end{aligned}$$

where $V_{ee}(k) = -4\pi e^2 k_{\mathrm{C}}/k^2$ is the bare electron-electron Coulomb interaction, $\Pi^0_{ee}(k,0)$ is the static electron-electron polarisation function in RPA and $G_{ee}(k,0)$ represents the static local field correction which can be treated using the effective static approximation [183]. In the highly degenerate limit, the polarisation function can be approximated using the Lindhard form,

$$\lim_{T\to 0} \Pi^0_{ee}(k,0) = -\frac{3n_e}{2E_{\mathrm{F}}}\frac{g(q_0)}{2q_0} = \frac{3n_e}{4q_0E_{\mathrm{F}}}\left(q_0 + \frac{1-q_0^2}{2}\ln\left|\frac{1+q_0}{1-q_0}\right|\right)\,, \qquad \text{(C.2.5)}$$

in which $q_0 = k/2k_{\mathrm{F}}$ and $k_{\mathrm{F}} = (2E_{\mathrm{F}}m_e)^{1/2} = (3\pi^2 n_e)^{1/3}$ is the Fermi wave number.

C.3 Ion-ion contribution

As with the electronic contribution, the ionic pressure, P_i, decomposes into ideal and interaction (due to ionic correlations) components,

$$\begin{aligned}P_i &= P_i^{\mathrm{id}} + P_i^{\mathrm{cor}} \\ &= n_i k_{\mathrm{B}} T - 2\pi n_i^2 \int_0^\infty \mathrm{d}r\, r^2 \left[g_{ii}(r; V_{ii}^{\mathrm{eff}}(r)) - 1\right] \mathcal{V}_{ii}^{\mathrm{eff},P}(r)\,, \qquad \text{(C.3.1)}\end{aligned}$$

in which the effective ion-ion interaction potential for the evaluation of the excess ion pressure is defined as

$$\mathcal{V}_{ii}^{\mathrm{eff},P}(r) = \left(\frac{r}{3}\frac{\partial}{\partial r} - n_i \frac{\partial}{\partial n_i}\right) V_{ii}^{\mathrm{eff}}(r)\,. \tag{C.3.2}$$

The pair distribution function, g_{ii}, of the ions [184] can be evaluated via the static structure factor using a consistent effective ion-ion potential„

$$g_{ii}(r; V_{ii}^{\mathrm{eff}}(r)) - 1 = \frac{1}{2\pi^2 r n_i} \int_0^\infty \mathrm{d}k\, k \left[S_{ii}(k; V_{ii}^{\mathrm{eff}}(r)) - 1\right] \sin(kr)\,. \tag{C.3.3}$$